Hindawi
BioMed Research International
Volume 2017, Article ID 9878109, 10 pages
https://doi.org/10.1155/2017/9878109

Research Article

Design and Testing of an Experimental Steam-Induced Burn Model in Rats

Vlad Porumb,[1,2] Alexandru Florentin Trandabăţ,[3] Cristina Terinte,[4] Irina Draga Căruntu,[5] Elena Porumb-Andrese,[6] Mihail Gabriel Dimofte,[1,2] and Dragoş Pieptu[2,7]

[1] *Department of Surgery, School of Medicine, Grigore T. Popa University of Medicine and Pharmacy, 16 University Street, 700115 Iaşi, Romania*
[2] *Second Surgery Clinic, Regional Institute of Oncology, 2-4 General Henri Mathias Berthelot Street, 700483 Iaşi, Romania*
[3] *Department of Electrical Measurements and Materials, School of Electrical Engineering, Gheorghe Asachi Technical University, 3 Dimitrie Mangeron Street, 700050 Iaşi, Romania*
[4] *Department of Pathology, Regional Institute of Oncology, 2-4 General Henri Mathias Berthelot Street, 700483 Iaşi, Romania*
[5] *Department of Morpho-Functional Sciences I-Histology, School of Medicine, Grigore T. Popa University of Medicine and Pharmacy, 16 University Street, 700115 Iaşi, Romania*
[6] *Department of Dermatology, School of Medicine, Grigore T. Popa University of Medicine and Pharmacy, 16 University Street, 700115 Iaşi, Romania*
[7] *Department of Plastic Surgery, School of Medicine, Grigore T. Popa University of Medicine and Pharmacy, 16 University Street, 700115 Iaşi, Romania*

Correspondence should be addressed to Alexandru Florentin Trandabăţ; ftranda@yahoo.com

Received 2 June 2017; Revised 18 July 2017; Accepted 7 September 2017; Published 12 October 2017

Academic Editor: François Berthiaume

Background. Most of the current models for experimental burns pose difficulties in ensuring consistency and standardization. *Aim of Study*. We aimed to develop an automated, reproducible technique for experimental burns using steam-based heat transfer. *Methods*. The system developed for steam exposure was based on a novel, integrated, computer-controlled design. Three groups of rats were exposed to steam for 1, 3, and 7 seconds. The lesions were evaluated after 20 minutes, 48 hours, and 72 hours after burn induction. *Results*. One-second steam application produced a superficial second-degree burn; three-second application induced deep second-degree burn; and seven-second application led to a third-degree burn. *Conclusion*. The high level of automation of our integrated, computer-controlled system makes the difference between our system and other models, by ensuring the control of the duration of exposure, temperature, and pressure and eliminating as many potential human generated errors as possible. The automated system can accurately reproduce specific types of burns, according to histological assessment. This model could generate the reproducible data needed in the study of burn pathology and in order to assess new treatments.

1. Introduction

The establishment of new approaches for experimental burns is an important tool in advancing the understanding of burn pathology. Adequate methods of experimental testing using different burn models were crucial to the development of novel treatments. Rat models have been used since the 1960s and have since then evolved to better represent and mimic human burn pathology [1]. Walker and Mason (1968) established the first straightforward and reproducible burn model in 1968, based on the production of burn on rats by direct contact with hot water [2]. The rat burn model can provide useful information on how human tissues react under specific conditions due to the similarity of the tissue structure and physiology between rats and humans. Data from rat models can be extrapolated to include post-burn physiopathology due to the similarity of both tissues, rat and human, in the burn and healing processes [3].

Burns are generally created using one of four different methods in animal models: hot water, hot metal tools, electricity, and heated paraffin [3–6]. The different burn models require specific parameters such as elevated temperatures, duration of exposure, and specific materials like hot water or aluminum previously heated in a hot water bath [7–10]. Other materials can be used in a rat model burn experiment, such as a hot metal plate or an electric coil; however, these materials are more likely to cause third-degree burns due to high temperatures reaching 170°C and 400°C, respectively [8, 9].

Although burn experiments using rat models yield data that may be useful in understanding burn pathology and physiology, it is difficult to consistently induce a certain type of burn because the various parameters are often difficult to reproduce consistently within and among applications [11–19]. The aim of this study is to create a model that will allow the objective collection of data in order to study burn pathology. The reproducible model will have strictly controlled variables such as exposure time to the heat, depth of the lesion, and source of the heat.

2. Materials and Methods

2.1. Experimental Design. This study was approved on January 21, 2015, by Grigore T. Popa University of Medicine and Pharmacy Research Ethics Committee under full compliance with the European Directive 206/27.04.2004. The study included 54 Wistar male rats, each having a weight of 300 ± 20 grams. Rats were housed in individually ventilated cages with 12/12-hour light/dark cycles, food and water ad libitum. The rats were divided into three equal groups, each containing 18 rats, and labeled Group 1, Group 2, and Group 3, respectively. Group 1 rats were exposed to hot steam for one minute, Group 2 rats were exposed for three seconds, and Group 3 rats were exposed for seven seconds. The rats were anaesthetized with Ketamine/Xylazine cocktail 0.1 mL/100 g of rat, intraperitoneally. Following anesthesia, the dorsa of the rats were shaved and depilated using hair removal cream (Farmec SA, Romania). Post-burn analgesia was provided by subcutaneous administration of buprenorphine 0.05 mg/kg three times daily (Bupredine Multidose 0.3 mg/ml Produlab Pharma B. V. Holland) for 7 days or until sacrifice, if scheduled earlier than 7 days. Throughout the experiment, the rat's general state was observed and we could see normal behaviors including normal exploratory behavior, walking, standing on their hind legs, stretching upright, burrowing, and nesting with no apparent indication of pain or suffering, like puffed out hair, pinched in sides, or weight loss. After the burn induction, skin changes based on the following aspects: swelling, redness, blistering, crust, secretion, granulation tissue, bleeding, scar tissue, and local complications or infections were documented by standardized digital photography imaging. Each group was further divided into three subgroups comprised of three rats each.

2.2. The Integrated Steam Application System. The integrated steam application system is comprised of the following:

(i) A computer regulates parameter control through a user interface (Figure 1) utilizing Lab VIEW 2010 software to enable the display of collected data, input, the status of the steam generator, valve activation and electrical relay, time exposure, temperatures along the steam circuit, the distance between steam nozzle and dermis, and the depth to which the steam pervaded the skin.

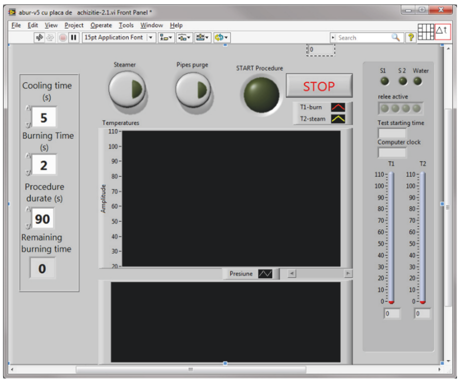

Cooling time (s) 5
Burning Time (s) 2
Procedure durate (s) 90
Remaining burning time 0

Figure 1: The main panel of the program's interface.

(ii) The data board, which can carry out programmed computer functions, was connected to temperature (LM35) and pressure sensors, electrical relays and valves (220 Volts), a water pump, a steam generator, an electrical 12 Volt power supply, steam pipes, and silicon steam nozzle (located between the steam jet and tegument).

The data board controls the relays and electric valves, which turn water into steam using the steam generator. The temperature of the steam is regulated by the data board and is monitored by temperature sensors. The schematic diagram of the integrated system for producing standardized burns is represented in Figure 2.

Firstly, the digital port D3 activated the steam generator producing hot steam through relay R3. Once the circuit is initiated, the acquisition card which controls the D1 port sends a signal to relay R1, activating the E1 solenoid valve, through which the steam from the steam generator is propelled. To ensure a uniform and standardized temperature of the causal burn agent, the temperature of the steam is monitored using the T1 temperature sensor.

The temperature of the steam was required to be greater than 90°C. If, however, the system was initiated accidentally, the human operator was alerted both visually and acoustically, not allowing initiation of the circuit. When the automated system is cocked, the first solenoid E1 valve is open, while the second solenoid E2 valve is closed. This prevents accidents and possibly lower temperatures that could occur if the steam would circulate within an appurtenant heat circuit.

The steam is oriented toward the silicon head by programming the T1 temperature sensor to detect temperatures greater than 90°C which allows the first solenoid E1 valve to close and the second solenoid E2 valve to open when button B1 is pressed.

Human error was avoided by creating a controlled time loop. Thus, skin steam exposure could only take place for a certain period of time. Time of exposure was calculated from the moment the silicon head touched the rat's skin via

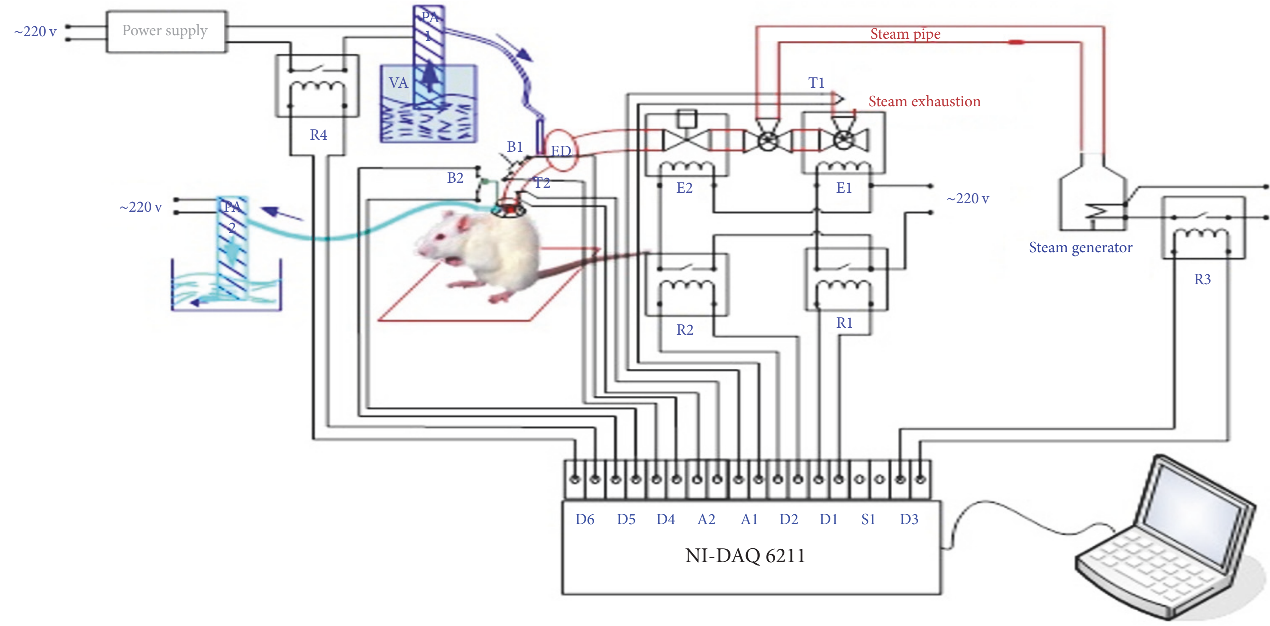

Figure 2: Schematic diagram of the standardized experimental model used to induce cutaneous burns in rats (R1, R2, R3, R4 - 5 Volt relays; E1, E2 - 220 V solenoid valves; T1, T2 - LM35 temperature sensors; PA1, PA2 - water pump; FD - filter sludge trap; B1 - cocking button; B2 – trigger button; NI-DAQ 6211 acquisition card with the following ports: A1 - analog input of temperature sensor T1, A2 - analog input of temperature sensor T2, D1 - digital output controlling relay R1 solenoid valve command E1, D2 - digital output controlling relay R2 solenoid valve command E2, D3 - digital output controlling steam generator, D4- digital input arming button B1, D5 - digital input trigger button B2, D6 - digital output controlling water pump command PA1; steam generator; laptop; 12 Volt power supply; steam pipe; silicone head).

a mechanical sensor attached to a chronometer. Once the set time of steam exposure was reached, an automated mechanism closed the second solenoid E2 valve while opening the first solenoid E1 valve, blocking the nozzle through which the steam was expelled. The water pump is then activated and directed cold water for a predefined amount of time towards the same point where heat stimulus occurred.

The duration of steam exposure was controlled due to a chronometer programmed at intervals of one second, three and seven seconds, after which the automated electric valves were deactivated, ending the heat exposure period.

The temperature of the steam was recorded and monitored by a temperature sensor on the rat's skin.

The silicon head was equipped with a special device that collects hot water droplets in order not to burn the surrounding skin via direct hot water droplets.

The time of exposure and the temperature of the steam were regulated by sensors within the circuit. The steam's temperature on the skin was 94°C ± 2°C. The information collected by the sensors was automatically stored in a .cvs file. The pressure exerted on the skin, monitored by a pressure sensor, remained constant throughout every trial. Using the Meeh-DuBois formula for surface area prediction, the burned surface represented 1% of the rat's skin, with the burn diameter being 20 mm and thus constant (represented by the number 10) $*$ weight$^{2/3}$ = burned surface area, K [20].

The heat transfer version of Newton's law ($Q_{\text{thermal energy}} = h_{\text{heat transfer coefficient}} A_{\text{heat transfer surface area}} (T_{\text{steam temp}} - T_{\text{skin temp}})$) requires a constant heat transfer coefficient that in thermodynamics is the proportionality constant between the heat flux and the thermodynamic driving force for the flow of heat. Knowing that thermal energy is the power propagated with time application, this means that the value of our heat transfer coefficient was 5,3 W/cm2K.

2.3. Evaluation of Morphological Changes following Steam Application

2.3.1. Macroscopic Examination. The evaluation of macroscopic transformations following steam exposure was conducted at different time intervals: 20 minutes, 48 hours, 72 hours, 7 days, 14 days, and 21 days, respectively.

The morphologic elements analyzed were color, consistency, and border (contour aspect). Following each evaluation, photos of the lesions were taken for further use in comparative evaluation.

2.3.2. Microscopic Examination. Rats were sacrificed at 20 minutes, 48 hours, and 72 hours post-exposure in order to study the elements of microscopic burn morphology. The rats were sacrificed according to the ethical principles of research, internationally regulated by European Directive number 63/2010 and nationally by law number 206 from May 24, 2004. Rats were euthanized by the administration of the lethal dose of 4 times the anesthetic dose of the combination anesthetic Ketamine/Xylazine in conformity with AVMA Guidelines for the Euthanasia of Animals: 2013 Edition.

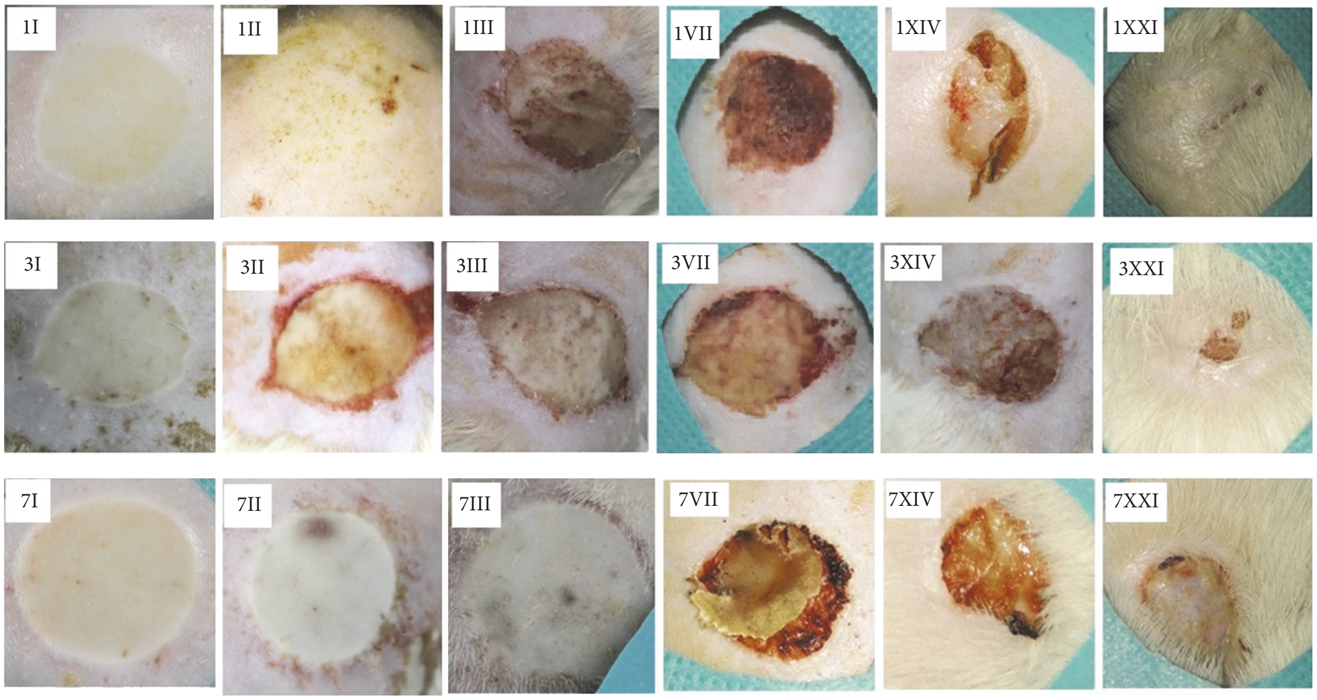

Figure 3: Lesions at different time intervals after steam-inflicted burns. The Arabic numerals represent the seconds of steam exposure (one second, three and seven seconds). The roman numerals represent the time intervals at which the lesions were examined once the heat was removed from the rat's skin (I = 20 minutes, II = 48 hours, III = 72 hours, VII = 7 days, XIV = 14 days, XXI = 21 days).

After representative samples of both burned and nonburned skin were harvested from the rat, the collected tissue samples were fixed in 3.5% formaldehyde prepared in PBS (0.01 M, pH 7.2). Sections of 0.4 micrometers were cut and then stained with standard hematoxylin-eosin (HE). All fragments were processed according to the classical protocol for the histopathologic examination of paraffin-embedded samples [4]. The histological examination was performed by an experienced pathologist. The parameters assessed included cell/tissue necrosis, acute and chronic inflammatory response, vascular lesions, granular tissue (represented by fibroblasts, myofibroblasts, neovascularization and new collagen), connective tissue repair/new connective tissue (healing), and reepithelialization.

3. Results

3.1. Overall Assessment of Steam-Induced Lesions. In each study group assessed, the burn lesions were macroscopically described as mainly uniform and homogenous with a round or slightly oval shape and a visible border (contour) separating the burned from nonburned skin (Figure 3). Moreover, the lesions healed uniformly with minimal differences noted in scab formation and detachment.

In each of the subgroups, it was observed that the histopathological changes between the three rats were similar, with minor differences concerning the degree of inflammatory infiltrate. Table 1 summarized the key histological features at several endpoints.

3.2. Morphological Changes after the One-Second Steam Exposure

3.2.1. Evaluation after 20 Minutes. Upon evaluating the epidermis, the stratum spinosum and the stratum granulosum were homogeneous and could not be precisely identified due to the abolishment of cellular outlines and cellular shadowing. The stratum corneum was intact. The collagen in the superficial papillary dermis was homogenous, which corresponds to the presence of coagulation necrosis (Figure 4(a)).

3.2.2. Evaluation after 48 Hours. Similar morphological aspects were identified within the epidermis and superficial papillary dermis in congruency with those found in the group of rats exposed to a one-second burn and the latter evaluation of the lesion 20 minutes after (Figure 4(b)).

3.2.3. Evaluation after 72 Hours. In comparison to the other rat groups in which the lesions were studied at an earlier time interval, the morphological changes encountered were dominated by an abundance of inflammatory infiltrate comprised of both acute and chronic phase cells in the superficial papillary dermis (Figure 4(c)).

3.3. Morphological Changes after the Three-Second Steam Exposure

3.3.1. Evaluation after 20 Minutes. In the epidermis, significant cell homogenization occurred between the stratum

Table 1: Synopsis of the key histopathological changes.

Steam exposure	Time point	Necrosis depth*	Collagenization**	Inflammatory infiltrate	Vascular lesions
One second	20 min	+	Absent	Absent	Absent
	48 hours	+	Absent	Absent	Absent
	72 hours	+	Absent	Mixt	Absent
3 seconds	20 min	++	++	Acute	Absent
	48 hours	++	++	Mixt	Present
	72 hours	++	+++	Acute	Present
7 seconds	20 min	+++	+++	Acute	Present
	48 hours	+++	+++	Mixt	Present
	72 hours	+++	+++	Acute	Present

*Necrosis depth: + = epidermis and superficial papillary dermis; ++ = epidermis, superficial papillary dermis, and upper level of deep reticular dermis; +++ = epidermis, superficial papillary dermis, and whole deep reticular dermis; **collagenization: + = superficial papillary dermis; ++ = upper level of deep reticular dermis; +++ = whole deep reticular dermis.

basale, stratum spinosum, and stratum granulosum due to the deletion of cellular limits, disappearance of the intercellular space, corresponding to desmosomes, and the persistence of the stratum lucidum and corneum. The coagulation necrosis present in the superficial papillary dermis continued into the upper part of deep reticular dermis. The lower area of the deep reticular dermis and the hypodermis maintained structural integrity (Figure 4(d)).

3.3.2. Evaluation after 48 Hours. The homogenous epidermis presented erased boundaries between stratum basale, stratum spinosum, and stratum granulosum. On the superficial papillary dermis, a scattered expansion of the coagulation necrosis toward the upper area of the deep reticular dermis could be seen (Figure 4(e)).

3.3.3. Evaluation after 72 Hours. The epidermal and dermal morphological changes were similar to the changes observed at the 48-hour evaluation mark; however, within the dermis an inflammatory infiltrate with acute phase cells was observed. A conglomeration of PMN's surrounded the hair follicles observed at the point where the deep reticular dermis met the area of coagulation necrosis in the superficial papillary dermis (Figure 4(f)).

3.4. Morphological Changes after the Seven-Second Steam Exposure

3.4.1. Evaluation after 20 Minutes. Coagulation necrosis was identified in the epidermis, the superficial papillary dermis, and the whole deep reticular dermis. The lower area of the deep reticular dermis is characterized by the thickening and homogenization of collagen fibers; these fibers were horizontally orientated and ran parallel to the coagulation necrosis area. No clear border between these two areas could be identified. However, the adipose tissue, which corresponds to the hypodermis, did not suffer microscopic morphological changes (Figure 4(g)).

3.4.2. Evaluation after 48 Hours. The specific aspect of coagulation necrosis was found in the epidermis, the superficial papillary dermis, and the whole deep reticular dermis (Figure 4(h)).

3.4.3. Evaluation after 72 Hours. The presence of coagulation necrosis in the epidermis, superficial papillary dermis, and the deep reticular dermis was associated with the presence of an inflammatory infiltrate with both acute and chronic phase cells. These microabscesses were also identified around the external epithelial sheath of the sebaceous follicles from the boundary between the remaining deep reticular dermis and the preserved coagulation necrosis area (Figure 4(i)).

4. Discussion

4.1. The Significance of Steam-Induced Burns according to the Established Clinical Burn Classification. According to the burn classification, the expansion in depth of the burn lesion within the exposed tissue can be of multiple types, ranging from first-degree, second-degree – type A, second-degree – type B, and third-degree burns [21–24].

The first-degree burn is superficial and the lesion is located at the surface of the dermis. A second-degree – type A burn, also known as a partial superficial burn or a superficial dermis burn, is when the lesion is located on the surface of the epidermis and the superficial papillary dermis. Type F, also known as a partial deep burn or a deep dermis burn, is when the lesion affects the superficial papillary dermis and the upper area of the deep reticular dermis. In this type of burn, the pilosebaceous complexes situated in the lower area of the deep reticular dermis remain intact. A deep burn or a third-degree burn affects the entire thickness comprising the epidermis, dermis, hypodermis and all cutaneous annexes, and, in some cases, even the adipose tissue.

Ideally, an experimental burn model should allow the operator to evaluate morphological and histopathological lesions and tissue modifications and to be able to assess different burn types according to burn classification. Currently, there is no reliable, reproducible burn model as the literature is limited. Initially, experimental burn systems would produce deep burns. In the last 10 to 15 years, experimental burn systems have aimed to produce partially deep burns. Over

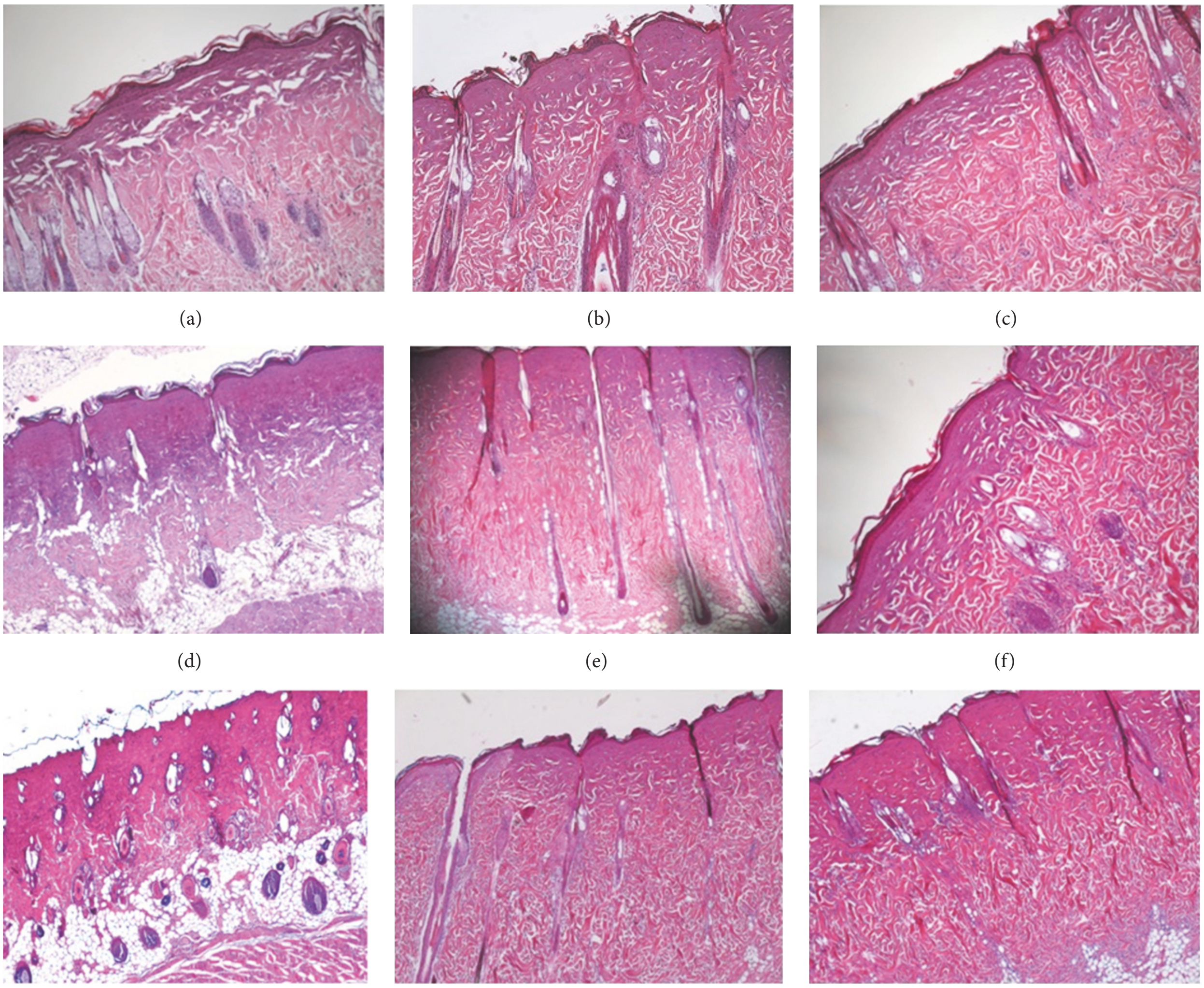
(a) (b) (c)

(d) (e) (f)

(g) (h) (i)

Figure 4: Dermal and epidermal morphological changes in a burn inflicted by (a) one-second steam exposure – assessment at 20 minutes post-burn, (b) one-second steam exposure – assessment at 48 hours post-burn, (c) one-second steam exposure – assessment at 72 hours post-burn, (d) three-second steam exposure – assessment at 20 minutes post-burn, (e) three-second steam exposure – assessment at 48 hours post-burn, (f) three-second steam exposure – assessment at 72 hours post-burn, (g) seven-second steam exposure – assessment at 20 minutes post-burn, (h) seven-second steam exposure – assessment at 48 hours post-burn, (i) seven-second steam exposure – assessment at 72 hours post-burn.

25% of modern studies do not mention burn classification. Moreover, partial superficial burns studied are rarely classified into type A or type D, which may lead to incongruent data [4, 5, 25–27]. The burn classification is based on different degrees of lesion severity represented by the histopathological modifications observed.

As shown above, applying hot steam to the skin for one second produces a partial superficial burn, a second-degree – type A burn, characterized by the histopathological modifications described such as the presence of coagulation necrosis in the epidermis and the superficial papillary dermis. Applying hot steam to the skin for three seconds produces deep partial burns consistent with second-degree – type B burns, which affects the entire epidermis, the superficial papillary dermis, and the upper area of the deep reticular dermis and the pilosebaceous complexes as noted by the presence of coagulation necrosis.

Third-degree burns are produced when coagulation necrosis reaches the hypodermis, affecting the epidermis, superficial papillary dermis, and the deep reticular dermis. As shown, applying hot steam for seven seconds to the skin can produce these lesions.

Evaluating reproducibility in an experimental burn model can be difficult and it is important to assess two elements: (i) the depth to which the burn affected the tissue and (ii) the scab formation and healing process important in regaining integrity of the affected tissue by evaluating epithelial, conjunctive and dermal cellular/structural components. Furthermore, maintaining a constant burn target area on the rat's dorsum allows for a correct classification of burn intensity affecting only the tissue layers present in the designated area and permits the comparison of burn types after different durations of steam exposure. The reproducibility of this setup favors the observation of burn intensity over a period of time.

The healing process for second-degree – type A and second-degree – type B burns produced by applying hot steam for one second or three seconds, respectively, starts around seven days post-exposure. In the deepest area of the burn lesion, young granulation tissue appears and evolves into mature granulation tissue. The formation of new conjunctive tissue structure takes place within the dermis.

4.2. Advantages of the Proposed Experimental Burn Model. The experimental steam burn model allows for a comparative analysis of pathological lesions produced by different durations of heat exposure and the healing progression at several time points post-exposure. This model permits the extrapolation of data based on comparing the similarities and differences at each time interval. Histopathological changes of the tissue in the burn lesions were observed along with specific mechanisms in the healing process, which were unique at the each interval. No other described experimental burn model compares time exposure to heat source, lesion depth and periodic evaluation post-burn, and healing from a macroscopic and microscopic viewpoint.

In experimental models, the animals frequently used are rats, mice, and pigs. None of the three species can be considered superior to the others, with the obtained information through their study being complementary [28].

One of the first burn models that was described in the literature was produced by using hot water on the rats' skin [2]. The use of hot water as a vector is reported in under 10% of the experimental models, while approximately 65% of the studies use metal as a means of induction having been previously heated with hot water [2–18]. This vector presents many disadvantages such as application difficulty and work safety.

However, the use of hot water could regulate the optimum contact time and temperature as well as the quantity of heat emanated. Exposure time is harder to measure because the fluid state increases the difficulty to standardize the process of elimination. Cuttle et al. developed a bottle with a bottom constructed of an elastic membrane that contains hot water [11]. When this hot water is applied on the skin it leads to a better adaptation to the skin's uneven surface, avoiding the overburn of the skin [11]. This membrane, as well as the heated metallic blocks, does not ensure the intimate adherence to the smallest uneven topographic parts of the surface of the skin. A limit of the experimental models on hot water or hot metal heated in hot water is that these vectors produce only one type of burn at a certain temperature, making the change of temperature to obtain another degree of burn necessary [8, 9, 19]. We also need to emphasize the fact that burn models based on heat transfer at the skin level, by applying a piece of hot metal or a different energy transfer, involve a different energy transfer, according to the materials used [18, 23, 24, 29, 30]. Moreover, different skin characteristics such as water content or amount of adipose tissue influence the process of heat transfer and modify the standard of the burn.

Another model described in the literature involves the hot plate and electrical coil. They are vectors that are described as having an even surface that have the disadvantage of application of extremely high temperatures (170°C and 400°C) and consecutively producing only third-degree burns [8, 9]. These vectors are easy to apply if their mass is big enough and if the thermal energy applied is sufficient and is constantly maintained on the skin. The contact with the skin is difficult to be standardized because of anatomical differences and physiological variables. Vectors exert uneven pressure on the exposed area, with greater pressure on the skin's prominent areas and less pressure at the interface between the skin and the vector.

The motivation to further study the steam burn experimental model was that steam has an advantage over other methods of heat transfer; steam does not need a transporter and can be better quantified in order to classify burn intensity. Another advantage of using steam is that once the cold water is introduced into the pipe system, the silicon head cools down rapidly, making time exposure more precise and allowing for possible standardization. However, because this study relies on an experimental burn model, lesion expansion due to prolonged heat exposure is a limitation [29].

This system functions due to a software system and data board with programmed automated functions and safeguard loop holes. The one variable controlled by the software was duration of heat exposure. The steam's temperature was difficult to control due to the interference of ambient temperature variations. The automated software allowed temperature data to be recorded in real time and permitted the system to turn off if one of the conditions specified in the program was not met. This allowed for less incongruence in the procedure.

The integrated system used in the experimental burn model is a customized design, all elements of which are in unison with the standard criteria for burn models. The system monitors the constant pressure of the heat application, time elapsed from the beginning of the experiment until the set time is reached, and variables verified by pressure and temperature sensors and applied chronometers. This design is congruent with other models [3, 31] which make note of different temperature parameters, producing varying burn intensities within the same experimental model. In the model developed by Campelo et al. electrically heated copper was used as a vector to produce a burn using a metal object [9]. An electric sensor connected to the plate at a two-millimeter distance ensured temperatures of 100°C, 150°C, and 200°C. In this model, time was kept by a chronometer and could be used at 5 minutes after being connected to electricity [9]. The hot metal was applied to the skin at constant nine seconds. However, only microscopic lesions were observed and no data as to burn intensity or depth could be provided. Similar models, based on the use of a metal vectors heated with the help of hot water, have been developed by research groups coordinated by Pereira, Crouzet, Nasiri and Selcuk [25, 30, 32–34]. One limitation of using metal to produce burns on the skin is that there is no instrument that has been used to record the exact temperature of the metal once it touches the skin. Also, there is no data as to the temperature maintained by the vector during exposure. A solution to correct this limitation is proposed by Venter et al. and Cai et al. by applying a temperature sensor at the tip of the metal vector that produces the burn which displays the temperature on a digital screen [4, 35]. Therefore our results obtained based on the tests done are a consequence of superior methods of temperature monitoring, automated on-off safeguard loop hole if experimental variables are not met and careful study of time interval marks.

Otherwise, because a human operator measures time by starting and stopping a chronometer once the silicon heat touches the rat's skin until the time interval is reached and is then removed [25, 28, 32, 36, 37], human error may intervene due to a delayed reaction. Considering that the time intervals are measured in seconds, it is harder to detect certain errors that may occur. It is important to note that, in burn experiments where a metal object is heated by hot water and then transferred and applied to the rat's skin, a three-second (±1 second) delay may occur in order to properly apply the heated vector on the rat's skin [35]. Moreover, after the application of heat vectors, the burn may evolve because of the skin cool down [29]. The major advantage of the device used in this study consists of the automatic turn off of the vector, doubled by an immediate cooling down process of the skin with the help of cool water sent through the pipe system. Additionally, the steam's temperature is directly measured as it is expelled from the silicon head and not from the heating tub as in other experimental models [28, 32, 36, 38]. Another major, beneficial advantage, in comparison to other devices [18, 20], is that because the heating element itself is not a hard surface that comes in contact with the rat's skin it ensures lesion uniformity via heat radiation from the steam.

The design and the concept behind the integrated system used simple and efficient methods to create burns that are easy to reproduce. This system allowed the classification of burn intensity by histopathological analysis of the burn lesions produced by uniform steam burns.

Due to low material investment in the burn apparatus this model is cost efficient and can further the understanding of burn types, lesions produced, and possible topical treatments for wounds produced via heat vectors.

The contribution made to furthering scientific knowledge of burn histopathology and physiopathology lies in the ingenuity of the integrated burn model system represented by the automated on/off circuit, reproducibility, and methodology upheld by established knowledge on experimental burn model criteria.

4.3. Pain Management. The use of analgesia in post-burning care against pain and suffering is a fundamental requirement for many laws of ethics that guide animal experimentation [39]. However in many burn studies, the use of analgesics in postoperative care is not mentioned [18]. Some authors justify the lack of use of post-burn analgesics in full thickness burn models by the fact that nerve endings in the skin are destroyed [40]. Nevertheless, some studies document the presence of hyperalgesia and allodynia even when full thickness thermal injury is induced, suggesting activation of afferent pain pathways in the regions surrounding the initial lesion, thus commanding the use of analgesia [41]. Pain management in experimental animals aims to achieve the well-being of the animal in such a manner that they will continue the daily routine so the experiment and the parameters that are observed will not be affected. Drugs can be administered subcutaneously, intramuscularly, or orally in the drinking water supplied to animals. Among the most commonly used opioids for postoperative pain in laboratory animals is buprenorphine, mainly because of its long duration of action [42].

4.4. Limitations. The validation of our model is applicable for the specific species, gender, age, and burn location presented (i.e., male Wistar rats, 300 g, dorsal burn injury). While generalizability of our model to other situations with the purpose to accurately mimic burn injury in patients would be highly desirable, the focus of this study was rather to overcome the inherent limitations associated with the energy delivery approach in the available models. The highly automated and nonexpensive system to achieve consistent thermal energy delivery will allow rapid and low-cost validation of burn models in other species, different gender or age and location of burn injury. Furthermore, the specific validated model we present here may be an important tool for experimental testing of various therapeutic approaches for burn injury.

5. Conclusions

The integrated system described here provides a useful tool for consistently inducing standardized burns. Duration of exposure, temperature, and pressure were controlled, corrected in real time, and recorded with the help of software, eliminating as many potential errors generated by the human operator as possible. The real time measurements were the key to the development of the burn model. Variables, some of which were affected by environmental inconsistencies or human error, were observed and later controlled. The integrated system allows the production of precise burns of constant depth, with histopathological profiles closely reproducing different degrees of clinical burns. The integrated system described has potential applicability in the study of burn pathology and in experimental assessment of new treatments.

Conflicts of Interest

The authors declare that they have no conflicts of interest.

Acknowledgments

This study was financially supported by the Grigore T. Popa University of Medicine and Pharmacy, Iași, "Program of excellence in multidisciplinary doctoral and postdoctoral research regarding chronic diseases" (POSDRU 159/1.5/S/133377). The authors are grateful to Radu Iliescu, the senior scientist who made valuable suggestions for improvements to the manuscript.

References

[1] L. M. Ferreira, B. Hochman, and M. V. J. Barbosa, "Experimental models in research," *Acta Cirurgica Brasileira*, vol. 20, no. 2, pp. 28–34, 2005.

[2] H. L. Walker and A. D. Mason, "A standard animal burn," *Journal of Trauma - Injury, Infection and Critical Care*, vol. 8, no. 6, pp. 1049–1051, 1968.

[3] W. A. Dorsett-Martin, "Rat models of skin wound healing: a review," *Wound Repair and Regeneration*, vol. 12, no. 6, pp. 591–599, 2004.

[4] N. G. Venter, A. Monte-Alto-Costa, and R. G. Marques, "A new model for the standardization of experimental burn wounds," *Burns*, vol. 41, no. 3, pp. 542–547, 2015.

[5] A. J. Singer, B. R. Taira, R. Anderson, S. A. McClain, and L. Rosenberg, "Does pressure matter in creating burns in a porcine model?" *Journal of Burn Care and Research*, vol. 31, no. 4, pp. 646–651, 2010.

[6] K. Pfurtscheller, T. Petnehazy, W. Goessler, I. Wiederstein-Grasser, V. Bubalo, and M. Trop, "Innovative scald burn model and long-term dressing protector for studies in rats," *Journal of Trauma and Acute Care Surgery*, vol. 74, no. 3, pp. 932–935, 2013.

[7] M. J. Hoekstra, P. Hupkens, R. P. Dutrieux, M. M. C. Bosch, T. A. Brans, and R. W. Kreis, "A comparative burn wound model in the New Yorkshire pig for the histopathological evaluation of local therapeutic regimens: silver sulfadiazine cream as a standard," *British Journal of Plastic Surgery*, vol. 46, no. 7, pp. 585–589, 1993.

[8] A. J. Singer, L. Berruti, H. C. Thode Jr., and S. A. Mcclain, "Standardized burn model using a multiparametric histologic analysis of burn depth," *Academic Emergency Medicine*, vol. 7, no. 1, pp. 1–6, 2000.

[9] A. P. B. S. Campelo, M. W. S. Campelo, G. A. de Castro Britto, A. P. Ayala, S. B. Guimarães, and P. R. L. de Vasconcelos, "An optimized animal model for partial and total skin thickness burns studies," *Acta Cirurgica Brasileira*, vol. 26, no. 1, pp. 38–42, 2011.

[10] R. Gurfinkel, A. J. Singer, E. Cagnano, and L. Rosenberg, "Development of a novel animal burn model using radiant heat in rats and swine," *Academic Emergency Medicine*, vol. 17, no. 5, pp. 514–520, 2010.

[11] L. Cuttle, M. Kempf, G. E. Phillips et al., "A porcine deep dermal partial thickness burn model with hypertrophic scarring," *Burns*, vol. 32, no. 7, pp. 806–820, 2006.

[12] A. G. T. Pessolato, D. D. S. Martins, C. E. Ambrósio, C. A. F. Manançares, and A. F. de Carvalho, "Propolis and amnion reepithelialise second-degree burns in rats," *Burns*, vol. 37, no. 7, pp. 1192–1201, 2011.

[13] S. Gurung and N. Skalko-Basnet, "Wound healing properties of *Carica papaya* latex: in vivo evaluation in mice burn model," *Journal of Ethnopharmacology*, vol. 121, no. 2, pp. 338–341, 2009.

[14] K. S. Priya, A. Gnanamani, N. Radhakrishnan, and M. Babu, "Healing potential of *Datura alba* on burn wounds in albino rats," *Journal of Ethnopharmacology*, vol. 83, no. 3, pp. 193–199, 2002.

[15] R. Eloy and A. M. Cornillac, "Wound healing of burns in rats treated with a new amino acid copolymer membrane," *Burns*, vol. 18, no. 5, pp. 405–411, 1992.

[16] N. K. Upadhyay, R. Kumar, S. K. Mandotra et al., "Safety and healing efficacy of Sea buckthorn (*Hippophae rhamnoides* L.) seed oil on burn wounds in rats," *Food and Chemical Toxicology*, vol. 47, no. 6, pp. 1146–1153, 2009.

[17] R. M. Zohdi, Z. A. B. Zakaria, N. Yusof, N. M. Mustapha, and M. N. H. Abdullah, "Gelam (*Melaleuca spp.*) honey-based hydrogel as burn wound dressing," *Evidence-Based Complementary and Alternative Medicine*, vol. 2012, Article ID 843025, 7 pages, 2012.

[18] J. K. Mitsunaga Jr., A. Gragnani, M. L. C. Ramos, and L. M. Ferreira, "Rat an experimental model for burns. A systematic review," *Acta Cirurgica Brasileira*, vol. 27, no. 6, pp. 417–423, 2012.

[19] A. Benson, W. A. Dickson, and D. E. Boyce, "ABC of wound healing: Burns," *British Medical Journal*, vol. 332, no. 7542, pp. 649–652, 2006.

[20] L. Diack, "The Determination of The Surface Area of The White Rat," *Journal of Nutrition*, vol. 3, pp. 289–296, 1930.

[21] D. N. Herdon, *Total Burn Care*, Sauders Elsevier, 3rd edition, 2007.

[22] S. E. Wolf and D. N. Herndon, *Burn Care*, Austin: Landes Bioscience, 1999.

[23] J. S. Knabl, G. S. Bayer, W. A. Bauer et al., "Controlled partial skin thickness burns: An animal model for studies of burnwound progression," *Burns*, vol. 25, no. 3, pp. 229–235, 1999.

[24] T. Kaufman, S. N. Lusthaus, U. Sagher, and M. R. Wexler, "Deep partial skin thickness burns: a reproducible animal model to study burn wound healing," *Burns*, vol. 16, no. 1, pp. 13–16, 1990.

[25] S. P. Ddos, M. H. Lima-Ribeiro, R. Santos-Oliveira et al. et al., "Topical application effect of the isolectinhydrogel(Cramoll1, 4) on second-degree burns: experimental model," *Journal of Biomedicine and Biotechnology*, vol. 2012, Article ID 184538, 2012.

[26] N. Tanideh, P. Rokhsari, D. Mehrabani, S. Mohammadi Samani, F. Sabet Sarvestani, and M. J. Ashraf MJ, "The healing effect of licorice on Pseudomonas aeruginosa infected burn wounds in experimental rat model," *World Journal of Plastic Surgery*, vol. 3, no. 2, pp. 99–106, 2014.

[27] H. Sayar, N. Gergerlioglu, N. Seringec, P. Ozturk, E. Bulbuloglu, and G. Karabay, "Comparison of efficacy of topical phenytoin with hypericin in second-degree burn wound healing: an experimental study in rats.," *Medical science monitor basic research*, vol. 20, pp. 36–46, 2014.

[28] A. Abdullahi, S. Amini-Nik, and M. G. Jeschke, "Animal models in burn research," *Cellular and Molecular Life Sciences*, vol. 71, no. 17, pp. 3241–3255, 2014.

[29] E. H. Wright, A. L. Harris, and D. Furniss, "Cooling of burns: Mechanisms and models," *Burns*, vol. 41, no. 5, pp. 882–889, 2015.

[30] T. N. Meyer and A. L. Silva, "A standard burn model using rats," *Acta Cirurgica Brasileira*, vol. 14, no. 4, 1999.

[31] C. T. Selçuk, M. Durgun, B. Özalp et al., "Comparison of the antibacterial effect of silver sulfadiazine 1%, mupirocin 2%, Acticoat and octenidine dihydrochloride in a full-thickness rat burn model contaminated with multi drug resistant *Acinetobacter baumannii*," *Burns*, vol. 38, no. 8, pp. 1204–1209, 2012.

[32] D. D. S. T. Pereira, M. H. M. Lima-Ribeiro, N. T. De Pontes-Filho, A. M. D. A. Carneiro-Leão, and M. T. D. S. Correia, "Development of animal model for studying deep second-degree thermal burns," *Journal of Biomedicine and Biotechnology*, vol. 2012, Article ID 460841, 7 pages, 2012.

[33] C. Gaines, D. Poranki, W. Du, R. A. F. Clark, and M. Van Dyke, "Development of a porcine deep partial thickness burn model," *Burns*, vol. 39, no. 2, pp. 311–319, 2013.

[34] C. Z. Wang, A. E. Ayadi, J. Goswamy et al., "Topically applied metal chelator reduces thermal injury progression in a rat model of brass comb burn," *Burns*, vol. 41, no. 8, pp. 1775–1787, 2015.

[35] E. Z. Cai, C. H. Ang, A. Raju et al., "Creation of consistent burn wounds: A rat model," *Archives of Plastic Surgery*, vol. 41, no. 4, pp. 317–324, 2014.

[36] D.-W. Zhang, Z.-Y. Gong, and Y.-Z. Peng, "Reproduction of a rat model of burn with infection," *Chinese Journal of Burns*, vol. 27, no. 2, pp. 104–108, 2011.

[37] S. Arndt, P. Unger, E. Wacker et al., "Cold atmospheric plasma (CAP) changes gene expression of key molecules of the wound healing machinery and improves wound healing in vitro and in vivo," *PLoS ONE*, vol. 8, no. 11, Article ID e79325, 2013.

[38] M. S. Arda, A. E. Koçman, E. Söztutar, B. Baksan, and C. Çetin, "A new apparatus for standardization of experimental burn models," *Burns*, 2017.

[39] P. Hawkins, "Recognizing and assessing pain, suffering and distress in laboratory animals: A survey of current practice in the UK with recommendations," *Laboratory Animals*, vol. 36, no. 4, pp. 378–395, 2002.

[40] Q. Yang, M. A. Orman, F. Berthiaume, M. G. Ierapetritou, and I. P. Androulakis, "Dynamics of short-term gene expression profiling in liver following thermal injury," *Journal of Surgical Research*, vol. 176, no. 2, pp. 549–558, 2012.

[41] M. Fowler, J. L. Clifford, T. H. Garza et al., "A rat model of full thickness thermal injury characterized by thermal hyperalgesia, mechanical allodynia, pronociceptive peptide release and tramadol analgesia," *Burns*, vol. 40, no. 4, pp. 759–771, 2014.

[42] L. I. Curtin, J. A. Grakowsky, M. Suarez et al., "Evaluation of buprenorphine in a postoperative pain model in rats," *Comparative Medicine*, vol. 59, no. 1, pp. 60–71, 2009.

chemosensors

IMPACT FACTOR 3.7

CITESCORE 7.3

Article

Ceramic Nanotubes—Conducting Polymer Assemblies with Potential Application as Chemosensors for Breath Ammonia Detection in Chronic Kidney Disease

Alexandru Florentin Trandabat, Romeo Cristian Ciobanu, Oliver Daniel Schreiner,
Thomas Gabriel Schreiner and Sebastian Aradoaei

MDPI

https://doi.org/10.3390/chemosensors12090198

chemosensors

Article

Ceramic Nanotubes—Conducting Polymer Assemblies with Potential Application as Chemosensors for Breath Ammonia Detection in Chronic Kidney Disease

Alexandru Florentin Trandabat [1], Romeo Cristian Ciobanu [1,*], Oliver Daniel Schreiner [1,2], Thomas Gabriel Schreiner [1,2] and Sebastian Aradoaei [1]

[1] Department of Electrical Measurements and Materials, Gheorghe Asachi Technical University, 700050 Iasi, Romania; ftranda@tuiasi.ro (A.F.T.); oliver090598@yahoo.com (O.D.S.); arsete@tuiasi.ro (S.A.)
[2] Department of Medical Specialties III, Faculty of Medicine, University of Medicine and Pharmacy "Grigore T. Popa", 700115 Iasi, Romania
* Correspondence: r.c.ciobanu@tuiasi.ro

Abstract: This paper describes the process of producing chemosensors based on hybrid nanostructures obtained from Al_2O_3, as well as ZnO ceramic nanotubes and the following conducting polymers: poly(3-hexylthiophene), polyaniline emeraldine-base (PANI-EB), and poly(3, 4-ethylenedioxythiophene)-polystyrene sulfonate. The process for creating ceramic nanotubes involves three steps: creating polymer fiber nets using poly(methyl methacrylate), depositing ceramic films onto the nanofiber nets using magnetron deposition, and heating the nanotubes to 600 °C to burn off the polymer support completely. The technology for obtaining hybrid nanostructures from ceramic nanotubes and conducting polymers is drop-casting. AFM analysis emphasized a higher roughness, mainly in the case of PANI-EB, for both nanotube types, with a much larger grain size dimension of over 5 µm. The values of the parameter Rku were close or slightly above 3, indicating, in all cases, the formation of layers predominantly characterized by peaks and not by depressions, with a Gaussian distribution. An ink-jet printer was used to generate chemiresistors from ceramic nanotubes and PANI-EB structures, and the metallization was made with commercial copper ink for printed electronics. Calibration curves were experimentally generated for both sensing structures across a wider range of NH_3 concentrations in air, reaching up to 5 ppm. A 0.5 ppm detection limit was established. The curve for the ZnO:PANI-EB structure presented high linearity and lower resistance values. The sensor could be used in medical diagnosis for the analysis of breath ammonia and biomarkers for predicting CKD in stages higher than 1. The threshold value of 1 ppm represents a feasible value for the presented sensor, which can be defined as a simple, low-value and robust device for individual use, beneficial at the patient level.

Keywords: ceramic nanotubes; conducting polymers; chemiresistor; chemosensor; breath ammonia detection; chronic kidney disease

check for updates

Citation: Trandabat, A.F.; Ciobanu, R.C.; Schreiner, O.D.; Schreiner, T.G.; Aradoaei, S. Ceramic Nanotubes—Conducting Polymer Assemblies with Potential Application as Chemosensors for Breath Ammonia Detection in Chronic Kidney Disease. *Chemosensors* **2024**, *12*, 198. https://doi.org/10.3390/chemosensors12090198

Received: 1 August 2024
Revised: 10 September 2024
Accepted: 19 September 2024
Published: 23 September 2024

1. Introduction

Metal oxides exhibit several critical advantages as gas sensor materials, including simple fabrication at a low cost and applicability to both sensing technologies of oxidizing or reducing gasses [1]. From a structural point of view, most commercial sensors currently present as active detection surfaces of metal oxides in the form of thick films [2]. The considerable difficulties encountered in obtaining sensors based on thin films and ceramic nanotubes prevents their large-scale manufacture. However, their apparent advantages in terms of compactness, precision, and high detection sensitivity encourage researchers to continuously improve the available technologies.

In the last 15 years, some studies have been dedicated to the synthesis of ceramic nanotubes using different technologies [3–12], but no research has specifically focused on ceramic nanotube composites, despite certain articles discussing carbon–ceramic nanotube composites or ceramic nanoparticles combined with carbon nanotubes, as in references [13–20]. Nanotube-based devices could alter their conductivity because of surface adsorption when they come into contact with chemical substances, similar to findings from extensive research on carbon nanotubes [21]. Adsorption on the surface can also occur with biomolecules like amino acids and proteins, indicating that nanotubes can also be used to detect bioagents [22,23]. Most authors focus on the surface properties of carbon nanotubes; however, none have examined the analogous properties of ceramic nanotubes.

On the other hand, many research results emphasize the advantages of using conducting polymers for sensor applications, alone or as composites with nano-carbon or metallic/ceramic particles, as in [24–31], but, in general, studies on hybrid structures obtained from ceramic nanotubes and conducting polymers are practically non-existent in the literature, despite their potential applications for various types of sensors, but also for photovoltaic energy generation, energy storage in supercapacitors, or other photocatalytic applications.

Resistive gas sensors are flexible and affordable options for identifying a variety of gasses in various scenarios [32,33]. By selecting the appropriate sensing material, resistive gas sensors can be customized to detect a particular gas of interest [34–36]. However, their selectivity decreases and their response and recovery times increase [36,37]. Temperature and humidity levels can affect how well resistive gas sensors operate [38]. However, these sensors have a simpler design, which enables easy integration into signal processing systems and efficient mass production. By choosing the right sensing material, resistive gas sensors can be customized to identify a particular gas, such as ammonia. Our paper intends to put the base of a new type of chemiresistors, based on ceramic nanotube composites with conducting polymers, with potential use in breath ammonia detection associated with chronic kidney disease (CKD) [39]. Ammonia breath testing [40,41] was recently appointed as an accurate diagnostic tool, based on the concept that some specific gasses represent by-products of a limited liver and kidney function, which leads to increased blood urea nitrogen (BUN) within the body. The damage to the kidneys may be caused by various conditions, e.g., diabetes, heart disease, age, etc., and a preliminary sign is a metallic taste, which is clearly related to elevated levels of ammonia (NH_3) in the mouth. Similarly, this occurrence could be linked to sensitivity to certain foods or food intolerances, highlighting the significance of utilizing these sensors. Regrettably, identifying ammonia in breath is difficult because of its low levels and inherent interferents. Only a few studies have been conducted on the topic of dedicated sensors for detecting ammonia, e.g., [42–44]. However, they are not adequate for detecting low concentrations in air, and no commercial biosensor for ammonia has been developed to date. It is known that resistive gas sensors have reduced selectivity and longer response and recovery times. Factors such as temperature, the influence of other exhaled gasses, and humidity may impact the performance of resistive gas sensors for biomedical applications. Yet, for initial inquiries regarding CKD or for regular home monitoring, chemiresistors are deemed effective under room temperature conditions, as long as the readings are not rapidly repeated. The syndrome detection is based on exceeding a threshold value and does not require an exact assessment of the value of the exhaled gas concentration.

The novelty of this paper is mainly related to the development of hybrid nanostructures obtained from ceramic nanotubes and conducting polymers with dedicated sensing features not yet presented in the literature. The surface architecture of ceramic nanotubes represents a critical element that may impact the future development of sensor applications. Another novelty is related to the direct application presented in the paper to evaluate breath ammonia, which can be associated with CKD, under circumstances in which only a few research papers have addressed the development of sensors for this purpose. The sensor principle presented in the paper is more straightforward, cost-effective, and efficient compared to the other currently proposed methods for ammonia detection in CKD, e.g., colorimetry, fluorescence chromatography, thermal decomposition, ion mobility spectrometry, gas chromatography, fluorescence, or photoacoustic detection [45–49].

2. Technology for Obtaining Hybrid Nanostructures from Ceramic Nanotubes and Conducting Polymers

2.1. Technological Equipment

The electrospinning process of polymethyl methacrylate (PMMA) nanofibers was carried out using Neu-Pro-BM equipment from TongLiTech in Wuhan, China.

The Tectra Sputter Coater (Tectra GmbH Physikalische Instrumente, Frankfurt, Germany) was the device employed for radiofrequency (RF) magnetron sputtering.

A specialized furnace, (Nabertherm GmbH, Lilienthal, Germany), operating at temperatures up to 800 °C, was utilized for the calcination of PMMA.

2.2. Materials and Preparation Methods

All chemical components (ceramic powders and polymers) were purchased from Merck (Darmstadt, Germany) and Kurt J. Lesker Company Ltd. (Hastings, UK) and used as received, without any further adjustments.

According to the general technological description in [4,15,50] (Figure 1), the technology for manufacturing Al_2O_3 and ZnO ceramic nanotubes was based on three stages.

(i) The initial production of polymer fiber meshes made of poly (methyl methacrylate (PMMA), with a molecular weight (Mw) of 300,000, using a 10 wt% solution with dimethylformamide (DMF) as the solvent. To produce freestanding polymer fiber webs, sizable (10×10 cm^2) square copper frames were employed as collectors within a conventional electrospinning arrangement. These frames were positioned between the syringe needle spinneret and a 20×20 cm^2 aluminum plate, which functioned as a grounded electrode. The separation distances between the copper frame collectors and the aluminum plate, as well as between the collectors and the spinneret, were approximately 5 cm and 10 cm, respectively. A syringe pump delivered the solution of 10 mL to a blunt needle with a diameter of 0.8 mm at a flow rate of 0.5 mL/h. The drum rotation was 5 rpm. After more tests, the optimum voltage value applied to the needle was 12 kV. Each copper frame was subjected to a collection time of 60 min. The fiber networks showed uniformity in spatial placement and consistency in diameter. However, since ceramic thin films are deposited on PMMA nanofibers, a minimum diameter of 0.3 µm was deemed ideal to ensure the structural stability of the fibers when covered from a mechanical perspective.

(ii) Magnetron deposition of ceramic films

The PMMA nanofibers nets in copper frames were coated with ceramic thin films on both sides using RF magnetron sputtering. In the deposition procedure, ceramic targets measuring 2 inches in diameter and 0.125 inches in thickness were utilized. Regarding the deposition of Al_2O_3, an RF power of 200 W was utilized on the magnetron, and the deposition duration for each side was 3 h. For ZnO deposition, the RF power applied to the magnetron was 100 W, and the deposition duration for each side was 2 h. In both cases, within the deposition chamber, an argon atmosphere with a purity of 99.99% at a pressure of 5.4×10^{-3} mbar was used as the working gas.

(iii) Thermal treatment of nanotubes

After this process, the PMMA nanofibers nets, coated on both sides with either Al_2O_3 or ZnO films, were transferred onto a Si/SiO_2 substrate and subjected to calcination using a convection oven. The calcination process was conducted at 600 °C for 12 h in ambient air at atmospheric pressure. Following this procedure, three-dimensional web-like networks of Al_2O_3 and, respectively, ZnO nanotubes were achieved after the complete combustion of PMMA occurring during the calcination process.

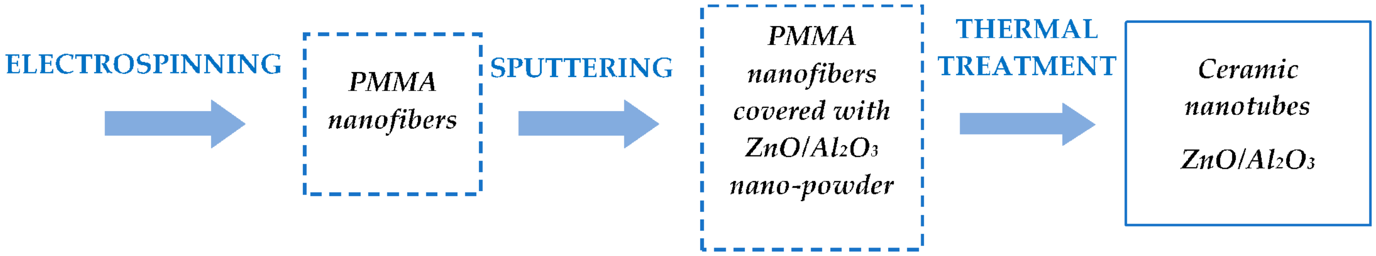

Figure 1. Technological phases for ceramic nanotube manufacturing.

The technology of drop-casting was used to obtain hybrid nanostructures from ceramic nanotubes (Al_2O_3 and ZnO) and the following conducting polymers: poly(3-hexylthiophene) (P3HT), polyaniline emeraldine-base (PANI-EB), and poly(3, 4-ethylenedioxythiophene)-polystyrene sulfonate (PEDOT-PS). Five samples of each type were manufactured to compare technological feasibility. The technological process involved the use of the following solutions:

(i) P3HT at a concentration of 15 mg/mL was mixed in chloroform at room temperature using an ultrasonic bath and left for 30 min to ensure even dispersion.

(ii) A solution of 20 mg/mL PANI-EB in N-methyl pyrrolidinone (NMP) was prepared by dissolving it at room temperature using an ultrasonic bath and allowing it to sit for 30 min to ensure even distribution.

(iii) A 1.3 wt% mixture of PEDOT-PS in water was placed in an ultrasonic bath at room temperature for 10 min to ensure even dispersion.

Next, 240 µL of every polymer solution was applied onto ceramic nanotubes (SiO_2/Si substrate) using the drop-casting technique with Pasteur pipettes in every instance. Each solvent was evaporated for 60 min in a vacuum, utilizing a Pfeiffer vacuum pump attached to a desiccator.

3. Results and Discussion

3.1. Characterization Equipment

Transmission electron microscopy (TEM) results were obtained using a JEOL 2100 Plus transmission electron microscope operating at an accelerating voltage of 80 kV (JEOL Ltd., Akishima, Tokyo, Japan). Electron diffraction (SAED) analysis was also performed.

Raman spectroscopy was performed using AvaRaman 532 equipment (Avantes B.V., Apeldoorn, The Netherlands).

Fourier-transform infrared spectroscopy (FTIR) was performed using JASCO equipment (Tokyo, Japan), 12000—50 cm^{-1} spectral range.

X-ray photoelectron spectroscopy (XPS) and energy-dispersive X-ray spectroscopy (EDS) were performed with an AXIS Supra+ unit (Kratos Analytical Ltd., Manchester, UK).

Scanning microscopy SEM was performed using Lyra III XMU equipment (TESCAN GROUP a.s., Brno-Kohoutovice, Czech Republic). To evaluate the obtained graphene layer, a progressive morphological analysis was conducted.

Atomic force microscopy (AFM) analysis using a Dimension Edge unit from Bruker in Billerica, MA, USA, was conducted for optical purposes. Average roughness parameters were provided for four scanned zones on every type of sample.

3.2. TEM and Selected Area (Electron) Diffraction (SAED) Analysis

The TEM images for ZnO nanotube composites are presented in Figures 2–4. The hexagonal ZnO phase was identified using SAED analysis. Pick intensity is related to the concentration of ZnO nanotubes in the composite assembly. For each diagram, the other picks beyond Zn are specific to the composition of the polymer.

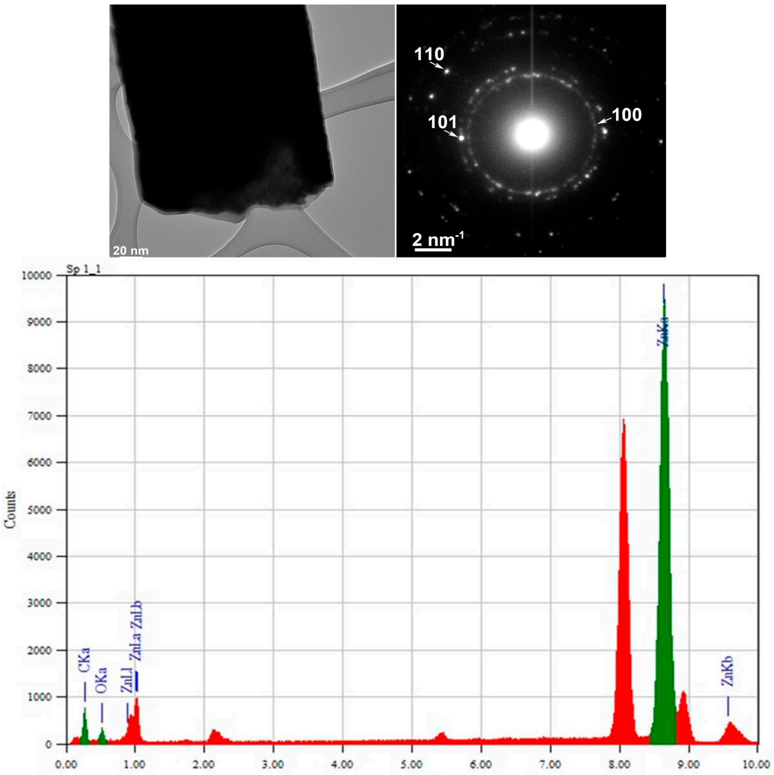

Figure 2. TEM image for the ZnO-P3HT composite.

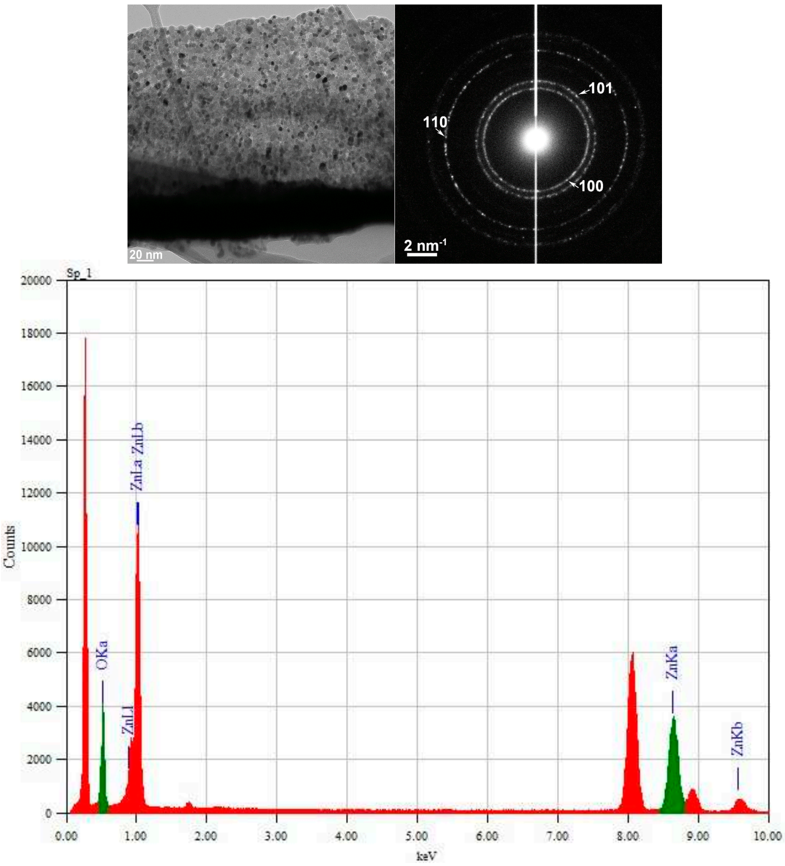

Figure 3. TEM image for the ZnO-PANI composite.

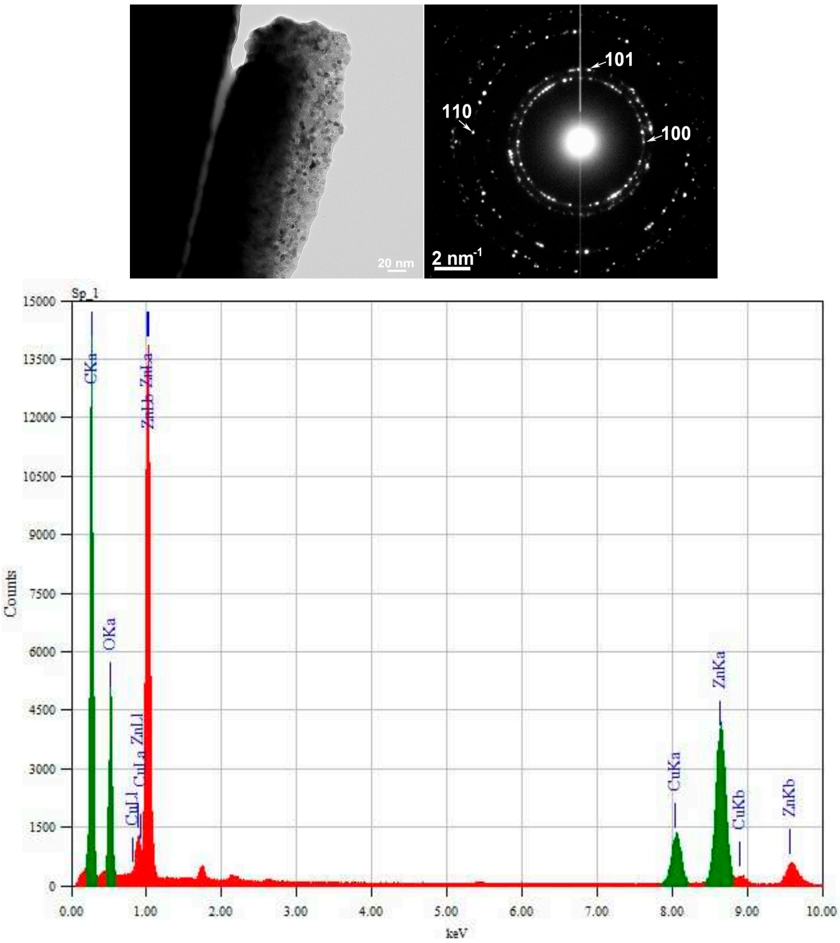

Figure 4. TEM image for the ZnO+PEDOT:PS composite.

3.3. Raman and FTIR, XPS, and EDS Analysis

Figures 5 and 6 show the Raman spectra recorded at an excitation wavelength of 514 nm for Al_2O_3, as well as ZnO nanotube composites with P3HT, PEDOT:PS, and PANI-EB. The Raman spectrum of P3HT is identified using the following Raman lines located at 729, 1013, 1092, 1184, 1380, 1442, 1515, and 1620 cm^{-1} attributed to C_{α}-S-$C_{\alpha'}$ bond deformation vibration modes, C_{β}-C_{alchil} stretching, C_{β}-H bond bending, C_{α}-$C_{\alpha'}$ stretching, C_{β}-H bending, C_{β}-C_{β} stretching, C_{α}=C_{β} stretching, $C_{\alpha'}$=$C_{\beta'}$ stretching, in addition to the quinoid structure [51]. The Raman lines of PANI-EB are identified at 814, 1176, 1247, 1352, 1414, 1501, 1565, and 1610 cm^{-1}, being attributed to the deformation vibration modes of the benzene ring (B) of the bond C-H in the benzene ring, C-N stretch, C-H bond in the quinoid ring, C-C stretch in the quinoid ring, C-H bond in the quinoid ring, C=N stretch, C=C stretch in the quinoid ring, and C-C stretch in the benzene ring [52]. The Raman spectrum of the PEDOT:PSS copolymer is characterized by the following Raman lines located at 439-574 -990, 1257, 1364, 1439, 1502, and 1569 cm^{-1}, which are attributed to the vibrational modes of deformation of the oxyethylene ring, C_{α}-$C_{\alpha'}$ stretching and C-H bending, C_{β}-$C_{\beta'}$ stretching, symmetric C-C stretching, and asymmetric C-C stretching [53]. In conclusion, regardless of the analyzed sample, only the absorption bands of the three polymers were mainly observed in the IR absorption spectra.

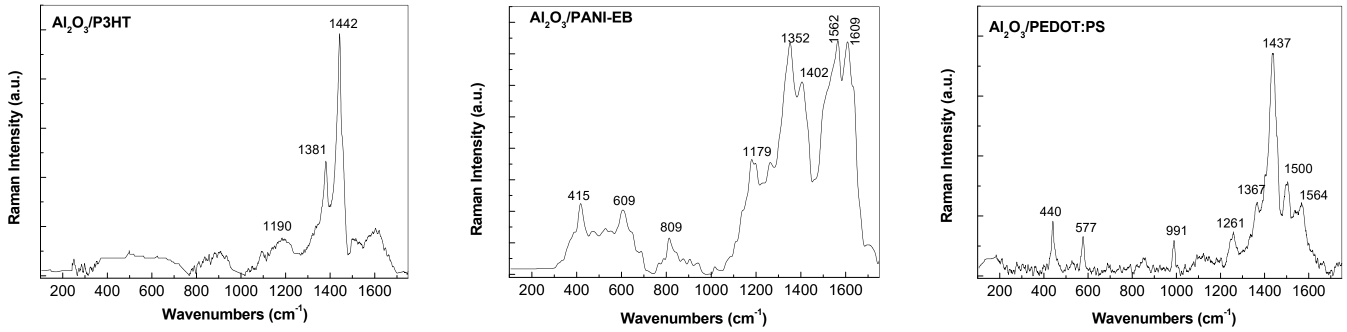

Figure 5. Raman spectra of Al_2O_3 nanotubes composites with P3HT, PANI-EB, and PEDOT:PS.

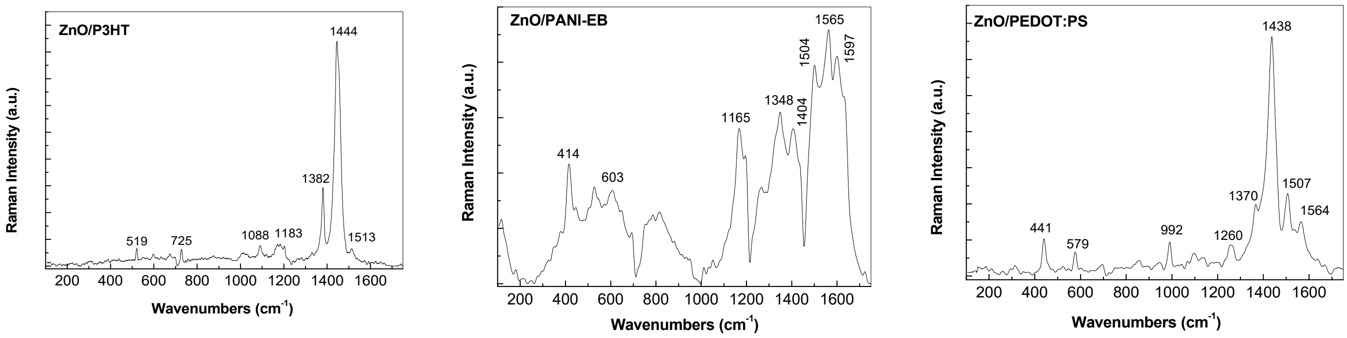

Figure 6. Raman spectra of ZnO nanotube composites with P3HT, PANI-EB, and PEDOT:PS.

The XPS analysis of the nanotube composites is presented in Figures 7 and 8.

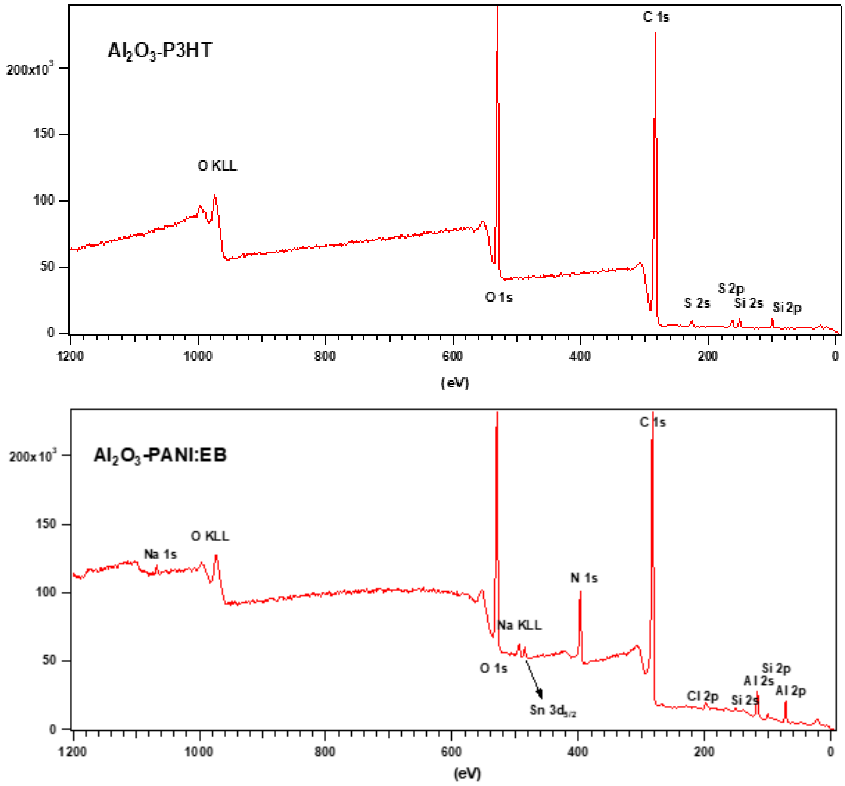

Figure 7. *Cont.*

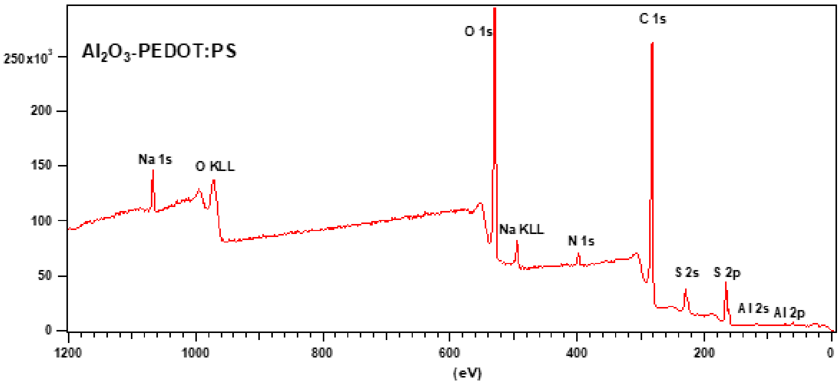

Figure 7. XPS analysis of Al_2O_3 nanotube composites with P3HT, PANI-EB, and PEDOT:PS.

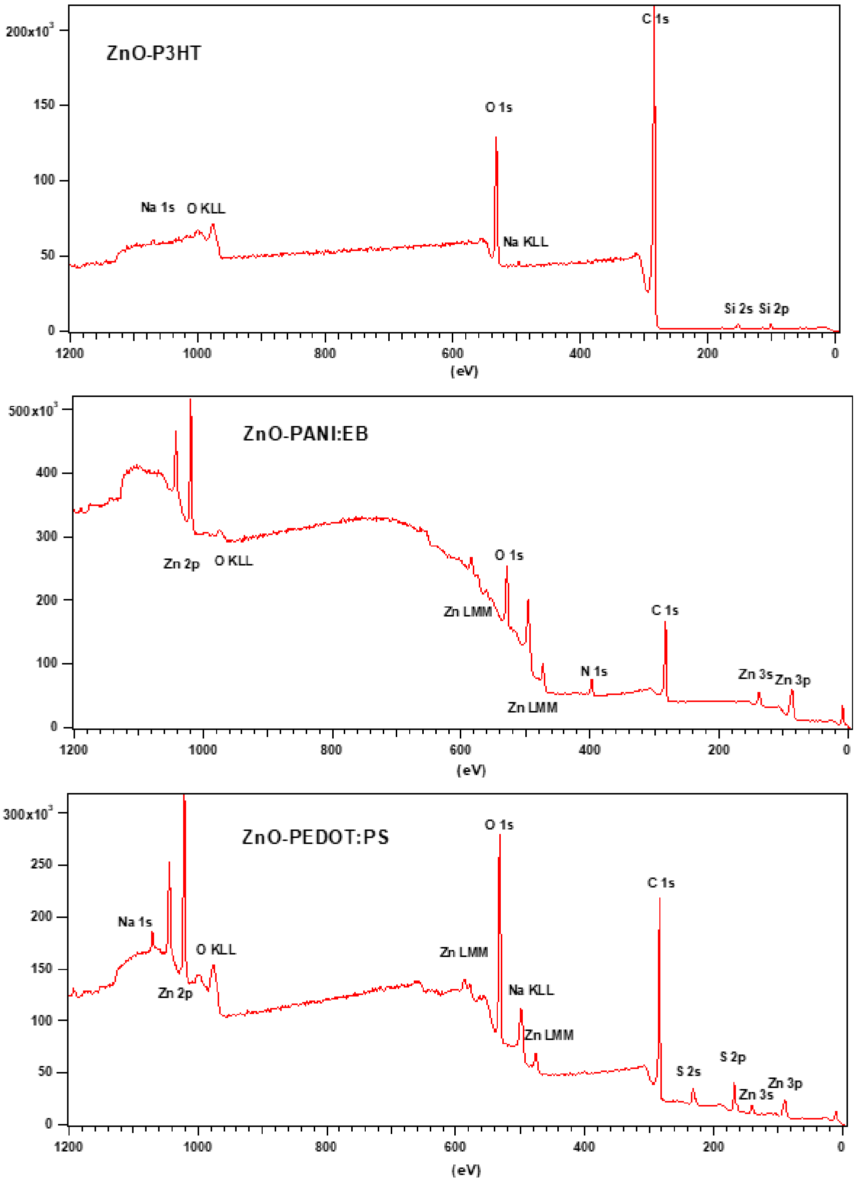

Figure 8. XPS analysis of ZnO nanotube composites with P3HT, PANI-EB, and PEDOT:PS.

As shown in Figure 3, the elements present on the surface of the Al_2O_3-P3HT sample and identified according to the general spectrum are oxygen, carbon, sulfur, and silicon; the elements present on the surface of the Al_2O_3-PANI:EB sample and identified according to the general spectrum are sodium, oxygen, nitrogen, carbon, sulfur, and aluminum; the elements present on the surface of the Al_2O_3-PEDOT:PSS sample and identified according to the general spectrum are sodium, oxygen, nitrogen, carbon, sulfur and aluminum.

As shown in Figure 4, the elements present on the surface of the ZnO-P3HT sample and identified according to the general spectrum are sodium, oxygen, carbon, silicon; the elements present on the surface of the ZnO-PANI:EB sample and identified according to the general spectrum are zinc, oxygen, nitrogen, carbon. The elements present on the surface of the ZnO-PEDOT:PS sample and identified according to the general spectrum are sodium, zinc, oxygen, carbon, sulfur.

Chemical interactions were also observed, but only between PANI-EB and ZnO ceramic nanotubes. In this case, an additional analysis of the EDS characteristic was performed (Figure 3). The chemical interactions are explained by the presence of oxygen in the polymer used and partially due to the large thickness of the samples.

3.4. SEM Analysis

Preliminary proof of the obtained ceramic nanotubes is presented in Figures 9 and 10.

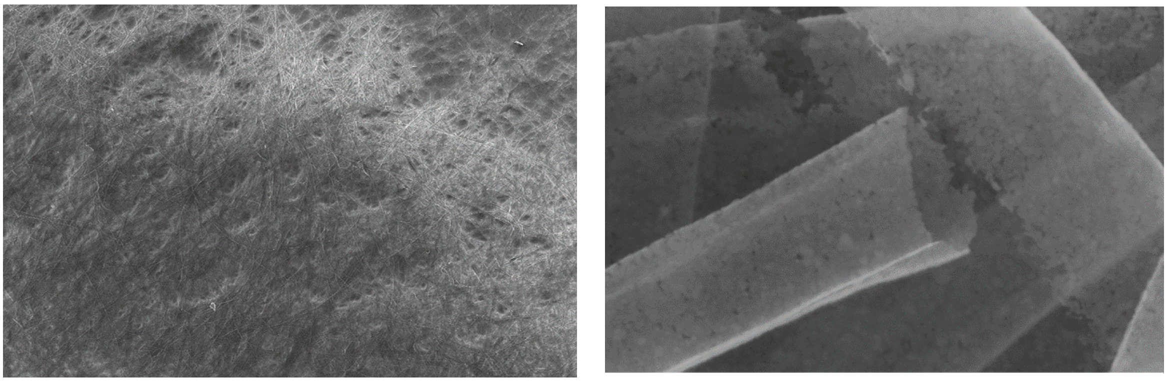

Figure 9. PMMA net with Al_2O_3 ceramic film (500 magnitudes, selected area); Al_2O_3 ceramic nanotubes after the thermal process (100 k magnitude, with image processing).

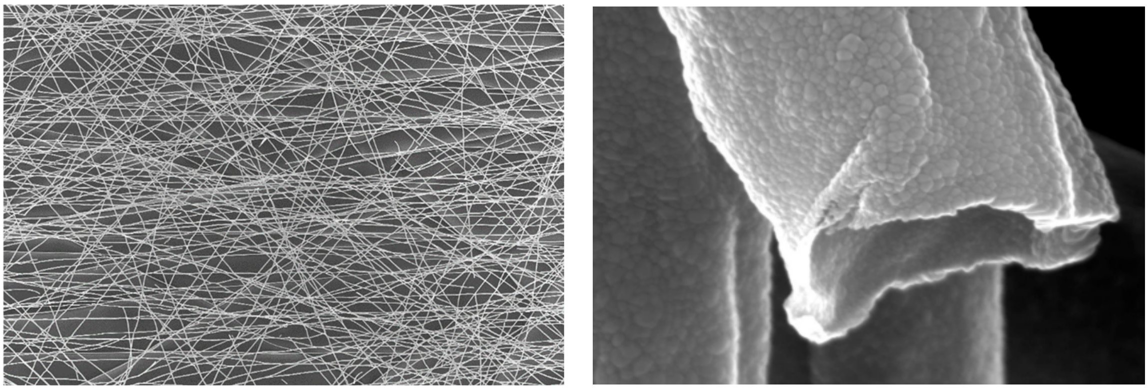

Figure 10. PMMA net with ZnO ceramic film (500 magnitudes, selected area); ZnO ceramic nanotubes after the thermal process (200 k magnitude, with image processing).

After conducting comprehensive chemical–physical analyses of the technological stages involved in the production of ceramic nanotubes, we observed a uniform dispersion of PMMA fibers within the deposited nets, along with a uniform deposition of ceramic film upon these fibers. Following the thermal process, the images of ceramic nanotubes confirmed the uniformity of the ceramic nanotube structures, which are hollow inside. Figures 11 and 12 show the SEM analysis at 1000x magnification for Al_2O_3 and ZnO nanotube composites with P3HT, PEDOT:PS, and PANI-EB. The difference in contrast is due to the thickness of the obtained material.

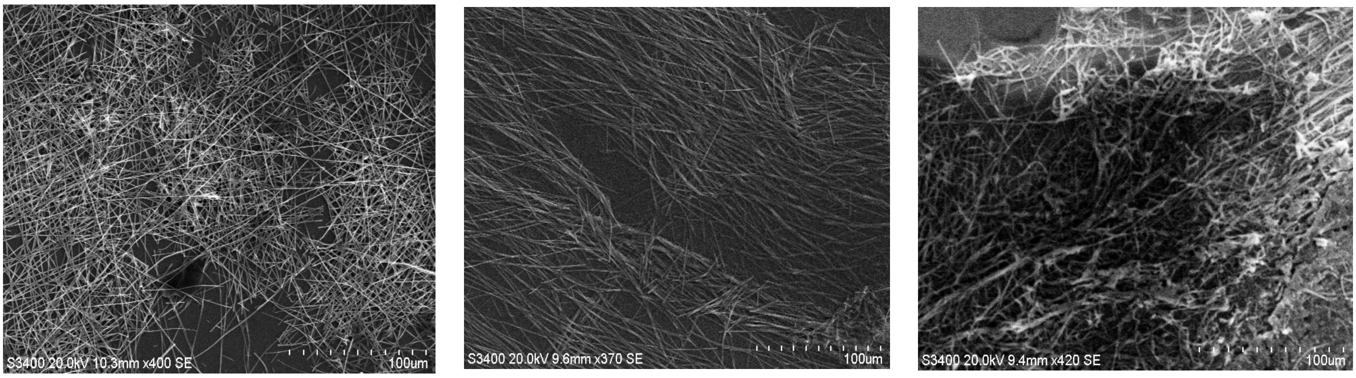

Figure 11. SEM image of Al_2O_3 nanotube composites with P3HT, PEDOT:PS, and PANI-EB.

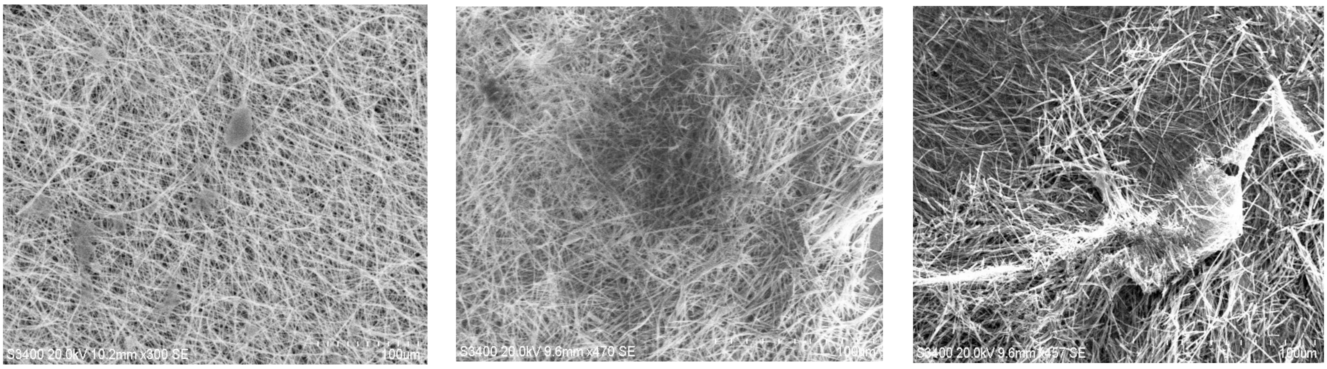

Figure 12. SEM analysis of ZnO nanotube composites with P3HT, PEDOT:PS, and PANI-EB.

In general, for both cases of ceramic nanotubes, a uniform morphology with a uniform distribution over the surface of composite nets is observed. There are no significant differences among the sizes of covered nanotubes with different polymers. In the ZnO-PANI:EB sample, the chemical interactions between the nanotube and polymer may lead to rare clusters. The SEM image in particular may offer a general view of the sample's morphology. Still, in the case of applications of sensors, the surface architecture, which is determined using AFM analysis, is decisive.

3.5. AFM Analysis

The AFM optical analysis shows the grain dimension, their distribution vs. surface area, and the general roughness of surfaces.

In the case of optical images (Figures 13 and 14), where the optical images are a little unclear, the composite film is characterized by a variable thickness. Very homogenous films are obtained for both ceramic nanotubes, mainly in the case of composites with PANI-EB.

After analyzing the AFM images (Figures 15–20), it is evident that for both ceramic nanotube composites, the grains are generally arranged either in smaller clusters or larger clusters, leading to the formation of zones with a symmetric distribution. Beyond this, the values of the parameter R_{ku}, close to or slightly above 3, indicate, in all cases, the formation of layers predominantly characterized by peaks and not by depressions, with a Gaussian distribution; Table 1.

In the case of Al_2O_3 nanotube composites with P3HT and PEDOT:PS, lower peaks of under 1 µm were obtained, and overall, the surfaces are smoother, with low roughness (Figures 15 and 16, Table 1).

In the case of Al_2O_3 nanotubes composites with PANI-EB, very high and agglomerated peaks of about 5 µm are obtained, and still, their distribution remains uniform despite larger roughness (Figure 17, Table 1). The architecture is settled in such a way that the peaks do not form large holes between them. For all composites based on Al_2O_3, the R_{Sk} parameters are positive and relatively high, indicating that the architecture of the surface is characterized more by higher spaces than by lower spaces.

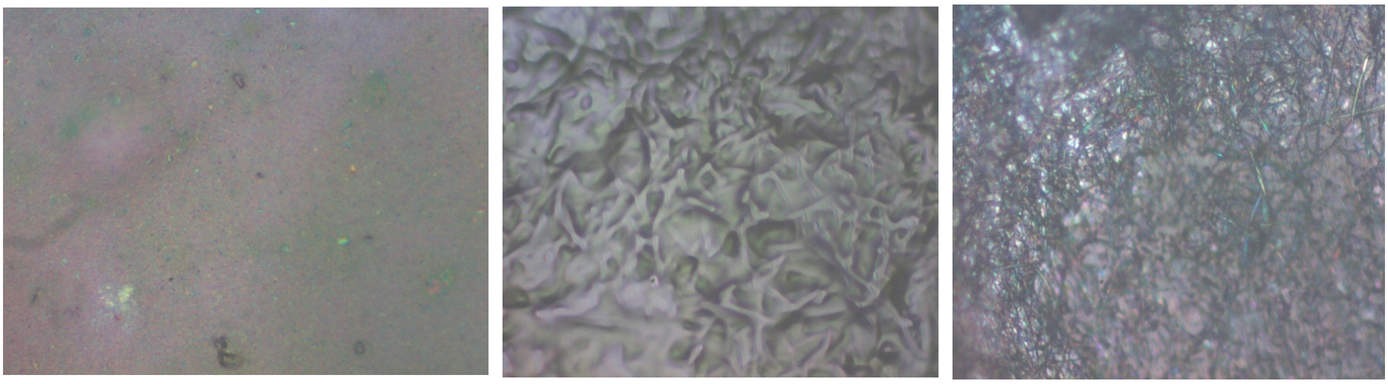

Figure 13. Optical analysis at 500x for Al_2O_3 nanotube composites with P3HT, PEDOT:PS, and PANI-EB.

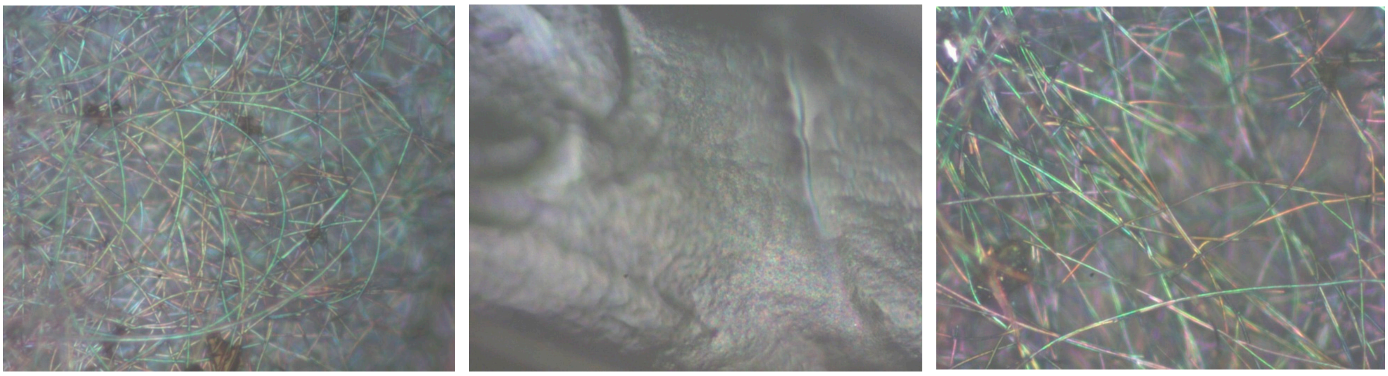

Figure 14. Optical analysis at 500x for ZnO nanotube composites with P3HT, PEDOT:PS, and PANI-EB.

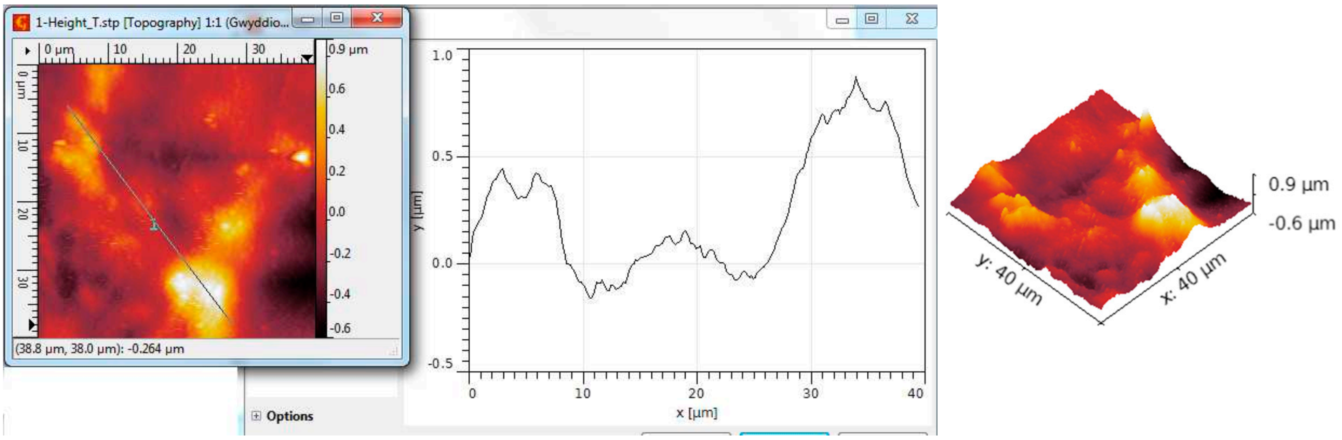

Figure 15. AFM topographic 2D and 3D images and profile lines—Al_2O_3 nanotube composites with P3HT.

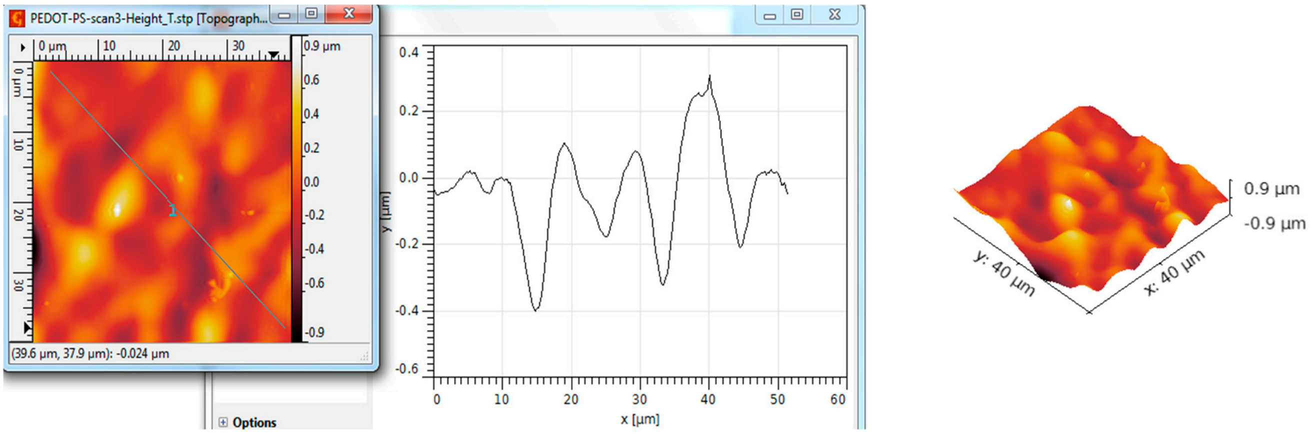

Figure 16. AFM topographic 2D and 3D images and profile lines—Al_2O_3 nanotube composites with PEDOT:PS.

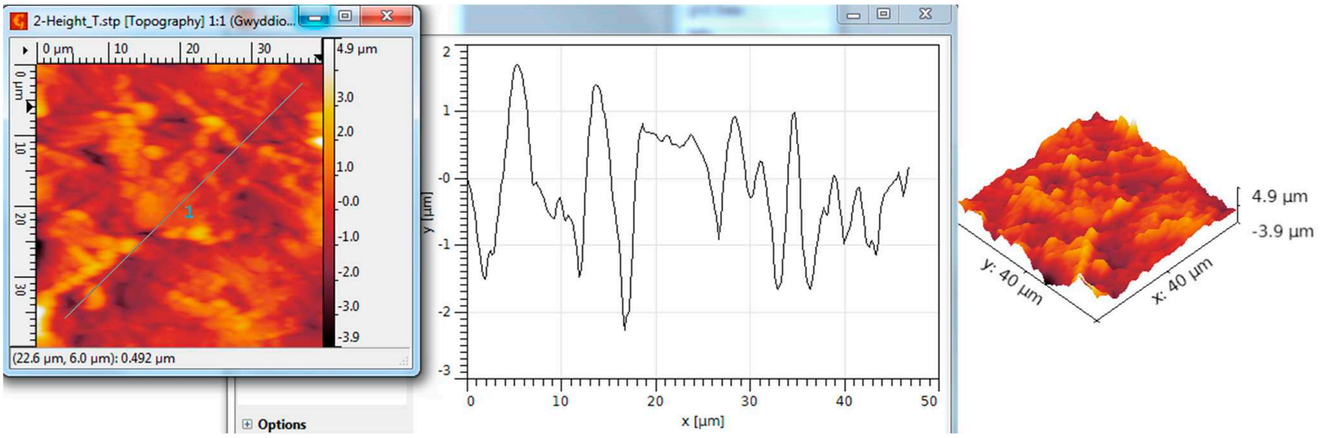

Figure 17. AFM topographic 2D and 3D images and profile lines—Al_2O_3 nanotube composites with PANI-EB.

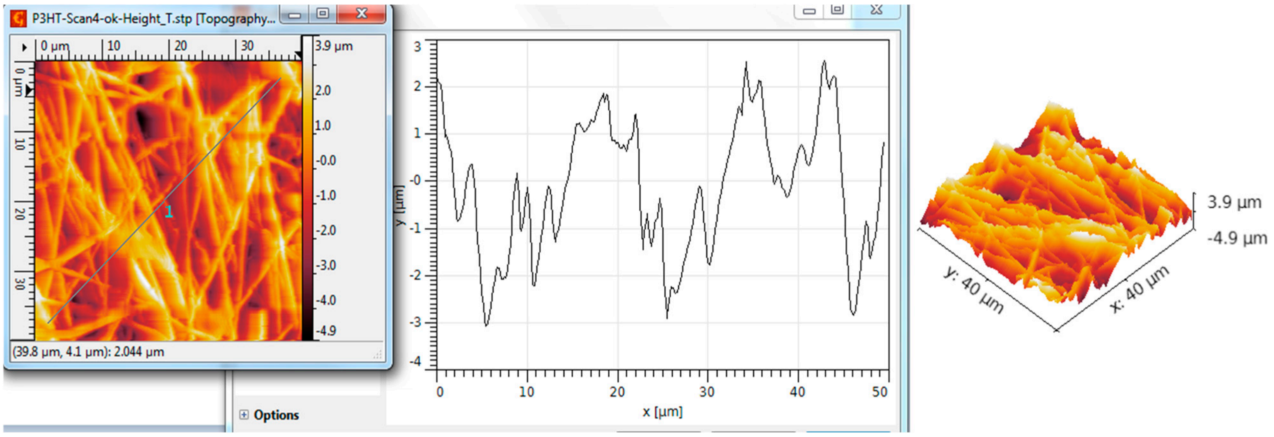

Figure 18. AFM topographic 2D and 3D images and profile lines—ZnO nanotube composites with P3HT.

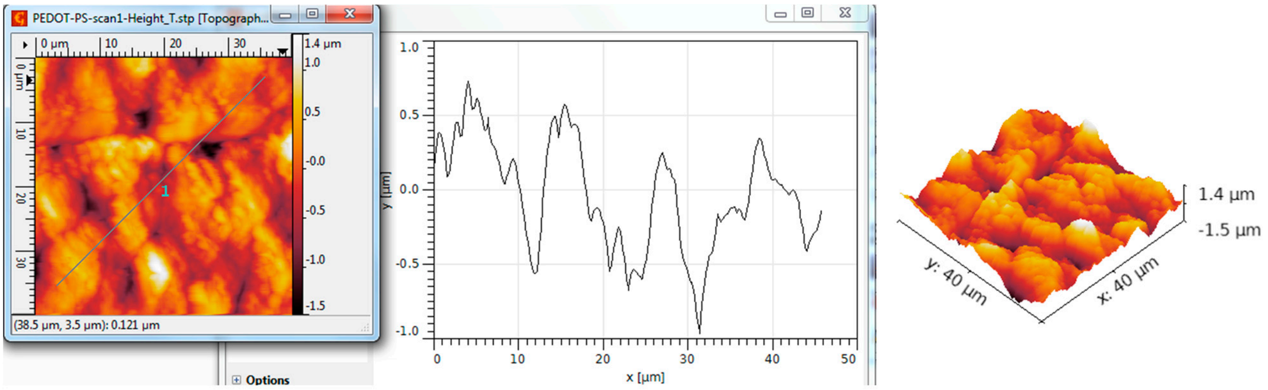

Figure 19. AFM topographic 2D and 3D images and profile lines—ZnO nanotubes composites with PEDOT:PS.

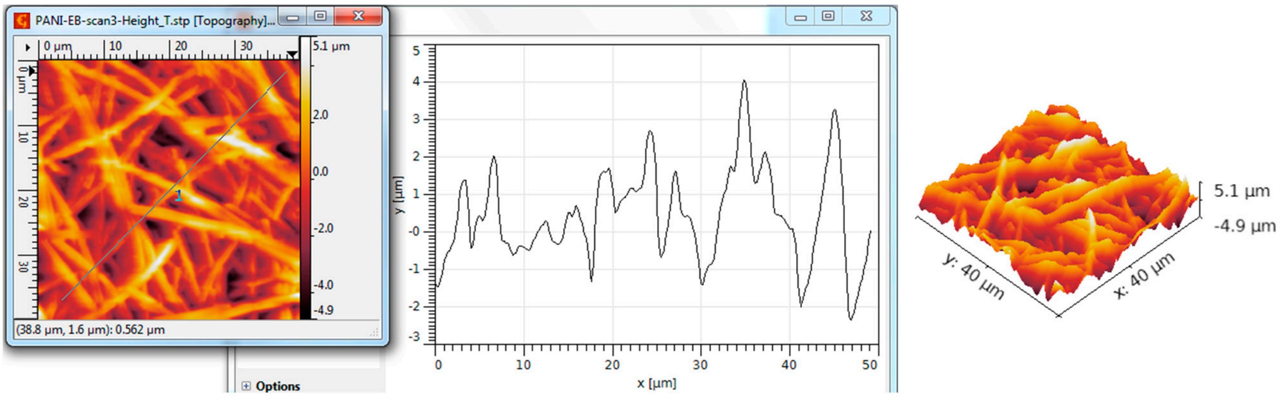

Figure 20. AFM topographic 2D and 3D images and profile lines—ZnO nanotube composites with PANI-EB.

Table 1. Average roughness parameters determined by AFM lines—scanned area 40x40 µm.

Scanned Material	RMS (nm)	Ra (nm)	R_{Sk}	R_{Ku}
Al_2O_3 nanotubes—P3HT	198	123	0.62	5.86
Al_2O_3 nanotubes—PEDOT:PS	273	194	0.16	3.97
Al_2O_3 nanotubes—PANI-EB	881	702	0.08	3.44
ZnO nanotubes—P3HT	1191	956	−0.15	2.88
ZnO nanotubes—PEDOT:PS	265	196	−0.13	4.23
ZnO nanotubes—PANI-EB	1413	1086	−0.21	2.89

Regarding the composites with ZnO nanotubes, in all cases, we noticed negative RSk parameters but relatively low values, indicating that the architecture of the surface is characterized more by lower spaces than by higher spaces; Table 1. Here, the peaks are higher for each polymer used compared to homolog Al_2O_3 nanotube composites. The ZnO nanotube composite also achieves the highest peaks with PANI-EB, exceeding 5 µm; Figure 20. Here, the parameters of RMS and Ra present the highest values of all samples, too, meaning the highest roughness; Table 1.

In summary, the AFM analysis emphasized a higher roughness in the case of PANI-EB for both nanotubes, with a much larger grain size dimension but an evenly distributed assortment of grains, with minimal empty space separating them. Structures with symmetrical distribution and high roughness dimensions at the µm scale are seen as ideal for gas sensor applications as they provide a significant active area for interacting with the gas being targeted.

4. Analysis of Functionality as Gas Sensors for Ammonia

In the literature, different processes of metallization of materials for chemiresitors are described, e.g., drop-casting, electrodeposition in solution, vacuum deposition, etc., but the majority of them are not suitable for basic sensor applications. In our situation, we utilized an ink-jet printer to apply commercial copper ink for printed electronic purposes. A resistor design was created, featuring an operational area of about 2 cm^2 (a relatively large surface because the concentration of potentially exhaled NH_3 to be detected was also very low) limited by two metalized regions that created the conductive links. The gas sensor's performance was evaluated with a test system that resembles the one detailed in [54]. The sensor was placed in a sealed container that only permitted gas exchange through two valves and access to the electric connections. A precision ohmmeter was used to externally measure the sensor's resistance. Different combinations of NH_3 in synthetic air (80% nitrogen and 20% oxygen) were transferred through the closed chamber via a valve and released through another valve to keep the pressure at 1 atm. The precise quantity of NH3 in artificial air was individually examined, sample by sample using an SGT-P portable ammonia gas detector (SENKO Advanced Components, Inc., Yokkaichi, Japan) in order to correlate the sensor resistance and NH_3 concentration on calibration curves.

Based on the conclusions related to the largest active area of composites with ceramic nanotubes and on a uniform distribution, hybrid structures of Al_2O_3 and ZnO nanotubes with PANI-EB were selected. Experimental calibration curves were plotted for both sensing structures for a larger domain of NH3 concentration in air of up to 5 ppm. The limit of detection (LoD) was found to be 0.5 ppm for both ceramic nanotube composites, a very reasonable value for the proposed applications; Figure 21. Under this concentration value, the resistance of both sensors presents extremely high and uncontrollable values, with low credibility to be compared with very low gas concentration, which is also difficult to measure with precision by any commercial ammonia gas detector.

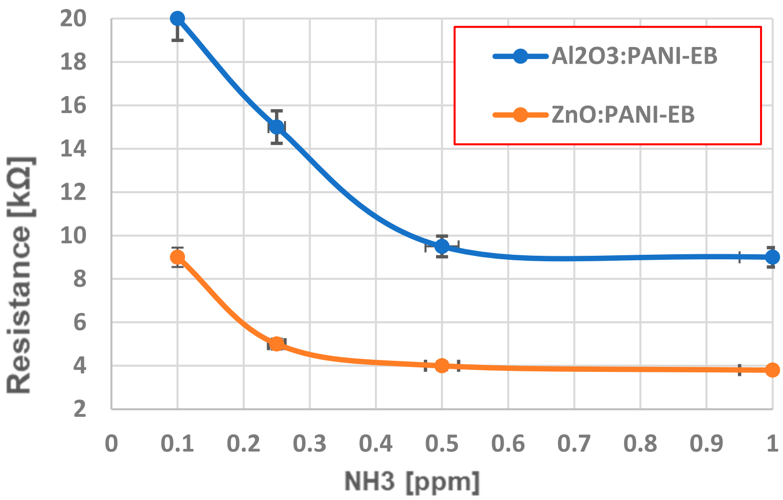

Figure 21. Limit of detection for sensing NH_3.

The experimental calibration curve for sensing NH_3 is presented in Figure 22. A high degree of correlation can be observed for both experimental calibration curves. The curve for ZnO: PANI-EB presents high linearity and lower resistance values, making it suitable for a broader assessment of NH_3 levels in air through a basic signal processing system. In contrast, the curve for Al_2O_3:PANI-EB can be represented by a polynomial curve of at least a second degree, leading to challenges in signal processing and potentially increasing the cost of the sensor. The explanation for the shapes of the characteristics is related to the electronic features of ceramic nanotubes in relation to the conductive polymer. ZnO is a wide-bandgap semiconductor of the II-VI n-type group, with native doping due to oxygen vacancies or zinc interstitials, compared to Al_2O_3, which exhibits more dielectric features and consequently determines a higher and nonlinear resistance.

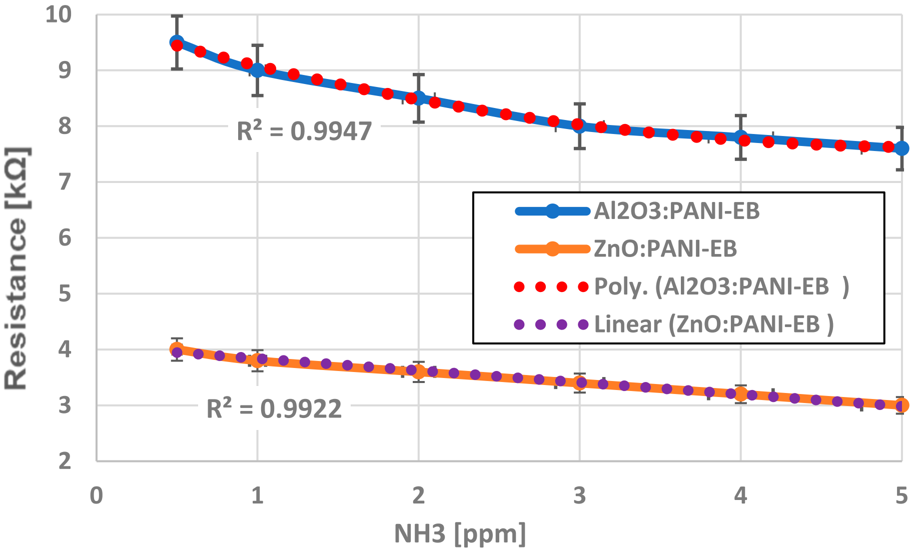

Figure 22. Experimental calibration curve for sensing NH_3.

For the application of breath ammonia detection, a threshold value of 1 ppm may indicate the syndrome occurrence, i.e., the occurrence of CKD stages greater than 1 [31,32], a threshold feasible for the presented sensor.

Figure 23 presents a comparison of the sensing structures of Al_2O_3:PANI-EB and ZnO: PANI-EB, showing the change in resistance over time for four NH_3 concentrations (0.5, 1, 2, and 3 ppm). The marker "On" is used to signify the start of measurements using NH_3 and customized mixtures of synthetic air until the resistance reaches a stable value, as shown in Figure 23. "Off" refers to the state in which only artificial air is directed to the sensor until it reaches its original resistance level in the air. Both resistance reduction and recovery exhibit a quasi-exponential nature. Initially, one can observe the heightened responsiveness of the ZnO: PANI-EB structure, resulting in a faster reaction.

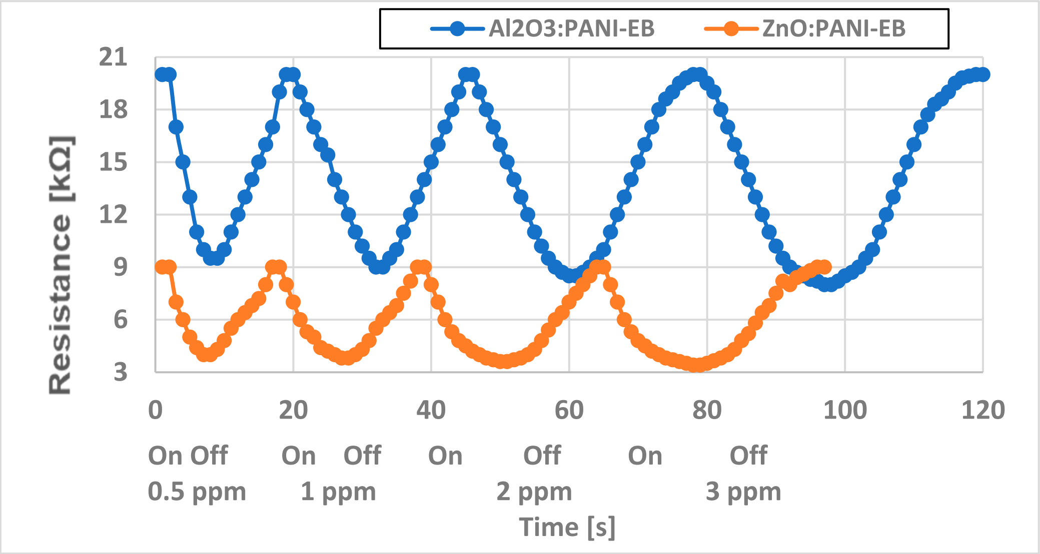

Figure 23. Experimental resistance–time curves for the sensing structures.

Figure 24 presents the assessment of the sensing structures' experimental response (on) and recovery time (off). In general, it was observed that the response and recovery times are shorter for the ZnO: PANI-EB structure. The discrepancy increases with greater NH_3 concentrations (2 or 3 ppm).

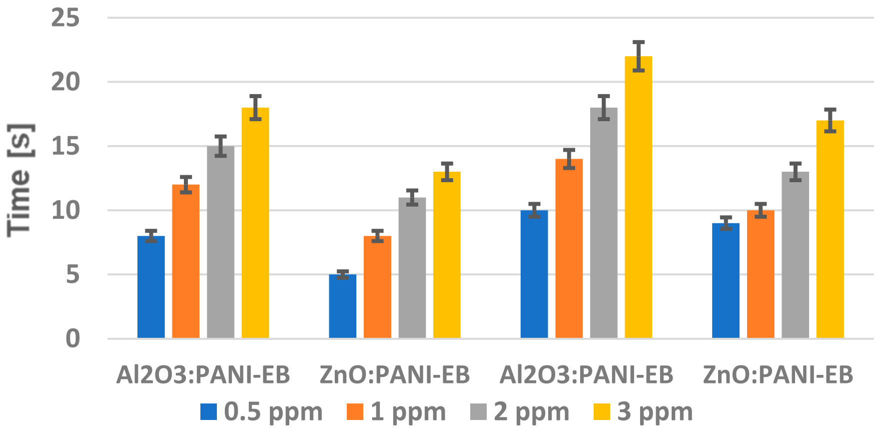

Figure 24. Experimental response (on) and recovery time (off) for the sensing structures.

The response time values around 5 s for ZnO: PANI-EB structure at 0.5 ppm NH_3 concentration are highly dependable for swiftly detecting CKD, linked to rapid exhalation of air through the mouth. After identifying the syndrome, its intensity can be reassessed by taking a slow breath out lasting around 10–11 s, which is a reasonable step to take. Regarding the recovery time value, it is deemed viable as, at higher NH3 concentrations, such as 3 ppm, the sensor only takes approximately 17 s to regain its initial resistance. Waiting approximately 1 min between consecutive measurements for medical purposes is reasonable, even when evaluating multiple patients using the same device.

The detection mechanism related to ceramic nanotube and conducting polymers is still under research due to the novelty of such assemblies. However, it can be related to the models presented, e.g., those in [55–57]. In principle, the effective absorption of gas molecules is the most significant way to achieve a high sensor response, and this is mainly due—in the case of hybrid assemblies—to the large dimension of grain size, with a pretty symmetrical distribution of grains, and with reduced free space between them (a high surface–volume ratio). On the other hand, the semiconducting properties of ceramic nanotubes and conducting polymer assemblies enhance the affinity to tailored gas molecules due to a higher carrier transport and the synergistic interaction between the components, which can be preliminarily evaluated from the XPS characteristic of ZnO-PANI:EB, i.e., by analyzing the high-resolution spectra for each main deep level—Zn 2p, O 1s, N 1s, and C 1s—in the energy domain related to each level (Figure 8). Even if the role of conducting polymer-based nanostructures is considered decisive for the sensing mechanism of gas sensors, as in [58–60], new approaches seem to consider that the architecture of hybrid assemblies of conducting polymers and metal oxide plays a major role in enhancing the affinity for detecting a certain gas [61–65]. The present research confirms this theory, in terms of the combination of these different materials resulting in synergistic outcomes. Combining conducting polymers with inorganic nanomaterials creates an efficient method to enhance the movement of charge carriers within and between polymer chains. It is considered that by introducing metal oxide nanostructures into the polymer matrix, a P-N heterojunction is created at the interfaces, which also leads to the generation of a depletion region in both the polymer and metal oxides, as shown by the AFM analysis. Efficient gas molecule absorption is crucial for achieving a strong sensing response in addition to interfacial interactions, as the physical absorption of gas molecules onto the film is the initial stage of gas detection. A coating with a significant surface area, the high volume of pores, and tailored pore size improve the absorption of gas molecules. The presence of target gas molecules on the surface of the nanocomposite film influences the electron levels in the polymers, resulting in a change in the depletion region width and potentially altering the conductive path of the polymers. The increased sensitivity of the nanocomposite films to the target analyte is caused by the combined impact of the altered conductivity and conductive pathway of the polymers in the films.

Regarding, the features of the presented sensor for ammonia, the reaction and restoration times of the sensing devices align with those of similar gas sensors, e.g., based on semiconductive assemblies found in references [49,66–70]. However, in our situation, the quicker response times are attributed to the direct utilization and increased conductivity of ZnO nanotubes and conducting polymer composites. Yet, the sensor characteristics remain inferior or equivalent at this stage regarding the minimum detection limit to other industrial sensors on the market for NH_3 concentrations in air, based on different testing methods (colorimetric, plasmonic, capacitive, electrochemical, etc.), as presented in [71–76]. However, practically none of those methods or related sensors are feasible for CKD evaluation in the medical environment. As long as the presented sensor can be tailored for different threshold values of NH_3 concentrations in air, with critical values of 1–2 ppm, it can be described as a basic, inexpensive, and durable device for personal use, helpful at the individual level, as it allows for better monitoring of the progression of the syndrome or effectiveness of treatment. Overall, the sensor characteristic is in line with the actual methods for CKD detection and evaluation. It can be customized for various threshold levels of NH_3 concentrations in the air based on the type of study and the extent of the syndrome. Utilizing a basic, inexpensive, and durable device for personal use can be advantageous for patients as it allows for a more efficient monitoring of syndrome progression or treatment effectiveness at an individual level.

Due to these preliminary successful results, the sensor features (mainly sensitivity, selectivity, response time, and reproducibility) will be further analyzed in the presence of perturbing factors, also determined by the breathing process. The potential influences of exhaled CO_2, exhaled humidity, and eventually, exhaled CH_4, will be assessed. The study may present additional relevance for associating related digestive syndromes, e.g., irritable bowel syndrome and exhaling CH_4 [77], a concept also suggested in [46] in relation to helicobacter pylori infection.

5. Conclusions

The process of producing chemiresistors, based on hybrid nanostructures obtained from Al_2O_3 and ZnO ceramic nanotubes and conducting polymers—poly(3-hexylthiophene), polyaniline emeraldine-base, and poly(3, 4-ethylenedioxythiophene)-polystyrene sulfonate—was technologically described.

The process of producing ceramic nanotubes from Al_2O_3 and ZnO involved three distinct and repeatable steps: creating polymer fiber nets using a 10 wt% solution of poly(methyl methacrylate) in dimethylformamide (DMF); depositing Al_2O_3 and ZnO films onto the PMMA nanofiber nets using magnetron deposition; and heating the nanotubes at 600 °C to completely burn off the PMMA support.

The technology for obtaining hybrid nanostructures from ceramic nanotubes, and subsequently conducting polymers, was drop-casting.

AFM analysis emphasized a higher roughness, mainly in the case of PANI-EB for both nanotube types, with a much larger grain size dimension of over 5 µm but with a relatively symmetrical distribution of grains, with reduced free space between them. The values of the parameter Rku were close or slightly above 3, indicating, in all cases, the formation of layers predominantly characterized by peaks and not by depressions, with a Gaussian distribution.

An ink-jet printer was used to generate chemiresistors from ceramic nanotubes: PANI-EB structures, and the metallization utilized copper ink designed for printed electronics. A resistor was created with a functional area of approximately 2 square centimeters. Calibration curves were experimentally created for both sensing structures, covering a wider range of NH_3 concentration in air, reaching up to 5 ppm. It was determined that the detection limit is 0.5 ppm. The ZnO:PANI-EB structure showed great linearity and lower resistance values, which makes it suitable for easily measuring NH_3 levels in the air on a large scale with a basic signal processing system. For the application of breath ammonia detection, a threshold value of 1 ppm may indicate the syndrome occurrence, i.e., appointment for CKD stages superior to 1, a threshold feasible for the presented sensor. As long as the sensor can be tailored for different threshold values of NH_3 concentrations in breath air, it can be defined as a simple, low-value, and robust device for individual use. This is beneficial at the patient level because the evolution of the syndrome or treatment efficiency can be surveyed more effectively.

Author Contributions: Conceptualization, A.F.T., R.C.C., T.G.S. and O.D.S.; methodology, R.C.C., O.D.S., T.G.S. and S.A.; validation, R.C.C., S.A. and A.F.T.; formal analysis, A.F.T., S.A., T.G.S. and R.C.C.; investigation, R.C.C., O.D.S., T.G.S., A.F.T. and S.A.; data curation, R.C.C., O.D.S., T.G.S. and A.F.T.; writing—original draft preparation, A.F.T. and R.C.C.; writing—review and editing, R.C.C., A.F.T. and S.A.; visualization, R.C.C., O.D.S., T.G.S. and A.F.T.; supervision, A.F.T. and R.C.C. All authors have read and agreed to the published version of the manuscript.

Funding: This research received no external funding.

Institutional Review Board Statement: Not applicable.

Informed Consent Statement: Not applicable.

Data Availability Statement: Data are contained within the article.

Conflicts of Interest: The authors declare no conflicts of interest.

References

1. Ohatkar, S.; Rane, S.; Ambesange, A.; More, A.; Rane, S. Nanostructured Metal Oxide Based Thick Film Sensors. *Int. J. Latest Technol. Eng. Manag. Appl. Sci.* **2016**, *5*, 93–97. Available online: https://www.ijltemas.in/DigitalLibrary/Vol.5Issue5/93-97.pdf (accessed on 12 June 2024).
2. Ayyala, S.; Covington, J. Nickel-Oxide Based Thick-Film Gas Sensors for Volatile Organic Compound Detection. *Chemosensors* **2021**, *9*, 247. [CrossRef]
3. Balhaddad, A.A.; Garcia, I.M.; Mokeem, L.; Alsahafi, R.; Collares, F.M.; de Melo, M.A.S. Metal Oxide Nanoparticles and Nanotubes: Ultrasmall Nanostructures to Engineer Antibacterial and Improved Dental Adhesives and Composites. *Bioengineering* **2021**, *8*, 146. [CrossRef]
4. Lee, M.; Kim, T.; Bae, C.; Shin, H.; Kim, J. Fabrication and applications of metal-oxide nano-tubes. *JOM* **2010**, *62*, 44–49. [CrossRef]
5. Researchers Learn to Control the Dimensions of Metal Oxide Nanotubes. 2007. Available online: https://phys.org/news/2007-08-dimensions-metal-oxide-nanotubes.html (accessed on 10 April 2023).
6. Enculescu, M.; Costas, A.; Evanghelidis, A.; Enculescu, I. Fabrication of ZnO and TiO_2 Nanotubes via Flexible Electrospun Nanofibers for Photocatalytic Applications. *Nanomaterials* **2021**, *11*, 1305. [CrossRef]
7. Ramasamy, P.; Lim, D.H.; Kim, J.; Kim, J. A general approach for synthesis of functional metal oxide nanotubes and their application in dye-sensitized solar cells. *RSC Adv.* **2014**, *4*, 2858–2864. [CrossRef]
8. Li, Y.; Yang, X.Y.; Feng, Y.; Yuan, Z.Y.; Su, B.L. One-Dimensional Metal Oxide Nanotubes, Nanowires, Nanoribbons, and Nanorods: Synthesis, Characterizations, Properties and Applications. *Crit. Rev. Solid State Mater. Sci.* **2012**, *37*, 1–74. Available online: https://www.tandfonline.com/doi/abs/10.1080/10408436.2011.606512 (accessed on 12 June 2024). [CrossRef]
9. Azevedo, J.; Fernández-García, M.P.; Magén, C.; Mendes, A.; Araújo, J.P.; Sousa, C.T. Double-walled iron oxide nanotubes via selective chemical etching and Kirkendall process. *Sci. Rep.* **2019**, *9*, 11994. [CrossRef]
10. Parthangal, P. Direct synthesis of tin oxide nanotubes on microhotplates using carbon nanotubes as templates. *J. Mater. Res.* **2011**, *26*, 430–436. [CrossRef]
11. Muench, F.; Sun, L.; Kottakkat, T.; Antoni, M.; Schaefer, S.; Kunz, U.; Molina-Luna, L.; Duerrschnabel, M.; Kleebe, H.-J.; Ayata, S.; et al. Free-Standing Networks of Core–Shell Metal and Metal Oxide Nanotubes for Glucose Sensing. *ACS Appl. Mater. Interfaces* **2017**, *9*, 1, 771–781. [CrossRef] [PubMed]
12. Kang, D.Y. Single-Walled Metal Oxide Nanotubes and Nanotube Membranes for Molecular Separations. Ph.D. Thesis, Georgia Institute of Technology, Atlanta, GA, USA, 2012. Available online: https://core.ac.uk/reader/10189860 (accessed on 10 April 2024).
13. Muto, H.; Sato, Y.; Tan, W.K.; Yokoi, A.; Kawamura, G.; Matsuda, A. Controlled formation of carbon nanotubes incorporated ceramic composite granules by electrostatic integrated nano-assembly. *Nanoscale* **2022**, *14*, 9669–9674. [CrossRef] [PubMed]
14. Mallakpour, S.; Khadem, E. Carbon nanotube–metal oxide nanocomposites: Fabrication, properties and applications. *Chem. Eng. J.* **2016**, *302*, 344–367. [CrossRef]

15. Rahat, S.S.M.; Hasan, K.M.Z.; Mondol, M.M.H.; Mallik, A.K. A comprehensive review of carbon nanotube-based metal oxide nanocomposites for supercapacitors. *J. Energy Storage* **2023**, *73*, 108847. [CrossRef]
16. Gupta, V.; Saleh, T. Syntheses of Carbon Nanotube-Metal Oxides Composites; Adsorption and Photo-Degradation. In *Carbon Nanotubes-From Research to Applications*; InTechOpen: London, UK, 2011; Available online: https://www.intechopen.com/chapters/16834 (accessed on 10 April 2024).
17. Trandabat, A.F.; Ciobanu, R.C.; Schreiner, O.D.; Aradoaei, M.; Aradoaei, S.T. Manufacturing of TiO_2, Al_2O_3 and Y_2O_3 Ceramic Nanotubes for Application as Electrodes for Printable Electrochemical Sensors. *Crystals* **2024**, *14*, 454. [CrossRef]
18. Saboor, F.H.; Ataei, A. Decoration of Metal Nanoparticles and Metal Oxide Nanoparticles on Carbon Nanotubes. *Adv. J. Chem.* **2024**, *7*, 122–145.
19. Kumar, N.; Navani, N.K.; Manhas, S.K. Effect of Metal Oxide Nanoparticles on Carbon Nanotube Device Characteristics. *J. Electron. Mater.* **2021**, *50*, 528–536. [CrossRef]
20. SUZHOU LEANSTAR ELECTRONICS TECH. Suzhou Industrial Park, Jiangsu Province, China: Preparation Method of Nano Metal Oxide Functionalized Carbon Nanotubes and Gas Sensor. Patent Application No. CN103058173B, 13 August 2014. Available online: https://eureka.patsnap.com/patent-CN103058173B (accessed on 10 April 2024).
21. Cho, H.H.; Smith, B.A.; Wnuk, J.D.; Fairbrother, D.H.; Ball, W.P. Influence of Surface Oxides on the Adsorption of Naphthalene onto Multiwalled Carbon Nanotubes. *Environ. Sci. Technol.* **2008**, *42*, 2899–2905. [CrossRef]
22. Ali, M.A.; Solanki, P.R.; Srivastava, S.; Singh, S.; Agrawal, V.V.; John, R.; Malhotra, B.D. Protein Functionalized Carbon Nanotubes-based Smart Lab-on-a-Chip. *ACS Appl. Mater. Interfaces* **2015**, *7*, 5837–5846.
23. Wang, H.; Boghossian, A. Covalent conjugation of proteins onto fluorescent single-walled carbon nanotubes for biological and medical applications. *Mater. Adv.* **2023**, *4*, 823–834. [CrossRef]
24. Lange, U.; Mirsky, V. Chemiresistors based on conducting polymers: A review on measurement techniques. *Anal. Chim. Acta* **2011**, *687*, 105–113. [CrossRef]
25. Lei, W.; Si, W.; Xu, Y.; Gu, Z.; Hao, Q. Conducting polymer composites with graphene for use in chemical sensors and bio-sensors. *Microchim. Acta* **2014**, *181*, 707–722. [CrossRef]
26. Rahman, A.; Pal, R.K.; Islam, N.; Freeman, R.; Berthiaume, F.; Mazzeo, A.; Ashraf, A. A Facile Graphene Conductive Polymer Paper Based Biosensor for Dopamine, TNF-α, and IL-6 Detection. *Sensors* **2023**, *23*, 8115. [CrossRef] [PubMed]
27. Wang, Y.; Liu, A.; Han, Y.; Li, T. Sensors based on conductive polymers and their composites: A review. *Polym. Int.* **2020**, *69*, 7–17. Available online: https://onlinelibrary.wiley.com/doi/abs/10.1002/pi.5907 (accessed on 12 June 2024). [CrossRef]
28. Lin, C.-H.; Lin, J.-H.; Chen, C.-F.; Ito, Y.; Luo, S.-C. Conducting polymer-based sensors for food and drug analysis. *J. Food Drug Anal.* **2021**, *29*, 544–558. [CrossRef]
29. Elanjeitsenni, V.P.; Vadivu, K.; Prasanth, M. A review on thin films, conducting polymers as sensor devices. *Mater. Res. Express* **2022**, *9*, 022001. [CrossRef]
30. Hira, S.A.; Yusuf, M.; Annas, D.; Nagappan, S.; Song, S.; Park, S.; Park, K.H. Recent Advances on Conducting Polymer-Supported Nanocomposites for Nonenzymatic Electrochemical Sensing. *Ind. Eng. Chem. Res.* **2021**, *60*, 13425–13437. [CrossRef]
31. Mooss, V.; Kesari, Y.; Athawale, A. Conducting polymer and metal-based sensors for the detection of vapours and toxic gases: A concise review. *J. Mater. Nanosci.* **2022**, *9*, 37–46.
32. Resistive Gas Sensor. Available online: https://www.electricity-magnetism.org/resistive-gas-sensor/ (accessed on 12 March 2024).
33. Baier, D.; Priamushko, T.; Weinberger, C.; Kleitz, F.; Tiemann, M. Selective Discrimination between CO and H_2 with Copper–Ceria-Resistive Gas Sensors. *ACS Sens.* **2023**, *8*, 1616–1623. [CrossRef]
34. Cheng, Y.; Li, Z.; Cheng, L.; Yuan, Y.; Xie, E.; Cao, X.; Xin, Z.; Liu, Y.; Tang, T.; Hu, X.; et al. Thickness-Dependent Room-Temperature Optoelectronic Gas Sensing Performances of 2D Nonlayered Indium Oxide Crystals from a Liquid Metal Printing Process. *ACS Appl. Mater. Interfaces* **2023**, *15*, 57496–57506. [CrossRef]
35. Elkady, M.F.; Hassan, H.S.; Amer, W.A.; Salama, E.; Algarni, H.; Shaaban, E.R. Novel Magnetic Zinc Oxide Nanotubes for Phenol Adsorption: Mechanism Modeling. *Materials* **2017**, *10*, 1355. [CrossRef]
36. Ansari, H.R.; Mirzaei, A.; Shokrollahi, H.; Kumar, R.; Kim, J.-Y.; Kim, H.W.; Kumar, M.; Kim, S.S. Flexible/wearable resistive gas sensors based on 2D materials. *J. Mater. Chem. C* **2023**, *11*, 6528–6549. [CrossRef]
37. Chesler, P.; Hornoiu, C. MOX-Based Resistive Gas Sensors with Different Types of Sensitive Materials (Powders, Pellets, Films), Used in Environmental Chemistry. *Chemosensors* **2023**, *11*, 95. [CrossRef]
38. Jian, Y.; Hu, W.; Zhao, Z.; Cheng, P.; Haick, H.; Yao, M.; Wu, W. Gas Sensors Based on Chemi-Resistive Hybrid Functional Nanomaterials. *Nano Micro Lett.* **2020**, *12*, 71. [CrossRef] [PubMed]
39. Chronic Kidney Disease. Available online: https://www.hopkinsmedicine.org/health/conditions-and-diseases/chronic-kidney-disease (accessed on 10 April 2024).
40. Chan, M.-J.; Li, Y.-J.; Wu, C.-C.; Lee, Y.-C.; Zan, H.-W.; Meng, H.-F.; Hsieh, M.-H.; Lai, C.-S.; Tian, Y.-C. Breath Ammonia is a Useful Biomarker Predicting Kidney Function in Chronic Kidney Disease Patients. *Biomedicines* **2020**, *8*, 468. [CrossRef]
41. Bevc, S.; Mohorko, E.; Kolar, M.; Brglez, P.; Holobar, A.; Kniepeiss, D.; Podbregar, M.; Piko, N.; Hojs, N.; Knehtl, M.; et al. Measurement of breath ammonia for detection of patients with chronic kidney disease. *Clin. Nephrol.* **2017**, *88*, 14–17. [CrossRef] [PubMed]

42. Ricci, P.; Gregory, O. Sensors for the detection of ammonia as a potential biomarker for health screening. *Sci. Rep.* **2021**, *11*, 7185. [CrossRef]
43. Wang, C.; Wang, T.; Li, Z.; Xu, X.; Zhang, X.; Li, D. An Electrochemical Enzyme Biosensor for Ammonium Detection in Aquaculture Using Screen-Printed Electrode Modified by Gold Nanoparticle/Polymethylene Blue. *Biosensors* **2021**, *11*, 335. [CrossRef]
44. Uzunçar, S.; Meng, L.; Turner, A.P.; Mak, W.C. Processable and nanofibrous polyaniline: Polystyrene-sulphonate (nano-PANI: PSS) for the fabrication of catalyst-free ammonium sensors and enzyme-coupled urea biosensors. *Biosens. Bioelectron.* **2021**, *171*, 112725. [CrossRef]
45. Ando, B.; Baglio, S.; Castorina, S.; Graziani, S.; Messina, M.; Petralia, S.; Tondepu, S.V.G. A Capacitive Readout Strategy for Ammonia Detection: Design Flow, Modeling and Simulation. In Proceedings of the 2021 IEEE Sensors Applications Symposium (SAS), Sundsvall, Sweden, 2–4 August 2021. [CrossRef]
46. Song, G.; Jiang, D.; Wu, J.; Sun, X.; Deng, M.; Wang, L.; Hao, C.; Shi, J.; Liu, H.; Tian, Y.; et al. An ultrasensitive fluorescent breath ammonia sensor for noninvasive diagnosis of chronic kidney disease and helicobacter pylori infection. *Chem. Eng. J.* **2022**, *440*, 135979. [CrossRef]
47. Silva, L.G.; Bueno, S.C.E.; da Silva, M.G.; Mota, L.; Sthel, M.S.; de Castro, M.P.P.; Neto, R.M.S.; Kuba, V.M. Photoacoustic detection of ammonia exhaled by individuals with chronic kidney disease. *Lasers Med. Sci.* **2022**, *37*, 983–991. [CrossRef]
48. Luo, S.-X.L.; Swager, T.M. Wireless Detection of Trace Ammonia: A Chronic Kidney Disease Biomarker. *ACS Nano* **2024**, *18*, 364–372. [CrossRef]
49. Latour, R.; Chumanov, G. *At-Home/Point-of-Care Breath-Based Ammonia In-vitro Diagnostic Platform for CKD Patients*; CURF: Clemson, SC, USA, 2021. Available online: https://curf.clemson.edu/technology/at-home-point-of-care-breath-based-ammonia-in-vitro-diagnostic-platform-for-ckd-patients/ (accessed on 10 April 2024).
50. Li, D.; McCann, J.T.; Xia, Y.; Marquez, M. Electrospinning: A Simple and Versatile Technique for Producing Ceramic Nanofibers and Nanotubes. *J. Am. Ceram. Soc.* **2006**, *89*, 1861–1869. [CrossRef]
51. Trznadel, M.; Zagórska, M.; Lapkowski, M.; Louarn, G.; Lefrant, S.; Pron, A. UV–VIS–NIR and Raman spectroelectrochemistry of regioregular poly(3-octylthiophene): Comparison with its non-regioregular analogue. *J. Chem. Soc. Faraday Trans.* **1998**, *24*, 3527–3780. [CrossRef]
52. Quillard, S.; Louarn, G.; Lefrant, S.; Macdiarmid, A.G. Vibrational analysis of polyaniline: A comparative study of leucoemeraldine, emeraldine, and pernigraniline bases. *Phys. Rev. B* **1994**, *50*, 12496. [CrossRef]
53. Garreau, S.; Louarn, G.; Buisson, J.P.; Froyer, G.; Lefrant, S. In Situ Spectroelectrochemical Raman Studies of Poly(3,4-ethylenedioxythiophene) (PEDT). *Macromolecules* **1999**, *32*, 6807–6812. [CrossRef]
54. Diédhiou, I.; Fall, B.; Gaye, C.; Sall, M.L.; Diaw, A.K.D.; Gningue-Sall, D.; Fall, M.; Raouafi, N. Preparations and applications of organic conducting polymers/graphene composites in heavy metal ion sensing: A review. *Int. J. Mater. Res.* **2023**, *114*, 79–99. [CrossRef]
55. Chen, W.; Zhou, Q.; Wan, F.; Gao, T. Gas Sensing Properties and Mechanism of Nano-SnO2-Based Sensor for Hydrogen and Carbon Monoxide. *J. Nanomater.* **2012**, *2012*, 612420. [CrossRef]
56. Niyat, F.Y.; Abadi, M.H.S. COMSOL-Based Modeling and Simulation of SnO_2/rGO Gas Sensor for Detection of NO_2. *Sci. Rep.* **2018**, *8*, 2149. [CrossRef]
57. Verma, A.; Gupta, R.; Verma, A.S.; Kumar, T. A review of composite conducting polymer-based sensors for detection of industrial waste gases. *Sens. Actuators Rep.* **2023**, *5*, 100143. [CrossRef]
58. Liu, X.; Zheng, W.; Kumar, R.; Kumar, M.; Zhang, J. Conducting polymer-based nanostructures for gas sensors. *Coord. Chem. Rev.* **2022**, *462*, 214517. [CrossRef]
59. Wong, Y.C.; Ang, B.C.; Haseeb, A.S.M.A.; Baharuddin, A.A.; Wong, Y.H.; Wong, Y.C.; Ang, B.C.; Haseeb, A.S.M.A.; Baharuddin, A.A.; Wong, Y.H. Conducting Polymers as Chemiresistive Gas Sensing Materials: A Review. *J. Electrochem. Soc.* **2020**, *167*, 037503. [CrossRef]
60. Cheon, H.J.; Shin, S.Y.; Van Tran, V.; Park, B.; Yoon, H.; Chang, M. Preparation of conjugated polymer/reduced graphene oxide nano-composites for high-performance volatile organic compound sensors. *Chem. Eng. J.* **2021**, *425*, 131424. [CrossRef]
61. Probst, D.; Lee, Y.; Dick, J.; Sode, K. Surface area independent response of closed bipolar electrodes. *Sens. Actuators Rep.* **2023**, *5*, 100138. [CrossRef]
62. Yan, Y.; Yang, G.; Xu, J.L.; Zhang, M.; Kuo, C.C.; Wang, S.D. Conducting polymer-inorganic nanocomposite-based gas sensors: A review. *Sci. Technol. Adv. Mater.* **2020**, *21*, 768–786. [CrossRef]
63. Zegebreal, L.; Tegegne, N.; Hone, F. Recent progress in hybrid conducting polymers and metal oxide nanocomposite for room-temperature gas sensor applications: A review. *Sens. Actuators A Phys.* **2023**, *359*, 114472. [CrossRef]
64. Sudheep, C.V.; Verma, A.; Jasrotia, P.; Hmar, J.J.L.; Gupta, R.; Verma, A.S.; Kumar, A.; Kumar, T. Revolutionizing gas sensors: The role of composite materials with conducting polymers and transition metal oxides. *Results Chem.* **2024**, *7*, 101255. [CrossRef]
65. Wuloh, J.; Agorku, E.S.; Boadi, N.O. Modification of Metal Oxide Semiconductor Gas Sensors Using Conducting Polymer Materials. *J. Sens.* **2023**, *2023*, 7427986. [CrossRef]
66. Nikolic, M.V.; Milovanovic, V.; Vasiljevic, Z.Z.; Stamenkovic, Z. Semiconductor Gas Sensors: Materials, Technology, Design, and Application. *Sensors* **2020**, *20*, 6694. [CrossRef]
67. Goel, N.; Kunal, K.; Kushwaha, A.; Kumar, M. Metal oxide semiconductors for gas sensing. *Eng. Rep.* **2023**, *5*, e12604. [CrossRef]

68. Witkiewicz, Z.; Jasek, K.; Grabka, M. Semiconductor Gas Sensors for Detecting Chemical Warfare Agents and Their Simulants. *Sensors* **2023**, *23*, 3272. [CrossRef]
69. Chai, H.; Zheng, Z.; Liu, K.; Xu, J.; Wu, K.; Luo, Y.; Liao, H.; Debliquy, M.; Zhang, C. Stability of Metal Oxide Semiconductor as Sensors: A Review. *IEEE Sens. J.* **2022**, *22*, 5470–5481. [CrossRef]
70. Molleman, B.; Alessi, E.; Krol, D.; Morton, P.A.; Daly, K. Application of metal oxide semiconductor for detection of ammonia emissions from agricultural sources. *Sens. Bio Sens. Res.* **2022**, *38*, 100541. [CrossRef]
71. Ammonia NH3 Sensor—50 PPM Range. Available online: https://www.pranaair.com/air-quality-sensor/ammonia-nh3-sensor/ (accessed on 10 April 2024).
72. Ammonia Sensors and Detectors. Available online: https://vocsens.com/ammonia-nh3-sensors/ (accessed on 10 April 2024).
73. NH3 Gas and Its Sensor. Available online: https://www.blacklinesafety.com/solutions/gas-sensors/nh3 (accessed on 10 April 2024).
74. Hagenaar, J.J.; Oshovsky, G.V.; Tempelman, C.H.; Majstorovic, M.; Herselman, J.F. Bio-Based Colorimetric Sensors for Detecting Ammonia in the Air. In Proceedings of the 2023 IEEE Sensors Conference, Vienna, Austria, 29 October–1 November 2023. [CrossRef]
75. Usman, F.; Ghazali, K.H.; Muda, R.; Dennis, J.O.; Ibnaouf, K.H.; Aldaghri, O.A.; Alsadig, A.; Johari, N.H.; Jose, R. Detection of Kidney Complications Relevant Concentrations of Ammonia Gas Using Plasmonic Biosensors: A Review. *Chemosensors* **2023**, *11*, 119. [CrossRef]
76. Fermion: MEMS Ammonia NH3 Gas Detection Sensor (Breakout, 1–300 ppm). Available online: https://www.dfrobot.com/product-2706.html (accessed on 10 April 2024).
77. Irritable Bowel Syndrome (IBS). Available online: https://www.nhs.uk/conditions/irritable-bowel-syndrome-ibs/ (accessed on 10 April 2024).

chemosensors

IMPACT FACTOR 3.7

CITESCORE 7.3

Article

TiO_2 Ceramic Nanotubes—Conducting Polymer Assemblies with Embedded Gold Particles for Potential Use as Chemosensors in the Detection of Oral Diseases

Oliver Daniel Schreiner, Alexandru F. Trandabat, Romeo Cristian Ciobanu and
Thomas Gabriel Schreiner

Special Issue
Novel Materials for Gas Sensing

Edited by
Dr. Cristian Viespe and Dr. Cornelia Enache

MDPI

https://doi.org/10.3390/chemosensors13040117

chemosensors

MDPI

Article

TiO_2 Ceramic Nanotubes—Conducting Polymer Assemblies with Embedded Gold Particles for Potential Use as Chemosensors in the Detection of Oral Diseases

Oliver Daniel Schreiner [1,2], Alexandru F. Trandabat [1], Romeo Cristian Ciobanu [1,*] and Thomas Gabriel Schreiner [2]

[1] Department of Electrical Measurements and Materials, Gheorghe Asachi Technical University, 700050 Iasi, Romania; oliver090598@yahoo.com (O.D.S.); ftranda@tuiasi.ro (A.F.T.)
[2] Department of Medical Specialties III, Faculty of Medicine, University of Medicine and Pharmacy “Grigore T. Popa”, 700115 Iasi, Romania
* Correspondence: r.c.ciobanu@tuiasi.ro

Abstract: Our research outlines a method for creating chemosensors utilizing hybrid nanostructures derived from TiO_2 ceramic nanotubes alongside conducting polymers, with embedded gold nanoparticles. The method used to create hybrid nanostructures from ceramic nanotubes and conducting polymers was drop-casting. AFM analysis highlighted an increased roughness, particularly for PANI-EB, exhibiting a significantly larger grain size exceeding 3.5 µm, with an increased inclusion of gold and uniform arrangement on the surface. The Rku parameter values being around three suggested that the layers primarily exhibited peaks rather than depressions, showing a Gaussian distribution. A chemiresistor was created by using an ink-jet printer and a multilayer metallization was achieved with commercial silver ink for printed electronics. Based on the experimental calibration curve, which exhibits adequate linearity over a wider range of H_2S concentrations in air up to 1 ppm, the detection limit was established at 0.1 ppm, a threshold appropriate for recognizing oral diseases. The sensor is a simple, affordable, and durable device designed for individual use, offering significant benefits for patients by enabling improved tracking of the syndrome’s advancement or treatment success.

Keywords: ceramic nanotubes; conducting polymers; gold nanoparticles; chemosensor; oral diseases

Received: 23 February 2025
Revised: 17 March 2025
Accepted: 19 March 2025
Published: 22 March 2025

Citation: Schreiner, O.D.; Trandabat, A.F.; Ciobanu, R.C.; Schreiner, T.G. TiO_2 Ceramic Nanotubes—Conducting Polymer Assemblies with Embedded Gold Particles for Potential Use as Chemosensors in the Detection of Oral Diseases. *Chemosensors* **2025**, *13*, 117. https://doi.org/10.3390/chemosensors13040117

1. Introduction

Oral diseases rank among the most prevalent human ailments, yet they are less researched. These illnesses impact the physical, mental, and social well-being of patients, leading to diminished quality of life. Inadequate oral care, genetic predispositions, and external influences significantly impact the onset and advancement of these conditions. Despite the existence of treatment alternatives for these conditions, recurrences limit their effectiveness [1]. The result is bad breath, a significant health issue. Despite its significance, patients often fail to notice their own oral malodor, and this challenge can lead to anxiety in those experiencing halitosis [1]. Foul odors arising from the mouth signify the metabolic activity of the entire oral microbial community. The breakdown of sulfur-containing amino acids in the mouth and upper/lower respiratory tract, and their exchange with blood in the alveoli, causes halitosis. Analytical methods relying on organoleptic assessments are essential for quantifying foul-smelling gases in the diagnosis and management of halitosis. However, it is possible that bad-smelling oral gases signify not just halitosis but also the pathogenic potential of oral microbiota.

Human breath that is exhaled includes nitrogen (approximately 78%), oxygen (16%), carbon dioxide (4–5%), hydrogen (5%), and water vapor. Oral volatile sulfur compounds (VSCs) are significantly generated in the oral cavity due to bacterial activity, stemming from the decomposition of sulfur-containing amino acids. Hydrogen sulfide (H_2S), methyl mercaptan (CH_3SH), and, to a smaller degree, dimethyl sulfide account for 90% of the VSCs associated with halitosis. H_2S is a gaseous neurotransmitter, mainly generated internally, which plays a role in the control of cellular functions. A significant rise in H_2S levels suggests the existence of different oral diseases in the individual [2].

Gas chromatography has been utilized to analyze hydrogen sulfide and methyl mercaptan, which are representative VSCs; however, this method is costly and necessitates skilled operators [3]. The VSC cut-off thresholds for identifying halitosis were determined by gas chromatography to be 65.79 ppb for females and 79.94 ppb for males, though these figures pertain to the group of individuals included in a specific clinical study [4]. Typically, any concentration exceeding 0.5 ppm is regarded as significant for the diagnosis of halitosis and associated metabolic issues [5], irrespective of the measurement technique employed [6]. Portable gas chromatography devices like Oral Chroma™ [7] can measure the levels of hydrogen sulfide, methyl mercaptan, and dimethyl sulfide separately. A portable sulfide detector like the Halimeter [8] is specifically designed to assess the overall concentration of sulfide. However, it requires a considerable amount of time for measurement and is exclusively fit for clinical use, despite it providing several clear benefits (portable, user-friendly, reproducible, and providing immediate outcomes). Conversely, it does not have the ability to distinguish between various sulfuric compounds when affected by non-sulfuric volatile substances, like Oral Chroma™ does [9]. Finally, the OralChroma™ device now merges gas chromatography with a gas sensor made of an indium oxide semiconductor. Another similar example is given in [10]. Such combined methods can determine the exact concentrations of each VSC component in 10 min, which is a practical duration for medical applications, but their cost remains fairly high. Lastly, Breathtron® [11] utilizes a semiconductor sensor made of a zinc oxide membrane that is responsive to VSCs. Its assessment is regarded as more precise than that of the Halimeter; however, it requires a lengthy measurement time and is applicable solely in clinical settings.

It is clear, however, that the practical aim of a sensor for oral diseases should not solely depend on its availability in a clinic, but rather the advancement of such sensors should primarily address the requirements of patients who monitor their own conditions. Different kinds of H_2S sensors have been suggested to meet the needs for halitosis investigation [12–14]. The most prevalent H_2S sensors utilize semiconducting metal oxides; they are inexpensive and can be operated quickly and effortlessly [15–19]. Nonetheless, metal oxide semiconductor (MOS) gas sensors generally exhibit low selectivity, since they respond to all reducing or oxidizing gases. Electrochemical sensors were tested as well; however, they are not as sensitive as MOS gas sensors and are affected by variations in temperature and humidity [20]. Various other H_2S-sensing technologies have been suggested, including colorimetric sensors [21], surface acoustic wave gas sensors [22,23], and devices created with different sensing structures based on thick metal oxides [24–27]. Nonetheless, these sensors face challenges linked to the need for selectivity or detection of ppb levels.

Embellishing sensorial frameworks with conductive substances, like graphene, carbon nanotubes (CNTs), or metallic nanoparticles has been widely discussed recently in the literature to improve sensor selectivity, and may be applied in H_2S detection applications. Combining metal oxides with various metal-based catalysts can enhance both sensitivity and selectivity. Certain doped metal oxides may interact with gases that contain sulfur, causing a modification in their electrical conductivity [28–31]. Recent research upon the chemisorption of H_2S on gold nano-structures [32] resulted in sensors exhibiting minimal variability, excellent selectivity, and enduring stability, positioning gold nanostructures as a strong candidate for further exploration. The impact of gold nano-structures is enhanced when the metal oxide base, where the gold particles are incorporated, is presented as nanowires or nano-sheets. Even though the nanofiber interacted with sulfur-based gases, the incorporation of metal increased its sensitivity to hydrogen sulfide [33–36]. Nevertheless, the complex nature of these processes impeded the production of H_2S sensors with reliable and repeatable attributes. On the other hand, because human exhaled breath contains substantial amounts of water vapor, there are considerable disadvantages for sensors lacking proper moisture resistance, a critical factor to consider alongside the impact of other gases released in human breath [37–39].

In conclusion, to our knowledge, an H_2S sensor that possesses high selectivity, detection capabilities at parts per billion levels, and a straightforward fabrication method resulting in consistent sensor properties has yet to be created, warranting further research in this area. The novelty of this paper mainly relates to the development of hybrid nanostructures formed from TiO_2 nanotubes and conductive polymers doped with gold nanoparticles, exhibiting unique sensing properties that are not present in the current literature. The choice of titanium dioxide is due to its properties as a wide-bandgap semiconductor that exhibits excellent chemical stability and remarkable resistance to corrosion from sulfur-bearing gases. The sensor principle described in the paper is less complex, more cost-effective, and more effective than the methods currently suggested for detecting sulfur-containing gases in breath, akin to the application with the previously mentioned sensor types.

2. Technology for Obtaining Hybrid Nanostructures from Ceramic Nanotubes and Conducting Polymers with Embedded Gold Nanoparticles

Materials and Methods of Preparation

According to the comprehensive technological stages widely described in [40,41], the process for producing ceramic nanotubes involved three steps: creating polymer fiber networks using poly(methyl methacrylate), depositing ceramic coatings onto the nanofiber networks through magnetron deposition, and heating the nanotubes to 600 °C to completely remove the polymer support. The optimal results were achieved with a 10% PMMA solution at 20 kV, with a drum rotation speed of 5 rpm, as the fiber nets exhibited greater homogeneity in both spatial deposition and diameter. Conversely, considering the properties of ceramic thin films to be applied on PMMA nanofibers, a minimum diameter of 0.3 µm was deemed ideal for PMMA nanofibers to ensure the structural stability of coated fibers from a mechanical perspective [41]. Concerning RF magnetron sputtering, ceramic targets measuring 2 inches in diameter and 0.125 inches in thickness were utilized during the deposition process. The deposition time lasted for 1 h, and the RF power supplied to the magnetron was 200 watts.

The process for subsequently obtaining hybrid nanostructures from TiO_2 nanotubes and conductive polymers such as poly(3-hexylthiophene) (P3HT), polyaniline emeraldine-base (PANI-EB), and poly(3, 4-ethylenedioxythiophene)-polystyrene sulfonate (PEDOT-PS) included drop-casting. Five samples of each type were created to evaluate technological feasibility. The technological process involved the use of the solutions outlined in [42]. In all instances, 240 µL of every polymer solution was applied onto ceramic nanotubes (SiO_2/Si substrate) using Pasteur pipettes. Each solvent underwent evaporation for 60 min in a vacuum, using a Pfeiffer vacuum pump linked to a desiccator.

The TiO_2-conductive polymer composite materials were further immersed in a diluted $HAuCl_4$/2-propanol solution (0.001 M) using the dip-coating technique, and stored for 24 h. Following impregnation, the samples were subjected to drying in an oven at 150 °C with a flow of Ar (100 sccm) for 30 min. The samples were subsequently cooled to room temperature in an argon stream. Au nanoparticles with an average size of 100 nm were quasi-uniformly integrated into the hybrid structures. This method for acquiring predefined Au nanoparticles from a highly diluted HAuCl4 solution on the polymer substrate, heated from ambient temperature to just over one hundred degrees Celsius, resembles those described in [43,44]. However, this method, presented in the paper, involves immersing the polymer film in a highly diluted $HAuCl_4$ solution, which has the benefit of forming and quasi-uniformly distributing gold nanoparticles over larger areas, a necessary requirement for creating more responsive gas sensors.

3. Results and Discussion

3.1. Characterization Equipment

Transmission electron microscopy (TEM) results were obtained using a JEOL 2100 Plus transmission electron microscope operating at an accelerating voltage of 80 kV (JEOL Ltd., Akishima, Tokyo, Japan). SAED assessment was carried out as well.

Raman Spectroscopy was performed using AvaRaman 532 instruments (Avantes B.V., Apeldoorn, The Netherlands).

Fourier transform infrared spectroscopy (FTIR) was performed using JASCO instruments (Tokyo, Japan), across a spectral range of 12,000–50 cm^{-1}.

X-ray photoelectron spectroscopy (XPS) and energy-dispersive X-ray spectroscopy (EDS) were performed utilizing an AXIS Supra+ system (Kratos Analytical Ltd., Manchester, UK).

Scanning electron microscopy (SEM) was performed with Lyra III XMU equipment (TESCAN GROUP a.s., Brno-Kohoutovice, Czech Republic). To evaluate the obtained graphene layer, a sequential morphological examination was performed.

An assessment using atomic force microscopy (AFM) was conducted with a Dimension Edge instrument from Bruker (Billerica, MA, USA) for optical purposes. Average roughness measurements are provided for four scanned regions on each type of sample. The analysis of the surface roughness parameters was according to [45,46].

3.2. TEM and Selected Area (Electron) Diffraction (SAED) Analysis of TiO_2—Conducting Polymers Composites

The TEM images for TiO_2 nanotube composites are presented in Figures 1–3, from which the tetragonal TiO_2 anatase phase can be identified, as nanotubes with diameters of approx. 400–500 nm with extended areas of crystalline coherence. The pick intensity from the EDX spectrum related to the concentration of TiO_2 nanotubes in the composite assembly is similar in all diagrams. But, for each diagram, the other picks beyond Ti are specific to the composition of the respective polymer corresponding to the composite assembly. In Figure 1, from the EDX spectrum, the TiO_2/PANI-EB ratio was 30:70 (% at).

In Figure 2, from the EDX spectrum, the TiO_2/PEDOT:PS ratio was 33.3:66.6 (% at).

In Figure 3, from the EDX spectrum, the TiO_2/P3HT ratio was 28:72 (% at).

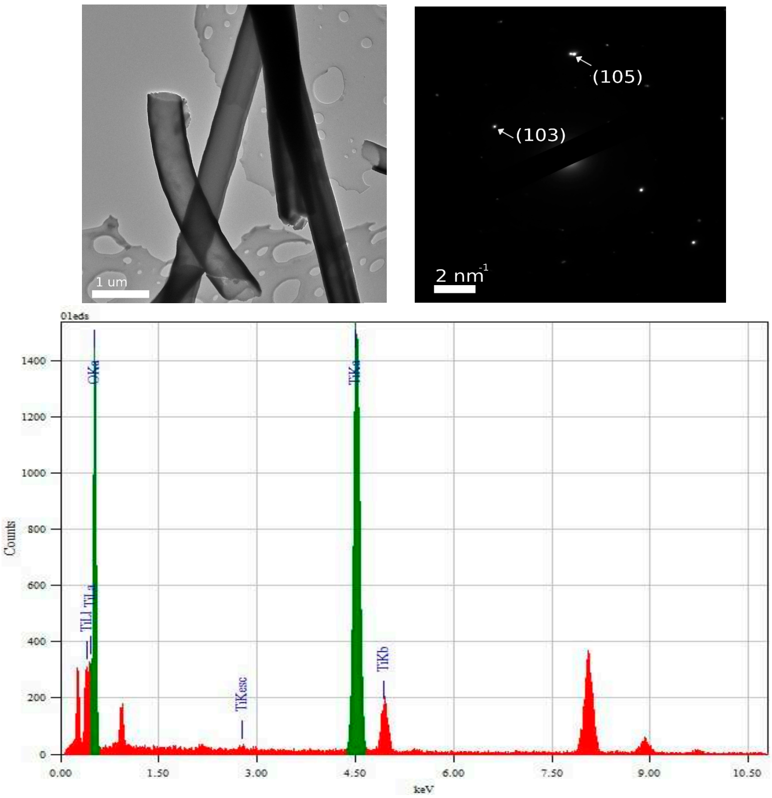

Figure 1. TEM image for TiO_2 nanotube–PANI-EB composite.

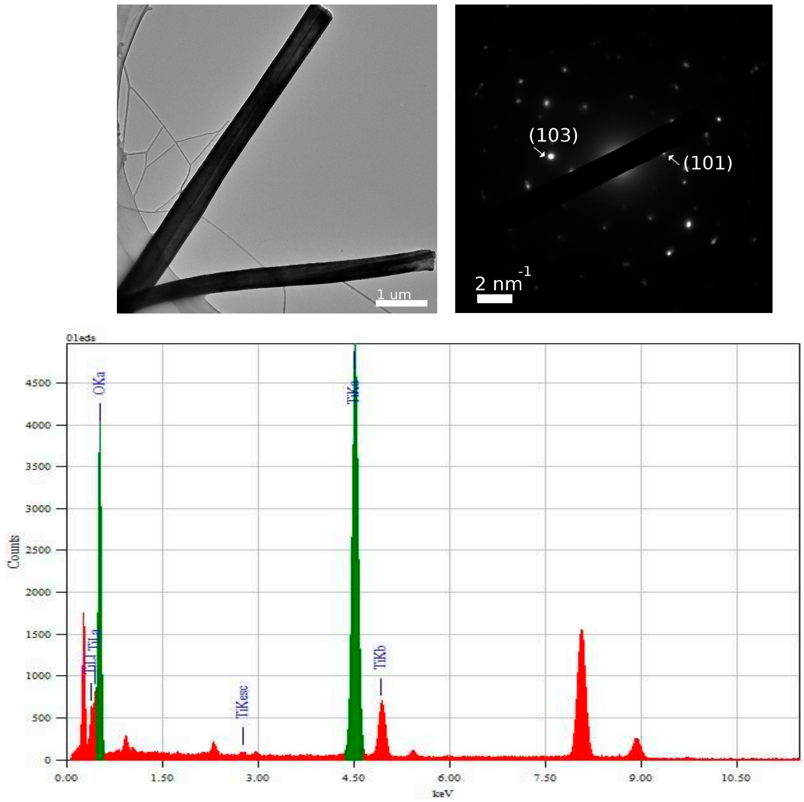

Figure 2. TEM image for TiO_2 nanotube–PEDOT:PS composite.

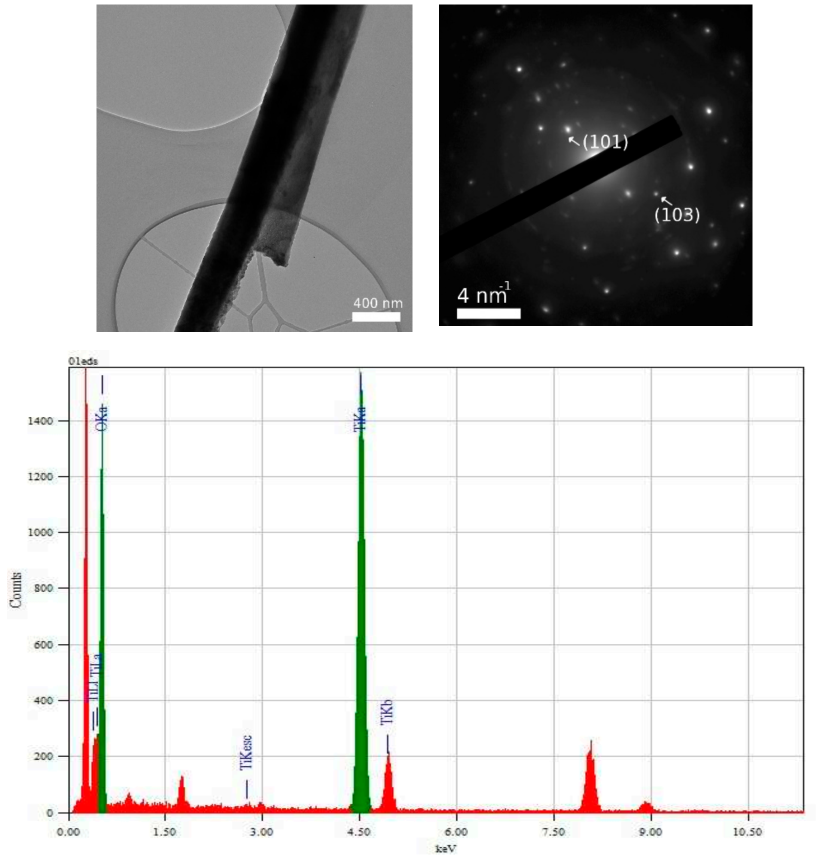

Figure 3. TEM image for TiO_2 nanotube–P3HT composite.

3.3. Raman and FTIR, XPS, and EDS Analysis of TiO_2—Conducting Polymers Composites

Figure 4 shows the Raman spectra recorded at an excitation wavelength of 514 nm for TiO_2 nanotube composites with PANI-EB, PEDOT:PS, and P3HT. The analysis reveals that the main Raman lines of the TiO_2 nanotubes are located at 144, 396, 519, and 639 cm^{-1}, attributed to the Eg, B_1g, A_1g, and Eg vibration modes [47]. In general, for all spectra of TiO_2 nanotube–polymer composites, each Raman spectrum corresponds to the sum of the two constituents of the respective composite materials. The absorption bands of the three polymers may be independently identified: (i) PANI-EB at approx. 814, 1176, 1247, 1352, 1414, 1501, 1565, and 1610 cm^{-1}, attributed to the deformation vibration modes of the benzene ring (B), of the C-H bond in the benzene ring, the C-N stretch, C-H bond in the quinoid ring, C-C stretch in the quinoid ring, and C-H bond in the quinoid ring, the C=N stretch, the C=C stretch in the quinoid ring and, respectively, the C-C stretch in the benzene ring [48]; (ii) PEDOT PS at approx. 439–574–990, 1257, 1364, 1439, 1502, and 1569 cm^{-1} are attributed to the vibrational modes of deformation of the oxyethylene ring, of C_α-$C_{\alpha'}$ stretching and C-H bending, of C_β-$C_{\beta'}$ stretching, of symmetric C-C stretching and of asymmetric C-C stretching [49]; (iii) 729, 1013, 1092, 1184, 1380, 1442, 1515 and 1620 cm^{-1} attributed to C_α-S-$C_{\alpha'}$ bond deformation vibration modes, C_β-C_{alchil} stretching, C_β-H bond bending, C_α-$C_{\alpha'}$ stretching, C_β-H bending, C_β-C_β stretching, C_α=C_β stretching, $C_{\alpha'}$=$C_{\beta'}$ stretching and, respectively, the quinoid structure [50].

The XPS analysis of the TiO_2 nanotube composites is presented in Figure 5. Measurement conditions are as follows: Anode Al (1486.74 eV); U = 15.kV; I = 15 mA; P = 225 W; p SAC 5 X 10–9 mbar; Parameter spectrum recording Line Extended spectrum E start (eV), 1200; Estop (eV), −5; step (eV), 0.1; Pass Energy (eV), 140; number of passes, 1.

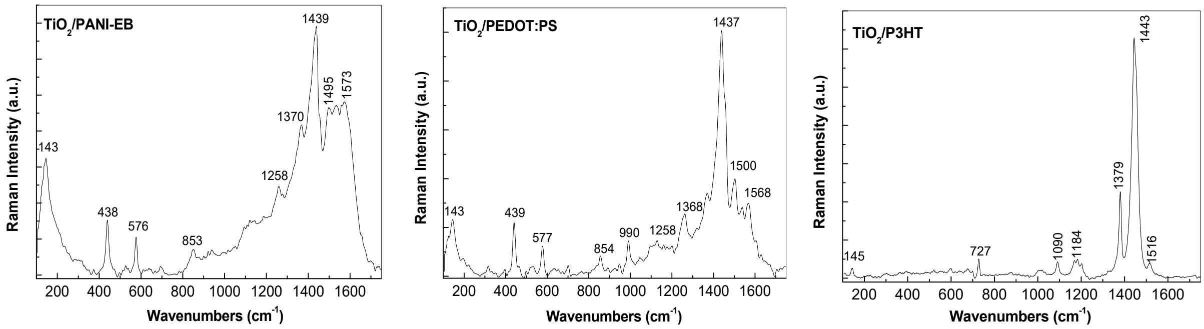

Figure 4. Raman spectra of TiO_2 nanotubes composites with PANI-EB, PEDOT:PS, and P3HT.

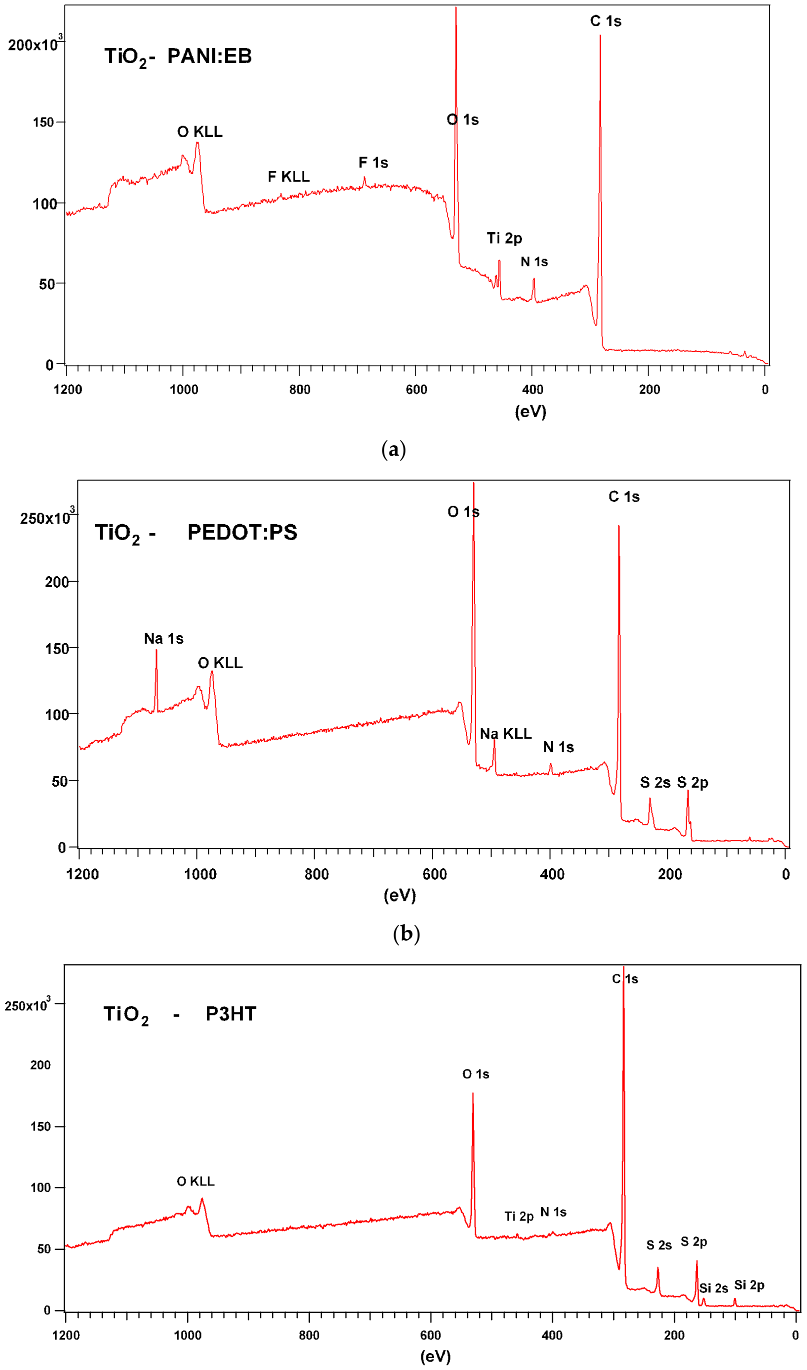

(**a**)

(**b**)

(**c**)

Figure 5. XPS analysis of TiO_2 nanotubes composites with (**a**) PANI-EB, (**b**) PEDOT:PS, and (**c**) P3HT.

In Figure 5a, related to the TiO_2-PANI:EB sample, the identified elements are as follows: fluorine, oxygen, titanium, nitrogen, and carbon, for which high-resolution spectra were recorded (main peaks: F 1s, O 1s, Ti 2p, N 1s, C 1s). In Figure 5b related to the TiO_2-PEDOT:PS sample, the elements present on the surface with main peaks were sodium, oxygen, nitrogen, carbon, and sulfur (Na 1s, O 1s, N 1s, C 1s, S 2p). Finally, in Figure 5c, related to the TiO_2-P3HT sample, the identified elements are as follows: oxygen, titanium, nitrogen, carbon, sulfur, and silicon (main peaks: O 1s, Ti 2p, N 1s, C1s, S 2p and Si 2p).

3.4. SEM Analysis of TiO_2—Conducting Polymers Composites with Au Addition

SEM image 6, of TiO_2/PANI-EB composites with Au, reveals that some gold nanoparticles attach to the TiO_2 nanotubes, while others fit into the gaps between the ceramic nanotubes. The dispersion of gold nanoparticles is quite uniform and the quantity is relevant, although some agglomerations are observable.

From SEM image 7, of TiO_2/PEDOT: PS composites with Au, it can be seen that gold was rarely deposited in the form of nanoparticles, but rather in the form of clusters. It seems that the area covered in gold seems to be reduced.

From SEM image 8 of TiO_2/P3HT composites with Au, it can be seen that gold was primarily deposited in the form of nanoparticles, but some forms of clusters are also visible. The morphology is similar to TiO_2/PANI-EB composites with Au; however, the area coated in gold appears to be slightly diminished.

3.5. AFM Analysis of TiO_2—Conducting Polymers Composites with Au Addition

Figures 6–8 emphasize the surface analysis via SEM. It is evident that the gold was deposited both in the form of nanoparticles and in clusters, influenced by the affinity to the polymer used for deposition support, but also related to the spatial architecture of TiO_2—conducting polymer composites before being submitted to the dip-coating technique, consistent with the findings shown in [42] for different ceramic nanotubes, yet utilizing the same polymers.

From an optical perspective, Figures 9–11 resulted in comparable conclusions to Figures 6–8, noting that the sample includes both TiO_2 nanotubes and Au.

It should be noted that the composite films exhibit varying thicknesses, and although uniform films were achieved for all polymer cases, more uniform structures were associated with the composite containing PEDOT-PS and PANI-EB, where it seems that the polymer was deposited more effectively, and covered, much more efficiently, the spaces formed between the nanotubes.

Additionally, the AFM optical examination displayed the grain size, their distribution across the surface, and the overall roughness of the surfaces [45,46].

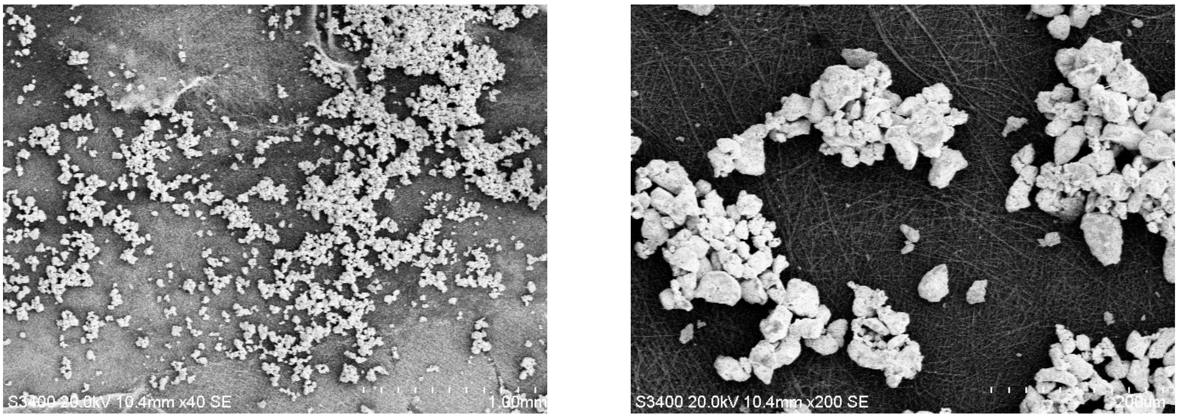

Figure 6. SEM image of TiO_2/PANI-EB composites with Au.

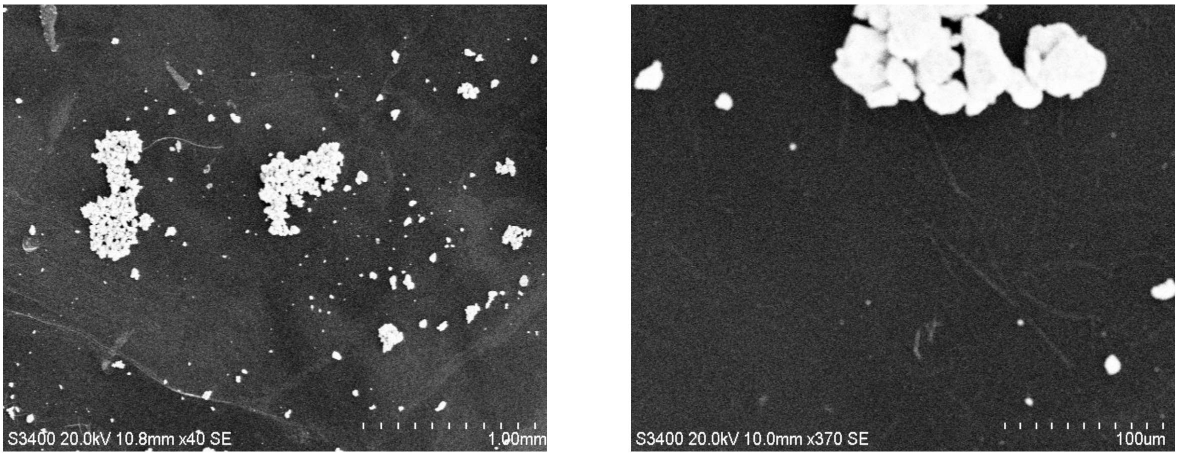

Figure 7. SEM image of TiO_2/PEDOT: PS composites with Au.

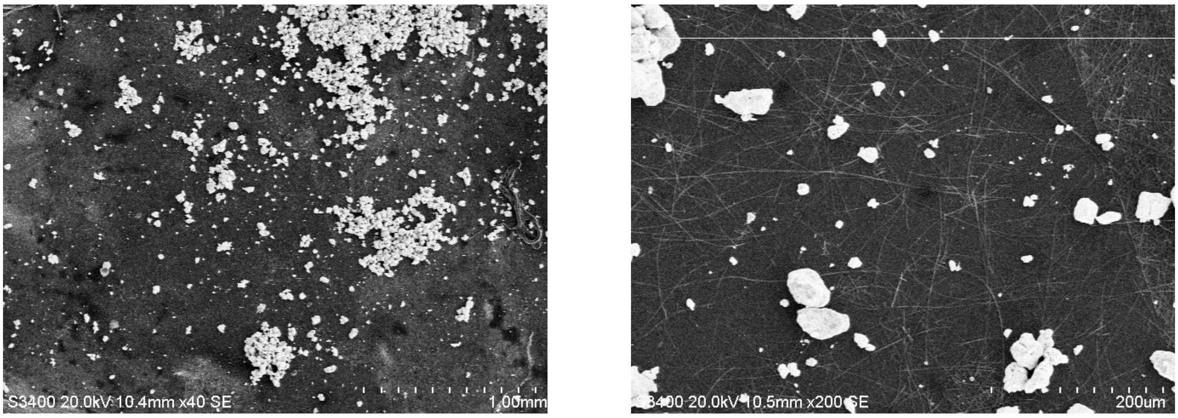

Figure 8. SEM image of TiO_2/P3HT composites with Au.

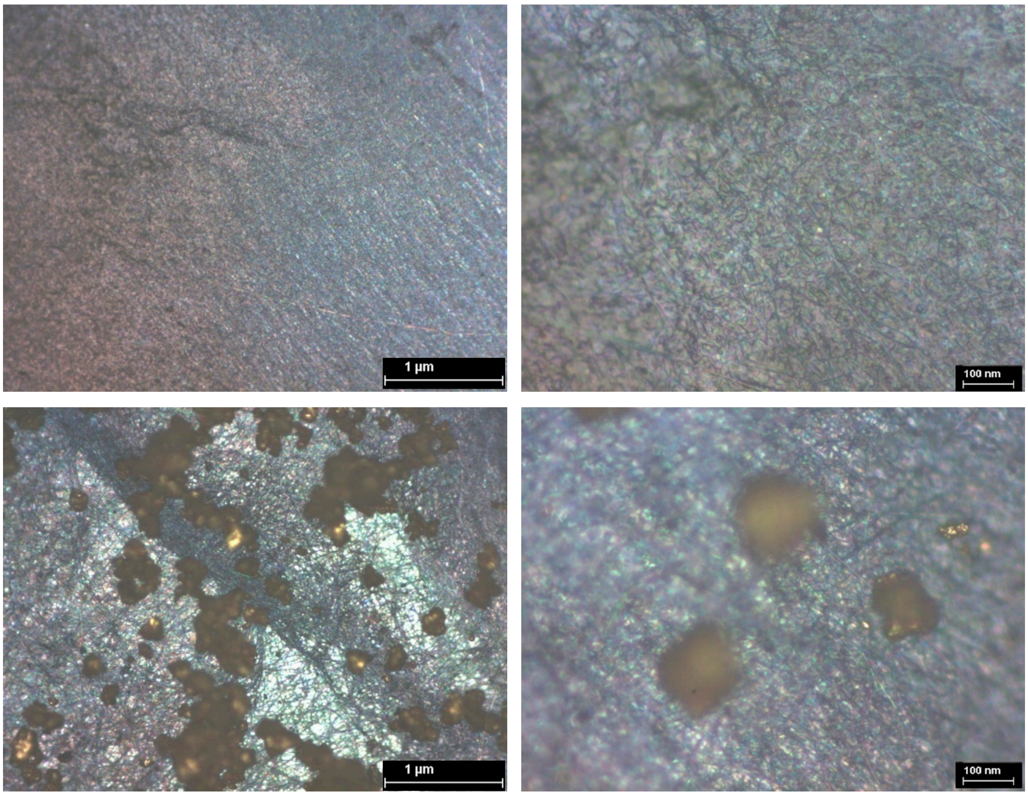

Figure 9. Optical analysis at 100× and 500× of TiO_2/PANI-EB composites without and with Au.

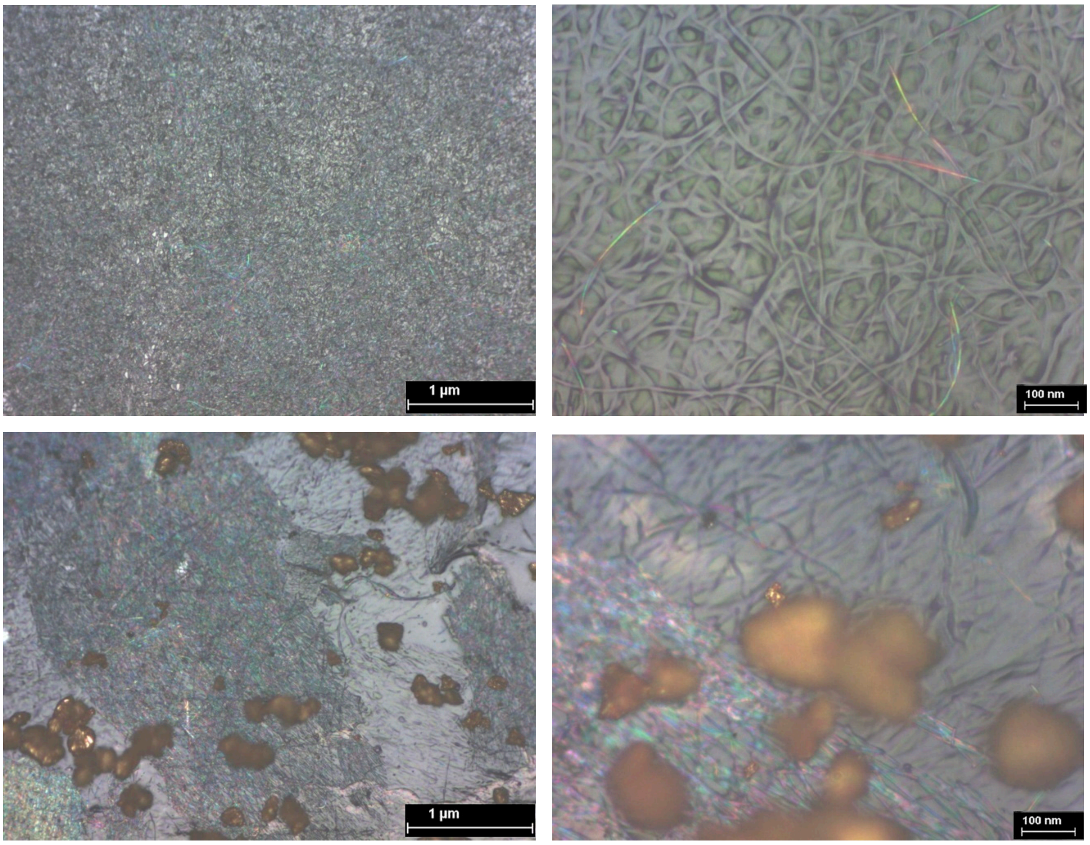

Figure 10. Optical analysis at 100× and 500× of TiO_2/PEDOT: PS composites without and with Au.

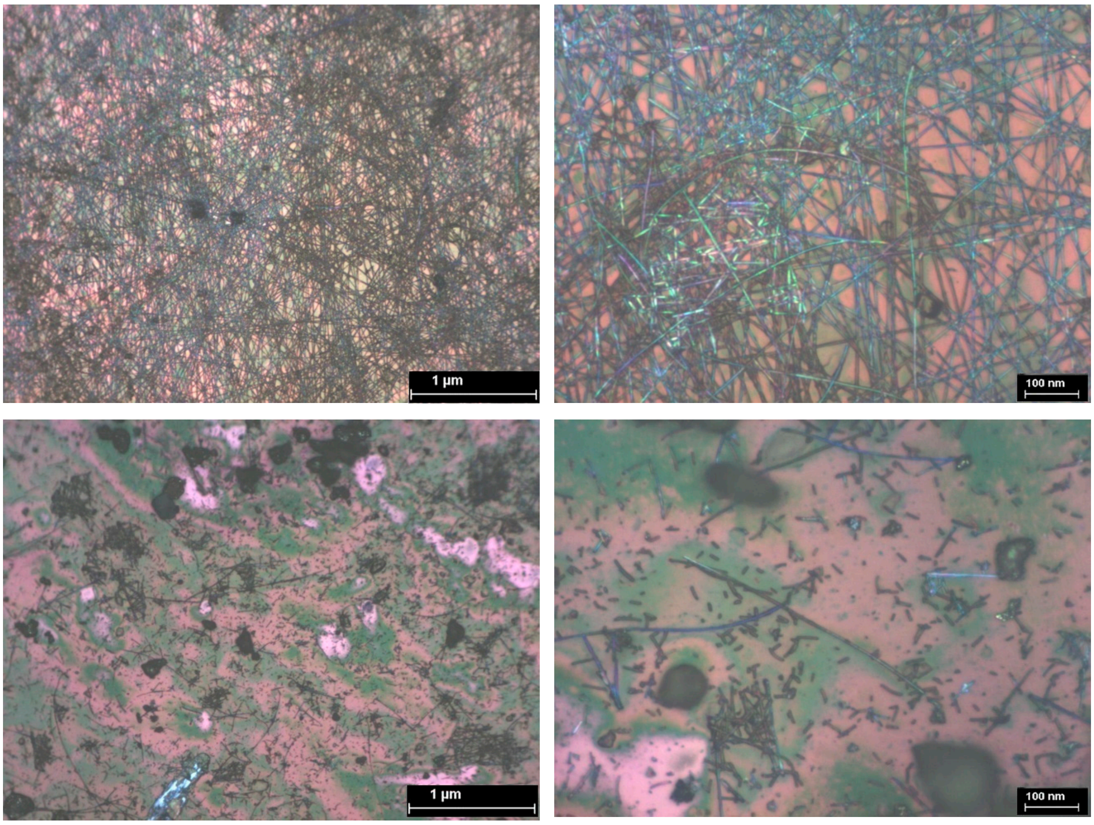

Figure 11. Optical analysis at 100× and 500× of TiO_2/P3HT composites without and with Au.

The results for the roughness parameters determined by AFM lines are comparatively presented in Table 1. In every instance, it was observed that there appears to be a relatively uniform grain distribution; however, the incorporation of gold nanoparticles alters the surface structure and forces the initial grains to create spaces for Au particles to penetrate deeper and accumulate into small clusters, which in turn slightly enhances the grain size and locally sharpens the peaks.

Table 1. Average roughness parameters, determined by AFM lines. Scanned area of 40 × 40 µm.

Scanned Material	RMS (nm)	Ra (nm)	R_{Sk}	R_{Ku}
TiO_2 nanotubes–PANI-EB	947	715	−0.18	4.04
TiO_2 nanotubes–PANI-EB/Au	1197	948	−0.01	2.97
TiO_2 nanotubes–PEDOT: PS	131	105	0.38	3.04
TiO_2 nanotubes–PEDOT: PS/Au	107	79	0.56	4.42
TiO_2 nanotubes–P3HT	362	298	0.17	2.53
TiO_2 nanotubes–P3HT/Au	420	341	0.42	2.89

As regards the profile lines of TiO_2/PANI-EB composites without and with Au, as in Figure 12, the formation of layers is predominantly characterized by peaks and not by depressions; the negative value of Rsk, seen in Table 1, indicates that many low spaces are present on the sample, so we are confronting significant roughness and asymmetry, which are largely mitigated by adding gold nanoparticles, which somewhat organizes the grains into more uniform clusters. This observation is reiterated by the Rku value, which reduces from 4 to about 3, indicating a transition from a random distribution to an almost Gaussian distribution of the grains, confirming that the presence of metal nanoparticles aids in the uniformity of the structure.

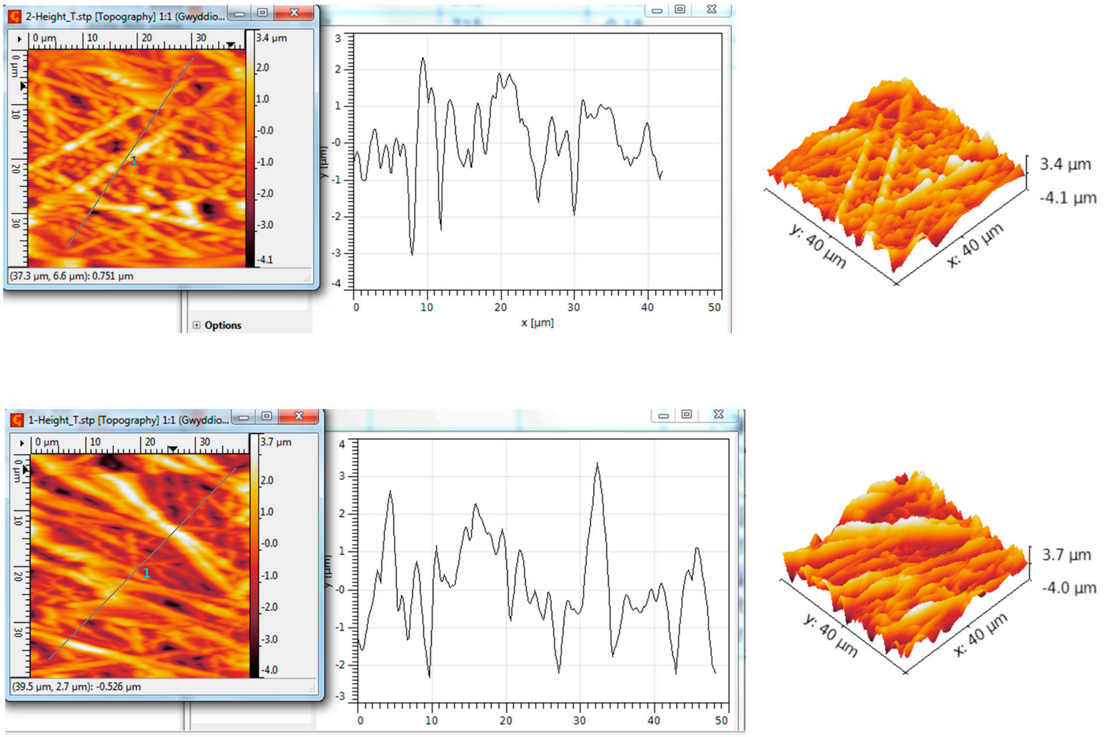

Figure 12. AFM Topographic 2D and 3D images and profile lines, and TiO_2/PANI-EB composites without and with Au.

As regards the profile lines of TiO_2/PEDOT: PS composites without and with Au, Figure 13, the formation of layers is predominantly characterized by large valleys and not by peaks; the presence of gold, predominantly in the form of clusters, explains the increased value of Rsk, suggesting the creation of even broader valleys among the elevated regions. Conversely, the change in symmetry is clear, as the Rku value, originally near three—indicative of a Gaussian distribution—increases beyond four, signifying that the addition of gold nanoparticles as clusters alters the original structure, which was more symmetrical.

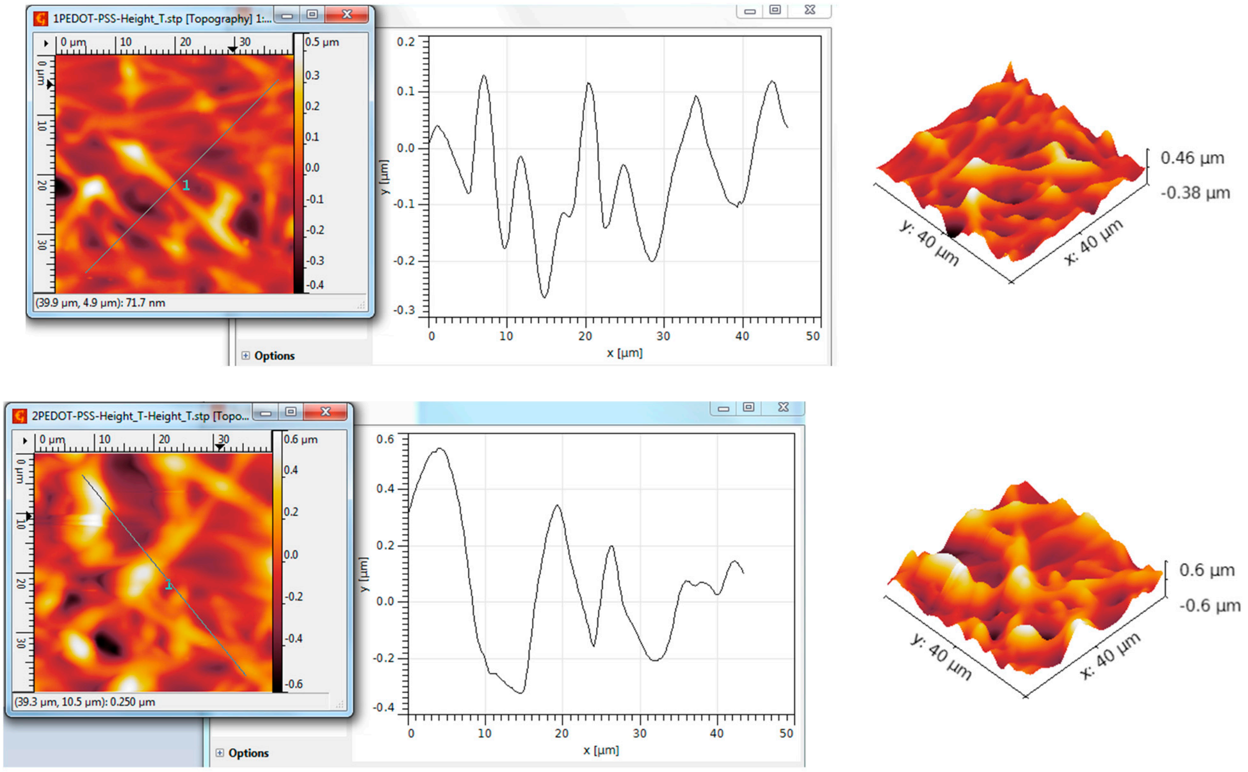

Figure 13. AFM Topographic 2D and 3D images and profile lines, and TiO_2/PEDOT: PS composites without and with Au.

Finally, as regards the profile lines of TiO_2/P3HT composites without and with Au, Figure 14, the grains are generally arranged in smaller clusters in both cases, and the formation of layers is predominantly characterized by peaks and not by depressions. The addition of metal nanoparticles presented a low influence, which confirms the low incorporation observed, e.g., in Figure 11; the Rku values remained near three, indicating that the grain distribution is symmetrical, and slightly more symmetrical in the case of gold incorporation.

Overall, the greatest roughness was obtained from the TiO_2 nanotube structure–PANI-EB with Au, with a much larger grain size dimension of over 3.5 μm, which also exhibits a decent symmetry in the distribution of grains, and greater uniformity in the distribution of polymers within the ceramic nanotubes. At first glance, considering the technical conclusions outlined earlier, this structure, considering the higher incorporation of gold and its distribution on the surface, along with the surface morphology, appears to be the most promising candidate for testing chemisensor properties. Structures exhibiting symmetrical distribution and high roughness dimensions at the μm scale are regarded as optimal for gas sensor applications, because they offer a substantial active area for engagement with the targeted gas. Anatase titanium dioxide experiences a quasi-doping effect when linked with gold nanoparticles, leading to the creation of new energy levels close to the conduction band, enhancing its sensitivity to sulfur-containing gases; a comparable effect is observed following metal doping for the detection of other gases, as presented in [51–53].

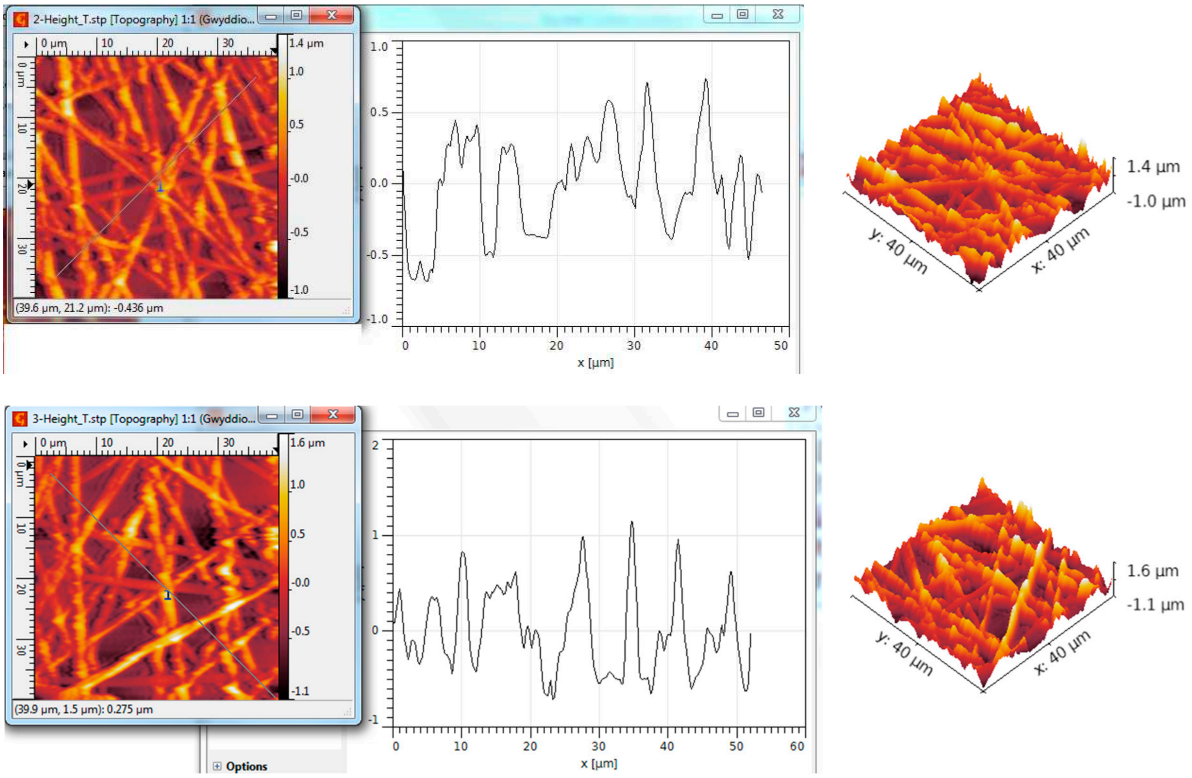

Figure 14. AFM Topographic 2D and 3D images and profile lines, and TiO_2/P3HT composites with Au.

4. Analysis of Functionality as Gas Sensors for H_2s of TiO_2–PANI-EB Composites with the Addition of Gold Nanoparticles

The literature outlines various metallization processes for chemiresistor materials, such as drop-casting, solution electrodeposition, vacuum deposition, and more; however, most of these methods are inappropriate for fundamental sensor applications. In our case, we employed an ink-jet printer to use commercial silver ink for printed electronic applications. A resistor design was developed, showcasing an operational area of roughly 2 cm^2 (a relatively large surface due to the minimal concentration of H_2S that may be exhaled and detected), constrained by two metalized areas forming the conductive connections. The metallization was performed by using commercial ORGACON SI-J20X silver ink (Ag-fa-Gevaert N.V., Mortsel, Belgium) designed for printed electronics, with a multilayer deposition to ensure minimal contact resistance. The design and sensor structure description are presented in Figure 15, with a general design for chemosensors [54].

The performance of the gas sensor was assessed using a testing system similar to the one described in [55]. The sensor was embedded inside a sealed enclosure that allowed gas exchange solely via two valves and access to the electrical connections. An accurate ohmmeter was employed to measure the sensor's resistance from the outside. Various mixtures of H_2S in synthetic air (80% nitrogen and 20% oxygen) were transferred through the closed chamber using one valve and then expelled through a second valve to maintain the pressure at 1 atm. The source of H_2S was a specialized cylinder—H2S SENSIT (Sensit Technologies LLC, Valparaiso, IN, USA)—that supplied a concentration of 25 ppm hydrogen sulfide in the air. The specific amount of H_2S in synthetic air was analyzed one sample at a time using a Gastec detection system equipped with tube no. 4 LT (Gastec Corporation, Kanagawa, Japan), which detects hydrogen sulfide within a range of 0.05 to 1 ppm. The detection limit was 0.01 ppm, which significantly surpasses the sensor's detection limit. The resistance of the sensor—as an average of five measurements—was linked to the concentration of H_2S on the calibration curve, for a range of H_2S concentrations in the air of up to 1 ppm. The reasonable detection limit (LoD) was determined to be 0.1 ppm, as shown in Figure 15, which is a suitable value for the suggested applications for personal external clinic usage. Under this concentration level, the resistance values are making the sensor unreliable for comparison with very low gas concentrations, which are also challenging to accurately measure with the gas detector used.

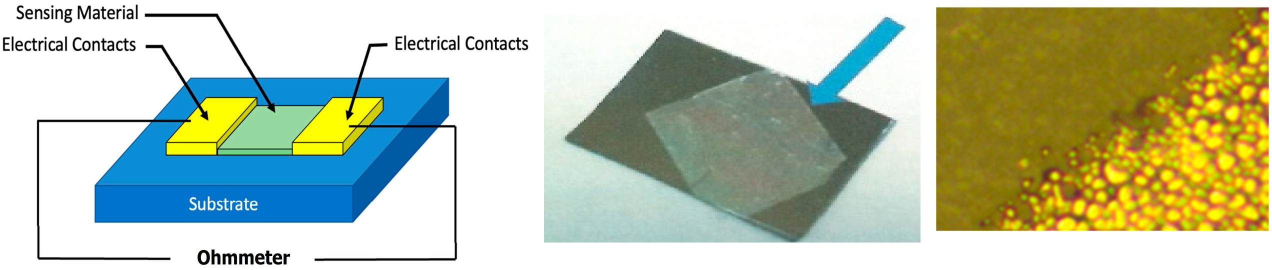

(**a**) (**b**) (**c**)

Figure 15. Sensor description: (**a**) design concept; (**b**) sensing material on SiO_2/Si substrate; (**c**) metalized electrical contact.

The experimental calibration curve for sensing H_2S is presented in Figure 16.

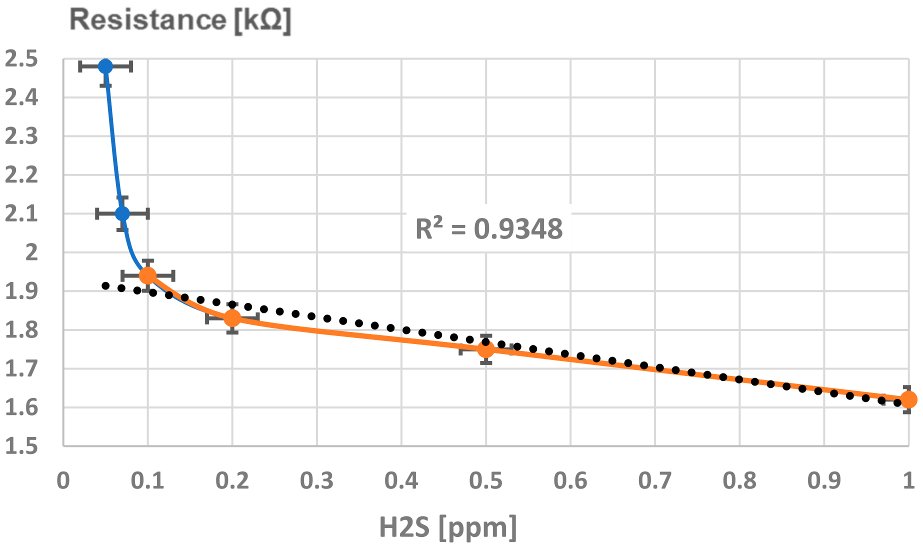

Figure 16. Experimental calibration curve with the limit of detection for sensing H_2S.

A strong correlation can be observed (R = 0.967), indicating high linearity for the domain of 0.1–1 ppm for sensing H_2S, thus making it appropriate for employing a basic signal processing system.

Figure 17 shows the variation in resistance over time for four different H_2S concentrations (0.1, 0.2, 0.5, and 1 ppm). The "On" marker indicates the beginning of measurements until the resistance attains a consistent value. "Off" denotes the condition where solely artificial air is channeled to the sensor until it attains its initial resistance level in the air. Both the decrease in resistance and the process of recovery display a quasi-exponential characteristic.

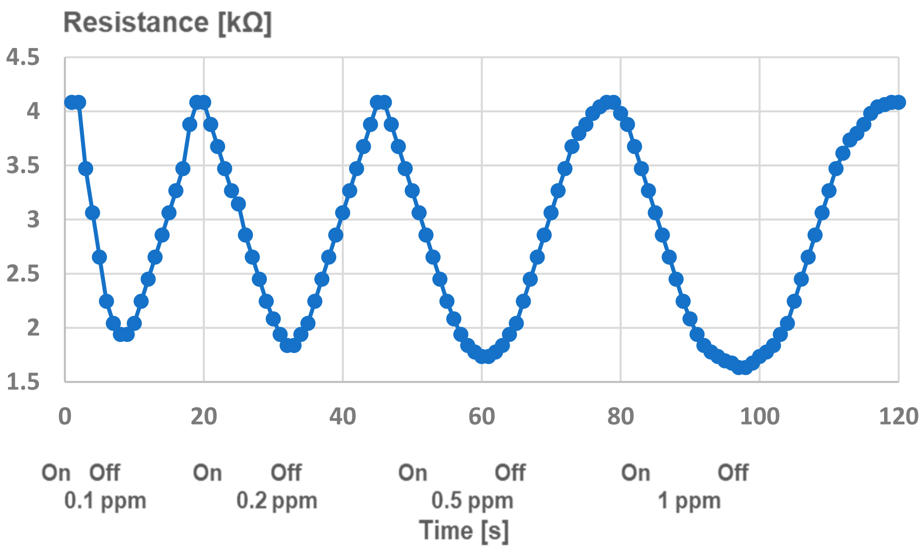

Figure 17. Experimental resistance–time curves.

Figure 18 illustrates the evaluation of the experimental response time and recovery time of the sensing structure.

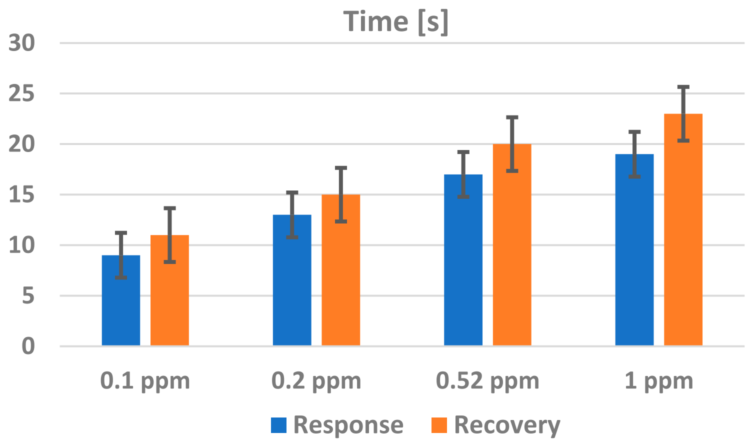

Figure 18. Experimental response and recovery time.

The response time values close to 10 s at 0.1 ppm H_2S concentration are associated with a gradually slow exhalation of air via the mouth. Concerning the recovery time value, it varies based on gas concentrations, and it is advised to go beyond 20 s for a more accurate repetitive measurement. However, it is reasonable to wait a few minutes between successive measurements for medical reasons, even if assessing several individuals with the same device.

The detection hybrid systems associated with ceramic nanotubes and conducting polymers are still of high interest, because these combinations are new, especially with the insertion of metal nanoparticles. The efficient uptake of gas molecules is key in attaining significant sensor responses, primarily attributed—particularly in hybrid assemblies—to the large grain sizes, with a high surface–volume ratios. Conversely, the semiconducting characteristics of ceramic nanotubes combined with conductive polymer assemblies, enhanced by the presence of gold nanoparticles, increases the affinity for specific gas molecules because of improved carrier transport and the synergistic interactions between the components. It is believed that incorporating metal oxide nanostructures into the polymer matrix creates a P-N heterojunction at the interfaces, at which the presence of gold nanoparticles—leading to the creation of new energy levels close to the conduction band—are essential for gas molecule absorption at low quantities. In our specific situation, the affinity of H_2S for TiO_2 anatase is attributed to the enhancement of electronic conductivity of TiO_2 when H_2S is present, indicating a significant interaction between TiO_2 and the adsorbate, a point also emphasized in [56,57], despite these studies not focusing on sensor applications. According to the activation energy barriers, the findings suggest that anatase TiO_2 displays high reactivity towards H_2S, leading to S-substitution at the O_2c sites on the TiO_2 surface, which reduces its band gap. Moreover, when compared to other metal oxides, TiO_2 appears to provide the strongest affinity for H_2S as well [58]. The formation of vacancies combined with S on the TiO_2 surface improves the H_2S adsorption energy, a factor that is amplified in our case by the increase of TiO_2's active surface in the form of nanotubes. In [58], it was demonstrated that surpassing 200 °C can cause adsorption to result in dissociation phenomena, highlighting the strong attraction of H_2S to TiO_2. This situation is not connected to our application, but any advancements that boost the H_2S affinity for TiO_2 at room temperature are essential. Thus, the embedding of Au nanoparticles might additionally lower the band gap of the hybrid structure. Additional studies highlighted the potential benefits of, e.g., Ag decoration on TiO_2 [59], or gold-nanoparticle-decorated SnO_2 [60] for H_2S gas detection, reinforcing the significance of metal inclusions, particularly, as conducted in our research, at the nanoscale, within more complex structures.

Concerning the characteristics of the sensor introduced here for hydrogen sulfide, its capabilities are evidently better than those of similar sensors that rely only on basic various nanostructured types of TiO_2, such as [61–63]. In those instances, the detection limit is significantly higher, and the sensitivity relies on operating at increased temperatures of over 100 °C, making them unsuitable for medical purposes. A comparable analysis could be made also regarding sensors that utilize metallic nanoparticles, as seen in [64,65], but while their detection limits align with our sensors, their detection mechanism is optical, making it inappropriate for medical applications.

Recent studies introduce alternative sensor types, such as those utilizing gold nanoclusters, MXene, or metal–organic frameworks, which could potentially measure hydrogen sulfide with greater accuracy [66]. Nonetheless, while the declared optimal detection limit is claimed to be 10–30 ppb, this must be weighed against the intricate technology employed, which is quite challenging to implement on an industrial scale for medical applications.

Concerning sensors utilizing embedded gold nanoclusters within metal–organic frameworks, the latest developments for gas sensors, as outlined in [67–69], show that their detection limit for H_2S of over 10 ppm is significantly greater than that of our sensors. On the other hand, their primary use pertains to identifying allowable occupational exposure limits for H_2S in industrial settings, rather than for the diagnosis of oral diseases.

As a result of these initial successful outcomes, the characteristics of the sensor (primarily in terms of sensitivity, selectivity, response time, and reproducibility) will undergo additional examination in the context of influencing factors, also linked to the breathing process. The possible influence effects of exhaled CO_2, exhaled moisture, and possibly exhaled CH_4 will be evaluated. This research could offer further significance in linking malodor with associated digestive syndromes, a topic of great interest in the medical field.

5. Conclusions

The process of producing active surfaces for chemiresistors, based on hybrid nanostructures obtained from TiO_2 ceramic nanotubes and conducting polymers (poly(3-hexylthiophene), polyaniline emeraldine-base, and poly(3,4-ethylenedioxythiophene)-polystyrene sulfonate) with the addition of gold nanoparticles, was technologically described.

The method used to fabricate hybrid nanostructures from TiO_2 nanotubes and conducting polymers was drop-casting. Additionally, the resulting structures were immersed in a $HAuCl_4$/2–propanol solution using an innovative dip-coating technique, and subsequently subjected to a regulated heating process from ambient temperature to slightly over one hundred degrees Celsius. The method provides a nearly uniformly dispersing of gold nanoparticles with an average dimension of 100 nm over more extensive surfaces of structures.

AFM analysis highlighted that the highest roughness was observed in the TiO_2–PANI-EB structure with Au, featuring a significantly larger grain size of over 3.5 µm and a fair symmetry in grain distribution relative to the surface. The Rku parameter values were around three, indicating that the respective grain layers mainly displayed peaks instead of depressions, exhibiting a Gaussian distribution. This configuration seems to be the most likely candidate for evaluating chemisensor characteristics, given the increased inclusion of gold and its arrangement on the surface, as well as the surface morphology.

A chemiresistor was produced using an ink-jet printer, the applied metallization being made with commercial silver ink for printed electronics. A resistor was designed with an active area of about 2 cm^2. A calibration curve was experimentally generated for the sensing structure, spanning a broader range of H_2S concentration in air, reaching up to 1 ppm, and providing a reasonable linearity. It was established that the detection limit is 0.1 ppm, a level suitable for the identification of oral diseases. The sensor can be described as a straightforward, low-cost, and robust device meant for personal use, proving to be highly advantageous at the patient level as it allows for more effective monitoring of the syndrome's progression or treatment effectiveness.

Author Contributions: Conceptualization, A.F.T., R.C.C., T.G.S. and O.D.S.; methodology, A.F.T., R.C.C. and O.D.S.; validation, R.C.C. and A.F.T.; formal analysis, A.F.T., T.G.S. and R.C.C.; investigation, R.C.C., O.D.S., T.G.S. and A.F.T.; data curation, R.C.C., O.D.S., T.G.S. and A.F.T.; writing—original draft preparation, A.F.T. and R.C.C.; writing—review and editing, R.C.C.; visualization, R.C.C., O.D.S., T.G.S. and A.F.T.; supervision, A.F.T. and R.C.C. All authors have read and agreed to the published version of the manuscript.

Funding: This research received no external funding.

Institutional Review Board Statement: Not applicable.

Informed Consent Statement: Not applicable.

Data Availability Statement: Data are contained within the article.

Conflicts of Interest: The authors declare no conflicts of interest.

References

1. Tanda, N.; Hoshikawa, Y.; Ishida, N.; Sato, T.; Takahashi, N.; Hosokawa, R.; Koseki, T. Oral malodorous gases and oral microbiota: From halitosis to carcinogenesis. *J. Oral. Biosci.* **2015**, *57*, 175–178. [CrossRef]
2. Wu, D.; Ngowi, E.; Zhai, Y.; Wang, Y.; Khan, N.; Kombo, A.; Khattak, S.; Li, T.; Ji, R. Role of Hydrogen Sulfide in Oral Disease. *Oxid. Med. Cell Longev.* **2022**, *25*, 1886277. [CrossRef]
3. Yoneda, M.; Suzuki, N.; Hirofuji, T. Current Status of the Techniques Used for Halitosis Analysis. *Austin Chromatogr.* **2015**, *2*, 1024.
4. Lee, Y.; Shin, S.; Hong, J. Investigation of volatile sulfur compound level and halitosis in patients with gingivitis and periodontitis. *Sci. Rep.* **2023**, *13*, 13175. [CrossRef] [PubMed]
5. Available online: https://www.breathinstitute.co.uk/medical-library-bad-breath/methods-of-diagnosis-and-causes-of-bad-breath/breath-gas-measurement-methods/ (accessed on 18 December 2024).
6. Nakhleh, M.K.; Quatredeniers, M.; Haick, H. Detection of Halitosis in Breath: Between the Past, Present and Future. *Oral Dis.* **2017**, *24*, 685–695. [CrossRef]
7. Available online: https://www.glsciencesinc.com/oralchroma?srsltid=AfmBOooEzSxQkIdBPg5LPXkIQN8xrjUGIM8hVsLnPX13nm0qTWZXdUXJ (accessed on 18 December 2024).
8. Available online: https://www.halimeter.com/ (accessed on 18 December 2024).

9. Salako, N.; Philip, L. Comparison of the use of the Halimeter and the Oral Chroma™ in the assessment of the ability of common cultivable oral anaerobic bacteria to produce malodorous volatile sulfur compounds from cysteine and methionine. *Med. Princ. Pract.* **2011**, *20*, 75. [CrossRef]
10. Hanada, M.; Koda, H.; Onaga, K.; Tanaka, K.; Okabayashi, T.; Itoh, T.; Miyazaki, H. Portable oral malodor analyzer using highly sensitive In_2O_3 gas sensor combined with a simple gas chromatography system. *Analytica Chimica Acta* **2003**, *475*, 27–35. [CrossRef]
11. Ikava, K.; Iwakura, M.; Washio, J.; Kusano, A.; Tanda, N.; Koseki, T. Circadian changes of volatile sulfur compounds measured by Breathtron™. *Int. Congr. Ser.* **2005**, *1284*, 89–90. [CrossRef]
12. Zhang, T.; Xue, Y.; Chen, Y.; Wan, H.; Wang, P. Research on Intelligent Electronic Nose Based on Exhaled Breath to Detect Halitosis. *ECS Meet. Abstr.* **2021**, *MA 2021-01*, 1348. [CrossRef]
13. Umapathy, V.; Natarajan, P.; Swamikannu, B.; Moses, J.; Jones, S.; Chandran, M.; Anbumozhi, M. Emerging Biosensors for Oral Cancer Detection and Diagnosis—A Review Unravelling Their Role in Past and Present Advancements in the Field of Early Diagnosis. *Biosensors* **2022**, *12*, 498. [CrossRef]
14. Li, Y.; Tang, H.; Liu, Y.; Qiao, Y.; Xia, H.; Zhou, J. Oral wearable sensors: Health management based on the oral cavity. *Biosens. Bioelectron.* **2022**, *10*, 100135. [CrossRef]
15. *EP0819940A2*; Method of Detecting Halitosis and Detector for Use in the Method. European Patent Office: Munich, Germany, 1997.
16. Dey, A. Semiconductor metal oxide gas sensors: A review. *Mater. Sci. Eng. B Solid-State Mater. Adv. Technol.* **2018**, *229*, 206–217. [CrossRef]
17. Wang, T.; Sun, P.; Liu, F.; Lu, G. Revealing the correlation between gas selectivity and semiconductor energy band structure derived from off-stoichiometric spinel $CdGa_2O_4$. *Sens. Actuators B* **2022**, *352*, 131039. [CrossRef]
18. He, H.; Zhao, C.; Xu, J.; Qu, K.; Jiang, Z.; Gao, Z.; Song, Y. Exploiting Free-Standing p-CuO/n-TiO_2 Nanochannels as a Flexible Gas Sensor with High Sensitivity for H_2S at Room Temperature. *ACS Sens.* **2021**, *6*, 3387–3397. [CrossRef] [PubMed]
19. Li, Z.; Wang, N.; Lin, Z.; Wang, J.; Liu, W.; Sun, K.; Fu, Y.; Wang, Z. Room-Temperature High-Performance H_2S Sensor Based on Porous CuO Nanosheets Prepared by Hydrothermal Method. *ACS Appl. Mater. Interfaces* **2016**, *8*, 20962–20968. [CrossRef]
20. Han, G.; Liu, C.; Guan, C.; Li, I.; Wang, Y.; Li, Z. Advances in electrochemical biosensors for the detection of common oral diseases. *Authorea.* **2023**. [CrossRef]
21. Se, A.; Albarella, J.; Carey, J.; Kim, P.; McNamara, W. Low-cost colorimetric sensor for the quantitative detection of gaseous hydrogen sulfide. *Sens. Actuators B Chem.* **2008**, *134*, 234–237. [CrossRef]
22. Lu, Y.; Wang, D.; Lv, W.; Xia, Y.; Ou, K.; Li, Y.; Du, Z.; He, Y.; Dai, J.; Wu, S.; et al. Surface acoustic wave hydrogen sulfide gas sensors based on porous SnO_2-SiO_2 composite films. *Sens. Actuators B Chem.* **2024**, *417*, 136117. [CrossRef]
23. Zhao, L.; Che, J.; Cao, Q.; Shen, S.; Tang, Y. Highly Sensitive Surface Acoustic Wave H_2S Gas Sensor Using Electron-beam-evaporated CuO as Sensitive Layer. *Sens. Mater.* **2023**, *35*, 2293–2304. Available online: https://sensors.myu-group.co.jp/sm_pdf/SM3323.pdf (accessed on 18 December 2024). [CrossRef]
24. Ohatkar, S.; Rane, S.; Ambesange, A.; More, A.; Rane, S. Nanostructured Metal Oxide Based Thick Film Sensors. *Int. J. Latest Technol. Eng. Manag. Appl. Sci.* **2016**, *5*, 93–97. Available online: https://www.ijltemas.in/DigitalLibrary/Vol.5Issue5/93-97.pdf (accessed on 18 December 2024).
25. Ayyala, S.; Covington, J. Nickel-Oxide Based Thick-Film Gas Sensors for Volatile Organic Compound Detection. *Chemosensors* **2021**, *9*, 247. [CrossRef]
26. Shin, H.; Kim, D.; Jung, W.; Jang, J.; Kim, Y.; Lee, Y.; Chang, K.; Lee, J.; Park, J.; Namkoong, K.; et al. Surface Activity-Tuned Metal Oxide Chemiresistor: Toward Direct and Quantitative Halitosis Diagnosis. *ACS Nano* **2021**, *15*, 9. [CrossRef]
27. Wang, C.; Jiang, L.; Wang, J.; Liu, F.; You, R.; Lv, S.; Yang, Z.; He, J.; Liu, A.; Yan, X.; et al. Mixed potential type H_2S sensor based on stabilized zirconia and a Co_2SnO_4 sensing electrode for halitosis monitoring. *Sens. Actuators B Chem.* **2020**, *321*, 128587. [CrossRef]
28. Ma, S.; Jia, J.; Tian, Y.; Cao, L.; Shi, S.; Li, X.; Wang, Z. Improved H_2S sensing properties of Ag/TiO_2 nanofibers. *Ceram. Int.* **2016**, *42*, 2041.
29. Shirsat, M.; Bangar, M.; Deshusses, M.; Myung, N.; Mulchandani, A. Polyaniline nanowires-gold nanoparticles hybrid network based chemiresistive hydrogen sulfide sensor. *Appl. Phys. Lett.* **2009**, *94*, 083502. [CrossRef]
30. Feng, D.; Du, L.; Xing, X.; Wang, C.; Chen, J.; Zhu, Z.; Tian, Y.; Yang, D. Highly Sensitive and Selective NiO/WO_3 Composite Nanoparticles in Detecting H_2S Biomarker of Halitosis. *ACS Sens.* **2021**, *6*, 733–741. [CrossRef]
31. Panes-Ruiz, L.; Riemenschneider, L.; Chawa, M.; Loffler, M.; Rellinghaus, B.; Tetzlaff, R.; Bezugly, V.; Ibarlucea, B.; Cuniberti, G. Selective and self-validating breath-level detection of hydrogen sulfide in humid air by gold nanoparticle-functionalized nanotube arrays. *Nano Res.* **2022**, *15*, 2512–2521. [CrossRef]
32. Kato, T.; Tanaka, T.; Uchida, K. Detection of PPB-Level H_2S Concentrations in Exhaled Breath Using Au Nanosheet Sensors with Small Variability, High Selectivity, and Long-Term Stability. *ACS Sens.* **2024**, *9*, 708–716. [CrossRef]

33. Ramgir, N.; Sharma, P.; Datta, N.; Kaur, M.; Debnath, A.; Aswal, D.; Gupta, S. Room temperature H_2S sensor based on Au modified ZnO nanowires. *Sens. Actuators B Chem.* **2013**, *186*, 718–726. [CrossRef]
34. Kaiser, A.; Ceja, E.; Huber, F.; Herr, U.; Thonke, K. Highly Sensitive H_2S Sensing with Gold and Platinum Surface-Modified ZnO Nanowire ChemFETs. *Proceedings* **2020**, *60*, 7. [CrossRef]
35. Vuong, N.; Kim, D.; Kim, H. Porous Au-embedded WO3 Nanowire Structure for Efficient Detection of CH_4 and H_2S. *Sci. Rep.* **2015**, *5*, 11040. Available online: https://www.nature.com/articles/srep11040 (accessed on 18 December 2024).
36. Punginsang, M.; Liewhiran, C.; Wisitsoraat, A.; Zappa, D.; Comini, E.; Sberveglieri, G. Selective H_2S Gas Sensors Based on Au-functionalized WO_3 Nanowires. In Proceedings of the 17th International Meeting on Chemical Sensors—IMCS 2018, Vienna, Austria, 15–19 July 2018; pp. 853–854. [CrossRef]
37. Hitchman, M.; Saffell, J. Considerations of Thermodynamics and Kinetics for the Effects of Relative Humidity on the Electrolyte in Electrochemical Toxic Gas Sensors. *ACS Sens.* **2021**, *6*, 3985–3993. [CrossRef]
38. Xu, Q.; Zong, B.; Li, Q.; Fang, X.; Mao, S.; Ostrikov, K. H_2S sensing under various humidity conditions with Ag nanoparticle functionalized $Ti_3C_2T_x$ MXene field-effect transistors. *J. Hazard. Mater.* **2022**, *424*, 127492. [CrossRef] [PubMed]
39. Deng, Z.; Wu, Z.; Liu, X.; Chen, Z.; Sun, Y.; Dai, N.; Ge, M. Humidity-tolerant and highly sensitive gas sensor for hydrogen sulfide based on WO_3 nanocubes modified with CeO_2. *RSC Adv.* **2024**, *14*, 15039–15047. [CrossRef]
40. Enculescu, M.; Costas, A.; Evanghelidis, A.; Enculescu, I. Fabrication of ZnO and TiO_2 Nanotubes via Flexible Electrospun Nanofibers for Photocatalytic Applications. *Nanomaterials* **2021**, *11*, 1305. [CrossRef] [PubMed]
41. Trandabat, A.F.; Ciobanu, R.C.; Schreiner, O.D.; Aradoaei, M.; Aradoaei, S. Manufacturing of TiO_2, Al_2O_3 and Y_2O_3 Ceramic Nanotubes for Application as Electrodes for Printable Electrochemical Sensors. *Crystals* **2024**, *14*, 454. [CrossRef]
42. Trandabat, A.F.; Ciobanu, R.C.; Schreiner, O.D.; Schreiner, T.G.; Aradoaei, S. Ceramic Nanotubes—Conducting Polymer Assemblies with Potential Application as Chemosensors for Breath Hydrogen sulfide Detection in Chronic Kidney Disease. *Chemosensors* **2024**, *12*, 198. [CrossRef]
43. Umeda, H.; Mezaki, Y.; Oshio, A.; Kaneko, Y.; Okamoto, R.; Kusumoto, S.; Kunimura, S. Gold Nanoparticles Produced by Low-temperature Heating of the Dry Residue of a Droplet of an HCl Acidic Solution of $HAuCl_4{\cdot}4H_2O$ in a Low Vacuum. *Anal. Sci.* **2021**, *37*, 1427–1432. [CrossRef]
44. Ii, K.; Kurita, Y.; Kida, N.; Kunimura, S. Preparation of gold nanoparticles using low-temperature heating of the dry residue of a droplet of an $HAuCl_4$ solution in air. *Anal. Sci.* **2024**, *40*, 213–217. [CrossRef]
45. Surface Roughness Parameters. Available online: https://www.keyence.eu/ss/products/microscope/roughness/line/tab03_b.jsp (accessed on 18 December 2024).
46. *ISO 21920-2:2021*; Geometrical Product specifications (GPS)—Surface Texture: Profile. ISO: Geneva, Switzerland. Available online: https://www.iso.org/standard/72226.html (accessed on 18 December 2024).
47. Taudul, B.; Tielens, F.; Calatayud, M. On the Origin of Raman Activity in Anatase TiO_2 (Nano)Materials: An Ab Initio Investigation of Surface and Size Effects. *Nanomaterials* **2023**, *13*, 1856. [CrossRef]
48. Quillard, S.; Louarn, G.; Lefrant, S.; Macdiarmid, A.G. Vibrational analysis of polyaniline: A comparative study of leucoemeraldine, emeraldine, and pernigraniline bases. *Phys. Rev. B* **1994**, *50*, 12496.
49. Garreau, S.; Louarn, G.; Buisson, J.P.; Froyer, G.; Lefrant, S. In Situ Spectroelectrochemical Raman Studies of Poly(3,4-ethylenedioxythiophene) (PEDT). *Macromolecules* **1999**, *32*, 6807–6812.
50. Trznadel, M.; Zagórska, M.; Lapkowski, M.; Louarn, G.; Lefrant, S.; Pron, A. UV–VIS–NIR and Raman spectroelectrochemistry of regioregular poly(3-octylthiophene): Comparison with its non-regioregular analogue. *J. Chem. Soc. Faraday Trans.* **1998**, *24*, 3527–3780.
51. Santos, E.; Catto, E.; Peterline, A.; Avansi, W. Transition metal (Nb and W) doped TiO_2 nanostructures: The role of metal doping in their photocatalytic activity and ozone gas-sensing performance. *Appl. Surf. Sci.* **2022**, *579*, 152146. [CrossRef]
52. Orizu, G.; Ugwuoke, P.; Asogwa, P.; Offiah, S. A review on the inference of doping TiO_2 with metals/nonmetals to improve its photocatalytic activities. *IOP Conf. Ser. Earth Environ. Sci.* **2023**, *1178*, 012008. [CrossRef]
53. Gartner, M.; Szekeres, A.; Stroescu, H.; Mitrea, D.; Covei, M. Advanced Nanostructured Coatings Based on Doped TiO_2 for Various Applications. *Molecules* **2023**, *28*, 7828. [CrossRef] [PubMed]
54. McGarrity, M.; Zhao, F. Graphene-Based Chemiresistor Sensors for Drinking Water Quality Monitoring. *Sensors* **2023**, *23*, 9828. [CrossRef]
55. Lin, Y.; Manalili, D.; Khodabakhsh, A.; Cristescu, S.M. Real-Time Measurement of CH_4 in Human Breath Using a Compact CH_4/CO_2 Sensor. *Sensors* **2024**, *24*, 1077. [CrossRef]
56. Yanxin, C.; Yi, J.; Wenzhao, L.; Rongchao, J.; Shaozhen, T.; Wenbin, H. Adsorption and interaction of H_2S/SO_2 on TiO_2. *Catal. Today* **1999**, *50*, 39–47. [CrossRef]
57. Junkaew, A.; Maitarad, P.; Arróyave, R.; Kungwan, N.; Zhang, D.; Shib, L.; Namuangruk, S. The complete reaction mechanism of H_2S desulfurization on an anatase TiO_2 (001) surface: A density functional theory investigation. *Catal. Sci. Technol.* **2017**, *7*, 356–365. [CrossRef]

58. Shahzad, N.; Hussain, A.; Mustafa, N.; Ali, N.; Kanounf, M.; Goumri-Said, S. First principles study of the adsorption and dissociation mechanisms of H_2S on a TiO_2 anatase (001) surface. *RSC Adv.* **2016**, *6*, 7941–7949. [CrossRef]
59. Hwang, J.; Kim, M.; Jin, C.; Mirzaei, A.; Choi, S.; Choi, M.; Lee, H. Surface Reaction Mechanism and Characteristics of 2-Dimensional TiO_2 and 0-Dimensional Ag Nanocomposites Specialized for H_2S Gas Sensing at Room Temperature. *Sens. Actuators Rep.* **2025**, *9*, 100290. [CrossRef]
60. Rodiawan; Wang, S.; Suhdi. Gold-nanoparticle-decorated Tin Oxide of a Gas Sensor Material for Detecting Low Concentrations of Hydrogen Sulfide. *Sens. Mater.* **2023**, *35*, 1121–1130. [CrossRef]
61. Nagmani; Pravarthana, D.; Tyagi, A.; Jagadale, T.C.; Prellier, W.; Aswal, D.K. Highly sensitive and selective H_2S gas sensor based on TiO_2 thin films. *Appl. Surf. Sci.* **2021**, *549*, 149281. [CrossRef]
62. Alaya, I.; Madani, M.; Bouguila, N.; El Mir, L.; Fazio, E.; Corsaro, C.; Neri, G. Conductometric H_2S Sensors Based on TiO_2 Nanoparticles. *Materials* **2024**, *17*, 3283. [CrossRef] [PubMed]
63. Tong, X.; Shen, W.; Chen, X.; Corriou, J. A fast response and recovery H_2S gas sensor based on free-standing TiO_2 nanotube array films prepared by one-step anodization method. *Ceram. Int.* **2017**, *43*, 14200–14209. [CrossRef]
64. Marquardt, N.; Dahlke, M.; Schaate, A. Cu-MOF-808 as a Sensing Material for Gaseous Hydrogen Sulfide. *ChemPlusChem* **2023**, *88*, e202300109. [CrossRef]
65. Yu, Q.; Gao, P.; Zhang, K.; Tong, X.; Yang, H.; Liu, S.; Du, J.; Zhao, Q.; Huang, W. Luminescent gold nanocluster-based sensing platform for accurate H_2S detection in vitro and in vivo with improved anti-interference. *Light Sci. Appl.* **2017**, *6*, e17107. [CrossRef]
66. Yang, M.; Zhou, Y.; Wang, K.; Luo, C.; Xie, M.; Shi, X.; Lin, X. Review of Chemical Sensors for Hydrogen Sulfide Detection in Organisms and Living Cells. *Sensors* **2023**, *23*, 3316. [CrossRef]
67. Nie, X.; Han, X.; Yu, S.; Liu, W.; Yang, Y. Embedding gold nanoclusters in metal-organic frameworks as a dual-channel hydrogel optical sensor for hydrogen sulfide detection. *J. Solid State Chem.* **2025**, *346*, 125283. [CrossRef]
68. Wang, Z.J.; Li, Q.; Tan, L.L.; Liu, C.; Shang, L. Metal–Organic Frameworks-Mediated Assembly of Gold Nanoclusters for Sensing Applications. *J. Anal. Test.* **2022**, *6*, 163–177. [CrossRef] [PubMed]
69. Ali, A.; Alzamly, A.; Greish, Y.; Bakiro, M.; Nguyen, H.; Mahmoud, S. A Highly Sensitive and Flexible Metal–Organic Framework Polymer-Based H_2S Gas Sensor. *ACS Omega* **2021**, *6*, 17690–17697. [CrossRef] [PubMed]

chemosensors

IMPACT FACTOR 3.7

CITESCORE 7.3

Article

Study on Hybrid Assemblies of Graphene and Conducting Polymers with Embedded Gold Nanoparticles for Potential Electrode Purposes

Alexandru F. Trandabat, Oliver Daniel Schreiner, Thomas Gabriel Schreiner, Olga Plopa and Romeo Cristian Ciobanu

MDPI

https://doi.org/10.3390/chemosensors13040130

chemosensors

Article

Study on Hybrid Assemblies of Graphene and Conducting Polymers with Embedded Gold Nanoparticles for Potential Electrode Purposes

Alexandru F. Trandabat [1], Oliver Daniel Schreiner [1,2], Thomas Gabriel Schreiner [2], Olga Plopa [1] and Romeo Cristian Ciobanu [1,*]

[1] Department of Electrical Measurements and Materials, Gheorghe Asachi Technical University, 700050 Iasi, Romania; ftranda@tuiasi.ro (A.F.T.); oliver090598@yahoo.com (O.D.S.); lesea_ro@yahoo.com (O.P.)

[2] Department of Medical Specialties III, Faculty of Medicine, University of Medicine and Pharmacy "Grigore T. Popa", 700115 Iasi, Romania; schreiner.thomasgabriel@yahoo.com

* Correspondence: r.c.ciobanu@tuiasi.ro

Abstract: This article outlines the method of creating electrodes for electrochemical sensors using hybrid nanostructures composed of graphene and conducting polymers with insertion of gold nanoparticles. The technology employed for graphene dispersion and support stabilization was based on the chemical vapor deposition technique followed by electrochemical delamination. The method used to obtain hybrid nanostructures from graphene and conductive polymers was drop-casting, utilizing solutions of P3HT, PANI-EB, and F8T2. Additionally, the insertion of gold nanoparticles utilized an innovative dip-coating technique, with the graphene-conducting polymer frameworks submerged in a $HAuCl_4$/2-propanol solution and subsequently subjected to controlled heating. The integration of gold nanoparticles differs notably, with P3HT showing the least adhesion of gold nanoparticles, while PANI-EB exhibits the highest. An inkjet printer was employed to create electrodes with metallization accomplished through the use of commercial silver ink. Notable variations in roughness (grain size) result in unique behaviors of these structures, and therefore, any potential differences in the sensitivity of the generated sensing structures can be more thoroughly understood through this spatial arrangement. The electrochemical experiments utilized a diluted sulfuric acid solution at three different scan rates. The oxidation and reduction potentials of the structures seem fairly alike. Nevertheless, a notable difference is seen in the anodic and cathodic current densities, which appear to be largely influenced by the active surface of gold nanoparticles linked to the polymeric grains. The graphene–PANI-EB structure with Au nanoparticles showed the highest responsiveness and will be further evaluated for biomedical applications.

Keywords: graphene; conducting polymers; gold nanoparticles; electrochemical sensors

check for updates

Received: 20 January 2025
Revised: 21 March 2025
Accepted: 2 April 2025
Published: 4 April 2025

Citation: Trandabat, A.F.; Schreiner, O.D.; Schreiner, T.G.; Plopa, O.; Ciobanu, R.C. Study on Hybrid Assemblies of Graphene and Conducting Polymers with Embedded Gold Nanoparticles for Potential Electrode Purposes. *Chemosensors* **2025**, *13*, 130. https://doi.org/10.3390/chemosensors13040130

1. Introduction

The electrochemical sensor is a common type of sensing device that converts biochemical events into electrical signals. In this kind of sensor, the working electrode is an essential element used as a solid base for the immobilization of biomolecules and the transfer of electrons. Owing to various nanomaterials with significant surface area, synergistic effects are facilitated by enhancing loading capacity and the mass transport of reactants, leading to improved performance in analytical sensitivity. The carbon allotropes can serve as electrodes and supporting scaffolds because of their extensive active surface area and efficient electron transfer rate. Conducting polymers represent other significant category of functional materials that have been extensively utilized in the production of electrochemical sensors, due to their adjustable chemical, electrical, and structural characteristics. Conducting polymers can also be engineered with other functional materials like nanoparticles to significantly enhance the sensitivity and selectivity of the sensor's reaction to various analytes. In recent years, hybrid materials made of graphene and different polymers have been thoroughly studied, considered to lead to considerable progress in electrochemical sensing. The creation of such hybrid nanostructures is associated with their unique electrical properties.

A method for producing graphene/polyaniline, graphene/poly(3,4-ethylene dioxythiophene), and graphene/polypyrrole (PPy) nanocomposites is highlighted in [1]. A detailed overview of various hybrid structures comprising metallic oxides, graphene, and conductive polymers like poly-indole, polypyrrole, and poly-aniline is provided in [2]. A review of analogous structures of graphene oxide/conducting polymer composites, now presented as hydrogels, is provided in [3]. Similar technologies are noted in additional sources [4–9]. The main use of hybrid structures made from graphene and conducting polymers is related to sensors. In the last 15 years, numerous sensors have been developed, starting from simple types like those for humidity [10,11], temperature [12], and gas detection [13–17], which also include waste gas evaluation [18] and various chemical sensors [19,20]; advancing to sensors with multiple applications for detecting dopamine, serotonin, cholesterol, bilirubin, uric acid, and others [21–26]; as well as specialized sensors for environmental monitoring that identify pollutants in water, such as heavy metals [27,28]; and finishing with examinations of food and pharmaceutical products [29,30].

A new research direction in the field of sensors involves integrating metallic nanostructures into the architecture of conducting polymers to improve the sensitivity and/or selectivity of sensors, as detailed in [31–35], with applications tested for impedimetric, electrochemical, or chemosensors. However, no research has so far attempted to improve the characteristics of sensors by incorporating gold nanoparticles into more complex structures, even if the advantage of simple use of gold nanoparticles for sensor application was noticed by some authors in recent studies [36,37]. Therefore it is worthwhile to further investigate the development of electrodes featuring more intricate structures that incorporate gold nanoparticles. Various techniques for integrating gold nanoparticles into polymer frameworks are extensively discussed in the literature, such as: drop-casting, dip-coating or in-situ synthesis and integration, [38–40], but the paper introduced an innovative approach in this domain based on dip-coating method.

The significance of this study lies in creating functional electrodes for electrochemical sensing systems by embedding gold nanoparticles within hybrid assemblies of graphene and conducting polymers, a complexity of materials for electrodes not previously detailed in the literature. An effective technique for incorporating gold nanoparticles into the surface of conducting polymers was presented, involving the immersion of the polymer film in a highly diluted $HAuCl_4$ solution, followed by controlled heating, resulting in a substantial impact on a broader surface, potentially serving as a working electrode. Three hybrid structures were analyzed, ultimately determining which one was the optimal selection based on responsive features evaluated through cyclic voltammetry.

2. Materials, Preparation and Characterizing Methods

2.1. Materials and Preparation Methods for Graphene Substate

The technology used for graphene synthesis, dispersion and support stabilization was widely describe in [41], and was based on the chemical vapor deposition method followed by an electrochemical delamination. The optimal process, by examining the outcomes achieved at 900 °C and correspondingly 950 °C as detailed in [41], was achieved at 950 °C, leading to enhanced grain structure and the formation of layers mainly characterized by peaks rather than hollows. The samples were ultimately moved onto a SiO_2/Si substrate, because a nonmetallic support allows a more efficient treatment with conducting polymers and can finally generate a functional precursor for an electrochemical electrode. The graphene structures resulted uniform and free from structural defects. The grain size ranged from 1.5 μm and the peak density was reduced, resulting in an improved equilibrium between peaks and hollows.

2.2. Materials and Preparation Methods for Hybrid Nanostructures from Graphene and Conducting Polymers

The method used for creating hybrid nanostructures from graphene and conducting polymers was drop-casting, and five samples of each type were created to evaluate technological feasibility, as widely described in [41]. For Poly 3-hexylthiophene (P3HT), 15 mg/mL of the polymer was dissolved in $CHCl_3$ at room temperature using an ultrasonic bath and allowed to sit for 30 min to achieve a uniform dispersion. In the case of Polyaniline emeraldine-base (PANI-EB), a 20 mg/mL polymer solution was prepared in N-methyl pyrrolidinone (NMP) by dissolving it at room temperature with an ultrasonic bath and allowing it to rest for 30 min for uniform distribution. For Poly[(9,9-dioctylfluorenyl-2,7-diyl)-co-bithiophene] (F8T2), a 20 mg/mL polymer solution was prepared in toluene at 60 °C using an ultrasonic bath and allowed to disperse uniformly for 30 min.

In all instances, 120 μL of each polymer solution was applied to graphene (SiO_2/Si substrate) via the drop-casting technique with Pasteur pipettes. The evaporation of each solvent occurred for 30 min under vacuum conditions, utilizing a Pfeiffer vacuum pump linked to a desiccator.

2.3. Materials and Preparation Methods for Embedding Au Nano-Particles Within Hybrid Graphene-Polymer Structures

The graphene-conductive polymer composite structures were impregnated with a $HAuCl_4$/2-propanol solution by the dip-coating method. The samples were completely immersed and kept for 24 h in a diluted $HAuCl_4$/2-propanol solution (0.001 M). After impregnation, the samples were dried in an oven at 150 °C in a stream of Ar (100 sccm) for 30 min. The system was then cooled to room temperature in a stream of Ar. As shown below, Au nanoparticles with an average size of 100 nm were quasi-uniformly integrated into the hybrid graphene-polymer structures. This approach for obtaining pre-defined Au nanoparticles from a very diluted $HAuCl_4$ solution on the polymeric substrate, heated from room temperature to slightly above one hundred degrees Celsius, is similar to those detailed in [42,43], in those instances handling with remnants of a droplet of $HAuCl_4$ solution and following the same process of heating. But this technique, introduced by the paper, using immersion of the polymer film in a very diluted $HAuCl_4$ solution, has the advantage of creating and quasi-uniformly dispersing gold nanoparticles on larger surfaces, along with several extra advantages: (1) the cost of generating gold nanoparticles is low; (2) the method is simple; (3) no waste liquid is produced following the synthesis of gold nanoparticles.

2.4. Characterization Equipment

Scanning electron microscopy (SEM) and energy-dispersive X-ray spectroscopy (EDX) were performed with a field emission and focused ion beam scanning electron microscope Lyra III XMU (TESCAN GROUP a.s., Brno-Kohoutovice, Czech Republic).

Optical analysis using atomic force microscopy (AFM) was conducted with a Dimension Edge device (Bruker, Billerica, USA). The assessment of roughness was performed using these derived parameters: Ra = Average Roughness; RSk = Skewness; RMS = Root Mean Square Roughness; RKu = Kurtosis. The outcomes for the roughness parameters are shown as averages for 4 scanned regions on each type of sample. The surface roughness parameters are described according to ISO 21920-2:2021 [44,45].

A PARSTAT 4000 potentiostat/galvanostat device (AMETEK Scientific Instruments Inc., Oak Ridge, TN, USA) along with its associated software linked to a computer via the VersaStudio electrochemistry graphical interface was used to assess electrochemical features of samples. Its K0264 Micro-Cell Kit was used as electrochemical cell assembly.

3. Results and Discussion

3.1. AFM Analysis

Along with the initial analysis presented in [41], a SEM analysis was also introduced for all hybrid structures of graphene-conducting polymers. In the case of graphene covered with P3HT, although, at first glance, it seems to have a fairly uniform grain distribution, Figure 1a), when relaying to the image at 500× Figure 1b), it can be noticed that the roughness is quite high. Grains of different sizes but also smoother stretches can be observed, Figure 2.

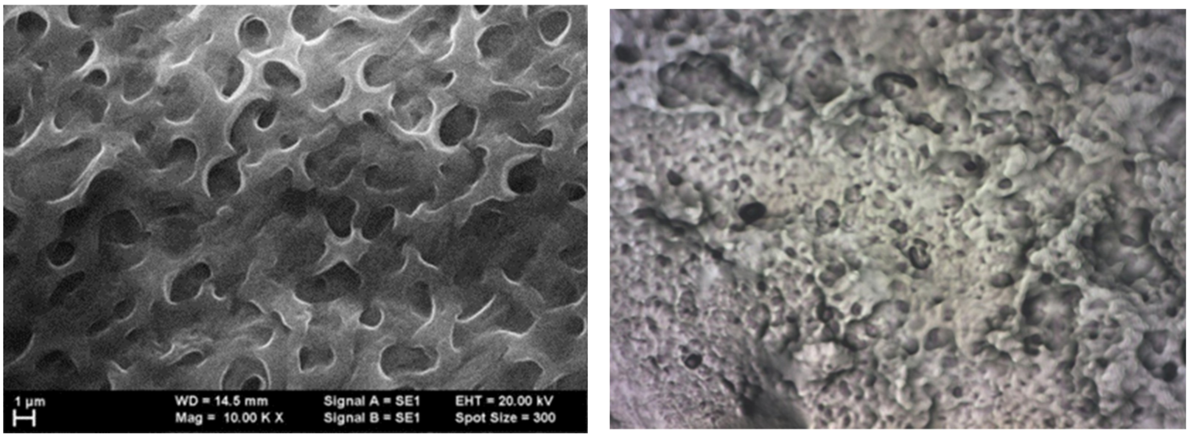

(**a**) (**b**)

Figure 1. Optical analysis of graphene–P3HT: (**a**) SEM at 10 kx and (**b**) optical at 500×.

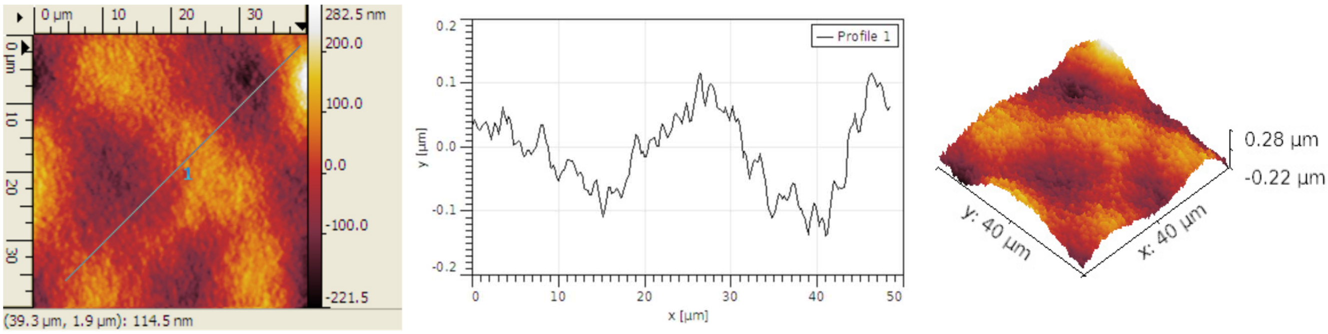

Figure 2. AFM Topographic image and profile lines for graphene–P3HT.

The grain size is small, typically below 0.3 µm. The grains are typically organized in bigger groups. The Rku values are near 3, Table 1, indicating that the grain distribution is fairly symmetrical. The Rsk values are minimal, and we can approximate a roughly equal percentage of peaks and hollow distributed across the surface.

Table 1. Average roughness parameters determined by AFM lines: graphene—P3HT.

Scanned Area	RMS (nm)	Ra (nm)	R_{Sk}	R_{Ku}
40 × 40 µm	64	53	0.143	3.31

In the case of graphene covered with PANI-EB, we can evaluate a roughly equal percentage of peaks and valleys distributed across the surface, but here the grains are organized in smaller groups and present a higher density, Figure 3. The grain size is larger, typically over 2.2 µm, Figure 4, and their concentration is heightened. The Rku values remained near 3, indicating that the grain distribution is symmetrical. The Rsk values are also minimal, comparable with the values for graphene–P3HT structures, suggesting that polymer deposition creates a similar architecture, see Table 2.

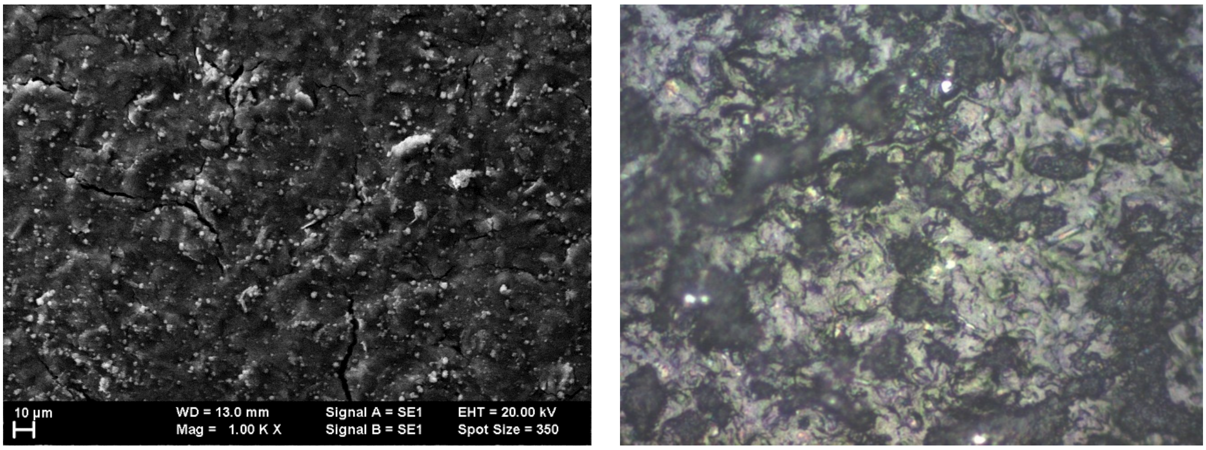

(**a**) (**b**)

Figure 3. Optical analysis of graphene–PANI-EB: (**a**) SEM at 1 kx and (**b**) optical at 500×.

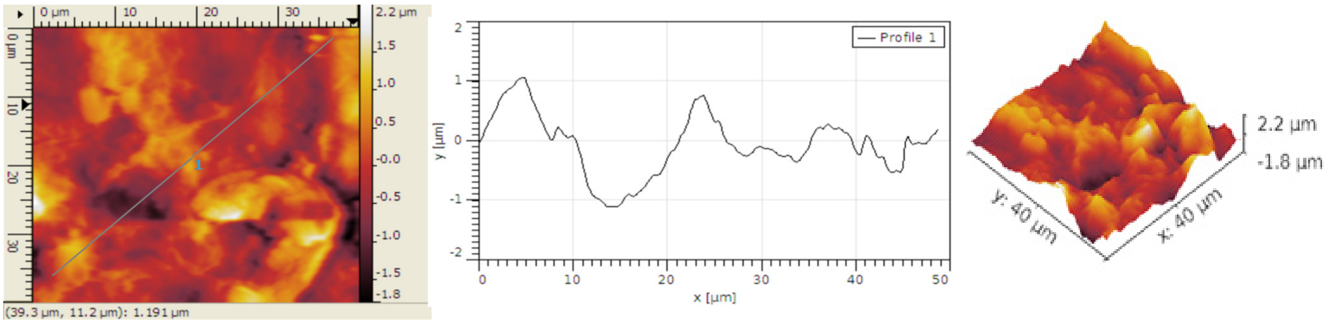

Figure 4. AFM Topographic image and profile lines for graphene–PANI-EB.

Table 2. Average roughness parameters determined by AFM lines: graphene—PANI-EB.

Scanned Area	RMS (nm)	Ra (nm)	R_{Sk}	R_{Ku}
40 × 40 µm	522	414	0.16	3.16

In the case of graphene covered with F8T2, a different topography is observed compared to the structures presented above. Analyzing Figure 5, even if it seems to present a fairly uniform grain distribution, the roughness is much higher compared to the graphene deposited with P3HT or PANI-EB. The grains are arranged less uniformly, and there are grains of different sizes separated by smoother stretches.

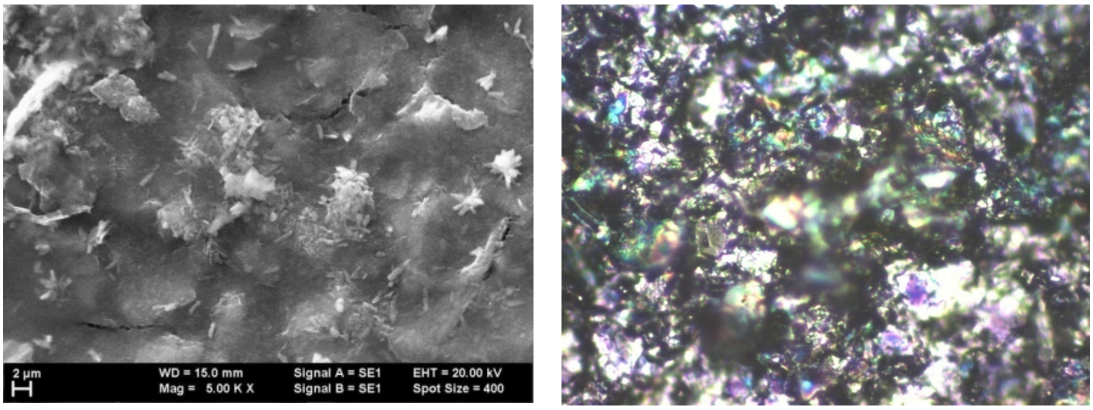

(**a**) (**b**)

Figure 5. Optical analysis of graphene–F8T2: (**a**) SEM at 5 kx and (**b**) optical at 500×.

The grain size is generally 3 µm, Figure 6, about 10 times larger compared to the graphene deposited with P3HT, where the grain dimension was 0.28 µm. But the grain size for graphene–F8T2 assembly is in line with the dimension for graphene deposited with PANI-EB, of 2.2 µm. The grains are generally arranged in smaller clusters, and according to the values of R_{Sk} and R_{ku} the grain distribution is quite symmetrical, Table 3.

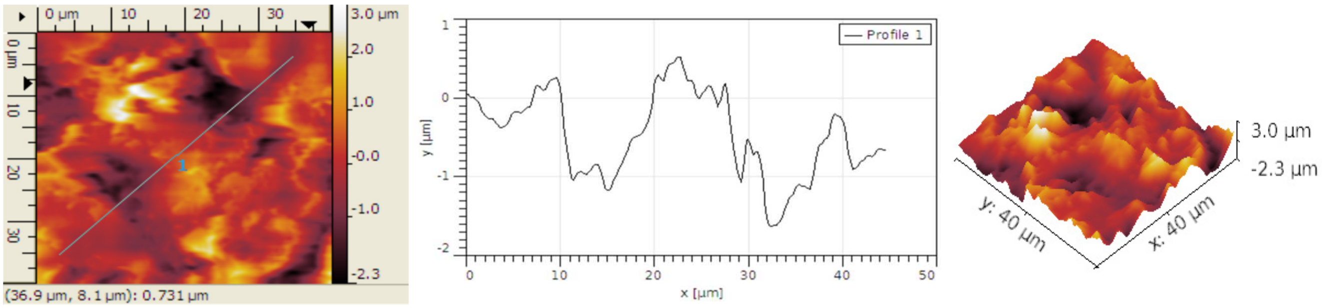

Figure 6. AFM Topographic image and profile lines for graphene–F8T2.

Table 3. Average roughness parameters determined by AFM lines—graphene–F8T2.

Scanned Area	RMS (nm)	Ra (nm)	R_{Sk}	R_{Ku}
40 × 40 µm	705	546	0.191	3.36

In all, AFM emphasized a higher roughness in the case of F8T2 compared to P3HT or PANI-EB, and a larger dimension of grain size.

The analysis of the structure obtained after inserting Au nanoparticles within graphene–P3HT assembly is presented in Figure 7. The existence of gold as quasi-spherical particles with the average dimension of approx. 100 nm is easily observable. However, at first glance, the number of gold particles bonded to the polymer is quite minimal.

The grain size typically measures 0.48 µm, consistent with the size of graphene deposited with PANI-EB without the addition of Au, as shown in Figure 8. The grains are usually organized in smaller groups too. The R_{Sk} values are elevated, suggesting the formation of distinct hollows post-Au deposition; however, the structure of these hollows is scattered due to the limited number of Au particles. The R_{ku} values exceed 4, indicating that the grain symmetry is somewhat altered by the addition of Au, as shown in Table 4.

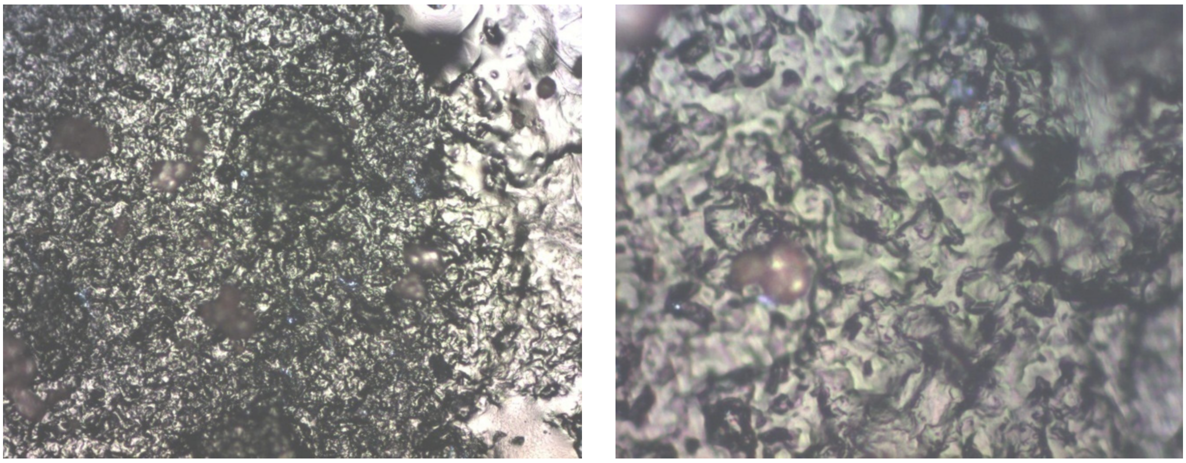

(**a**) (**b**)

Figure 7. Optical analysis of graphene–P3HT+Au: (**a**) at 100× and (**b**) at 500×.

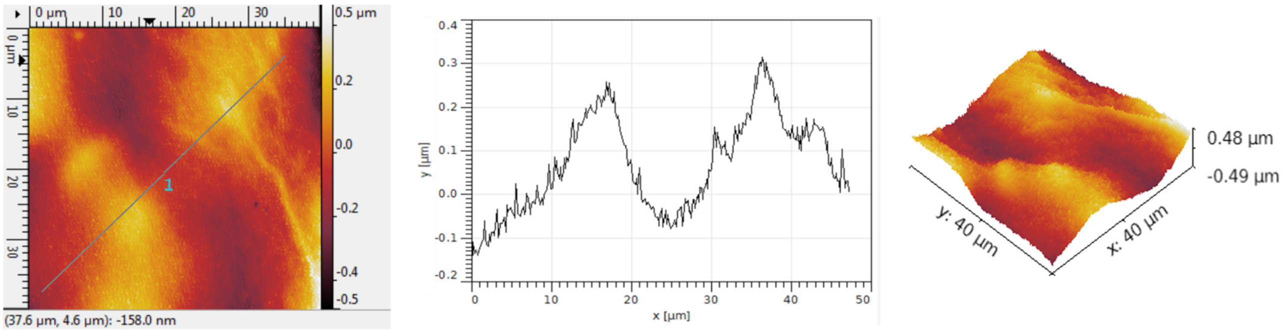

Figure 8. AFM Topographic image and profile lines for graphene–P3HT+Au.

Table 4. Average roughness parameters determined by AFM lines: graphene—P3HT+Au.

Scanned Area	RMS (nm)	Ra (nm)	R_{Sk}	R_{Ku}
40 × 40 µm	255	197	0.51	4.59

Figure 9 shows the analysis of the structure achieved after incorporating Au nanoparticles into the graphene—PANI-EB assembly. The presence of gold in the form of quasi-spherical particles with an average size of about 100 nm is clearly visible, yet the quantity of metallic particles is greater and somewhat grouped in small clusters.

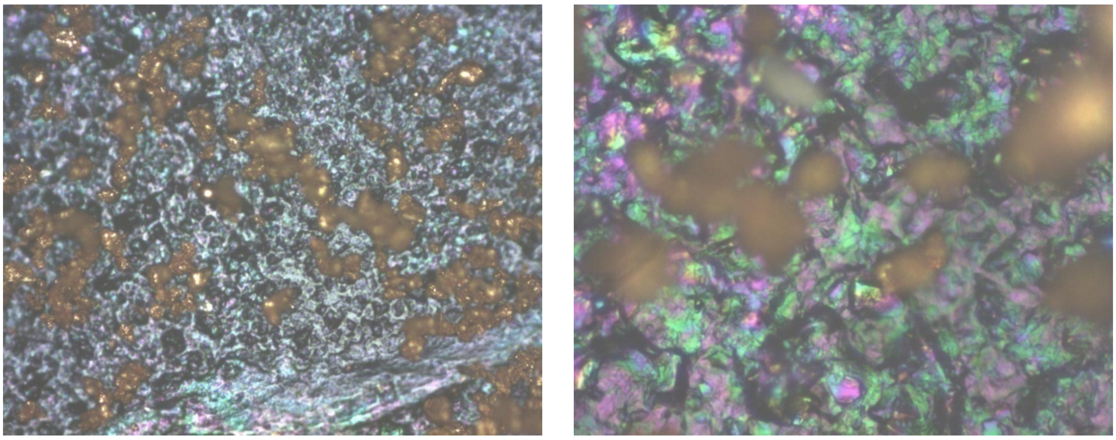

(**a**) (**b**)

Figure 9. Optical analysis of graphene–PANI-EB+Au: (**a**) at 100× and (**b**) at 500×.

The grain size is generally 1.8 µm, in line with the dimension for graphene deposited with PANI-EB without Au addition, Figure 10. The grains are usually organized in larger groups. The R_{Sk} values are high, indicating the development of unique hollows after Au deposition, characterized by a specific arrangement featuring large hollows among the groups of grains. The R_{ku} values are over 7, demonstrating that the grain symmetry is completely altered by the inclusion of Au, as illustrated in Table 5, as integration of metal compels the initial grains to form gaps for Au particles to delve further and gather into small clusters, thereby sharpening the peaks.

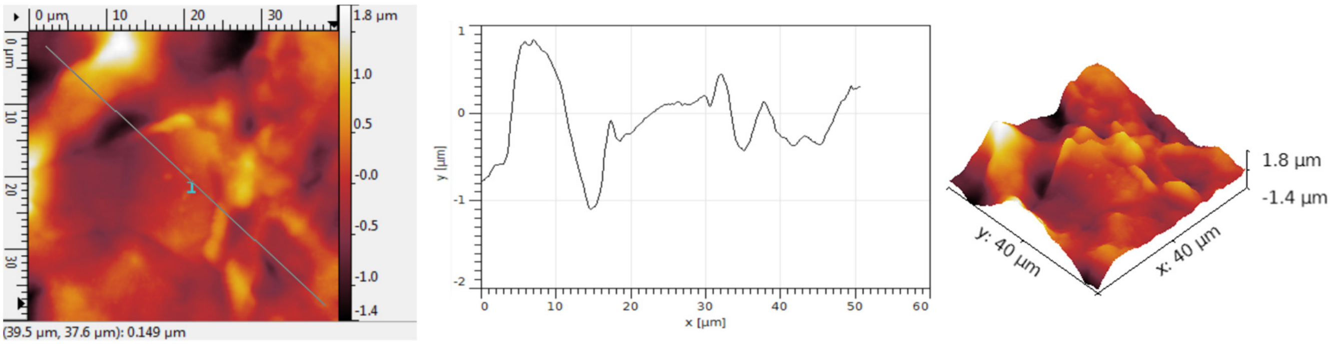

Figure 10. AFM Topographic image and profile lines for graphene–PANI-EB+Au.

Table 5. Average roughness parameters determined by AFM lines: graphene—PANI-EB+Au.

Scanned Area	RMS (nm)	Ra (nm)	R_{Sk}	R_{Ku}
40 × 40 µm	465	297	0.42	7.44

Figure 11 illustrates the analysis of the structure obtained after adding Au nanoparticles to the graphene–F8T2 composite. Gold is noticeably present. At first glance, when comparing Figures 7, 9 and 11, in this instance, the area covered with nanoparticles surpasses that of the graphene–P3HT assembly but is fewer compared to the graphene–PANI-EB assembly. The metallic particles are somewhat clustered in larger groups, but the respective clusters are quite dispersed among the graphene–F8T2 grains.

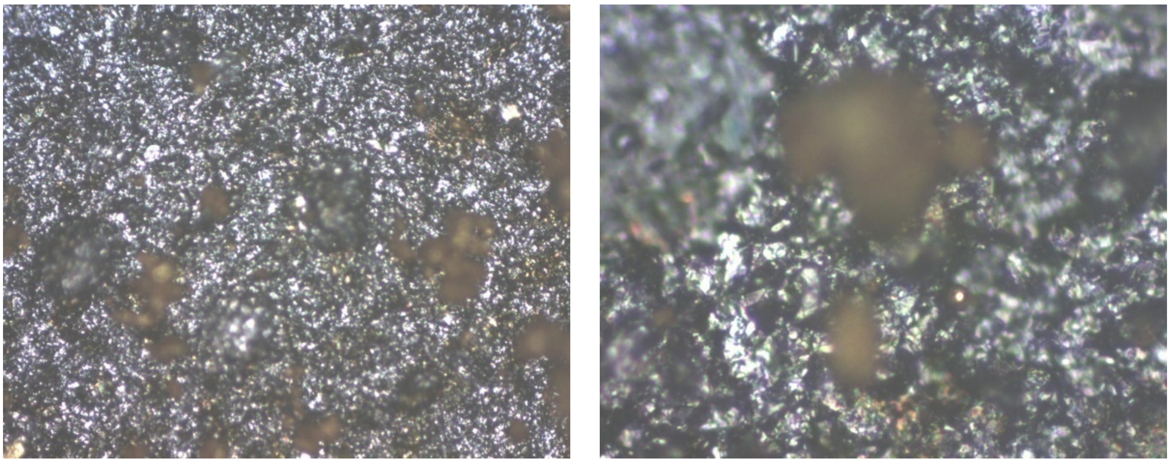
(**a**) (**b**)

Figure 11. Optical analysis of graphene–F8T2+Au: (**a**) at 100× and (**b**) at 500×.

The grain size typically reaches 3.8 µm, aligning with the dimensions for graphene deposited with F8T2 without the addition of Au, as shown in Figure 12. The grains are typically arranged in smaller clusters. The low R_{Sk} values suggest the formation of some hollows; however, the architecture of these hollows is scattered, due to the fairly dispersed gold clusters, and overall, the grains settle closely together, resulting in minimal free space among them. The R_{ku} values exceed 4, indicating that the grain symmetry is somewhat modified by the presence of Au, as shown in Table 6, although this modification is less significant compared to the graphene–PANI-EB assembly case, since, despite clustering, the Au particle clusters are few and fairly dispersed.

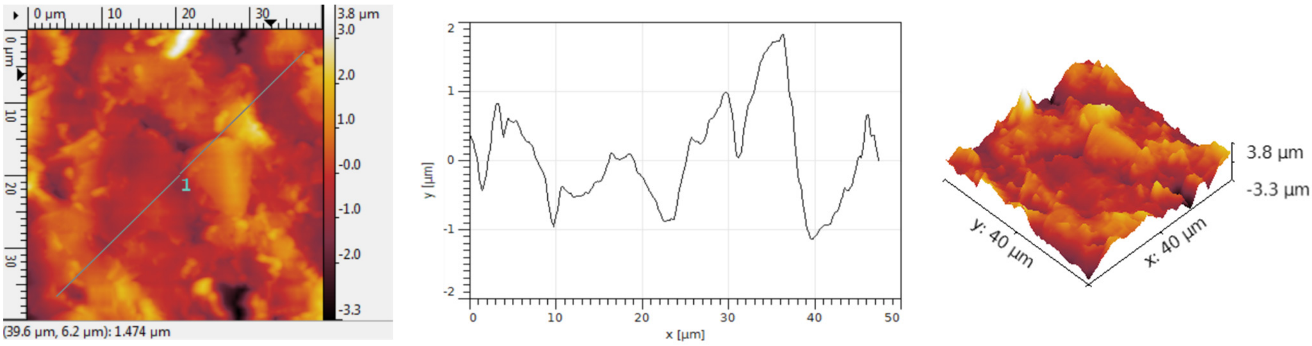

Figure 12. AFM Topographic image and profile lines for graphene–F8T2+Au.

Table 6. Average roughness parameters determined by AFM lines: graphene—F8T2+Au.

Scanned Area	RMS (nm)	Ra (nm)	R_{Sk}	R_{Ku}
40 × 40 µm	767	563	0.195	4.63

To evaluate the amount of gold in these hybrid structures, energy dispersive X-ray analyses were performed. The images have been very challenging to identify differences regarding the Au peak intensities, as there is a very low amount of gold relative to the graphene quantity, and minimal fluctuation in atomic percentage of gold as well, which renders the images irrelevant. Conversely, because of the weak EDS signal from small nanoparticles, the detection time for these particles increased, and other elements, such as Cu, Fe, and Co (likely connected to the sample holders etc.), appeared in the images, affecting the quality of the Au peak intensities. EDS analysis, a semi-quantitative method, has reasonably confirmed the incorporation of gold nanoparticles into hybrid structures. Table 7 depicts the weight and atomic percentage of gold atoms in the hybrid samples, but under the previously mentioned experimental conditions, the accuracy of this information is constrained.

Table 7. Weight and atomic percentage of gold atoms in the hybrid samples.

Hybrid Structure	Weight Percentage (%)	Atomic Percentage (%)
Graphene–P3HT+Au	3.79 ± 0.14	0.25 ± 0.05
Graphene–PANI-EB+Au	9.81 ± 0.16	0.65 ± 0.04
Graphene–F8T2+Au	6.02 ± 0.12	0.39 ± 0.08

In assessing the incorporation of gold nanoparticles into graphene-conducting polymer assemblies, we can infer that the interaction of gold with the polymer structures varies significantly, with P3HT exhibiting the weakest physical connection and lowest quantity of linked gold nanoparticles and PANI-EB showing the strongest. Conversely, the effect of incorporating gold nanoparticles varies, being more individual and dispersed for P3HT, and distinctly clustered and more agglomerated for the other two structures.

In every instance, a fairly symmetrical arrangement of grains was observed, with minimized space between them. Structures featuring symmetrical distribution and roughness dimensions at the micrometer scale are regarded as ideal for use as electrochemical sensors, although electrochemical evaluations in various reactants could determine their definitive usefulness.

3.2. Analysis of Electrochemical Functionality

The literature describes various metallization processes for graphene-supported composite materials, such as in [46], but many of them are unsuitable for a basic sensor application. In our instance, an ink-jet printer was utilized, and the metallization was performed using commercial ORGACON SI-J20X ink (Agfa-Gevaert N.V., Mortsel, Belgium) designed for printed electronics, by deposition in 2 layers. A uniform dispersion of the ink on the active area was observed, Figure 13a. An electrode structure was created from each of the earlier shown hybrid samples, featuring an active surface approximately 1–1.5 cm^2, linked on one side to the connecting conducting path.

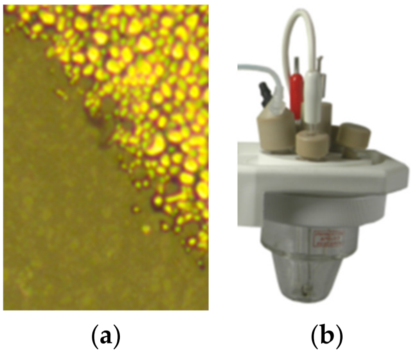
(**a**) (**b**)

Figure 13. (**a**) Sample of working electrode; (**b**) K0264 Micro-Cell Kit configuration used as electrochemical cell assembly.

The electrochemical cell utilized for obtaining the cyclic voltammograms consisted of three electrodes: one of the previously mentioned electrodes served as the working electrode, the reference electrode was Silver/Silver chloride, and the counter electrode was a Pt spiral of 0.3 mm diameter. The K0264 Micro-Cell Kit configuration, used as electrochemical cell assembly, is presented in Figure 13b.

The solution employed for the preliminary testing the three working electrodes was a 0.5 M aqueous H_2SO_4 solution, a typical method associated with cyclic voltammetry for examining proton reduction [47–49], primarily if pertaining to electrodes that include metallic elements. Figure 14 displays the cyclic voltammograms of the graphene–P3HT electrode with Au nanoparticles, employing 3 scanning rates of: 200, 100, and 50 mV/s respectively.

A thorough examination of Figure 14 shows that the peaks of oxidation and reduction in the voltammograms are found at 439 and 325 mV, respectively, indicating an irreversible process related to the electrochemical doping of P3HT by HSO_4^- anions in the vicinity of Au nanoparticles, similar with the cases described in [50,51]. As the scanning speed slows down, a reduction in both the anodic and cathodic current densities of the voltammograms is noted.

Figure 15 presents the cyclic voltammograms of the graphene–PANI-EB electrode with Au nanoparticles, at the same scanning rates.

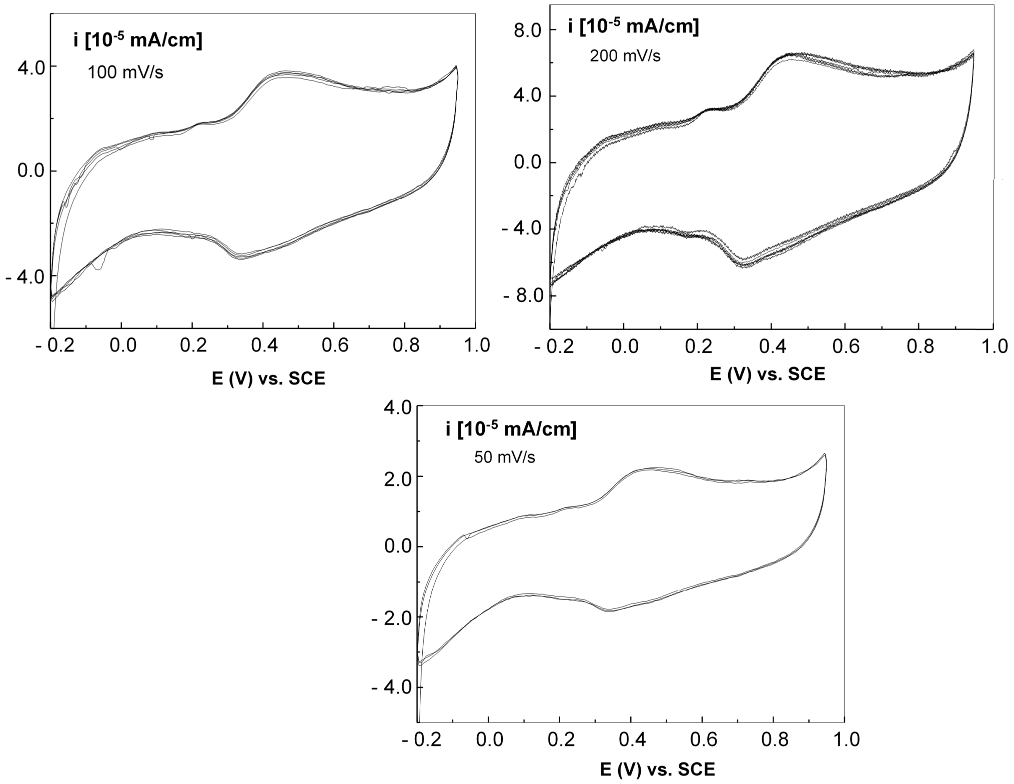

Figure 14. Cyclic voltammograms for graphene–P3HT+Au at scanning speeds of 200, 100, and 50 mV/s.

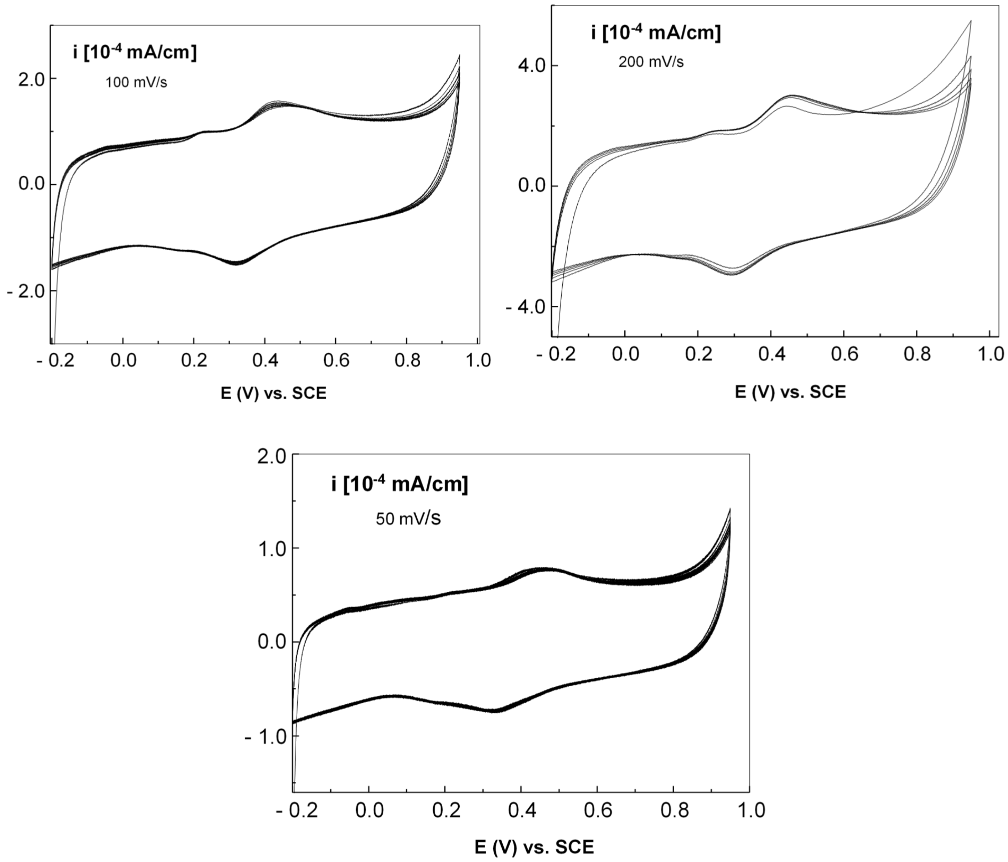

Figure 15. Cyclic voltammograms for graphene–PANI-EB+Au at scanning speeds of 200, 100, and 50 mV/s.

It was observed that regardless of the scanning speed, the cyclic voltammograms display an oxidation peak at 450 mV and a reduction peak at 291 mV. This difference in potential between the maximum oxidation and reduction indicates an irreversible process resulting from the doping of PANI-EB, which leads to the creation of emeraldine polyaniline salt (PANI-ES). Furthermore, as the scanning speed decreases, there is a nearly linear drop in the anodic and cathodic current densities, suggesting that the electrochemical process is controlled by diffusion.

Finally, Figure 16 presents the cyclic voltammograms of the graphene– F8T2 electrode with Au nanoparticles, at the same scanning rates.

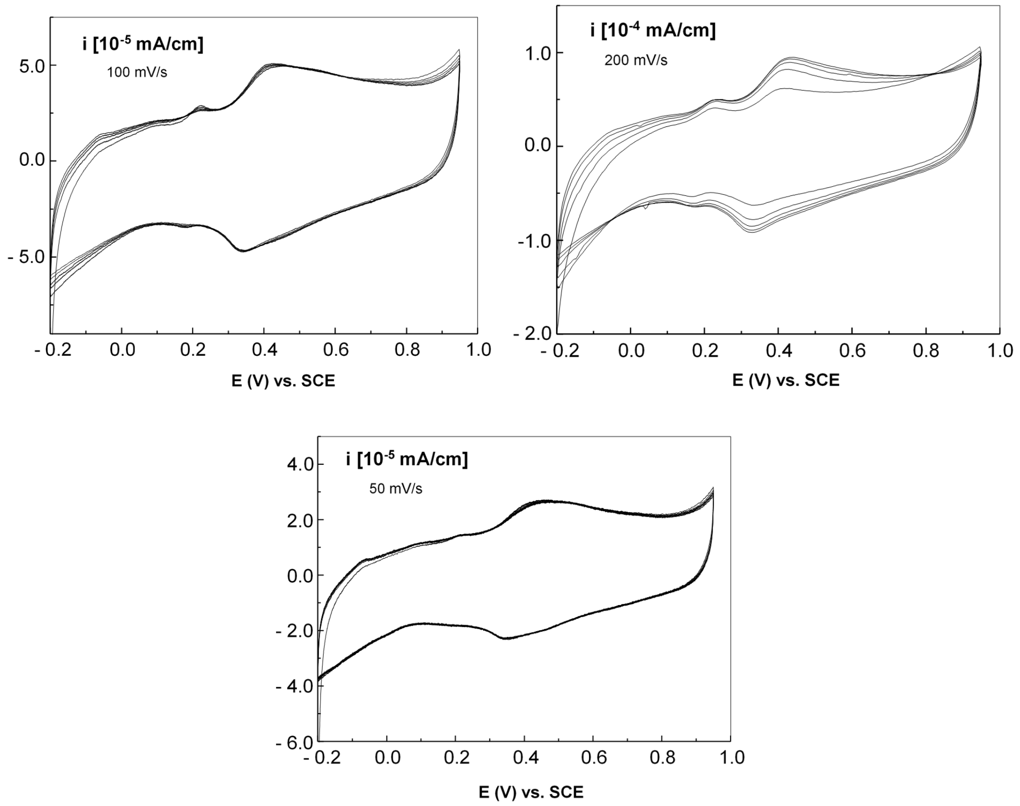

Figure 16. Cyclic voltammograms for graphene–F8T2+Au at scanning speeds of 200, 100, and 50 mV/s.

Upon examining the voltammograms collected at a sweep rate of 200 mV/s, it is evident that the maximum anodic and cathodic current densities increase with a growing number of cyclic voltammograms. By the conclusion of the 5 cycles, the process generally starts to stabilize, with the oxidation and reduction potentials of 428 and 325 mV, respectively. This effect is reduced at slower scanning speeds. More than this, a slower sweep speed leads to a decreased density of the anodic and cathodic currents, with a slight shift in the positions of the oxidation and reduction peaks; at a sweep speed of 50 mV/s, the potentials of the anodic and cathodic maxima are 448 mV and 337 mV, respectively. The voltage variation linked to the anodic and cathodic peaks suggests an irreversible process tied to the doping of the F8T2 macromolecular compound with gold nanoparticles, especially concerning their clustering in large quantities.

In all cases, especially at higher scanning speeds, preliminary minor oxidation and reduction processes, at potentials of about 200 and 180 mV, respectively, were noticed. They can be explained by the surface oxidation of gold nanoparticles, especially if pertaining to electrodes that include a carbon-based support, as described e.g., in [52]. A piece of evidence supporting this hypothesis is that for the graphene–F8T2 electrode, the effect is somewhat intensified when taking into account the clustering of Au nanoparticles in greater amounts. The variations of the electrochemical features demonstrated by the three electrodes when exposed to the 0.5 M H_2SO_4 solution distinctly show that the oxidation and reduction reactions at the electrode/electrolyte interface possess an irreversible nature due to the doping of the conjugated polymers, enhanced by the presence of gold nanoparticles.

The notable differences in roughness (grain size) and the arrangement of Au nanoparticles distribution within polymer grains lead to differing behaviors of those structures, and thus, any possible discrepancies in the sensitivity of the created sensing structures can be further clarified by this spatial configuration. At first glance, the oxidation and reduction potentials of the structures appear quite similar, particularly in the presence of sulfuric acid solution. However, a significant distinction can be observed in the values of the anodic and cathodic current densities, which seem to be greatly influenced by the amount and the way the gold nanoparticles are attached to the polymeric grains. In examining the slight oxidation and reduction reactions of Au nanoparticles for graphene–P3HT assembly, the effect appears comparable to that observed for graphene-F8T2 assembly, despite a noticeable difference in the atomic percentage of Au nanoparticles attached to each polymer surface, Table 7. Conversely, the oxidation and reduction processes of Au nanoparticles are hardly significant for the graphene–PANI-EB assembly, despite the amount of Au nanoparticles attached to the respective polymer surface being similar to that of the graphene-F8T2 assembly. For graphene–P3HT and graphene-F8T2 assemblies, the incorporation of Au nanoparticles appears to provide a distinct effect that does not necessarily improve the polymer’s electrochemical activity. In contrast, for the graphene–PANI-EB assembly, the impact is more synergistic, the oxidation and reduction processes of Au nanoparticles being negligible. These findings are supported by the analysis of Au nanoparticle dispersion linked to Figures 7, 9 and 11, where a more uniform and consistent distribution of Au nanoparticles among the polymer grains is observed solely in the case of the graphene–PANI-EB assembly.

In Figure 17, the current densities of structures at different scanning speeds is presented for the three graphene-polymer assemblies. The tests were repeated five times, and the results presented achieved a confidence level exceeding 90%. As shown, the most responsive structure is validated to be graphene–PANI-EB integrating Au nanoparticles. The explanation is founded on an adequately large grain size of 1.8 μm of the structure, with a significant quantity of Au nanoparticles, arranged as small clusters uniformly dispersed among the polymer grains, which become sharper due to arrangement of Au nanoparticles.

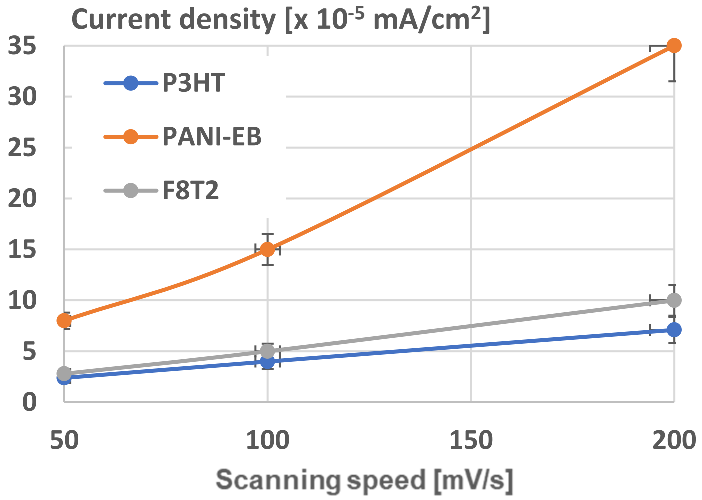

Figure 17. Current densities of structures at different scanning speeds.

In contrast to other research on graphene-polyaniline composites that may serve as electrochemical sensors [53–57], which primarily focus on graphene clusters embedded within PANI chains and utilize Van der Waals interactions on larger surfaces, the electrode technology introduced in this paper is groundbreaking and highlights a novel approach in altering at the nanoscale the architecture of sensing structures traditionally composed solely of graphene and conducting polymers. Additionally, incorporating gold nanoparticles enhances sensitivity regarding redox potential, both of which are critical attributes for an electrochemical sensor that targets specific biomolecular components for testing. Future research will focus on specifying hybrid structures of graphene–PANI-EB integrating Au nanoparticles for cancer diagnosis, aiming to exceed the results presented in [58,59], where the properties of PANI and graphene are examined independently, or the results presented in [60–63], where gold nanoparticles and graphene are examined independently.

4. Conclusions

This paper describes the process of fabricating electrodes utilizing hybrid nanostructures made from graphene and conductive polymers, as well as integrating gold nanoparticles.

The technique employed to create hybrid nanostructures from graphene and conducting polymers was drop-casting, using solutions of P3HT, PANI-EB, and F8T2. Furthermore, the graphene-conducting polymer structures were submerged in a $HAuCl_4$/2-propanol solution employing a novel dip-coating method, followed by a controlled heating from room temperature to just above one hundred degrees Celsius. The technique offers the benefit of generating and quasi-uniformly distributing gold nanoparticles with an average size of 100 nm across larger graphene-polymer structure surfaces. The incorporation of gold nanoparticles into polymer structures varies significantly, as P3HT shows the least affinity while PANI-EB exhibits the greatest.

An ink-jet printer was utilized to fabricate electrodes for electrochemical experiments from the relevant hybrid structures, with metallization carried out using commercially available silver ink intended for printed electronics. The electrochemical experiments used a 0.5 M aqueous $H2SO_4$ solution at three different scanning rates. The significant difference in roughness (grain size) leads to diverse behaviors of these structures, and thus, any possible variation in sensitivity can be better comprehended through this spatial configuration. At a glance, the oxidation and reduction potentials of the structures appear quite similar. However, a significant distinction is observable in the anodic and cathodic current density values, which seem to be greatly influenced by the active surface and structure of gold nanoparticles attached to the polymeric grains. The most responsive structure seems to be graphene–PANI-EB with Au nanoparticles, featuring a grain size of 1.8 µm and a significant quantity of Au nanostructures, arranged in small clusters that are evenly spread across the polymer grains.

Upcoming studies will target the specification of this electrode type for cancer detection.

Author Contributions: Conceptualization, A.F.T., R.C.C. and O.D.S.; methodology, R.C.C., O.D.S. and T.G.S.; validation, R.C.C., T.G.S. and A.F.T.; formal analysis, A.F.T., O.P. and R.C.C.; investigation, R.C.C., O.D.S., T.G.S., O.P. and A.F.T.; data curation, R.C.C., O.D.S., T.G.S., O.P. and A.F.T.; writing—original draft preparation, A.F.T. and R.C.C.; writing—review and editing, R.C.C.; visualization, R.C.C., O.D.S. and A.F.T.; supervision, A.F.T. and R.C.C. All authors have read and agreed to the published version of the manuscript.

Funding: This research received no external funding.

Institutional Review Board Statement: Not applicable.

Informed Consent Statement: Not applicable.

Data Availability Statement: Data are contained within the article.

Conflicts of Interest: The authors declare no conflicts of interest.

References

1. Zamiri, G.; Haseeb, A.S.M.A. Recent Trends and Developments in Graphene/Conducting Polymer Nanocomposites Chemiresistive Sensors. *Materials* **2020**, *13*, 3311. [CrossRef] [PubMed]
2. Cai, X.; Sun, K.; Qiu, Y.; Jiao, X. Recent Advances in Graphene and Conductive Polymer Composites for Supercapacitor Electrodes: A Review. *Crystals* **2021**, *11*, 947. [CrossRef]
3. Bai, H.; Sheng, K.; Zhang, P.; Li, C.; Shi, G. Graphene oxide/conducting polymer composite hydrogels. *J. Mater. Chem.* **2011**, *21*, 18653–18658. [CrossRef]
4. Conducting Polymer/Graphene-Based Material Composites, and Methods for Preparing the Composites. Available online: https://patents.google.com/patent/US20140087192A1/en (accessed on 12 March 2024).
5. Chauhan, A.K.; Gupta, S.K.; Taguchi, D.; Manaka, T.; Jha, P.; Veerender, P.; Sridevi, C.; Koiry, S.P.; Gadkari, S.C.; Iwamoto, M. Enhancement of the carrier mobility of conducting polymers by formation of their graphene composites. *RSC Adv.* **2017**, *7*, 11913–11920. [CrossRef]
6. Kausar, A. Conjugated Polymer/Graphene Oxide Nanocomposites—State-of-the-Art. *J. Compos. Sci.* **2021**, *5*, 292. [CrossRef]
7. Sharma, S.; Sudhakara, P.; Omran, A.A.B.; Singh, J.; Ilyas, R.A. Recent Trends and Developments in Conducting Polymer Nanocomposites for Multifunctional Applications. *Polymers* **2021**, *13*, 2898. [CrossRef]
8. Dunlop, M.J.; Bissessur, R. Nanocomposites based on graphene analogous materials and conducting polymers: A review. *J. Mater. Sci.* **2020**, *55*, 6721–6753. [CrossRef]
9. Adedoja, O.S.; Sadiku, E.R.; Hamam, Y. Prospects of Hybrid Conjugated Polymers Loaded Graphene in Electrochemical Energy Storage Applications. *J. Inorg. Organomet. Polym. Mater.* **2023**, *33*, 3915–3934. [CrossRef]
10. Shalini, A.; Kothai, S.; Jaisankar, V. Graphene Deposited Conducting Polymers: Synthesis and Sensing Applications. *Int. J. Curr. Res. Aca. Rev.* **2021**, *9*, 94–103. [CrossRef]
11. Zhu, Z.; Lin, W.-D.; Lin, Z.-Y.; Chuang, M.-H.; Wu, R.-J.; Chavali, M. Conductive Polymer (Graphene/PPy)–$BiPO_4$ Composite Applications in Humidity Sensors. *Polymers* **2021**, *13*, 2013. [CrossRef]
12. Das, P.; Chakraborty, K.; Pan, A.; Ghosh, S.; Pal, T. Conductivity relaxation and photocurrent generation in reduced graphene oxide-poly(9,9′-dioctyl-fluorene-co-bithiophene) composite with application in temperature sensing. *J. Appl. Phys.* **2019**, *125*, 085104. [CrossRef]
13. Pinelli, F.; Nespoli, T.; Fiorati, A.; Farè, S.; Magagnin, L.; Rossi, F. Graphene nanoplatelets can improve the performances of graphene oxide—Polyaniline composite gas sensing aerogels. *Carbon Trends* **2021**, *5*, 100123. [CrossRef]
14. Lee, S.J.; Yoon, S.J.; Jeon, I.-Y. Graphene/Polymer Nanocomposites: Preparation, Mechanical Properties, and Application. *Polymers* **2022**, *14*, 4733. [CrossRef]
15. Cheng, S.; Wang, Y.; Zhang, R.; Wang, H.; Sun, C.; Wang, T. Recent Progress in Gas Sensors Based on P3HT Polymer Field-Effect Transistors. *Sensors* **2023**, *23*, 8309. [CrossRef] [PubMed]
16. Cheon, H.J.; Shin, S.Y.; Van Tran, V.; Park, B.; Yoon, H.; Chang, M. Preparation of conjugated polymer/reduced graphene oxide nano-composites for high-performance volatile organic compound sensors. *Chem. Eng. J.* **2021**, *425*, 131424. [CrossRef]
17. Khanh, T.S.T.; Trung, T.Q.; Giang, L.T.T.; Nguyen, T.Q.; Lam, N.D.; Dinh, N.N. Ammonia Gas Sensing Characteristic of P3HT-rGO-MWCNT Composite Films. *Appl. Sci.* **2021**, *11*, 6675. [CrossRef]
18. Verma, A.; Gupta, R.; Verma, A.S.; Kumar, T. A review of composite conducting polymer-based sensors for detection of industrial waste gases. *Sens. Actuators Rep.* **2023**, *5*, 100143. [CrossRef]
19. Lei, W.; Si, W.; Xu, Y.; Gu, Z.; Hao, Q. Conducting polymer composites with graphene for use in chemical sensors and sensors. *Microchim. Acta* **2014**, *181*, 707–722. [CrossRef]
20. Kim, Y.; An, T.K.; Kim, J.; Hwang, J.; Park, S.; Nam, S.; Cha, H.; Park, W.J.; Baik, J.M.; Park, C.E. A composite of a graphene oxide derivative as a novel sensing layer in an organic field-effect transistor. *J. Mater. Chem. C* **2014**, *2*, 4539–4544. [CrossRef]
21. Rahman, A.; Pal, R.K.; Islam, N.; Freeman, R.; Berthiaume, F.; Mazzeo, A.; Ashraf, A. A Facile Graphene Conductive Polymer Paper Based Sensor for Dopamine, TNF-α, and IL-6 Detection. *Sensors* **2023**, *23*, 8115. [CrossRef]
22. Kumar, A.; Gupta, G.H.; Singh, G.; More, N.; Keerthana, M.; Sharma, A.; Jawade, D.; Balu, A.; Kapusetti, G. Ultrahigh sensitive graphene oxide/conducting polymer composite based sensor for cholesterol and bilirubin detection. *Biosens. Bioelectron. X* **2023**, *13*, 100290. [CrossRef]
23. Al-Graiti, W.; Foroughi, J.; Liu, Y.; Chen, J. Hybrid Graphene/Conducting Polymer Strip Sensors for Sensitive and Selective Electrochemical Detection of Serotonin. *ACS Omega* **2019**, *4*, 22169–22177. [CrossRef] [PubMed]
24. Văduva, M.; Baibarac, M.; Cramariuc, O. Functionalization of Graphene Derivatives with Conducting Polymers and Their Applications in Uric Acid Detection. *Molecules* **2023**, *28*, 135. [CrossRef]

25. Song, J.; Kim, Y.; Kang, K.; Lee, S.; Shin, M.; Son, D. Stretchable and Self-Healable Graphene–Polymer Conductive Composite for Wearable EMG Sensor. *Polymers* **2022**, *14*, 3766. [CrossRef] [PubMed]
26. DiFrancesco, M.L.; Colombo, E.; Papaleo, E.D.; Maya-Vetencourt, J.F.; Manfredi, G.; Lanzani, G.; Benfenati, F. A hybrid P3HT-Graphene interface for efficient photostimulation of neurons. *Carbon* **2020**, *162*, 308–317. [CrossRef]
27. Yazid, S.N.A.M.; Adnan, A.A.C.; Isa, I.M.; Saidin, M.I.; Ahmad, M.S.; Fun, C.S. Conducting polymer functionalized graphene-based electrochemical sensors for sensing pollutants in water. *J. Electrochem. Sci. Eng.* **2023**, *13*, 251–274. [CrossRef]
28. Diédhiou, I.; Fall, B.; Gaye, C.; Sall, M.L.; Diaw, A.K.D.; Gningue-Sall, D.; Fall, M.; Raouafi, N. Preparations and applications of organic conducting polymers/graphene composites in heavy metal ion sensing: A review. *Int. J. Mater. Res.* **2023**, *114*, 79–99. [CrossRef]
29. Lin, C.-H.; Lin, J.-H.; Chen, C.-F.; Ito, Y.; Luo, S.-C. Conducting polymer-based sensors for food and drug analysis. *J. Food Drug Anal.* **2021**, *29*, 544–558. [CrossRef]
30. Mulyono, T.; Siswoyo, A.; Lestari, P.B.; Zulfikar; Mufliha, Y.M. Development of A Resistive Sensor Array Based on Graphene and Conducting Polymer Composites for Coffee Aroma Classification. In Proceedings of the International Conference on Sustainable Chemistry (ICSChem 2023), Malang, Indonesia, 22–23 August 2023; Volume 481, p. 06012. [CrossRef]
31. Avelino, K.Y.; Oliveira, L.S.; Lucena-Silva, N.; Andrade, C.A.; Oliveira, M.D. Flexible sensor based on conducting polymer and gold nanoparticles for electrochemical screening of HPV families in cervical specimens. *Talanta* **2021**, *226*, 122118. [CrossRef] [PubMed]
32. Avelino, K.; Oliveira, L.; Lucena-Silva, N.; de Melo, C.; Andrade, C.; Oliveira, M. Metal-polymer hybrid nanomaterial for impedimetric detection of human papillomavirus in cervical specimens. *J. Pharm. Biomed. Anal.* **2020**, *185*, 113249. [CrossRef] [PubMed]
33. Rahman, A.; Son, J.I.; Won, M.-S.; Shim, Y.-B. Gold Nanoparticles Doped Conducting Polymer Nanorod Electrodes: Ferrocene Catalyzed Aptamer-Based Thrombin Immunosensor. *Anal. Chem.* **2009**, *81*, 6604–6611. [CrossRef] [PubMed]
34. Yan, Y.; Yang, G.; Xu, J.-L.; Zhang, M.; Kuo, C.-C.; Wang, S.-D. Conducting polymer-inorganic nanocomposite-based gas sensors: A review. *Sci. Technol. Adv. Mater.* **2020**, *21*, 768–786. [CrossRef]
35. Fabregat, G.; Armelin, E.; Alemán, C. Selective Detection of Dopamine Combining Multilayers of Conducting Polymers with Gold Nanoparticles. *J. Phys. Chem. B* **2014**, *118*, 4669–4682. [CrossRef] [PubMed]
36. Kumalasari, M.; Alfanaar, R.; Andreani, A. Gold nanoparticles (AuNPs): A versatile material for sensor application. *Talanta Open* **2024**, *9*, 100327. [CrossRef]
37. Petrucci, R.; Bortolami, M.; Di Matteo, P.; Curulli, A. Gold Nanomaterials-Based Electrochemical Sensors and Sensors for Phenolic Antioxidants Detection: Recent Advances. *Nanomaterials* **2022**, *12*, 959. [CrossRef]
38. Hou, J.; Li, B.; Jang, W.; Yun, J.; Eyimegwu, F.M.; Kim, J.-H. Integration of Gold Nanoparticles into Crosslinker-Free Polymer Particles and Their Colloidal Catalytic Property. *Nanomaterials* **2023**, *13*, 416. [CrossRef]
39. Hou, J.; Yun, J.; Jang, W.; Li, B.; Adehinmoye, A.A.; Kim, J.-H.; Byun, H. Rapid incorporation of gold nanoparticles onto graphene oxide-polymer nanofiber membranes for photothermally-accelerated water purification. *J. Polym. Eng.* **2022**, *43*, 156–166. [CrossRef]
40. Chekkaramkodi, D.; El Turk, S.; Ali, M.; Butt, H. In-situ synthesis and integration of gold nanoparticles into 3D printed optical fiber probes. *Sci. Rep.* **2024**, *14*, 29736. [CrossRef]
41. Trandabat, A.F.; Ciobanu, R.C.; Schreiner, O.D.; Schreiner, T.G.; Aradoaei, S. Chemiresistors Based on Hybrid Nanostructures Obtained from Graphene and Conducting Polymers with Potential Use in Breath Methane Detection Associated with Irritable Bowel Syndrome. *Int. J. Mol. Sci.* **2024**, *25*, 5552. [CrossRef]
42. Umeda, H.; Mezaki, Y.; Oshio, A.; Kaneko, Y.; Okamoto, R.; Kusumoto, S.; Kunimura, S. Gold Nanoparticles Produced by Low-temperature Heating of the Dry Residue of a Droplet of an HCl Acidic Solution of $HAuCl_4 \cdot 4H_2O$ in a Low Vacuum. *Anal. Sci.* **2021**, *37*, 1427–1432. [CrossRef]
43. Ii, K.; Kurita, Y.; Kida, N.; Kunimura, S. Preparation of gold nanoparticles using low-temperature heating of the dry residue of a droplet of an HAuCl4 solution in air. *Anal. Sci.* **2024**, *40*, 213–217. [CrossRef]
44. Surface Roughness Parameters. Available online: https://www.keyence.eu/ss/products/microscope/roughness/line/tab03_b.jsp (accessed on 20 November 2024).
45. *ISO 21920-2:2021 (previously ISO 4287:1997)*; Geometrical Product Specifications (GPS)—Surface Texture: Profile—Part 2: Terms, Definitions and Surface Texture Parameters. International Organization for Standardization: Geneva, Switzerland, 2021. Available online: https://www.iso.org/standard/72226.html (accessed on 20 November 2024).
46. Rafailović, L.D.; Jovanović, A.Z.; Gutić, S.J.; Wehr, J.; Rentenberger, C.; Trišović, T.L.; Pašti, I.A. New Insights into the Metallization of Graphene-Supported Composite Materials–from 3D Cu-Grown Structures to Free-Standing Electrodeposited Porous Ni Foils. *ACS Omega* **2022**, *7*, 4352–4362. [CrossRef]
47. Zeng, Q.; Xia, K.; Zhang, Y.; Wu, T. Well Controlled 3D Iridium Oxide/Platinum Nanocomposites with Greatly Enhanced Electrochemical Performances. *Adv. Mater. Interfaces* **2019**, *6*, 1900356. [CrossRef]

48. Tamilselvi, B.; Bhuvaneshwari, D.S.; Karuppasamy, P.; Padmavathy, S.; Nikhil, S.; Siddegowda, S.B.; Murthy, H.C.A. Investigation of Corrosion Inhibition of Mild Steel in 0.5 M H2SO4 with Lachancea fermentati Inhibitor Extracted from Rotten Grapefruits (*Vitis vinifera*): Adsorption, Thermodynamic, Electrochemical, and Quantum Chemical Studies. *ACS Phys. Chem. Au* **2024**, *4*, 67–84. [CrossRef] [PubMed]
49. Zhong, W.; Xiao, B.; Lin, Z.; Wang, Z.; Huang, L.; Shen, S.; Zhang, Q.; Gu, L. $RhSe_2$: A Superior 3D Electrocatalyst with Multiple Active Facets for Hydrogen Evolution Reaction in Both Acid and Alkaline Solutions. *Adv. Mater.* **2021**, *33*, 2007894. [CrossRef] [PubMed]
50. Choi, W.; Bard, A. Doping of the Semiconducting Polymer Poly(3-hexylthiophene) (P3HT) in Organic Photoelectrochemical Cells. *J. Phys. Chem. C* **2020**, *124*, 3439–3447. [CrossRef]
51. Zhao, D.; Li, L.; Niu, W.; Chen, S. Highly conductive polythiophene films doped with chloroauric acid for dual-mode sensing of volatile organic amines and thiols. *Sens. Actuators B Chem.* **2017**, *243*, 380–387. [CrossRef]
52. Wang, Y.; Laborda, E.; Crossley, A.; Compton, R.G. Surface oxidation of gold nanoparticles supported on a glassy carbon electrode in sulphuric acid medium: Contrasts with the behaviour of 'macro' gold. *Phys. Chem. Chem. Phys.* **2013**, *15*, 3133–3136. [CrossRef]
53. Farooqi, B.A.; Yar, M.; Ashraf, A.; Farooq, U.; Ayub, K. Graphene-polyaniline composite as superior electrochemical sensor for detection of cyano explosives. *Eur. Polym. J.* **2020**, *138*, 109981. [CrossRef]
54. Wei, L.; Fan, L.; Yang, H.; Wu, Y. Graphene/Polyaniline Nanocomposite as an Electrochemical Sensor for Ultrasensitive Detection of Pb(II). *Int. J. Electrochem. Sci.* **2019**, *14*, 10720–10728. [CrossRef]
55. Hadano, F.S.; Gavim, A.E.X.; Stefanelo, J.C.; Gusso, S.L.; Macedo, A.G.; Rodrigues, P.C.; Yusoff, A.R.b.M.; Schneider, F.K.; de Deus, J.F.; da Silva, W.J. NH_3 Sensor Based on rGO-PANI Composite with Improved Sensitivity. *Sensors* **2021**, *21*, 4947. [CrossRef] [PubMed]
56. Xie, A.; Du, J.; Zhang, J.; Xiong, Z.; Shao, F.; Luo, S. A High-Performance Nonenzymatic Urea Sensor Based on Graphene-NiO-Polyaniline. *J. Electrochem. Soc.* **2019**, *166*, B456. [CrossRef]
57. Santos-Ceballos, J.C.; Salehnia, F.; Güell, F.; Romero, A.; Vilanova, X.; Llobet, E. Room-Temperature Ammonia Sensing Using Polyaniline-Coated Laser-Induced Graphene. *Sensors* **2024**, *24*, 7832. [CrossRef] [PubMed]
58. Hosseine, M.; Bakhshi, A.; Naghib, S.M.; Rabiee, N. Recent advancements in polyaniline-based sensors for diagnosis of cancers: A comprehensive review. *TrAC Trends Anal. Chem.* **2024**, *181*, 118040. [CrossRef]
59. Al-Salman, H.; Hsu, C.-Y.; Jawad, Z.N.; Mahmoud, Z.H.; Mohammed, F.; Saud, A.; Al-Mashhadani, Z.I.; Abu Hadal, L.S.; Kianfar, E. Graphene oxide-based sensors for detection of lung cancer: A review. *Results Chem.* **2024**, *7*, 101300. [CrossRef]
60. Pothipor, C.; Jakmunee, J.; Bamrungsap, S.; Ounnunkad, K. An electrochemical sensor for simultaneous detection of breast cancer clinically related microRNAs based on a gold nanoparticles/graphene quantum dots/graphene oxide film. *Analyst* **2021**, *146*, 4000–4009. [PubMed]
61. Li, Y.; Wang, X.; Wang, X.; Qin, Z.; Li, C.; Yang, J.; Cao, M. Electrochemical sensor based on composite of gold nanoparticle/reduced-graphene oxide/graphitic carbon nitride and a caprolactone polymer for highly sensitive detection of CEA. *Bioelectrochemistry* **2025**, *163*, 108897. [CrossRef]
62. Li, C.-H.; Chan, M.-H.; Chang, Y.-C.; Hsiao, M. Gold Nanoparticles as a Sensor for Cancer Biomarker Determination. *Molecules* **2023**, *28*, 364. [CrossRef]
63. Gao, C.; Jiang, Z. Gold Nanoparticles (Aunps)-Based Sensors for Cancer Detection. *Trans. Mater. Biotechnol. Life Sci.* **2024**, *4*, 31–35. [CrossRef]

coatings

IMPACT FACTOR 2.8

CITESCORE 5.4

Article

Active Surfaces in Sensor Technologies Utilizing Ceramic Nanotube-Conducting Polymer Composites Containing Embedded Gold Nanoparticles

Alexandru Florentin Trandabat, Romeo Cristian Ciobanu and Oliver Daniel Schreiner

Special Issue
Advances in Nanostructured Thin Films and Coatings, 3rd Edition

Edited by
Prof. Dr. Yujun Song and Prof. Dr. Qingwei Liao

MDPI

https://doi.org/10.3390/coatings15101211 coatings

MDPI

Article

Active Surfaces in Sensor Technologies Utilizing Ceramic Nanotube-Conducting Polymer Composites Containing Embedded Gold Nanoparticles

Alexandru Florentin Trandabat [1], Romeo Cristian Ciobanu [1,*] and Oliver Daniel Schreiner [1,2]

[1] Department of Electrical Measurements and Materials, Gheorghe Asachi Technical University, 700050 Iasi, Romania; ftranda@tuiasi.ro (A.F.T.); oliver090598@yahoo.com (O.D.S.)

[2] Department of Medical Specialties III, Faculty of Medicine, University of Medicine and Pharmacy "Grigore T. Popa", 700115 Iasi, Romania

* Correspondence: r.c.ciobanu@tuiasi.ro

Abstract

This study describes the approach to develop hybrid nanostructures made of four varieties of ceramic nanotubes and three types of conductive polymers embedded with gold nanoparticles through a novel technique, which can exhibit distinct sensory properties not documented in the existing literature. Atomic force microscopy (AFM) analysis highlighted the characteristics of their surface roughness, identifying which could be the best choice for electrochemical electrodes depending on their surface structure. The incorporation of gold nanoparticles modifies the surface structure and forces the original grains to create voids that allow the gold particles to penetrate deeper and gather in small clusters, which in turn leads to a minor increase in grain size and localized sharpening of the peaks. The analysis mainly identified the peaks that were higher in relation to the valleys to identify a Gaussian distribution. It turned out that the configuration of ZnO nanotubes in the composites leads to the highest Ra values, with Al_2O_3 nanotubes coming in second place. Regarding the contribution of conducting polymers, PANI:EB presented the highest importance for all composites, while P3HT was relevant in several other cases. The evaluation of the electrode roughness, as described in this paper, is essential for the evaluation of its potential electrochemical activity and acts as a reliable measure that goes beyond the role of the evaluation of the active surface area (EASA). In our opinion, the evaluation of the EASA by traditional approaches described in the literature is not relevant for sensor applications, since the evaluation of the electrode surface structure must be performed before electrochemical tests, because the general electrochemical tests designed for sensor applications do not evaluate the EASA. Consequently, a thorough assessment of the electrode surface structure is advised, choosing the optimal electrodes according to this design, and additional data obtained from cyclic voltammetry will finally ascertain the true EASA and the actual performance of the respective electrode for identifying the target molecules.

Keywords: ceramic nanotubes; conducting polymers; gold nanoparticles; surface roughness; electrochemical sensors

check for updates

Academic Editor: Gianfranco Carotenuto

Received: 9 September 2025
Revised: 2 October 2025
Accepted: 3 October 2025
Published: 14 October 2025

Citation: Trandabat, A.F.; Ciobanu, R.C.; Schreiner, O.D. Active Surfaces in Sensor Technologies Utilizing Ceramic Nanotube-Conducting Polymer Composites Containing Embedded Gold Nanoparticles. *Coatings* **2025**, *15*, 1211. https://doi.org/10.3390/coatings15101211

1. Introduction

Electrochemical analysis offers numerous benefits, including high sensitivity, selectivity, simplicity, lower cost compared to alternative methods, and rapid analysis [1]. The binding interaction occurs between the target molecule and the active site. As a prerequisite, a larger surface area and surface texture are essential for optimal adhesion of the molecules of interest. The electrical signal generated originates from either the generation or consumption of electroactive species in stoichiometric amounts. However, the use of bare electrodes presents several disadvantages, including electrode fouling and inadequate electron transfer. The intercalation of physical modifiers plays a crucial role in addressing the problems associated with the use of bare electrodes. Nanomaterials are often used as modifiers that lower the potential required for electron propagation, thereby enhancing the selectivity and sensitivity of an electrode. Numerous studies have investigated the application of nanomaterials to achieve higher sensitivity, including hybridization of transition metals [2,3], metal oxides [4,5], carbon nanomaterials [6–8], nanowires [9,10], metallic nanomaterials [11–14], and various hybrid nanostructures, among others [15–19]. Typically, it has been shown that higher surface roughness improves the adsorption of target molecules onto the sensing surface by providing more active sites, leading to significant interaction between the adsorbed molecules and the sensing material [20–25]. Conversely, it has been shown that a higher degree of electrode roughness positively influences the shapes of cyclic voltammograms, and the corresponding peak currents are at significantly higher levels [26].

The effect of higher roughness on sensor performance impacts reaction kinetics, which are improved, charge transfer rates, by modifying ion/electron motion, and generally, sites for reactant adsorption, by providing additional sites. The main focus has been on the development of optical sensors, as shown in [27–31], but in recent years, there has been an increased interest in custom-designed electrodes with specific architectures for electrochemical applications, including sensors, as well [32–36]. The texture and irregularities present on the surface of an electrode, known as roughness, can significantly influence its electrochemical properties, including charge transfer and capacitance. In the last 15 years, numerous studies have focused on the synthesis of ceramic nanotubes using different technologies [37–42]. While many authors have focused on the surface characteristics of hybrid structures involving carbon nanotubes or graphene, especially those incorporating conducting polymers for sensing applications, none have investigated the properties of composites comparable to ceramic nanotubes, despite their potential for various types of electrochemical sensors. However, the clear advantages that such hybrid structures offer in terms of compactness, precision, and improved detection sensitivity should inspire researchers to continuously improve current ceramic nanotube-based composite technologies, primarily in terms of improving their electrochemical active surface area (EASA) [43,44], by tailoring the electrode surface structure.

The innovation of this work mainly concerns the development of hybrid nanostructures made of ceramic nanotubes and conductive polymers containing embedded gold nanoparticles, which could exhibit unique sensing capabilities not recorded in the current literature. The surface structure of ceramic nanotube-based electrodes is an important aspect that may have an impact on future advances in electrochemical sensor applications. This work presents hybrid structures of four types of ceramic nanotubes associated with three types of conductive polymers, with the aim of evaluating their physical characteristics and surface roughness properties and, finally, determining which of them could be the optimal selection for electrochemical electrodes based on their surface architecture.

2. Materials, Technology, and Characterization Methods

2.1. Sample Preparation

Based on the technological steps detailed in [38,42,45–47], the method for fabricating ceramic nanotubes consisted of three phases: forming polymer fiber networks with poly(methyl methacrylate), applying ceramic coatings to the nanofiber networks by magnetron sputtering, and heating the nanotubes to 600 °C for complete removal of the polymer support, [38,42,46,47]. Figure 1 shows the images of TiO_2, Al_2O_3, Y_2O_3, and ZnO ceramic nanotubes, respectively, emphasizing the uniformity of the ceramic nanotube structures, which are hollow inside.

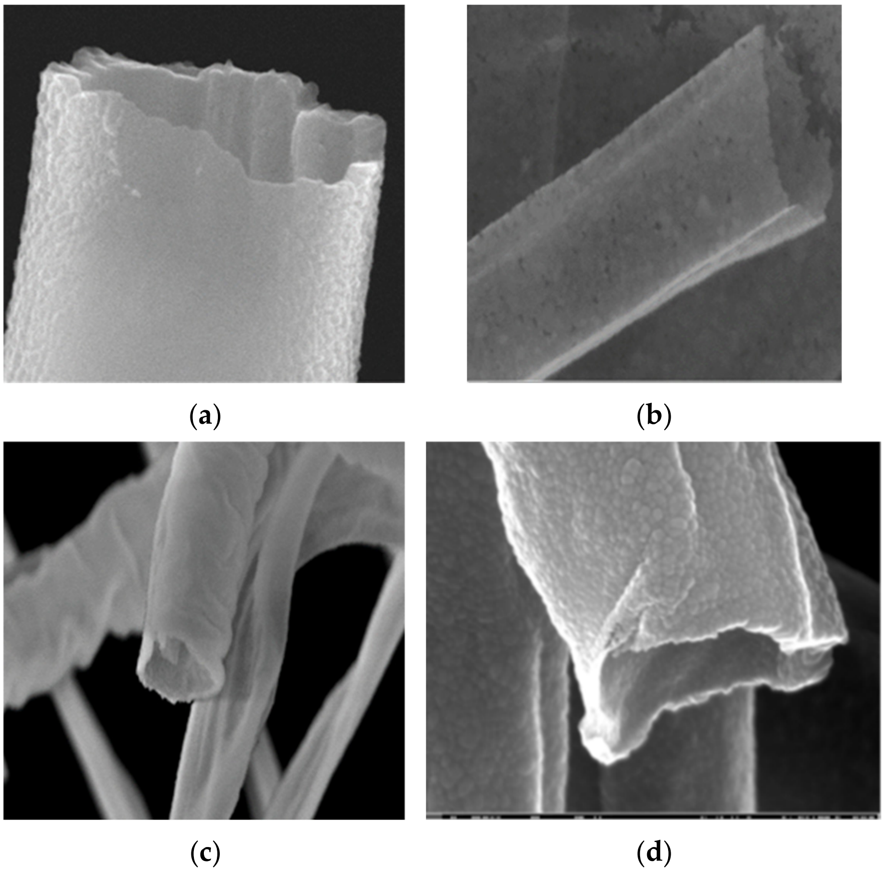
(**a**) (**b**) (**c**) (**d**)

Figure 1. Images of nanotubes of (**a**) TiO_2, (**b**) Al_2O_3, (**c**) Y_2O_3, and (**d**) ZnO (200 k magnitude, with image processing) [38,42,46,47].

The subsequent method of obtaining hybrid nanostructures from ceramic nanotubes and conducting polymers, including emeraldine-based polyaniline (PANI:EB), poly(3, 4-ethylenedioxy-thiophene)-polystyrene sulfonate (PEDOT:PSS), and poly(3-hexylthiophene) (P3HT), involved drop-casting. Five specimens from each category were prepared to evaluate the technological feasibility. The technological procedure used the solutions detailed in [46,47]. In each case, 240 µL of each polymer solution was deposited onto ceramic nanotubes (SiO_2/Si substrate) using Pasteur pipettes. Each solvent was evaporated for 60 min under vacuum conditions, using a Pfeiffer vacuum pump connected to a desiccator [42]. Figures 2–5 show the deposition process of PANI:EB, PEDOT:PSS, and P3HT on TiO_2, Al_2O_3, Y_2O_3, and ZnO nanotubes, respectively. A different adhesion of the polymers to the nanotubes can be briefly observed. As for the nanotubes, Al_2O_3 and Y_2O_3 are applied over a large surface. As for the polymers, it happens that PEDOT:PSS covers the nanotube network with a thicker film; for Al_2O_3, Y_2O_3, and ZnO, the ceramic nanotubes are completely covered, which raises questions about their influence on the new hybrid structure in terms of surface parameters.

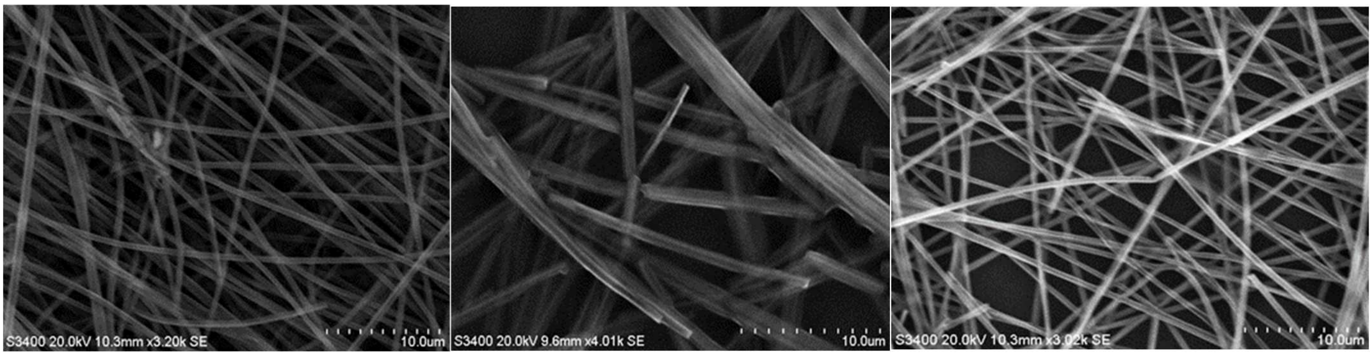

(**a**) (**b**) (**c**)

Figure 2. Deposition of (**a**) PANI:EB, (**b**) PEDOT:PSS, and (**c**) P3HT upon TiO_2 nanotubes.

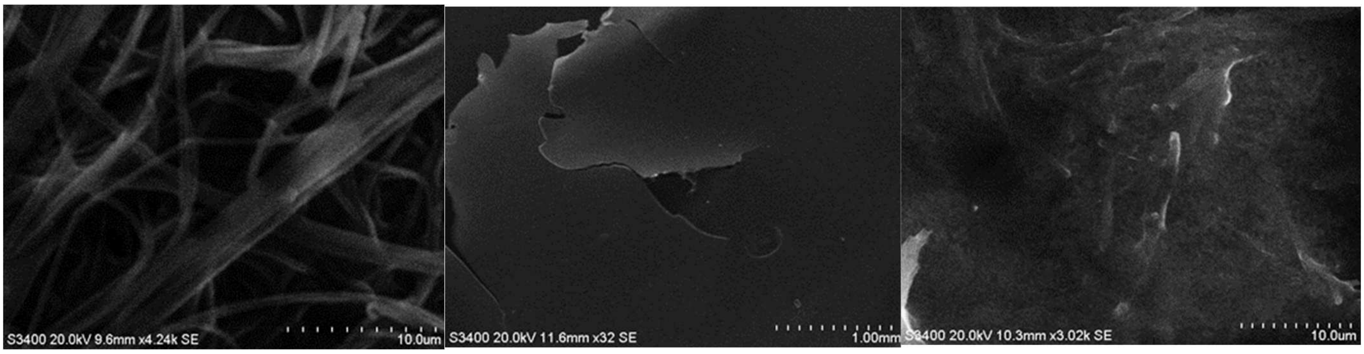

(**a**) (**b**) (**c**)

Figure 3. Deposition of (**a**) PANI:EB, (**b**) PEDO:PSS, and (**c**) P3HT upon Al_2O_3 nanotubes.

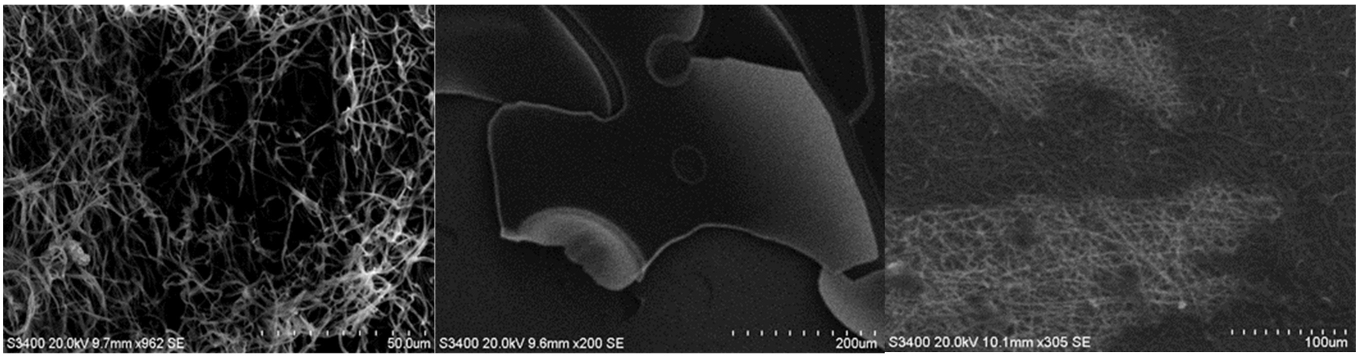

(**a**) (**b**) (**c**)

Figure 4. Deposition of (**a**) PANI:EB, (**b**) PEDO:PSS, and (**c**) P3HT upon Y_2O_3 nanotubes.

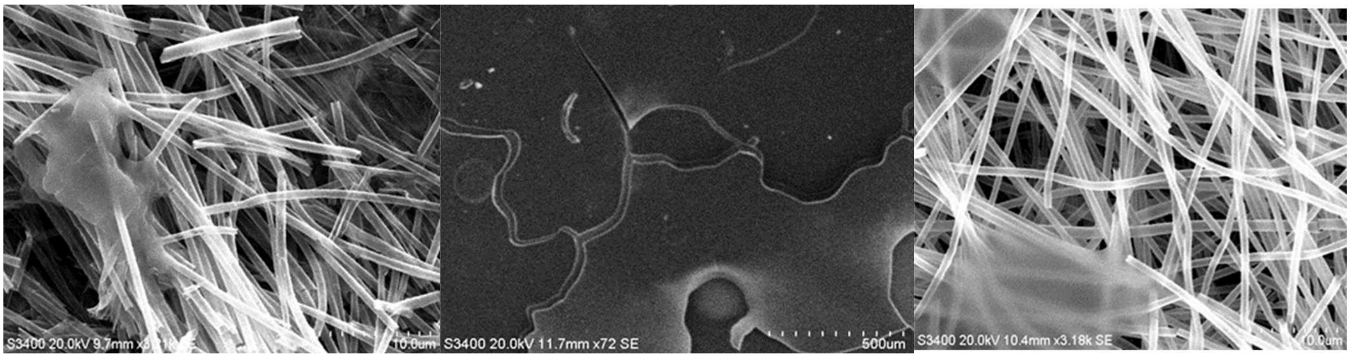

(**a**) (**b**) (**c**)

Figure 5. Deposition of (**a**) PANI:EB, (**b**) PEDOT:PSS, and (**c**) P3HT upon ZnO nanotubes.

However, these initial findings may change significantly upon deposition of gold nanoparticles. A more comprehensive examination of the gold nanotube composites will discuss X-ray photoelectron spectroscopy (XPS), energy-dispersive X-ray spectroscopy (EDS), and scanning electron microscopy (SEM) analysis later, which could clarify the structure of these materials. The conductive polymer composites with ceramic nanotubes were further immersed in a dilute $HAuCl_4$/2-propanol solution (0.001 M) by dip-coating and allowed to stand for 24 h. After impregnation, the samples were dried in an oven at 150 °C with an Ar flow (100 sccm) for 30 min. The samples were then cooled to room temperature in an argon flow. Au nanoparticles with an average size of 100 nm were quasi-uniformly integrated into the hybrid structures. This approach to obtain specific Au nanoparticles from a highly dilute 132 $HAuCl_4$ solution on the polymer substrate, heated from room temperature to just over one hundred degrees Celsius, is similar to those presented in [48,49]. However, the approach described in this paper involves immersing the polymer film in a significantly dilute 135 $HAuCl_4$ solution, which helps in the generation and almost uniform spreading of gold nanoparticles over larger regions, an essential factor for the development of more sensitive electrochemical sensors.

2.2. Characterization Equipment

X-ray photoelectron spectroscopy (XPS) and energy-dispersive X-ray spectroscopy (EDS) were performed with an AXIS Supra+ unit (Kratos Analytical Ltd., Manchester, UK). Measurement conditions: anode Al (1486.74 eV), U = 15.kV, I = 15 mA, P = 225 W, p SAC 5 X 10-9 mbar, parameter spectrum recording line extended spectrum E start (eV) 1200, Estop (eV) −5, step (eV) 0.1, pass energy (eV) 140, number of passes 1.

Scanning electron microscopy (SEM) provides insights into the surface structure and was conducted using Lyra III XMU equipment from TESCAN GROUP a.s., located in Brno-Kohoutovice, Czech Republic.

Atomic force microscopy (AFM) delivers high-resolution visuals to measure surface roughness at the nanoscale. AFM was performed with a Dimension Edge device from Bruker (Billerica, MA, USA) for optical applications. The roughness evaluation was performed with the following derived parameters: Ra = Roughness Average; Rsk = Skewness; RMS = Root Mean Square Roughness; Rku = Kurtosis. Average roughness values are given for four scanned areas on each sample type. The evaluation of the surface roughness parameters was conducted in accordance with ISO 21920-2:2021 [45,50].

3. Results and Discussion

3.1. XPS and EDS Analysis

The novel XPS analysis of Y_2O_3–nanotube composites is presented in Figure 6, and the rest of the XPS analyses for the other nanotube composites, are included as Supplementary Materials Figures S1–S3 [46,47].

In all these figures that highlight the samples of ceramic nanotube-P3HT, the elements recognized on the basis of the general spectrum include oxygen, carbon, sulfur, and silicon, as well as the metal that produces the specific oxide of the corresponding nanotubes. Regarding all figures that highlight the ceramic nanotube-PANI:EB, elements recognized on the basis of the general spectrum include sodium, oxygen, nitrogen, carbon, and sulfur, as well as the metal that produces the specific oxide of the corresponding nanotubes. In figures that highlight the samples of ceramic nanotube-PEDOT:PSS, the elements recognized on the general spectrum include sodium, oxygen, nitrogen, carbon, and sulfur, as well as the metal responsible for the specific oxide of the corresponding nanotubes. X-ray analysis with energy dispersion was performed to evaluate the amount of gold. Identifying the differences between the intensities of the golden peaks in the images has proven to be quite difficult, because the amount of gold is very low compared to the ceramic nanotube-conductive polymers, and there are few variations in the gold atomic percentage, which makes the images inconclusive. On the other hand, due to the low EDS signal of tiny nanoparticles, the time of detection for these particles has become longer, and other elements, such as Cu, Fe, and Co (probably related to sample supports, etc.), appeared in images, diminishing the quality of the golden peaks.

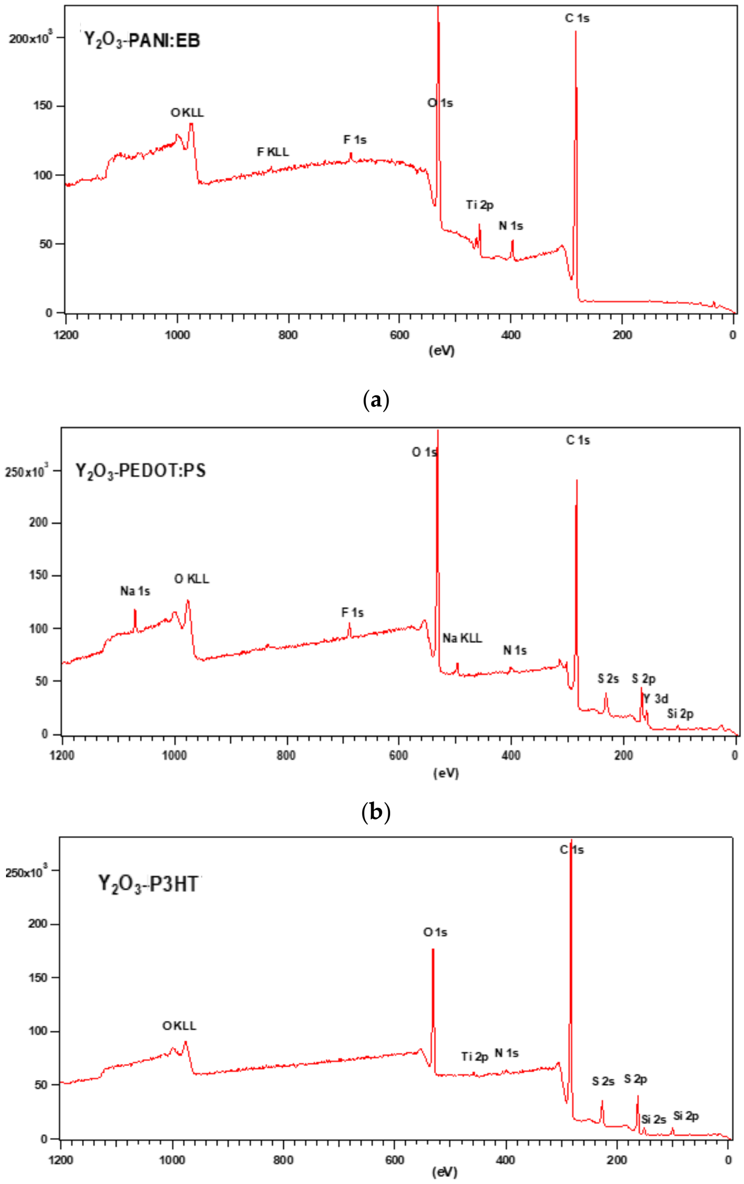

(**a**)

(**b**)

(**c**)

Figure 6. XPS analysis of Y_2O_3 nanotube composites with (**a**) PANI:EB, (**b**) PEDOT:PSS, and (**c**) P3HT.

However, the EDS analysis, being a semi-quantitative technique, has satisfactorily validated the inclusion of gold nanoparticles in hybrid structures. Table 1 illustrates the weight percentage of gold nanoparticles in hybrid samples, but the accuracy of these data is limited under the previously mentioned experimental conditions. Because the metals responsible for the specific oxides of the respective nanotubes have different atomic masses, a direct comparison for all the hybrid structures collectively is not feasible. Conversely, a clear comparison can be made for hybrid structures containing the same nanotube in terms of polymer activity. A clearer understanding of the effect of Au nanoparticles upon hybrid structures can be related to SEM analysis. No special chemical interaction between ceramic nanotubes and conductive polymers was observed, nor between gold nanoparticles and polymers. The XPS/EDS analysis indicates that the attachment of the gold nanoparticles to the ceramic nanotubes and conductive polymers is a primary physical interface interaction, in accordance with the comparable results reported in [51,52].

Table 1. Weight percentages of gold nanoparticles in the hybrid structures.

Hybrid Structure	Weight Percentage (%)
TiO_2/PANI:EB+Au	1.66 ± 0.14
TiO_2/PEDOT:PSS+Au	0.64 ± 0.11
TiO_2/P3HT+Au	0.92 ± 0.08
Al_2O_3/PANI:EB+Au	0.22 ± 0.04
Al_2O_3/PEDOT:PSS+Au	1.78 ± 0.16
Al_2O_3/P3HT+Au	0.89 ± 0.12
Y_2O_3/PANI:EB+Au	0.37 ± 0.07
Y_2O_3/PEDOT:PSS+Au	0.54 ± 0.08
Y_2O_3/P3HT+Au	0.26 ± 0.03
ZnO/PANI:EB+Au	0.46 ± 0.09
ZnO/PEDOT:PSS+Au	1.85 ± 0.18
ZnO/P3HT+Au	1.66 ± 0.15

An analysis of the data in Table 1 must be made in relation with each ceramic nanotube type, one the one hand, and related to the influence of the conducting polymer used, on the other hand. The highest values of the weight percentage of gold nanoparticles in the hybrid structures were found for ZnO/PEDOT:PSS+Au (1.85%), Al_2O_3/PEDOT:PSS+Au (1.78%), and, respectively, TiO_2/PANI:EB+Au and ZnO/P3HT+Au (both with 1.66%). Even if the lowest values of weight percentage of gold nanoparticles were found for Y_2O_3 nanotubes in all their configurations, we need to note that a direct comparison cannot be made because the atomic mass of Y is much larger comparing to, e.g., Al, or Ti. For this reason, a more reliable comparison might be made between, e.g., Zn and Y nanotubes with different conducting polymers, due to closer atomic mass values. In this peculiar case, it is clear that ZnO nanotubes may offer a better affinity compared to Y_2O_3 nanotubes. As regards the influence of the conducting polymers, PEDOT:PSS and P3HT seem to positively influence the gold affinity to the hybrid structures in most of the cases.

3.2. SEM Analysis

The SEM imagery in Figure 7 for TiO_2/PANI:EB composites containing Au shows that most gold nanoparticles adhere to the TiO_2 nanotubes, while others occupy the spaces between the ceramic nanotubes. Gold was frequently found in the form of individual nanoparticles, but some agglomerations may be noted at µm size, up to 30 µm. The distribution of gold nanoparticles is quite uniform, and the quantity is significant.

In the SEM imagery in Figure 8 of TiO_2/PEDOT:PSS composites with Au, it can be seen that gold was rarely found as nanoparticles, but more frequently in the form of clusters with dimensions of tens of micrometers. It seems that the gold-occupied region is clearly limited, and hence the gold particles to be adhered are few.

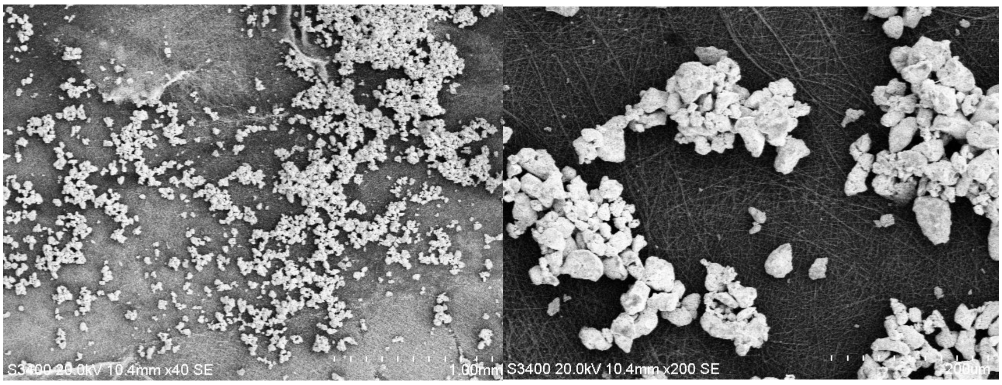

Figure 7. SEM images of TiO_2/PANI:EB composites with Au [46].

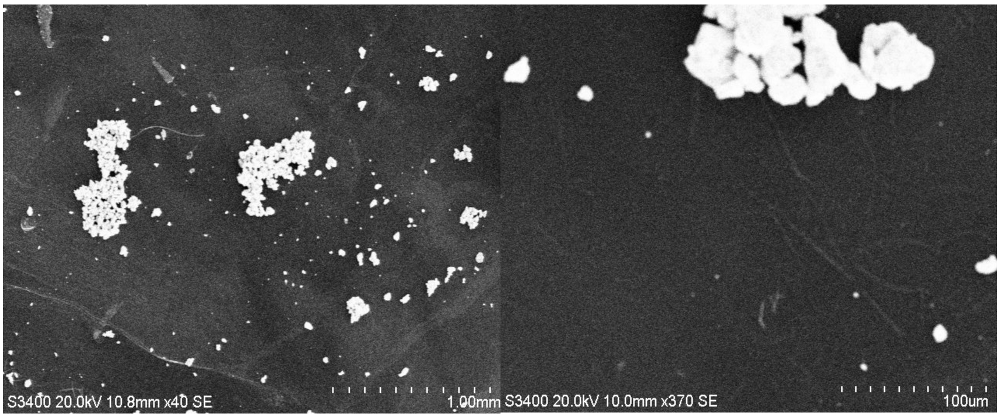

Figure 8. SEM images of TiO_2/PEDOT:PSS composites with Au [46].

In the SEM imagery in Figure 9 of TiO_2/P3HT composites with Au, it is clear that gold appears mainly in the form of nanoparticles, although some groups are visible at µm size, mainly up to 20 µm. The morphology resembles the composites of TiO_2/PANI:EB with Au, but the surface covered with gold seems to be somewhat smaller.

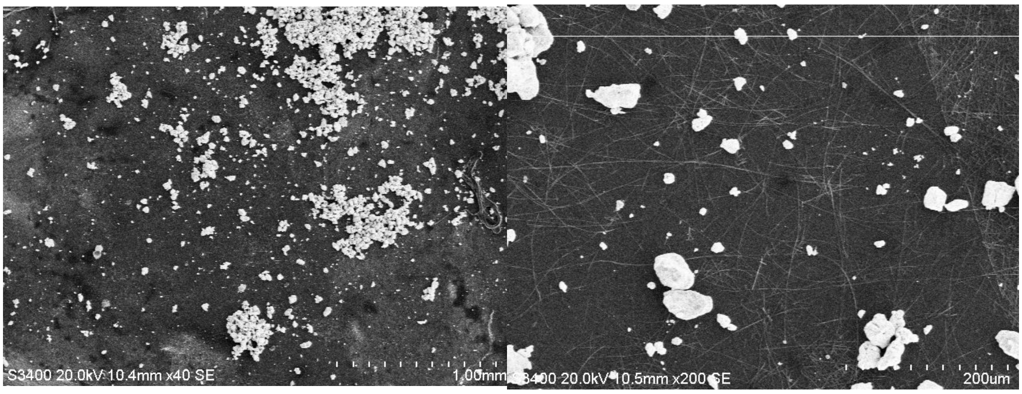

Figure 9. SEM images of TiO_2/P3HT composites with Au.

The SEM imagery in Figure 10 for Al_2O_3/PANI:EB composites with gold shows that very few gold nanoparticles adhere individually to nanotubes. The distribution of gold nanoparticles is rare and the quantity is insignificant, with the adhesion effect being minimal.

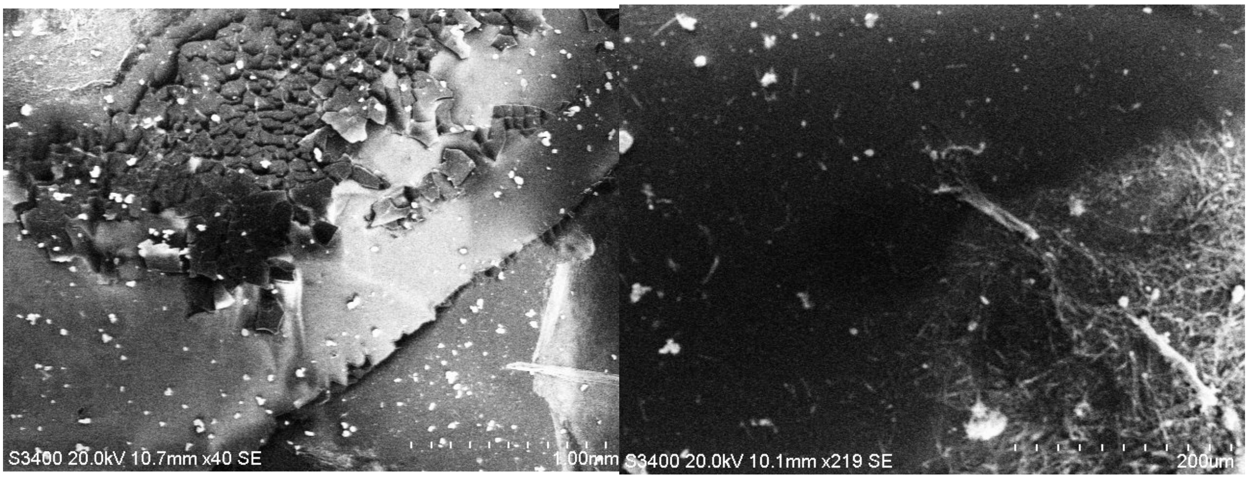

Figure 10. SEM images of Al_2O_3/PANI:EB composites with Au.

From the SEM imagery in Figure 11 for Al_2O_3/PEDOT:PSS composites containing Au, it is clear that the gold was mainly deposited in the form of small clusters of 10–30 μm dimensions, presenting an almost uniform distribution of these clusters on the surface of the composite. The morphology resembles the composites of TiO_2/PANI:EB with Au, but, here being predominantly clusters, the surface covered with gold seems larger, and the amount of gold is clearly larger.

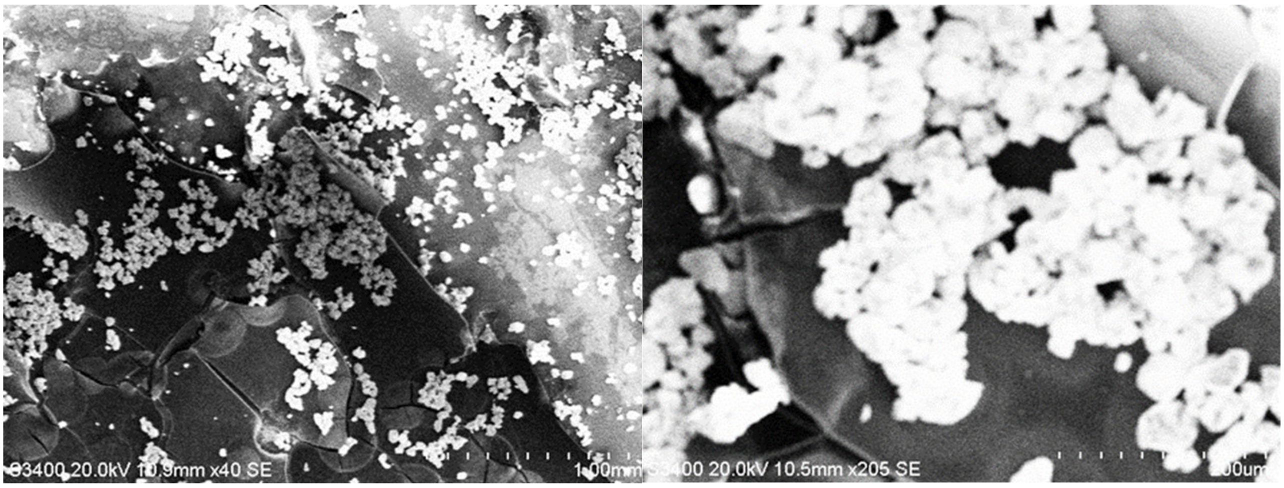

Figure 11. SEM images of Al_2O_3/PEDOT:PSS composites with Au.

From the SEM imagery in Figure 12 for Al_2O_3/P3HT composites with Au, it is clear that gold has mainly been deposited in the form of separate nanoparticles, although a few small groups can be observed at μm size, mainly up to 10 μm, presenting an almost uniform distribution on the entire surface of the composite. The structure looks similar to the TiO_2/P3HT composite with Au, in terms of the region covered with gold and the amount of gold deposited, which are comparable.

The SEM imagery in Figure 13 for Y_2O_3/PANI:EB composites containing Au shows that gold is deposited mainly in the form of individual nanoparticles on nanotubes, while other particles fall into the spaces between ceramic nanotubes.

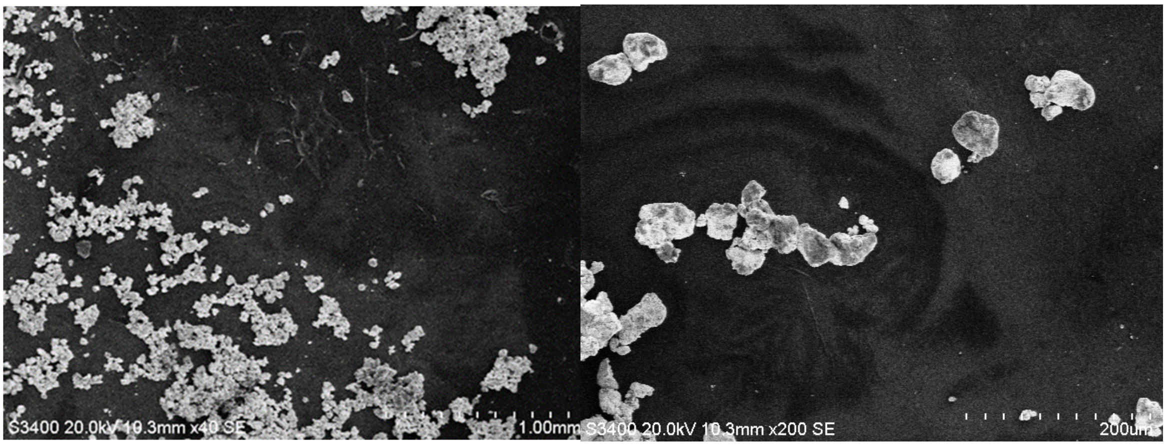

Figure 12. SEM images of Al_2O_3/P3HT composites with Au.

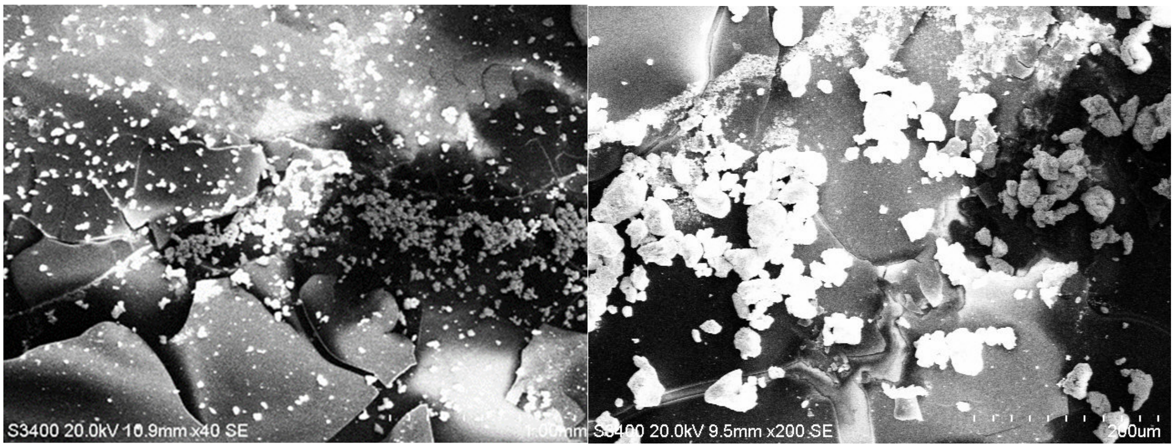

Figure 13. SEM images of Y_2O_3/PANI:EB composites with Au.

The distribution of gold nanoparticles is relatively uniform, even if some small groups of nanoparticles up to 10 μm can be observed, but the quantity is significant.

From the SEM imagery in Figure 14 for Y_2O_3/PEDOT:PSS composites containing Au, it can be seen that the morphology resembles the structure of the composites Y_2O_3/PANI-EB with Au, presenting a significant number of dispersed nanoparticles and small clusters on and among nanotubes. However, here, the gold region and the amount of gold are larger.

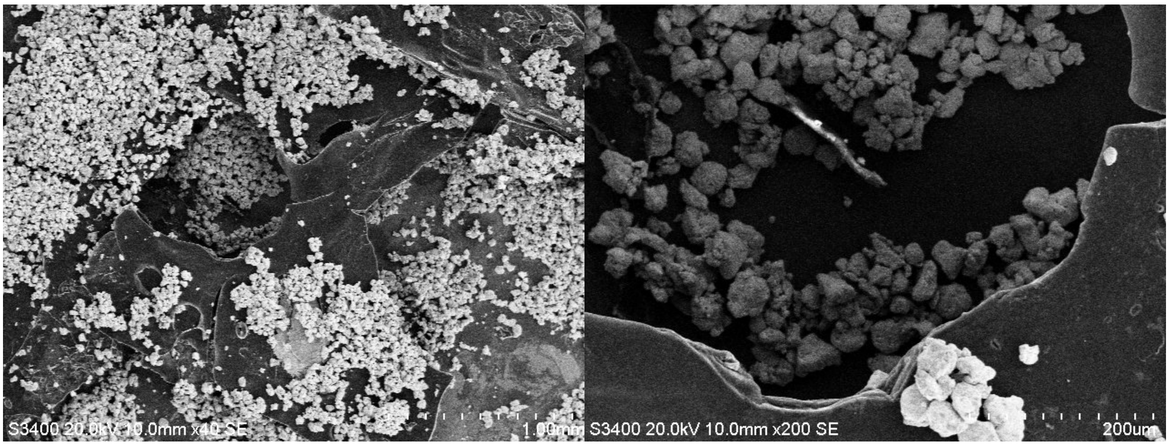

Figure 14. SEM images of Y_2O_3/PEDOT:PSS composites with Au.

From the SEM imagery in Figure 15 for Y_2O_3/P3HT composites containing Au, it is observed that gold was mainly deposited in the form of nanoparticles and very small clusters, ideally filling the spaces between nanotubes. The morphology shows a very uniform distribution of nanoparticles. However, the amount of gold is quite minimal and the surface covered with gold seems significantly reduced comparing to the precedent cases.

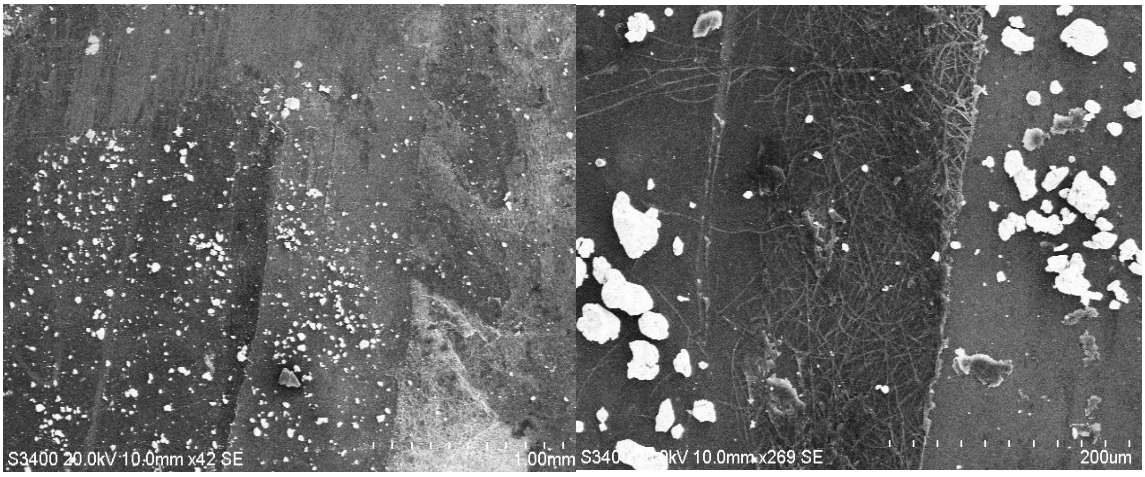

Figure 15. SEM images of Y_2O_3/P3HT composites with Au.

The SEM imagery in Figure 16 for ZnO/PANI:EB composites containing Au shows that gold appeared primarily in the form of nanoparticles with deep penetration within the structure. The distribution of gold nanoparticles is quite uniform, although in a few cases, some larger groups of nanoparticles may be identified. The gold quantity is less significant, suggesting a weak attraction of gold nanoparticles to this composite structure.

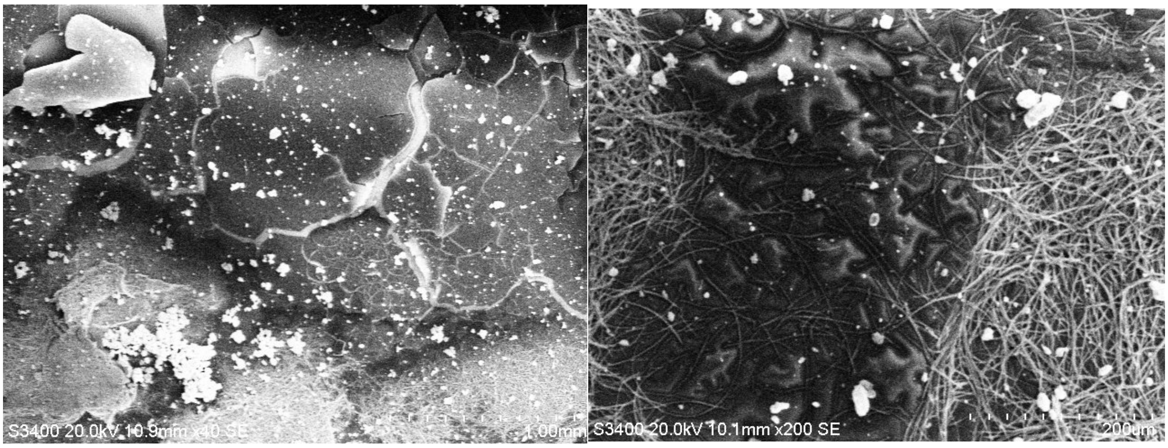

Figure 16. SEM images of ZnO/PANI:EB composites with Au.

The SEM imagery in Figure 17 for ZnO/PEDOT:PSS composites containing Au may resemble Al_2O_3/PEDOT:PSS composites that include Au, presenting a substantial amount of gold deposited in the form of individual nanoparticles and small clusters of 10–30 µm dimensions, with a rather uniform distribution on the surface. The surface containing gold and the amount of gold are significantly larger comparing to the ZnO/PANI:EB structure.

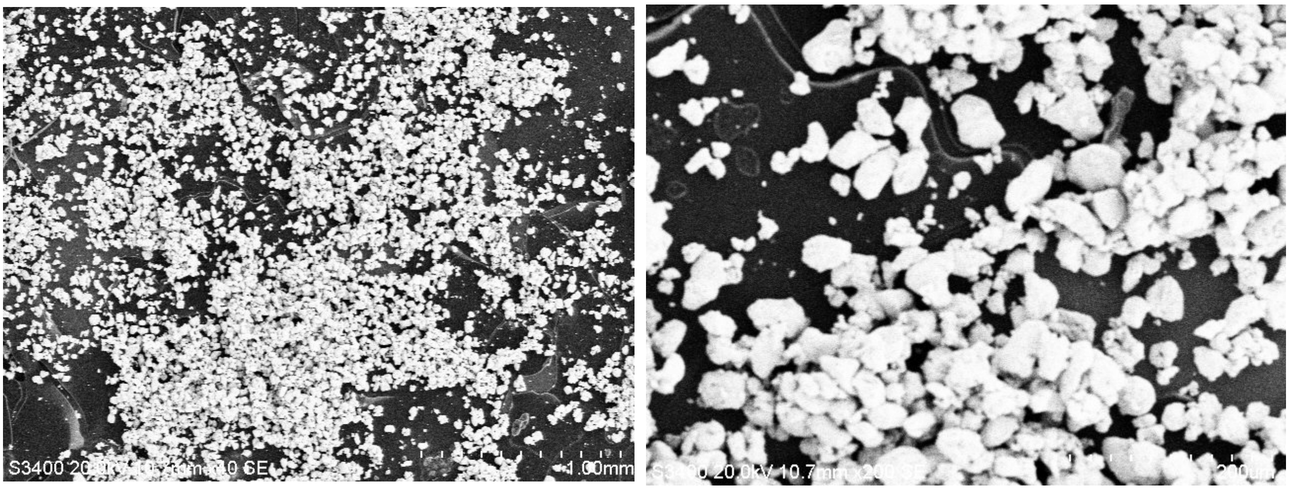

Figure 17. SEM images of ZnO/PEDOT:PSS composites with Au.

From the SEM imagery in Figure 18 for ZnO/P3HT composites containing Au, it turns out that gold was deposited in the form of nanoparticles and small clusters up to 10 µm dimensions that crowd and even overlap. There is a larger region full of gold, but there are also some sections with smaller gold deposition, which makes the general distribution to be seen uneven, presenting a combination of two distinct areas. The amount of gold seems to be considerable, comparable to ZnO/PEDOT:PSS composites.

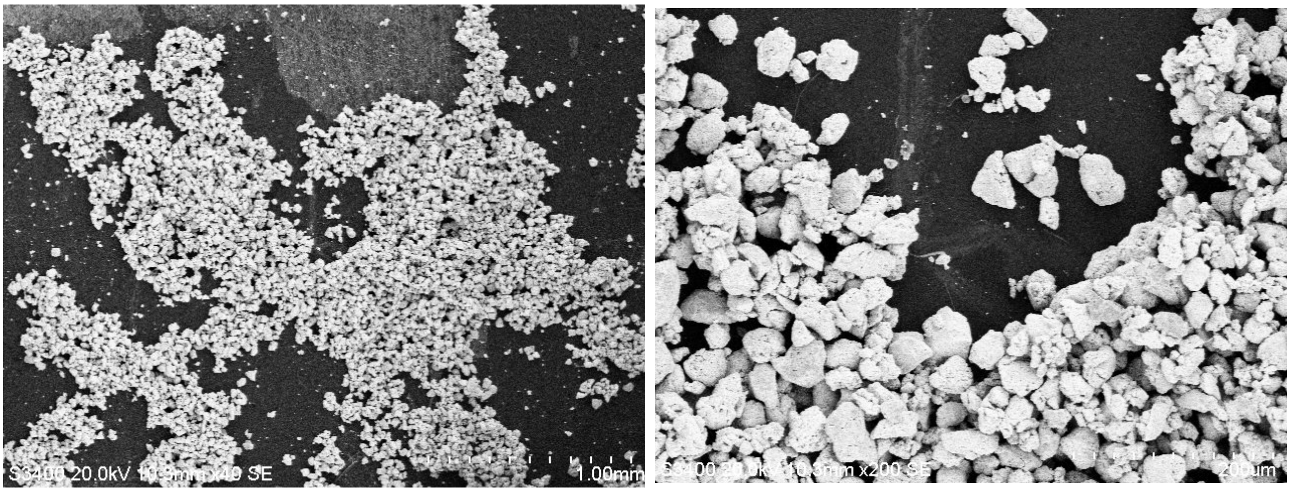

Figure 18. SEM images of ZnO/P3HT composites with Au.

In general, it is believed that the deposition of gold nanoparticles on composite sites can mainly be influenced by the type of polymer, as well as its deposition on ceramic nanotubes, which was firstly observed when analyzing Figures 2–5. However, when evaluating the integration of gold nanoparticles with polymers and ceramic nanotubes through EDS and SEM, it becomes clear that the interaction between gold and polymer structures varies significantly, contrary to expectations, and the gold nanotubes and architecture of the surface are distinctly affected by the ceramic nanotubes.

An overview of the distribution of gold nanoparticles upon the surface of hybrid composites of ceramic nanotubes and conducting polymers is briefly given in Table 2.

Table 2. Type of distribution and area covered with gold nanoparticles in the hybrid structures.

Hybrid Structure	Type of Distribution/Area Covered
TiO_2/PANI:EB+Au	uniform/large
TiO_2/PEDOT:PSS+Au	uniform/very reduced
TiO_2/P3HT+Au	uniform/reduced
Al_2O_3/PANI:EB+Au	uneven/very reduced
Al_2O_3/PEDOT:PSS+Au	uniform/very large
Al_2O_3/P3HT+Au	uniform/large
Y_2O_3/PANI:EB+Au	uniform/quite large
Y_2O_3/PEDOT:PSS+Au	uniform/large
Y_2O_3/P3HT+Au	uniform/very reduced
ZnO/PANI:EB+Au	uniform/reduced
ZnO/PEDOT:PSS+Au	uniform/very large
ZnO/P3HT+Au	relatively uniform/very large

The analysis of the SEM images and the conclusions from Table 2 generally correspond to the results presented in Table 1. Based on the interpretation of the SEM images, the PANI:EB polymer has shown the most relevant physical connection with the gold nanoparticles, mainly when the nanotubes of TiO_2 and Y_2O_3 are present, while the bond is weak with other nanotubes. The PEDOT:PSS polymer has demonstrated a more significant deposition of gold nanoparticles only in connection with Al_2O_3, Y_2O_3, and ZnO. Finally, regarding the P3HT polymer, the gold deposition is considerable only in relation to TiO_2, Al_2O_3, and ZnO, while in the case of Y_2O_3, the effect is minimal.

However, the optimal placement of gold nanoparticles on the surface of ceramic nanotubes and their content are essential requirements for improving the sensitivity of the material for sensory purposes, but this effect must be increased by the special structure from the surface of the material, which will be evaluated below by the AFM analysis.

3.3. AFM Analysis

The AFM optical analysis shows the size of the grains, their distribution on the surface, and the general roughness of the surface. The qualitative correlation between the shape and density of the peaks and the values of the roughness parameters are described by Figure 19 and explained in [45]. Essentially, the ideal architecture for efficient sensors would be the one with a higher value of the roughness of the peaks (RA), more sharpened peaks (characterized by RSK), and a reasonably consistent distribution of peaks and valleys, with a greater uniformity of their form and a lower asymmetry (characterized by RKU).

The optical analysis was performed up to 100 nm size, and the individual particles of gold can be easily identified as dispersion and dimensions, in most cases confirming their individual dimensions of 100 nm. It is clear that gold was deposited in both nanoparticles and clusters, affected by the affinity of the polymer used as a deposition support and also related to the spatial structure of a ceramic nanotube–conductor polymer before being subjected to coverage with Au nanoparticles by the dip-coating method.

It should be noted that in the case of the optical analysis at 100× and 500×, specifically the images shown in Figures 20–31, these images completely validate the technical discussion presented in the SEM images of homologous structures shown in Figures 7–18, regarding the formation and distribution of nanoparticles on the surfaces of the composites.

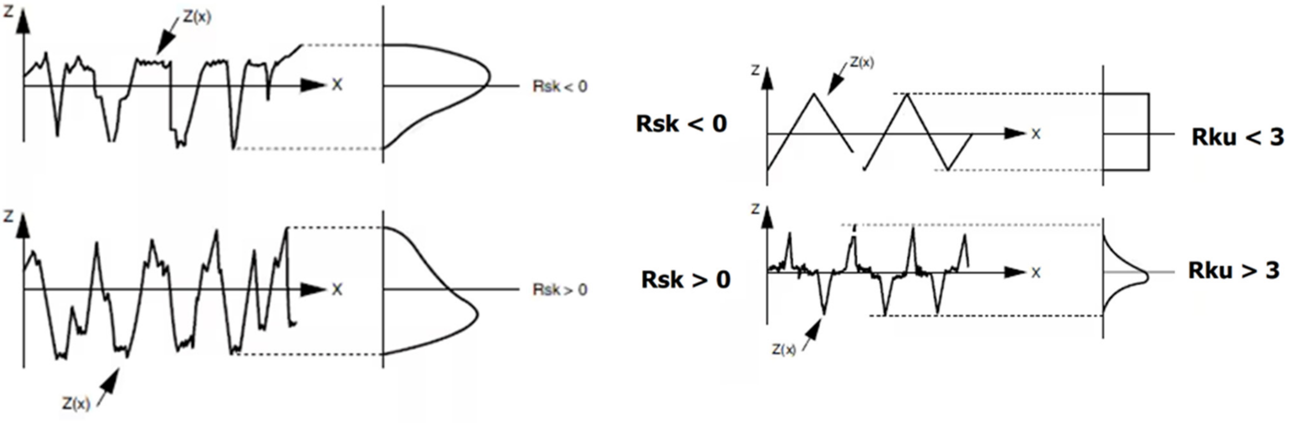

Figure 19. Roughness parameters values vs. peak shape and density [45].

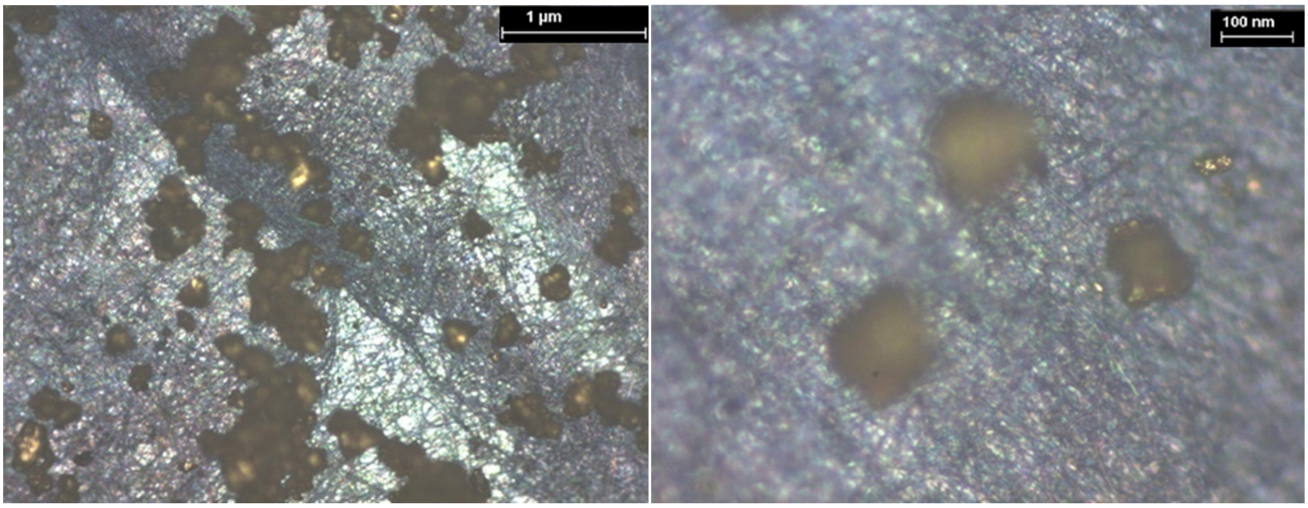

(**a**) (**b**)

Figure 20. Optical analysis at (**a**) 100× and (**b**) 500× of TiO_2/PANI:EB composites with Au.

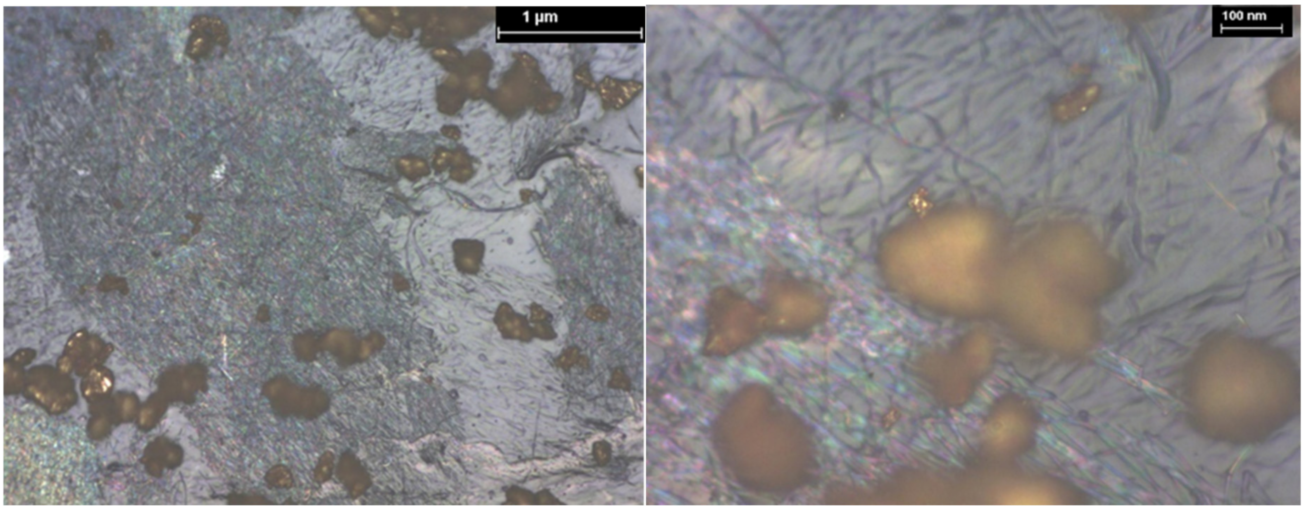

(**a**) (**b**)

Figure 21. Optical analysis at (**a**) 100× and (**b**) 500× of TiO_2/PEDOT:PSS composites with Au.

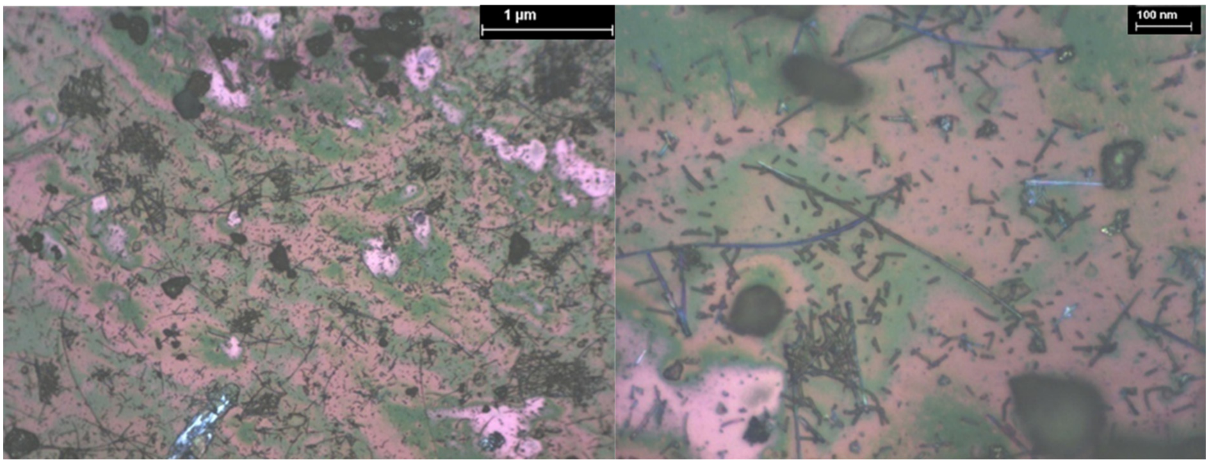

(**a**) (**b**)

Figure 22. Optical analysis at (**a**) 100× and (**b**) 500× of TiO_2/P3HT composites with Au.

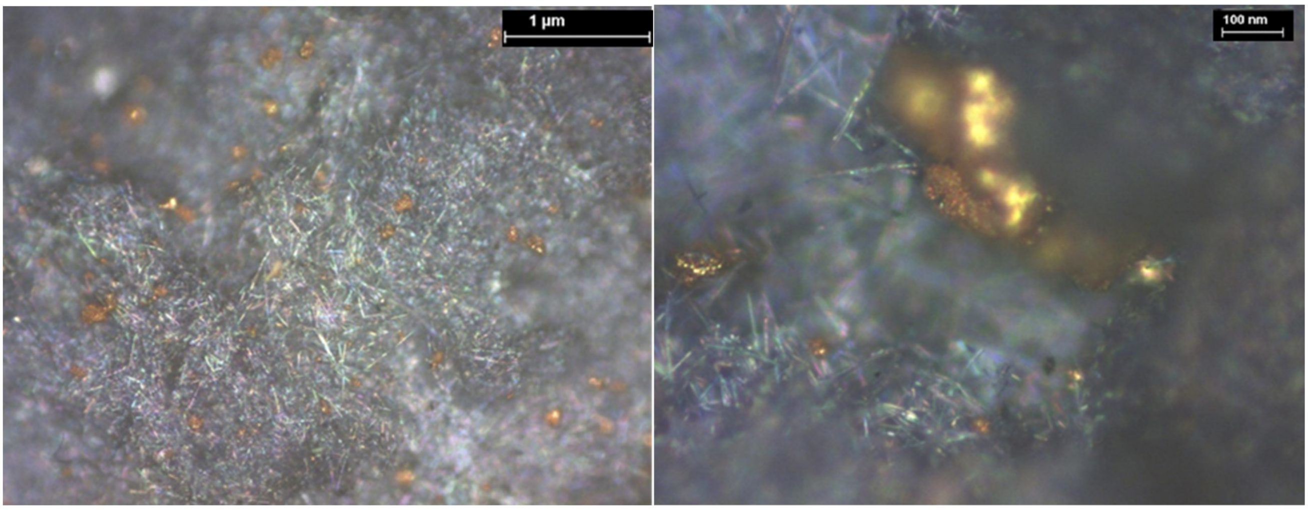

(**a**) (**b**)

Figure 23. Optical analysis at (**a**) 100× and (**b**) 500× of Al_2O_3/PANI:EB composites with Au.

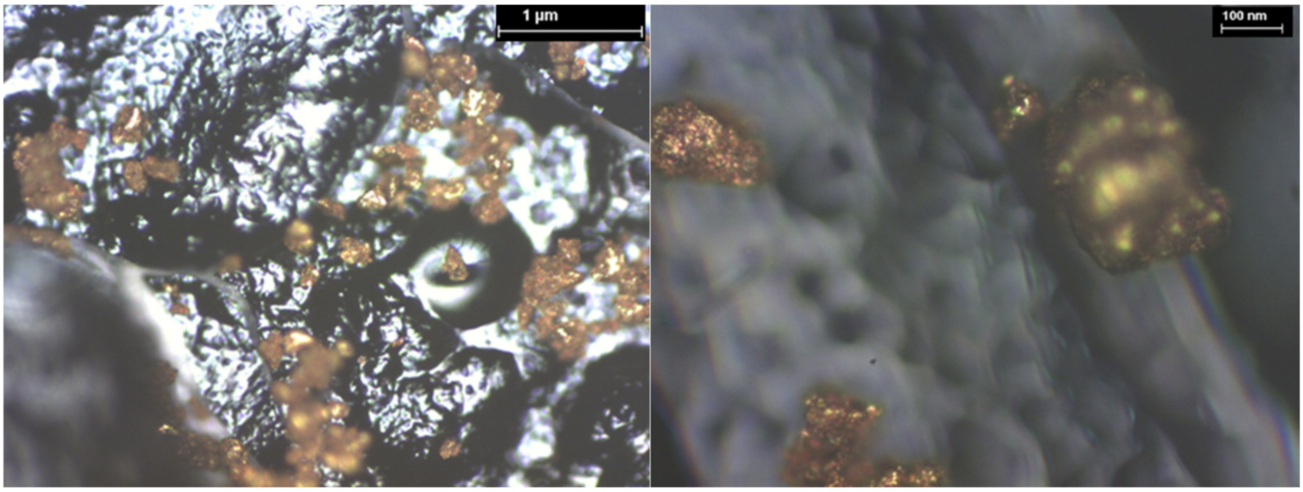

(**a**) (**b**)

Figure 24. Optical analysis at (**a**) 100× and (**b**) 500× of Al_2O_3/PEDOT:PSS composites with Au.

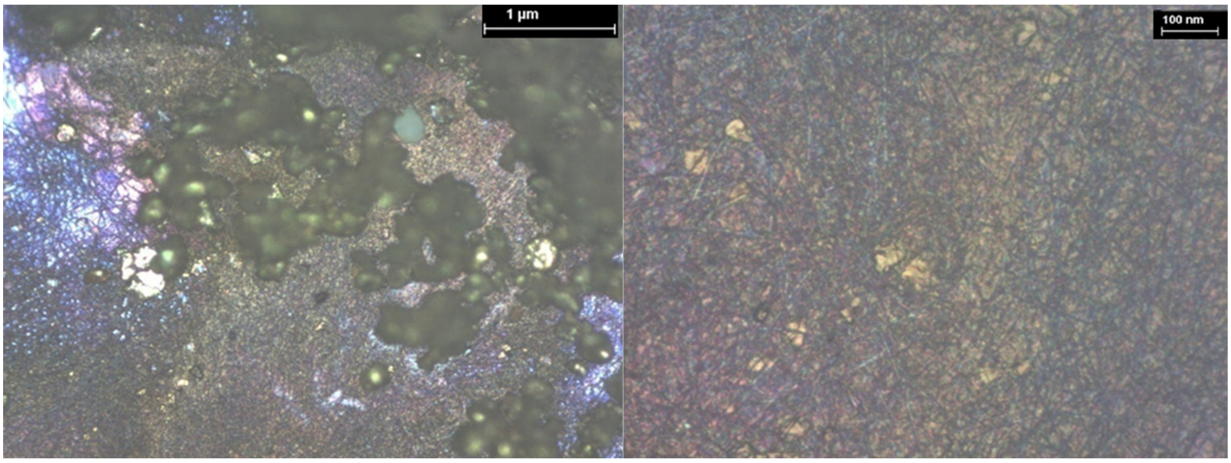

(**a**) (**b**)

Figure 25. Optical analysis at (**a**) 100× and (**b**) 500× of Al_2O_3/P3HT composites with Au.

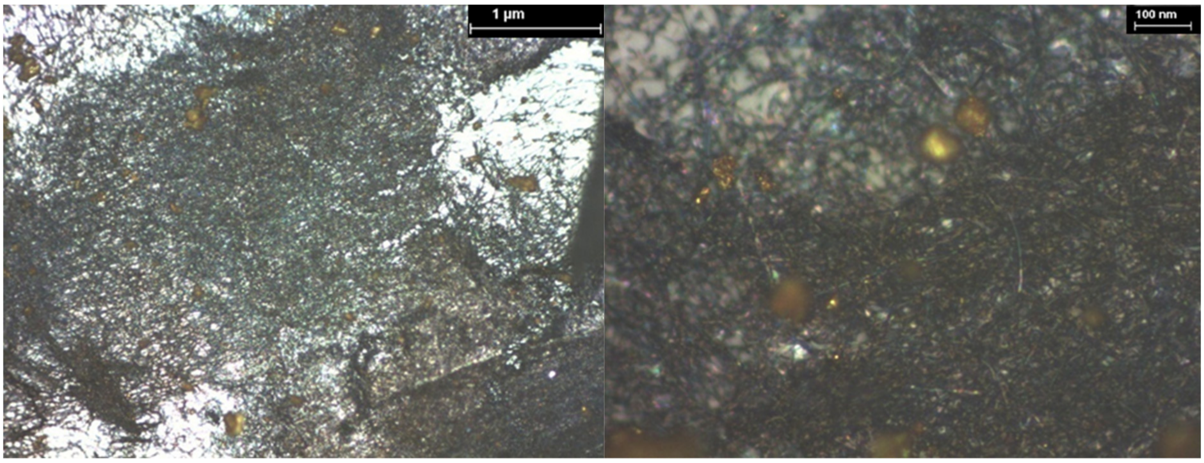

(**a**) (**b**)

Figure 26. Optical analysis at (**a**) 100× and (**b**) 500× of Y_2O_3/PANI:EB composites with Au.

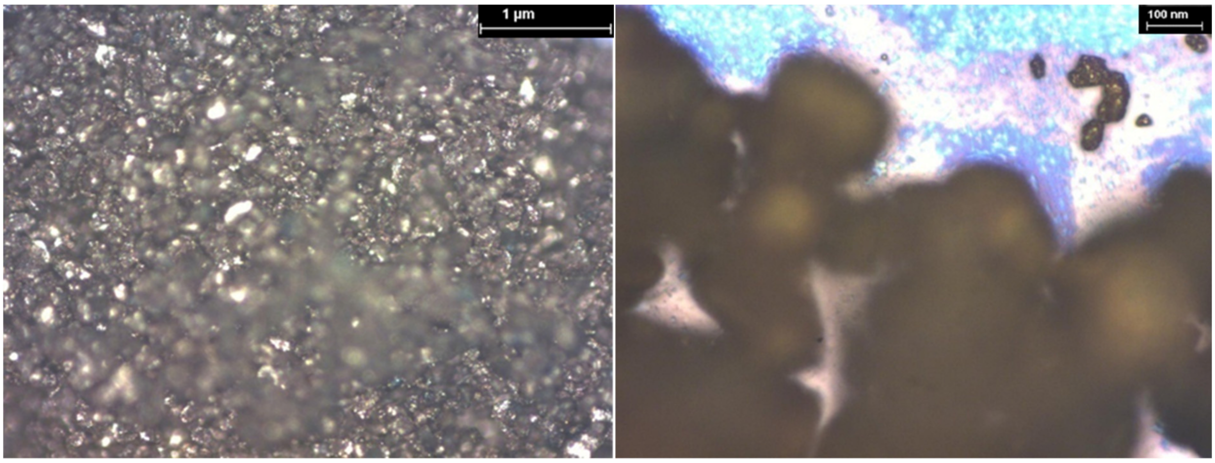

(**a**) (**b**)

Figure 27. Optical analysis at (**a**) 100× and (**b**) 500× of Y_2O_3/PEDOT:PSS composites with Au.

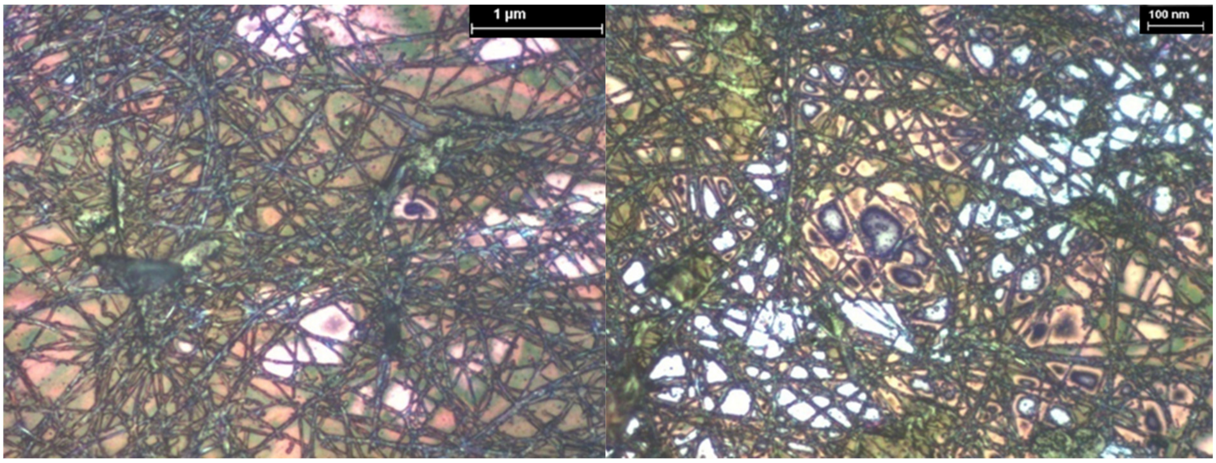

(**a**) (**b**)

Figure 28. Optical analysis at (**a**) 100× and (**b**) 500× of Y_2O_3/P3HT composites with Au.

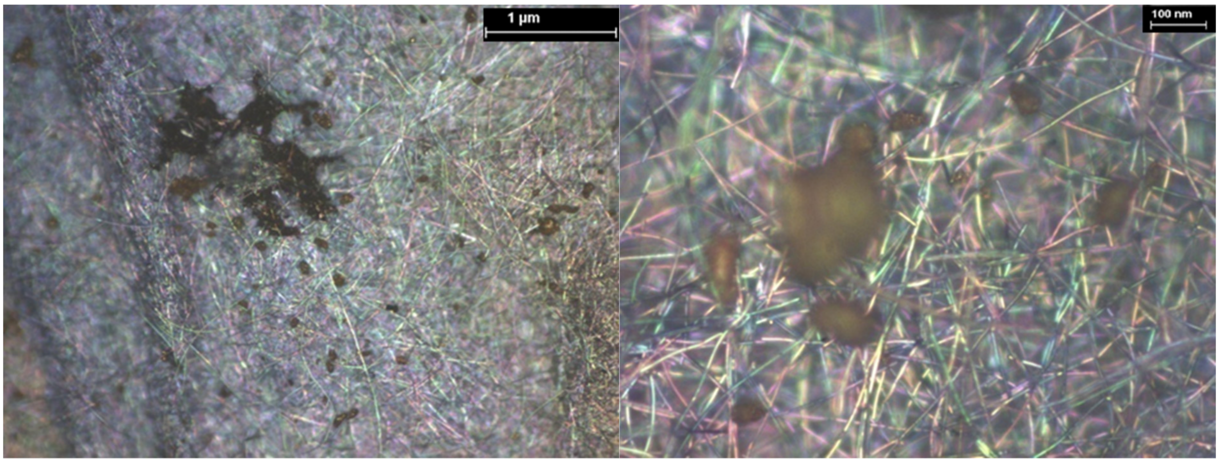

(**a**) (**b**)

Figure 29. Optical analysis at (**a**) 100× and (**b**) 500× of ZnO/PANI-EB composites with Au.

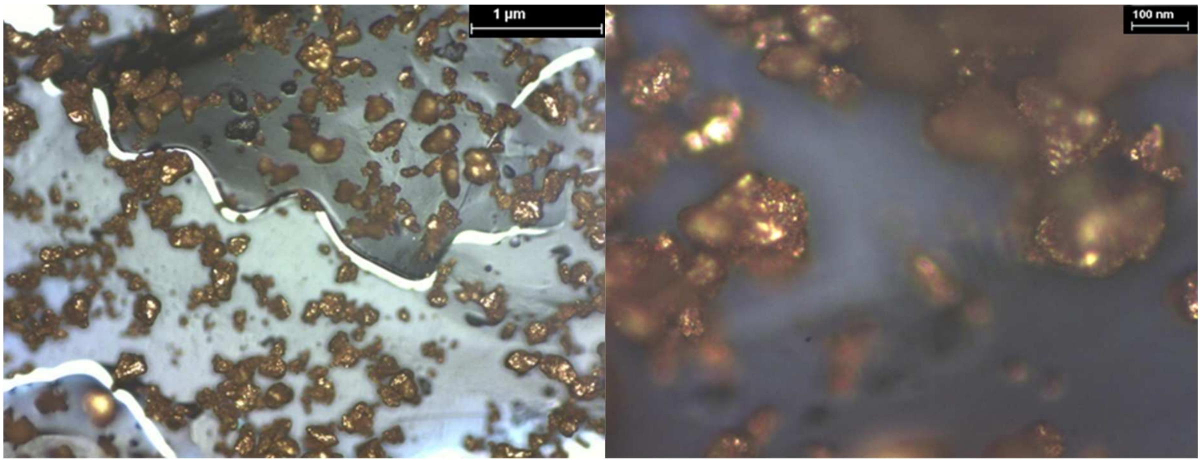

(**a**) (**b**)

Figure 30. Optical analysis at (**a**) 100× and (**b**) 500× of ZnO/PEDOT:PSS composites with Au.

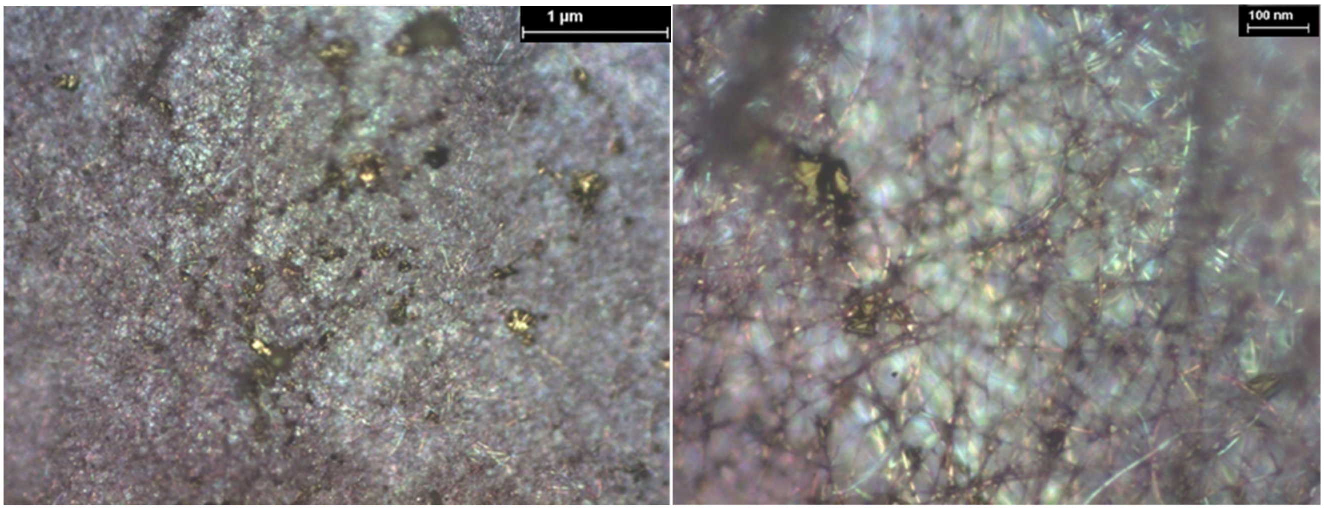

(**a**) (**b**)

Figure 31. Optical analysis at (**a**) 100× and (**b**) 500× of ZnO/P3HT composites with Au.

As regards the profile lines of TiO_2/PANI:EB composites with Au, shown in Figure 32 [46], the formation of layers is predominantly characterized by peaks and not by valleys, demonstrated also by the Rsk value; the Rku value is close to 3, indicating an almost Gaussian distribution of the grains. The grain size is exceptionally large, at about 3.7 µm.

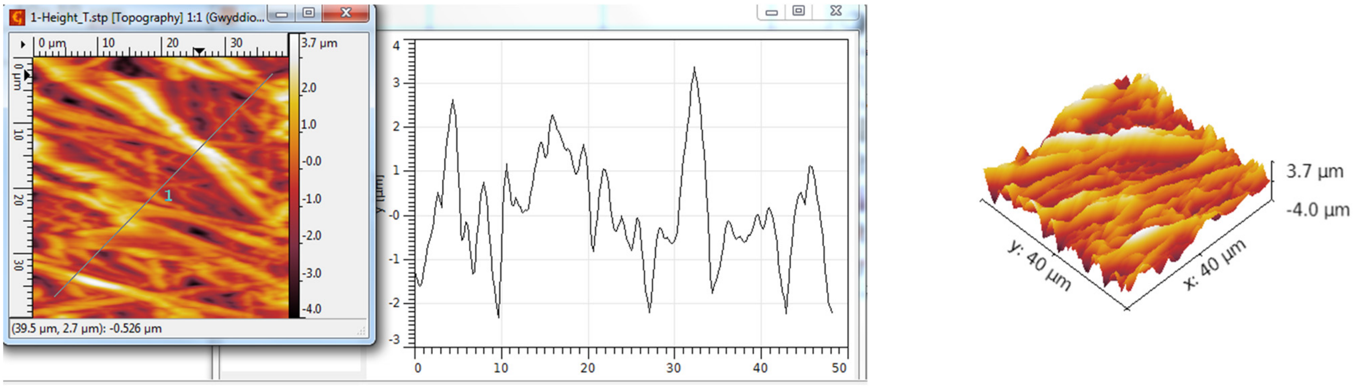

Figure 32. AFM topographic 2D and 3D images and profile lines—TiO_2/PANI:EB composites with Au [46].

As regards the profile lines of TiO_2/PEDOT:PSS composites with Au, shown in Figure 33 [46], the formation of layers is predominantly characterized by large valleys and fewer peaks. The Rsk value increases beyond 4, indicating a distinct asymmetry, and indicating that the inclusion of gold nanoparticles in the clusters significantly changes the initial structure. The size of the granules is very low, at about 0.6 µm, which raises doubts about the effectiveness of such a structure for detection applications.

As regards the profile lines of TiO_2/P3HT composites with Au, shown in Figure 34 [46], the grains are generally arranged in smaller clusters, and the formation of layers is predominantly characterized by peaks and not by valleys (Rsk = 0.42); the Rku values remained near 3, indicating that the grain distribution is symmetrical.

In the case of Al_2O_3 PANI:EB composites with Au, shown in Figure 35, the structure resembles that of TiO_2/PANI:EB composites with Au, but the Rsk value is reduced, which means a balance between peaks and valleys.

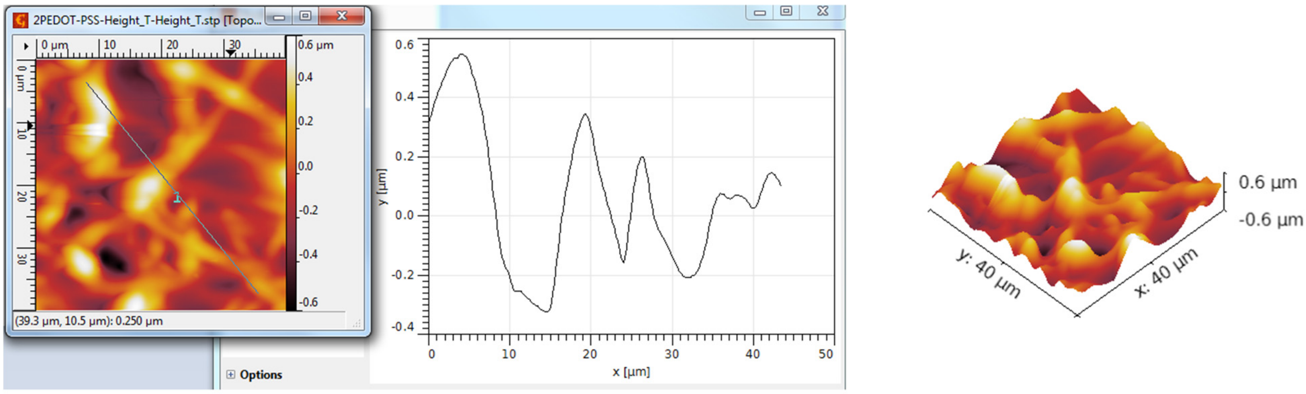

Figure 33. AFM topographic 2D and 3D images and profile lines—TiO_2/PEDOT:PSS composites with Au [46].

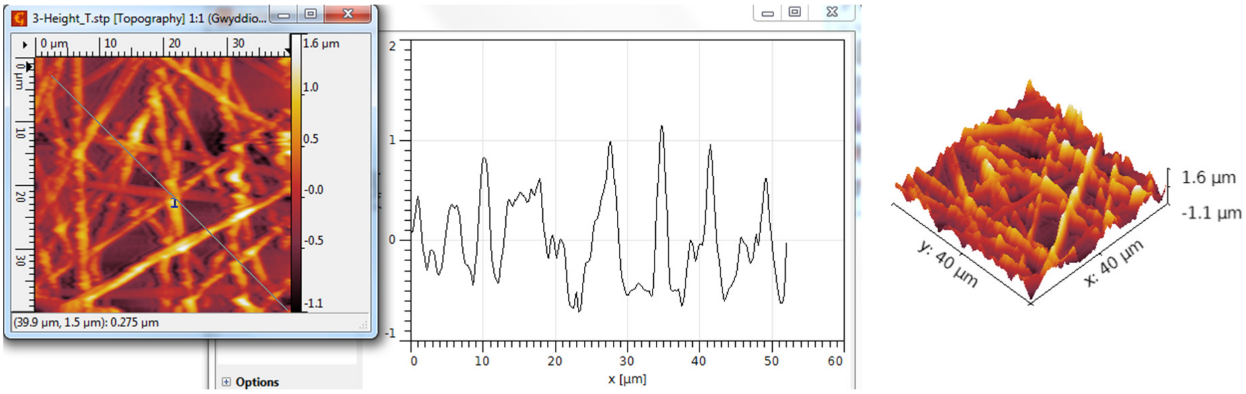

Figure 34. AFM topographic 2D and 3D images and profile lines—TiO_2/P3HT composites with Au [46].

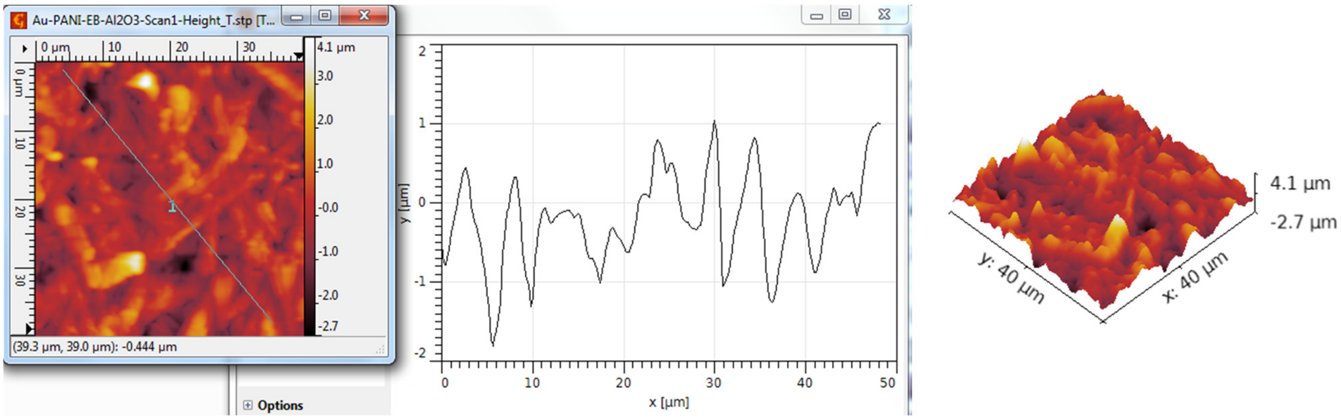

Figure 35. AFM topographic 2D and 3D images and profile lines—Al_2O_3/PANI-EB composites with Au.

The Rku value is close to 3, indicating an almost Gaussian distribution of the grains. The grain size is remarkably large, at about 4.1 µm.

In the case of Al_2O_3/PEDOT:PSS composites with Au, shown in Figure 36, the surface architecture resembles that of TiO_2/PEDOT:PSS composites with Au. The formation of layers presents larger valleys and shorter peaks, of about 0.51 µm; the Rku value exceeds 3, indicating a beginning of asymmetry.

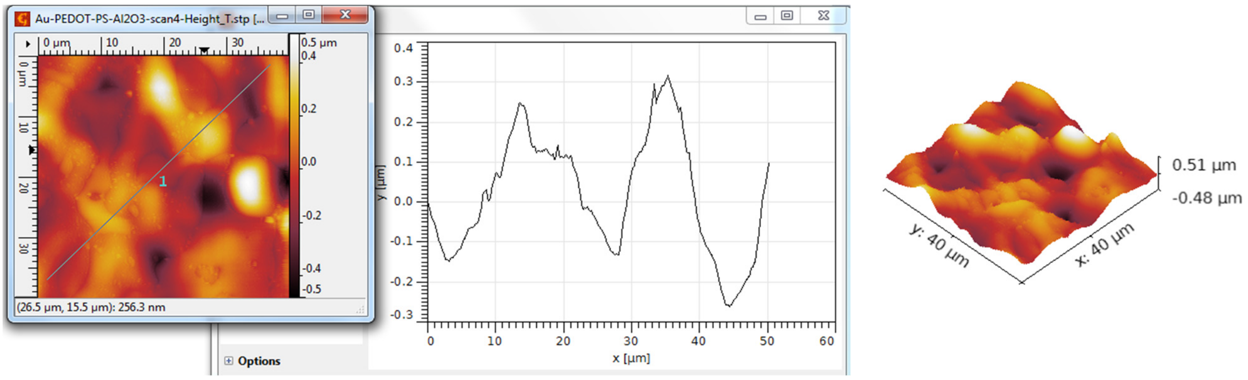

Figure 36. AFM topographic 2D and 3D images and profile lines—Al_2O_3/PEDOT:PSS composites with Au.

As regards the architecture of Al_2O_3/P3HT composites with Au, shown in Figure 37, small, but very crowded peaks are obtained, of about 0.62 µm. Their distribution has highlighted a balance between peaks and valleys (RSK near zero), remaining uniform despite the larger roughness (the RKU parameter is close to 3).

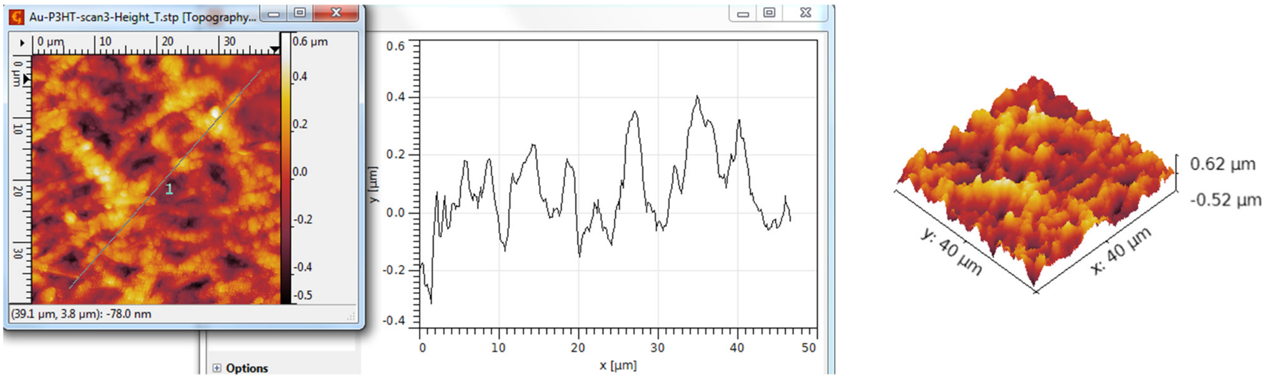

Figure 37. AFM topographic 2D and 3D images and profile lines—Al_2O_3/P3HT composites with Au.

The topography of Y_2O_3/PANI:EB composites with Au is presented in Figure 38. Both Rku and Rsk are higher, indicating the formation of layers with larger valleys and irregular peaks, with a clear asymmetry. Although the architecture seems chaotic, the size of the granules, of about 2.1 µm, encourages us to consider this structure to still be suitable for detection applications.

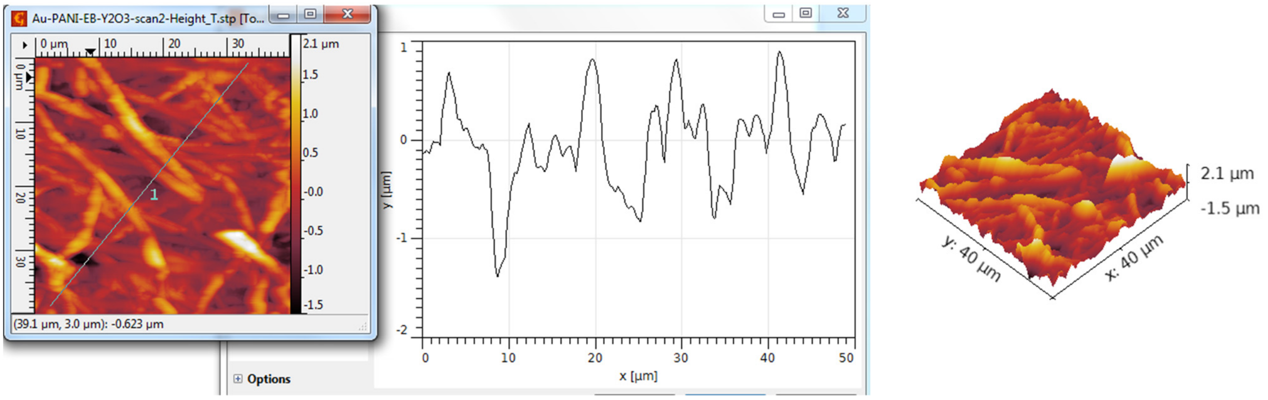

Figure 38. AFM topographic 2D and 3D images and profile lines—Y_2O_3/PANI:EB composites with Au.

As regards the architecture of Y_2O_3/PEDOT:PSS with Au, shown in Figure 39, we observed the creation of layers that have chaotic dimensions and the spread of peaks and valleys, a fact also demonstrated by the significantly increased values of RKU and RSK. The unique presence of certain peaks with higher values, such as 1.9 µm, does not indicate an advantage when taking into account increased asymmetry.

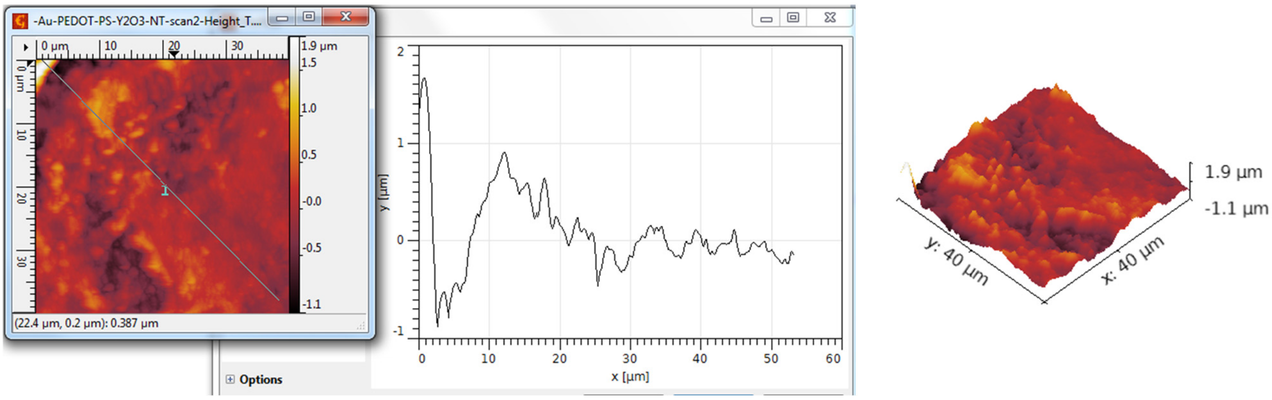

Figure 39. AFM topographic 2D and 3D images and profile lines—Y_2O_3/PEDOT:PSS composites with Au.

As regards the architecture of Y_2O_3/P3HT composites with Au, shown in Figure 40, it resembles that of Y_2O_3/PEDOT:PSS with Au. We observed the creation of layers that have chaotic dimensions of narrower peaks and valleys, which was demonstrated by the much higher values of RKU and RSK. In conclusion, the composites made up of Y_2O_3 nanotubes, regardless of the conductive polymer used, despite their exotic presence, do not offer the essential properties for an efficient electrode, first of all because of their accentuated asymmetry.

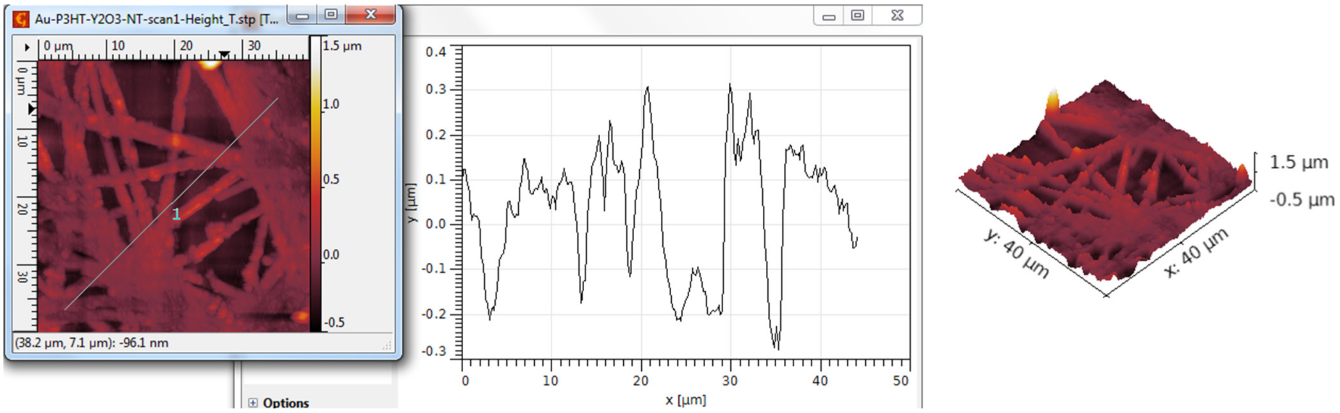

Figure 40. AFM topographic 2D and 3D images and profile lines—Y_2O_3/P3HT composites with Au.

As regards the topography of ZnO/PANI:EB composites with Au, shown in Figure 41 it resembles that of Y_2O_3/PANI:EB composites with Au. Both Rku and Rsk are higher, indicating the formation of layers with irregular tips and valleys, with a clear asymmetry. Although the architecture seems disorganized, the existence of a substantial number of high peaks, with a notable size of the granules of about 5.1 µm, motivates us to consider this framework to still be suitable for sensing applications.

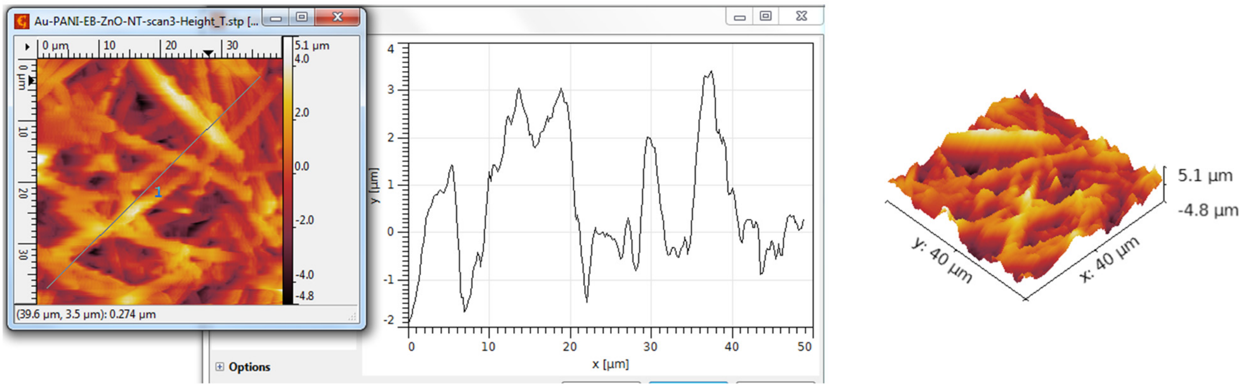

Figure 41. AFM topographic 2D and 3D images and profile lines—ZnO/PANI:EB composites with Au.

As regards the architecture of ZnO/PEDOT:PSS composites with Au, shown in Figure 42, it resembles that of Al_2O_3/P3HT composites with Au, presenting very crowded, irregular peaks, separated by very narrow valleys. The RKU and RSK values are both raised. There are still a few granules with a size of 1.7 µm, but not enough to justify the use of this structure for detection purposes.

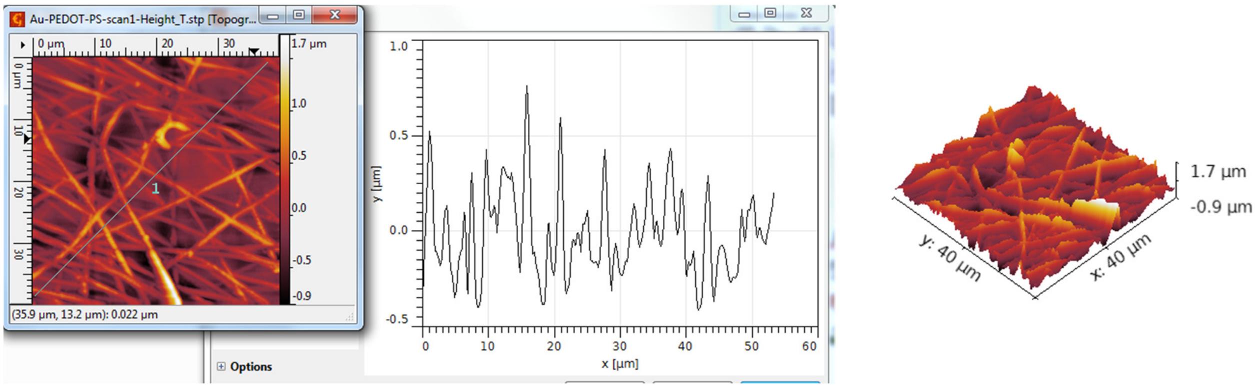

Figure 42. AFM topographic 2D and 3D images and profile lines—ZnO/PEDOT:PSS composites with Au.

Finally, the architecture of ZnO/P3HT composites with Au is presented in Figure 43. There are significant grains of larger size, of 4.5 µm. The Rku value is slightly negative, confirming the presence of the balance between the narrow peaks and larger valleys. The Rku value is close to 3, indicating an almost Gaussian distribution of the grains.

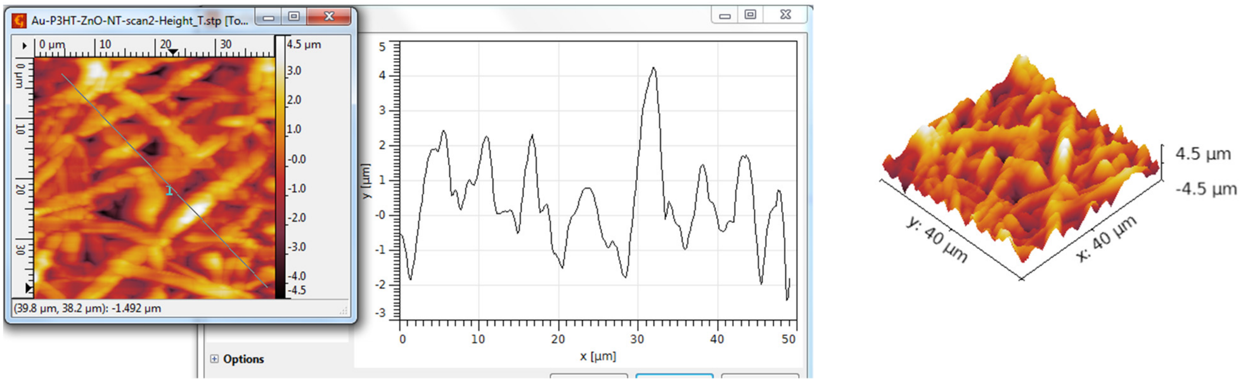

Figure 43. AFM Topographic 2D and 3D images and profile lines—ZnO/P3HT composites with Au.

In summary, the composites created from ZnO nanotubes, irrespective of the conducting polymer used, could offer the necessary characteristics for a highly effective electrode, mainly due to their reasonable symmetry and higher grain values, presenting an almost Gaussian distribution.

Table 3 presents a comparison of the roughness parameters of the composites with gold nanoparticles discussed above and those before incorporating gold nanoparticles by the immersion coverage method, in accordance with the results presented in [46,47] for different ceramic nanotubes while using the same polymers.

Table 3. Average roughness parameters determined by AFM lines—scanned area 40 × 40 µm.

Scanned Material	Ra (nm)	RMS (nm)	R_{Sk}	R_{Ku}
TiO_2 nanotubes—PANI:EB	715	947	−0.18	4.04
TiO_2 nanotubes—PANI:EB/Au	948	1197	0.28	2.97
TiO_2 nanotubes—PEDOT:PSS	105	131	−0.15	3.04
TiO_2 nanotubes—PEDOT:PSS/Au	79	107	0.16	4.42
TiO_2 nanotubes—P3HT	298	362	0.17	2.53
TiO_2 nanotubes—P3HT/Au	341	420	0.42	2.89
Al_2O_3 nanotubes—PANI:EB—	702	881	0.08	3.44
Al_2O_3 nanotubes—PANI:EB/Au	1053	1321	0.03	3.12
Al_2O_3 nanotubes—PEDOT:PSS	194	273	0.16	3.97
Al_2O_3 nanotubes—PEDOT:PSS/Au	115	146	0.22	3.35
Al_2O_3 nanotubes—P3HT	123	198	0.62	5.86
Al_2O_3 nanotubes—P3HT/Au	134	166	0.02	2.69
Y_2O_3 nanotubes—PANI:EB	362	464	0.31	3.16
Y_2O_3 nanotubes—PANI:EB/Au	368	465	0.50	3.84
Y_2O_3 nanotubes—PEDOT:PSS	218	289	0.34	5.44
Y_2O_3 nanotubes—PEDOT:PSS/Au	269	342	0.74	4.21
Y_2O_3 nanotubes—P3HT	132	166	0.46	5.86
Y_2O_3 nanotubes—P3HT/Au	172	257	0.52	7.11
ZnO nanotubes—PANI:EB	1086	1413	−0.21	2.89
ZnO nanotubes—PANI:EB/Au	1134	1418	−0.11	2.87
ZnO nanotubes—PEDOT:PSS	196	265	−0.13	4.23
ZnO nanotubes—PEDOT:PSS/Au	332	466	0.46	5.86
ZnO nanotubes—P3HT	956	1191	−0.15	2.88
ZnO nanotubes—P3HT/Au	1042	1327	−0.03	3.29

According to the explanations offered in [45], the ideal values in our scenario would be, preferably, RA > 400 nm to ensure a better fixation of the target molecules, RSK > 0, but not excessively high, ideally below 0.5 for a reasonable acuity of the peaks and valleys, and RKU around 3, to provide a dense structure (almost Gaussian distribution). When comparing the roughness parameters obtained from the AFM composite lines before and after incorporating the gold nanoparticles, in Table 2, it was constantly observed that there is a relatively uniform distribution of granules.

However, the addition of gold nanoparticles changes the structure of the surface and forces the original granules to form spaces that allow the gold particles to penetrate deeper and accumulate in small groups, which leads to a slight increase in the size of the granules (higher Ra values) and to a local sharpening of the peaks (increased RSK values). In many cases, the shape of the peaks compared to that of the valleys is improved by narrowing the RKU value to about 3, indicating a transition from a random distribution to an almost Gaussian granule distribution, confirming that the presence of metal nanoparticles contributes to the uniformity of structures.

In our scenario, the optimal structures regarding the ideal roughness parameters are TiO_2 nanotubes—PANI:EB/Au; TiO_2 nanotubes—P3HT/Au; Al_2O_3 nanotubes—PANI:EB/Au; Y_2O_3 nanotubes—PANI:EB/Au; ZnO nanotubes—PANI:EB/Au; and ZnO nanotubes—P3HT/Au. The greatest Ra value was attained in order by ZnO nanotubes—PANI:EB/Au; ZnO nanotubes—P3HT/Au; and finally, TiO_2 nanotubes—PANI:EB/Au. It seems that the disposition of the nanotubes of ZnO within composites results in the highest Ra values, followed by Al_2O_3 nanotubes. As for conductive polymers' contribution, PANI:EB showed the greatest significance for all composites, with P3HT being relevant in some other instances. In the particular situation of the PANI:EB polymer, although the incorporation of gold nanoparticles may not be particularly significant, such as in relation with Al_2O_3, Y_2O_3, and ZnO (according to SEM images and the interpretation in Tables 1 and 2), their presence greatly improves the surface structure of materials. Given the conditions regarding the surface architecture, the use of PEDOT:PSS for detection electrodes is not recommended, even if, in some cases, the inclusion of gold nanoparticles together with, for example, Al_2O_3 and ZnO could be relevant, but without great improvement.

In applications that involve electrochemical reactions, the area responsible for transferring charge from species in solution is the crucial factor, and this is why AFM analysis may be more relevant than EDS or SEM analysis. This is based on the efficiency with which the electrolyte reaches the pores and is affected by the texture of the surface. The region available for an electrochemical reaction, the EASA, frequently varies with the geometric surface area, and the ratio between them is called "electrochemical roughness". However, comparing porous electrodes is not a simple task. In fact, from a practical perspective, increasing the surface of the electrode to increase the current density is a typical method of increasing the general density of the current or, in other words, the activity of the electrode. Consequently, establishing the EASA or, more generally, connecting slightly quantifiable parameters (such as peak shape, surface geometry) to the performance of the electrode would allow the systematic design of surfaces with specific characteristics.

Regardless of the theoretical approach to calculate the EASA [44], the values given in Table 1 for the roughness parameters determined by the AFM lines produce the optimal surface under the experimental conditions described above and can be verified by any calculation method.

It should be emphasized that the EASA can be evaluated qualitatively by taking into account the roughness of the anterior presented electrodes. However, it can often be identified by alternative methods, based, e.g., on roughness approaches [53]. Another related method is the capacity of the double layer, obtained from the slope of a current graph according to the scan speed and then divided by the capacity per surface unit [54,55]. However, this approach is recognized for the significant inaccuracies it causes. An alternative approach is the spectroscopy of the electrochemical impedance, used to measure the capacity on the surface unit and, subsequently, to evaluate the capacity of the double layer [56,57]. It is essential to emphasize that each electrical component must have a physical significance, and in reality, the behavior of the double layer is not perfect.

Conversely, the integration of redox peaks can also be used to evaluate the surface of the electrode [50–60]. It is important to note that the ability obtained from galvanostatic loading and cyclical voltammetry experiments is called whole capacity, while the capacity obtained from impedance spectroscopy measurements is known as differential capacity.

Specifically, the cathodic and anodic peaks correspond to the creation and reduction in the different reactors, and the area below these peaks is associated with the load involved in the transition. A possible source of error in this type of measurement comes from the inclusion of possible non-pharadaic or parasitic currents, as well as from the potential development of unwanted species.

In summary, the evaluation of the roughness of the electrode, as presented in this work, is essential for determining its potential electrochemical activity and serves as a reliable indicator for the EASA value. The determination of the EASA by the previously mentioned methods remains approximate, partly due to the inaccuracy of these methods and also due to the use of electrolytes that may not be relevant to the potential application of such electrolytes in the practical use of certain electrochemical sensors.

From our point of view, evaluation of the EASA by the previously mentioned methods is not relevant to sensor applications, although it could be applicable for corrosion, sources of electrochemical energy, or electrochemical synthesis. In the case of sensors, the true importance of the EASA depends on the actual use of the electrode, especially in terms of its interaction with the molecules of interest, and not as a general measurement with a regular reactive. Thus, after evaluating the architecture of the electrode surface and after choosing the optimal electrodes based on this architecture during the initial phase, the following real measurements in the cyclic voltammetry experiments can evaluate the true EASA, as well as the real functionality of the respective electrode for measuring the chosen molecules of interest.

Our research will continue in this direction, in particular by evaluating optimal structures, such as ZnO nanotubes—PANI:EB/Au, ZnO nanotubes—P3HT/Au, or TiO_2 nanotubes—PANI:EB/Au, by use of cyclic voltammetry experiments, as electrochemical sensors with dedicated biomedical applications aimed at various chosen biomarkers.

This study could be relevant for the practical development of sensing areas, particularly because there are limited investigations into electrochemical nanosensors that focus on the roughness of their active surfaces, which is often treated only as a secondary analysis linked to a specific technology applied, as described in [32–37,61–65], with no explicit enhancement of surface roughness aimed at obtaining more sensitive measurements. Nevertheless, research studies aligned more with our approach regarding roughness analysis were linked more to the performance of optical sensors [27,29,66], where those characteristics were considered more significant. However, in none of the aforementioned cases was a detailed analysis of roughness parameters obtained through AFM lines conducted to link the roughness characteristics with the sensing capabilities.

4. Conclusions

This research presents the surface analysis of hybrid nanostructures derived from four types of ceramic nanotubes (ZnO, TiO_2, Al_2O_3, and Y_2O_3) with three types of conducting polymers: poly(3-hexylthiophene), polyani-line emeraldine-base (PANI:EB), and poly(3, 4-ethylenedioxythiophene)-polystyrene sulfonate, with embedded Au nanoparticles. The method for manufacturing ceramic nanotubes followed three stages: manufacturing of polymer fiber networks with poly(methyl methacrylate), applying ceramic coatings onto the nanofiber networks via magnetron deposition, and heating the nanotubes to 600 °C to eliminate the polymer support. Hybrid nanostructures from ceramic nanotubes and conducting polymers were further obtained by drop-casting. Finally, the gold nanoparticles were embedded within a ceramic nanotube–conductive polymer composite, utilizing a dip-coating technique with a diluted $HAuCl_4$/2-propanol solution (0.001 M) followed by controlled heating, which represents a novelty in the domain of nanosensor development.

It is usually believed that placing gold nanoparticles on composite locations can mainly be affected by the type of polymer and its positioning on ceramic nanotubes. However, when the incorporation of gold nanoparticles into conductive polymers with ceramic nanotubes through EDS and SEM is evaluated, it is clear that the relationship between gold and polymer structures differs greatly, contrary to assumptions, and the gold nanotubes and the surface structure are significantly influenced by the ceramic nanotubes.

However, the ideal positioning of gold nanoparticles on the surfaces of ceramic nanotubes and their concentration are essential factors for increasing the sensitivity of the material in order for it to be used in sensory applications. This effect must be amplified by the specific structure of the surface of the material, evaluated by AFM analysis. The AFM analysis highlighted the characteristics of the roughness of the surfaces of the different structures, eventually determining which materials could be the most suitable options for electrochemical electrodes due to their optimal surface structure. It has been shown that the addition of gold nanoparticles changes the structure of the surface and forces the granulations inherent in the ceramic–polymer composites to form gaps that allow the particles to advance deeper and to aggregate in small groups, leading to a slight increase in the granulation and to a localized intensification. The evaluation of roughness has mainly focused on the higher peaks in relation to the valleys to recognize a Gaussian distribution. In our case, the optimal structures have been designated, e.g., ZnO nanotubes—PANI:EB/Au, ZnO nanotubes—P3HT/Au, or TiO_2 nanotubes—PANI:EB/Au, which will be tested further by use of cyclic voltammetry experiments, as electrochemical sensors with dedicated biomedical applications for various chosen biomarkers.

The evaluation of electrode roughness, as presented in this work, is essential for determining its potential electrochemical activity. We consider that the EASA evaluation using the conventional methods described in the specialized literature is not applicable for sensor design. Thus, an initial comprehensive evaluation of the electrode surface structure is recommended, selecting the best electrodes based on this design, and further information gathered from cyclic voltammetry will ultimately confirm the accurate EASA and the genuine effectiveness of the respective electrode in detecting the target molecules.

Supplementary Materials: The following supporting information can be downloaded at https://www.mdpi.com/article/10.3390/coatings15101211/s1, Figure S1: XPS analysis of TiO_2 nanotube composites with (a) PANI:EB, (b) PEDOT:PSS, and (c) P3HT [46]. Figure S2: XPS analysis of Al_2O_3 nanotube composites with (a) PANI:EB, (b) PEDOT:PSS, and (c) P3HT [47]. Figure S3: XPS analysis of ZnO nanotube composites with (a) PANI:EB, (b) PEDOT:PSS, and (c) P3HT [47].

Author Contributions: Conceptualization, R.C.C., A.F.T. and O.D.S.; methodology, R.C.C. and A.F.T.; validation, R.C.C. and A.F.T.; formal analysis, A.F.T., O.D.S. and R.C.C.; investigation, R.C.C., A.F.T. and O.D.S.; data curation, R.C.C. and A.F.T.; writing—original draft preparation, A.F.T. and R.C.C.; writing—review and editing, R.C.C.; visualization, R.C.C. and A.F.T.; supervision, A.F.T. and R.C.C. All authors have read and agreed to the published version of the manuscript.

Funding: This research received no external funding.

Institutional Review Board Statement: Not applicable.

Informed Consent Statement: Not applicable.

Data Availability Statement: Data are contained within the article.

Conflicts of Interest: The authors declare no conflicts of interest.

References

1. Baranwal, J.; Barse, B.; Gatto, G.; Broncova, G.; Kumar, A. Electrochemical Sensors and Their Applications: A Review. *Chemosensors* **2022**, *10*, 363. [CrossRef]

2. Iacob Dinu, I.; Constantin, A.; Apetrei, C. Development of Polypyrrole Modified Screen-Printed Carbon Electrode Based Sensors for Determination of L-Tyrosine in Pharmaceutical Products. *J. Mol. Sci.* **2021**, *22*, 7528. [CrossRef]
3. Zhiyang, L.Z.; Leung, C.; Gao, F.; Gu, Z. Effects of Nanowire Length and Surface Roughness on the Electrochemical Sensor Properties of Nafion-Free, Vertically Aligned Pt Nanowire Array Electrodes. *Sensors* **2015**, *15*, 22473–22489. [CrossRef]
4. Miller, C.; Keattch, O.; Shergill, R.; Patel, B. Evaluating diverse electrode surface patterns of 3D printed carbon thermoplastic electrochemical sensors. *Analyst* **2024**, *149*, 1502–1508. [CrossRef]
5. Kılıç, Y.; Manickham, P.; Bhansali, S. Brief Fine Polishing of Thin-film Gold Electrode Sensors Leads to Better Reproducibility than Electrochemical Pretreatment. *Int. J. Electrochem. Sci.* **2020**, *15*, 5067–5075. [CrossRef]
6. Sarmphim, P.; Teeparuksapun, K.; Wunsri, S.; Sorngodchagorn, S.; Duangsiri, W.; Tapparak, P.; Sirisathitkul, C. Facile Fabrication of Screen-Printed Carbon Electrodes for Electrochemical Sensors. *Int. J. Nanoelectron. Mater.* **2021**, *14*, 1–10. Available online: https://ijneam.unimap.edu.my/index.php/vol-14-no-1-january-2021 (accessed on 17 July 2025).
7. González-Martínez, E.; Saem, S.; Beganovic, N.; Moran-Mirabal, J. Electrochemical Nano-Roughening of Gold Microstructured Electrodes for Enhanced Sensing in Biofluids. *Angew. Chem.* **2023**, *62*, e202218080. [CrossRef]
8. Ostertag, B.; Porshinsky, E.; Nawarathne, C.; Ross, A. Surface-Roughened Graphene Oxide Microfibers Enhance Electrochemical Reversibility. *Langmuir* **2024**, *40*, 12124–12136. [CrossRef] [PubMed]
9. Min, K.; Yoon, S.; Kim, D. Effect of surface roughness on the extinction-based localized surface plasmon resonance biosensors. *Appl. Opt.* **2008**, *47*, 5886–5892. [CrossRef] [PubMed]
10. AL-Mosht, S.; Al-Fandi, M.; Al-Ebbini, L. Nanoarchitectonics of composite biosensor for early detection of hepatocellular carcinoma. *Appl. Phys. A* **2022**, *128*, 536. [CrossRef]
11. El-Said, W.; Saleh, T.; Al-Bogami, A.; Wani, M.; Choi, J. Development of Novel Surface-Enhanced Raman Spectroscopy-Based Biosensors by Controlling the Roughness of Gold/Alumina Platforms for Highly Sensitive Detection of Pyocyanin Secreted from Pseudomonas aeruginosa. *Biosensors* **2024**, *14*, 399. [CrossRef]
12. Shergill, R.S.; Miller, C.L.; Patel, B.A. Influence of instrument parameters on the electrochemical activity of 3D printed carbon thermoplastic electrodes. *Sci. Rep.* **2023**, *13*, 339. [CrossRef] [PubMed]
13. Patil, M.; Ganbavle, V.V.; Rajpure, K.Y.; Deshmukh, H.P.; Mujawar, S.H. Fast response and highly selective nitrogen dioxide gas sensor based on Zinc Stannate thin films. *Mater. Sci. Energy Technol.* **2020**, *3*, 36–42. [CrossRef]
14. Ghaderi, A.; Sabbaghzadeh, J.; Dejam, L.; Pour, G.; Moghimi, E.; Matos, R.; da Fonseca Filho, H.; Ţălu, S.; Salehishayegan, A.; Aval, L.; et al. Nanoscale morphology, optical dynamics and gas sensor of porous silicon. *Sci. Rep.* **2024**, *14*, 3677. [CrossRef]
15. Abdelkarem, K.; Saad, R.; El Sayed, A.M.; Fathy, M.I.; Shaban, M.; Hamdy, H. Design of high-sensitivity La-doped ZnO sensors for CO_2 gas detection at room temperature. *Sci. Rep.* **2023**, *13*, 18398. [CrossRef] [PubMed]
16. Sehit, E.; Altintas, Z. Significance of nanomaterials in electrochemical glucose sensors: An updated review. *Biosens. Bioelectron.* **2020**, *159*, 112165. [CrossRef]
17. Zeng, Y.; Camarada, M.B.; Lu, X.; Tang, K.; Li, W.; Qiu, D.; Wen, Y.; Wu, G.; Luo, Q.; Bai, L. A portable wireless intelligent electrochemical sensor based on layer-by-layer sandwiched nanohybrid for terbutaline in meat products. *Food Chem.* **2022**, *371*, 131140. [CrossRef]
18. Zeng, Y.; Camarada, M.B.; Lu, X.; Tang, K.; Li, W.; Qiu, D.; Wen, Y.; Wu, G.; Luo, Q.; Bai, L. Detection and electrocatalytic mechanism of zearalenone using nanohybrid sensor based on copper-based metal-organic framework/magnetic Fe3O4-graphene oxide modified electrode. *Food Chem.* **2022**, *370*, 131024. [CrossRef]
19. Kumar, N.; Navani, N.K.; Manhas, S.K. Effect of Metal Oxide Nanoparticles on Carbon Nanotube Device Characteristics. *J. Electron. Mater.* **2021**, *50*, 528–536. [CrossRef]
20. Hovancová, J.; Šišoláková, I.; Oriňaková, R.; Oriňak, A. Nanomaterial-based electrochemical sensors for detection of glucose and insulin. *J. Solid. State Electrochem.* **2017**, *21*, 2147–2166. [CrossRef]
21. Tee, S.Y.; Teng, C.P.; Ye, E. Metal nanostructures for non-enzymatic glucose sensing. *Mater. Sci. Eng. C* **2017**, *70*, 1018–1030. [CrossRef]
22. Lu, Y.; Yang, M.; Qu, F.; Shen, G.; Yu, R. Enzyme-functionalized gold nanowires for the fabrication of biosensors. *Bioelectrochemistry* **2007**, *71*, 211–216. [CrossRef]
23. Hira, S.A.; Yusuf, M.; Annas, D.; Saravanan Nagappan, S.; Song, R.; Park, S.; Park, K. Recent Advances on Conducting Polymer-Supported Nanocomposites for Nonenzymatic Electrochemical Sensing. *Ind. Eng. Chem. Res.* **2021**, *60*, 13425–13437. [CrossRef]
24. Saboor, F.H.; Ataei, A. Decoration of Metal Nanoparticles and Metal Oxide Nanoparticles on Carbon Nanotubes. *Adv. J. Chem.* **2024**, *7*, 122–145.
25. Wang, H.; Li, P.; Sun, G.; Jiang, Z. Influence of substrate surface roughness on the properties of a planar-type CO_2 sensor using evaporated Li_3PO_4 film. In Proceedings of the 8th Annual IEEE International Conference on Nano/Micro Engineered and Molecular Systems 2013, Suzhou, China, 7–10 April 2013. [CrossRef]

26. MenshykauIan, D.; Compton, R. Influence of Electrode Roughness on Cyclic Voltammetry. *J. Phys. Chem. C* **2008**, *112*, 14428–14438. [CrossRef]
27. Treebupachatsakul, T.; Shinnakerdchoke, S.; Pechprasarn, S. Analysis of Effects of Surface Roughness on Sensing Performance of Surface Plasmon Resonance Detection for Refractive Index Sensing Application. *Sensors* **2021**, *21*, 6164. [CrossRef] [PubMed]
28. Possan, A.; Menti, C.; Beltrami, M.; Santos, A.; Roesch-Ely, M.; Missell, F. Effect of surface roughness on performance of magnetoelastic biosensors for the detection of *Escherichia coli*. *Mater. Sci. Eng. C Mater. Biol. Appl.* **2016**, *58*, 541–547. [CrossRef]
29. Alvez, H.; de Barros, T.; Nascimento, D.; Silva, D.; Peixoto e Silva, M.; do Nascimento, J.; Fontana, E.; Martins-Filho, J. Influence of surface roughness on the sensitivity of a D-shaped optical fiber-based refractive index sensor. *Sens. Actuators A Phys.* **2022**, *344*, 113702. [CrossRef]
30. Saitta, L.; Celano, G.; Tosto, C.; Arcadio, F.; Zeni, L.; Sergi, C.; Cennamo, N.; Cicala, G. The effect of surface roughness on the performance of 3D printed surface plasmon resonance sensors for refractive index measurements. *Int. J. Adv. Manuf. Technol.* **2024**, *132*, 5503–5519. [CrossRef]
31. Hashim, J.; Salim, M.; Qazi, H.; Noor, M.; Azmi, A.; Ibrahim, M.; Manap, H. Effect of Surface Roughness on Sensitivity of Unclad Fiber-Optic Sensors. *J. Phys. Conf. Ser.* **2023**, *2550*, 12018. [CrossRef]
32. Zhang, J.; Kuang, Z.; Li, H.; Li, S.; Xia, F. Electrode surface roughness greatly enhances the sensitivity of electrochemical non-enzymatic glucose sensors. *J. Electroanal. Chem.* **2022**, *919*, 116541. [CrossRef]
33. Dutta, G.; Fernandes, F.; Estrela, P.; Moschou, D.; Bueno, P. Impact of surface roughness on the self-assembling of molecular films onto gold electrodes for label-free biosensing applications. *Electrochim. Acta* **2021**, *378*, 138137. [CrossRef]
34. Golba, S.; Kubisztal, J. The Influence of Roughness on the Properties of Electroactive Polypyrrole. *Molecules* **2024**, *29*, 5436. [CrossRef] [PubMed]
35. Perry, S.; Gateman, S.; Sifakis, J.; Pollegioni, L.; Mauzeroll, J. Enhancement of the Enzymatic Biosensor Response through Targeted Electrode Surface Roughness. *J. Electrochem. Soc.* **2018**, *165*, G3074. [CrossRef]
36. Surdo, S.; Barillaro, G. Impact of Fabrication and Bioassay Surface Roughness on the Performance of Label-Free Resonant Biosensors Based On One-Dimensional Photonic Crystal Microcavities. *ACS Sens.* **2020**, *5*, 2894–2902. [CrossRef]
37. Dobri, G.; Banu, A.; Donath, C.; Neacsu, E.; Anastasescu, M.; Maxim, M.; Vasilescu, C.; Preda, L.; Marcu, M. Effect of Surface Roughness on the Electrochemical Behavior and Corrosion Resistance of TiTaNbZrAg Alloy with Different Amounts of Tantalum in Bulk Composition. *Materials* **2024**, *17*, 5217. [CrossRef] [PubMed]
38. Enculescu, M.; Costas, A.; Evanghelidis, A.; Enculescu, I. Fabrication of ZnO and TiO2 Nanotubes via Flexible Electrospun Nanofibers for Photocatalytic Applications. *Nanomaterials* **2021**, *11*, 1305. [CrossRef]
39. Ramasamy, P.; Lim, D.H.; Kim, J.; Kim, J. A general approach for synthesis of functional metal oxide nanotubes and their application in dye-sensitized solar cells. *RSC Adv.* **2014**, *4*, 2858–2864. [CrossRef]
40. Li, Y.; Yang, X.Y.; Feng, Y.; Yuan, Z.Y.; Su, B.L. One-Dimensional Metal Oxide Nanotubes, Nanowires, Nanoribbons, and Nanorods: Synthesis, Characterizations, Properties and Applications. *Crit. Rev. Solid. State Mater. Sci.* **2012**, *37*, 1–74. [CrossRef]
41. Muench, F.; Sun, L.; Kottakkat, T.; Antoni, M.; Schaefer, S.; Kunz, U.; Molina-Luna, K.; Duerrschnabel, M.; Kleebe, H.; Ayata, S.; et al. Free-Standing Networks of Core-Shell Metal and Metal Oxide Nanotubes for Glucose Sensing. *ACS Appl. Mater. Interfaces* **2017**, *9*, 771–781. [CrossRef]
42. Trandabat, F.; Ciobanu, R.; Schreiner, O.; Aradoaei, M.; Aradoaei, S. Manufacturing of TiO_2, Al_2O_3 and Y_2O_3 Ceramic Nanotubes for Application as Electrodes for Printable Electrochemical Sensors. *Crystals* **2024**, *14*, 454. [CrossRef]
43. Trasatti, S.; Petrii, O.A. Real Surface Area Measurements in Electrochemistry. *Pure Appl. Chem.* **1991**, *63*, 711–734. [CrossRef]
44. Coelho, D.; Luiz, G.; Machado, S. Estimating the Electrochemically Active Area: Revisiting a Basic Concept in Electrochemistry. *J. Braz. Chem. Soc.* **2021**, *32*, 1912–1917. [CrossRef]
45. Surface Roughness Parameters. Available online: https://www.keyence.eu/ss/products/microscope/roughness/line/tab03_b.jsp (accessed on 17 July 2025).
46. Schreiner, O.; Trandabat, A.F.; Ciobanu, R.; Schreiner, T. TiO_2 Ceramic Nanotubes—Conducting Polymer Assemblies with Embedded Gold Particles for Potential Use as Chemosensors in the Detection of Oral Diseases. *Chemosensors* **2025**, *13*, 117. [CrossRef]
47. Trandabat, A.F.; Ciobanu, R.; Schreiner, O.; Schreiner, T.; Aradoaei, D. Ceramic Nanotubes—Conducting Polymer Assemblies with Potential Application as Chemosensors for Breath Hydrogen sulfide Detection in Chronic Kidney Disease. *Chemosensors* **2024**, *12*, 198. [CrossRef]
48. Umeda, H.; Mezaki, Y.; Oshio, A.; Kaneko, Y.; Okamoto, R.; Kusumoto, S.; Kunimura, S. Gold Nanoparticles Produced by Low-temperature Heating of the Dry Residue of a Droplet of an HCl Acidic Solution of $HAuCl_4{\cdot}4H_2O$ in a Low Vacuum. *Anal. Sci.* **2021**, *37*, 1427–1432. [CrossRef]
49. Ii, K.; Kurita, Y.; Kida, N.; Kunimura, S. Preparation of gold nanoparticles using low-temperature heating of the dry residue of a droplet of an $HAuCl_4$ solution in air. *Anal. Sci.* **2024**, *40*, 213–217. [CrossRef]

50. ISO 21920-2:2021 (Previously ISO 4287:1997). Available online: https://www.iso.org/standard/72226.html (accessed on 17 July 2025).
51. Zhang, R.; Sun, D.; Zhang, R.; Lin, W.; Macias-Montero, M.; Patel, J.; Askari, S.; McDonald, C.; Mariotti, D.; Maguire, P. Gold nanoparticle-polymer nanocomposites synthesized by room temperature atmospheric pressure plasma and their potential for fuel cell electrocatalytic application. *Sci. Rep.* **2017**, *7*, 46682. [CrossRef] [PubMed]
52. Yi, G.; Hoffmann, M.; Seçkin, S.; König, T.; Hermes, I.; Rossner, C.; Fery, A. Toward coupling across inorganic/organic hybrid interfaces: Polyaniline-coated gold nanoparticles with 4-aminothiophenol as gold-anchoring moieties. *Colloid. Polym. Sci.* **2024**, *303*, 1743–1751. [CrossRef]
53. Lai, L.; Irene, E. Area evaluation of microscopically rough surfaces. *J. Vac. Sci. Technol. B* **1999**, *17*, 33–39. [CrossRef]
54. Sekretareva, A.; Vagin, M.; Volkov, A.; Zozoulenko, I.; Eriksson, M. Evaluation of the Electrochemically Active Surface Area of Microelectrodes by Capacitive and Faradaic Currents. *ChemElectroChem* **2019**, *6*, 4411–4417. [CrossRef]
55. Connor, P.; Schuch, J.; Kaiser, B.; Jaegermann, W. The determination of electrochemical active surface area and specific capacity revisited for the system MnOx as an oxygen evolution catalyst. *Z. Phys. Chem.* **2020**, *234*, 979–994. [CrossRef]
56. Cossar, E.; Houache, M.; Zhang, Z.; Baranova, E. Comparison of electrochemical active surface area methods for various nickel nanostructures. *J. Electroanal. Chem.* **2020**, *870*, 114246. [CrossRef]
57. Serapinienė, B.; Gudavičiūtė, L.; Tutlienė, S.; Grigucevičienė, A.; Selskis, A.; Juodkazytė, J.; Ramanauskas, R. On the Electrochemically Active Surface Area Determination of Electrodeposited Porous Cu 3D Nanostructures. *Coatings* **2023**, *13*, 1335. [CrossRef]
58. Queiroz, M.A.R.; Vasconcellos, S.; Ribeiro, M.A.; Luz, P.; de Moura Souza, F.; dos Santos, M.; Guimarães, M.; Salgado, J.; Pedicini, R.; Ribeiro, J. Determination of the electrochemically active surface area by CO and hydrogen of PtSnRuTa/C-based electrocatalysts and their relationship with catalytic activity against alcohol oxidation. *Chem. Pap.* **2022**, *76*, 4597–4613. [CrossRef]
59. Martínez-Hincapié, R.; Wegner, J.; Anwar, M.; Raza-Khan, A.; Franzka, S.; Kleszczynski, S.; Čolić, V. The determination of the electrochemically active surface area and its effects on the electrocatalytic properties of structured nickel electrodes produced by additive manufacturing. *Electrochim. Acta* **2024**, *476*, 143663. [CrossRef]
60. Watzele, S.; Hauenstein, P.; Liang, Y.; Xue, S.; Fichtner, J.; Garlyyev, B.; Scieszka, D.; Claudel, F.; Maillard, F.; Bandarenka, A. Determination of electroactive surface area of Ni-, Co-, Fe-, and Ir-based oxide electrocatalysts. *ACS Catal.* **2019**, *9*, 9222–9230. [CrossRef]
61. Lai, T.; Shu, H.; Yao, B.; Lai, S.; Chen, T.; Xiao, X.; Wang, Y. A Highly Selective Electrochemical Sensor Based on Molecularly Imprinted Copolymer Functionalized with Arginine for the Detection of Chloramphenicol in Honey. *Biosensors* **2023**, *13*, 505. [CrossRef]
62. Tan, C.; Yin, H.; Brooks, V.; Arumugam, P.U.; Siddiqui, S. A Study of the Effect of Electrochemical Roughening of Platinum on the Sensitivity and Selectivity of Glutamate Biosensors. *J. Electrochem. Soc.* **2022**, *169*, 037510. [CrossRef]
63. Darvishi, S.; Ensafi, A.A.; Mousaabadi, K.Z. Design and fabrication of electrochemical sensor based on NiO/Ni@C-Fe_3O_4/CeO_2 for the determination of niclosamide. *Sci. Rep.* **2024**, *14*, 7576. [CrossRef]
64. Huang, J.; Liu, P.; Wang, Y.; Dai, K.; Dou, Q.; Yin, Y.; Wang, X.; You, Z. Double-kill contribution of high-roughness high-density porous carbon electrodes to mechanically self-sensing supercapacitors. *Nano Res.* **2024**, *17*, 6157–6167. [CrossRef]
65. Liu, J.; Shen, J.; Ji, S.; Zhanga, Q.; Zhao, W. Research progress of electrode materials for non-enzymatic glucose electrochemical sensors. *Sens. Diagn.* **2023**, *2*, 36–45. [CrossRef]
66. Zhong, N.; Zhu, X.; Liao, Q.; Wang, Y.; Chen, R.; Sun, Y. Effects of surface roughness on optical properties and sensitivity of fiber-optic evanescent wave sensors. *Appl. Opt.* **2013**, *52*, 3937–3945. [CrossRef] [PubMed]

crystals

IMPACT FACTOR 2.4

CITESCORE 5.0

Article

Manufacturing of TiO_2, Al_2O_3 and Y_2O_3 Ceramic Nanotubes for Application as Electrodes for Printable Electrochemical Sensors

Alexandru Florentin Trandabat, Romeo Cristian Ciobanu, Oliver Daniel Schreiner, Mihaela Aradoaei and Sebastian Teodor Aradoaei

Special Issue
Metal Oxide Thin Films, Nanomaterials and Nanostructures

Edited by
Dr. Zahira El Khalidi, Prof. Dr. Elisabetta Comini and Dr. Abderrahim Moumen

MDPI

https://doi.org/10.3390/cryst14050454

crystals

MDPI

Article

Manufacturing of TiO_2, Al_2O_3 and Y_2O_3 Ceramic Nanotubes for Application as Electrodes for Printable Electrochemical Sensors

Alexandru Florentin Trandabat, Romeo Cristian Ciobanu *, Oliver Daniel Schreiner, Mihaela Aradoaei and Sebastian Teodor Aradoaei

Department of Electrical Measurements and Materials, Gheorghe Asachi Technical University, 700050 Iasi, Romania; ftranda@tuiasi.ro (A.F.T.); oliver090598@yahoo.com (O.D.S.); mosneagum@yahoo.com (M.A.); arsete@tuiasi.ro (S.T.A.)
* Correspondence: r.c.ciobanu@tuiasi.ro

Abstract: This paper describes the process to obtain ceramic nanotubes from titanium dioxide, alumina and yttrium oxide by a feasible, replicable and reliable technology, including three stages, starting from an electrospinning process of poly(methyl methacrylate) solutions. A minimum diameter of 0.3 µm was considered optimal for PMMA nanofibers in order to maintain the structural stability of covered fibers, which, after ceramic film deposition, leads to a fiber diameter of 0.5–0.6 µm. After a chemical and physical analysis of the stages of obtaining ceramic nanotubes, in all cases, uniform deposition of a ceramic film on PMMA fibers and, finally, a uniform structure of ceramic nanotubes were noted. The technological purpose was to use such nanotubes as ingredients in screen-printing inks for electrochemical sensors, because no study directly targeted the subject of ceramic nanotube applications for printed electronics to date. The printing technology was analyzed in terms of the ink deposition process, printed electrode roughness vs. type of ceramic nanotubes, derived inks, thermal curing of the electrodes and the conductivity of electrodes on different support (rigid and flexible) at different curing temperatures. The experimental inks containing ceramic nanotubes can be considered feasible for printed electronics, because they offer fast curing at low temperatures, reasonable conductivity vs. electrode length, good printability on both ceramic or plastic (flexible) supports and good adhesion to surface after curing.

Keywords: ceramic nanotubes; electrospinning; screen-printing inks; electrochemical sensors

Citation: Trandabat, A.F.; Ciobanu, R.C.; Schreiner, O.D.; Aradoaei, M.; Aradoaei, S.T. Manufacturing of TiO_2, Al_2O_3 and Y_2O_3 Ceramic Nanotubes for Application as Electrodes for Printable Electrochemical Sensors. *Crystals* **2024**, *14*, 454. https://doi.org/10.3390/cryst14050454

Academic Editor: Lin Gan

Received: 23 April 2024
Revised: 9 May 2024
Accepted: 10 May 2024
Published: 11 May 2024

1. Introduction

Metal oxides exhibit several key advantages for multiple applications, such as sensors, solar cells, cathode material for batteries, and photocatalysis, which has encouraged researchers' efforts to improve their technology and architecture. But the considerable difficulties encountered in obtaining ceramic thin films, respectively ceramic nanotubes, prevented their large-scale manufacture.

Although there are some studies on ceramic nanotubes technology from the last 15 years, e.g., [1–11], no study directly targeted the subject of ceramic nanotube composites. Some papers addressed, e.g., carbon–ceramic nanotube composites and ceramic nanoparticles associated with carbon nanotubes, as in [12–19]. On the other hand, no study directly targeted the subject of ceramic nanotube applications for printed electronics, e.g., printed sensors based on specific inks including ceramic nanotubes, which is the subject of the present paper. Nanotube-based devices change their conductivity due to surface adsorption when exposed to chemical species [20,21]. The same adsorption on the surface may be also present in the case of biomolecules such as amino acids and proteins, which means that the nanotubes are also applicable for the detection of bio-agents [22,23]. The main problem is that most of the authors addressed the surface properties of carbon nanotubes, but none targeted the homologue properties of ceramic nanotubes. The surface architecture of ceramic nanotubes represents a critical element that may impact the future development of sensor applications.

Electrospinning is a high-throughput, cost-effective, and versatile technology used for the manufacturing of nanofiber nets of a large pellet of polymers by applying an electrostatic force [24,25]. Systematic investigations on the effect of electrospinning parameters on fiber diameter and morphology have been reported by several researchers [25–28]. The major factors controlling the diameter of the fibers are: (1) the concentration of the polymer in the solution, (2) the type of solvent used, (3) the conductivity of the solution, and (4) the solution feed rate. Recently, it has been established that the nature of the collector significantly influences the morphological and physical characteristics of spun fibers [29,30]. The density of fibers per unit area on the collector and the arrangement of the fibers is affected by the degree of charge dissipation upon fiber deposition. The most commonly used target is the conductive metal plate, which results in the collection of randomly oriented fibers in a nonwoven form. Electrospun polymer nanofibers can be further used in the manufacturing process of hollow tubes, in particular ceramic nanotubes. The process implies coating the polymer nanofiber nets with metallic oxides, followed by the removal of the fiber core. Radiofrequency magnetron sputtering is a common deposition technique used to obtain controlled thin films with high technological reproducibility, and can be successfully used for coating polymer nanofiber nets with the metallic oxides [31–36]. There are some ceramic nanotubes described in the literature, from simple ceramic nanotubes, such ZnO, CuO, Co_3O_4, SnO_2, MnO_2 or TiO_2 nanotubes, to more complex ceramic nanotubes, such as $Li_3V_2(PO_4)_3$, $Na0_{.7}Fe_{0.77}Mn_{0.3}O_2$, $LiMn_2O_4$, $LiCoO_2$, $NiCo_2O_4$ or LiV_3O_8, based on fabrication processes of large spectrum, e.g., electrodeposition [37,38], hydrothermal [39,40], precipitation [41,42], electrospinning combined with calcination [43,44], and atomic layer deposition [45,46].

In our research titanium, aluminum and yttrium oxides were analyzed in order to obtain uniform ceramic nanotubes by a feasible, replicable and reliable technology, in order to use such nanotubes as ingredients in screen-printing inks dedicated to printed electronics, with further target on innovative nano-sensor development.

2. Technology for Obtaining Ceramic Nanotube Nets

2.1. Technological Equipment

Neu-Pro-BM equipment (TongLiTech, Wuhan, China) was used for the electrospinning process of poly(methyl methacrylate) nanofibers (PMMA nanofibers).

A Tectra Sputter Coater (Tectra GmbH Physikalische Instrumente, Frankfurt, Germany) was the equipment used for radiofrequency (RF) magnetron sputtering.

A Forced convection chamber furnace up to 800 °C (Nabertherm GmbH, Lilienthal, Germany) was used for the PMMA calcination process.

A Keko P200A (Keko Equipment, Žužemberk, Slovenia) screen-printer equipment for printed electronics was used for nanostructured inks testing.

2.2. Materials and Preparation Method

All chemical constituents (ceramic powders and polymers) were procured from Merck (Darmstadt, Germany), and Kurt J. Lesker Company Ltd. (Hastings, UK), and employed without additional refinement. The nanostructured inks were purchased from NovaCentrix, Austin, TX, USA.

The technology of manufacturing TiO_2, Al_2O_3 and Y_2O_3 ceramic nanotubes was based on three stages, according to the general description in [3,4], and included:

(i) Preliminary manufacturing of polymer fibers nets of poly(methyl methacrylate) (PMMA), with a molecular weight (Mw) of 300,000, from a solution of 10 wt%, with dimethylformamide (DMF) as solvent.

An experimental plan was conceived, as described in Table 1, with different technological parameters: 5% and 10% concentration of PMMA solution; voltages of 12, 15 and 20 kV were applied; the distance between the needle and the drum was set to 80 and 100 mm;

the flow was of 1 mL/h (1 h total time of processing) and the rotation speed of the drum varied between 0 and 5 rpm. The electrospun nanofibers are randomly deposited on a fixed support in the form of a square Cu metal frame (20 × 20 cm^2) attached to the collector.

Table 1. Experimental plan for electrospinning process.

Sample	PMMA (%)	U (kV)	Distance (mm)	Rotation Speed (rpm)
1	10	12	100	-
2	10	15	100	-
3	10	20	100	-
4	10	20	80	-
5	10	15	80	5
6	10	12	80	5
7	5	12	80	5
8	5	15	80	5
9	5	20	80	5
10	5	20	100	5
11	5	15	100	5
12	5	12	100	5

The samples were analyzed under the optical microscope where the dimensions of the microstructure, material defects and cracks were studied.

Figure 1 shows the microscopic image of the nanofibers obtained by using the PMMA solution of 10% and an applied voltage of 12 kV, the distance between the needle and the drum being 100 mm. The average size of the obtained fiber was 0.262 µm.

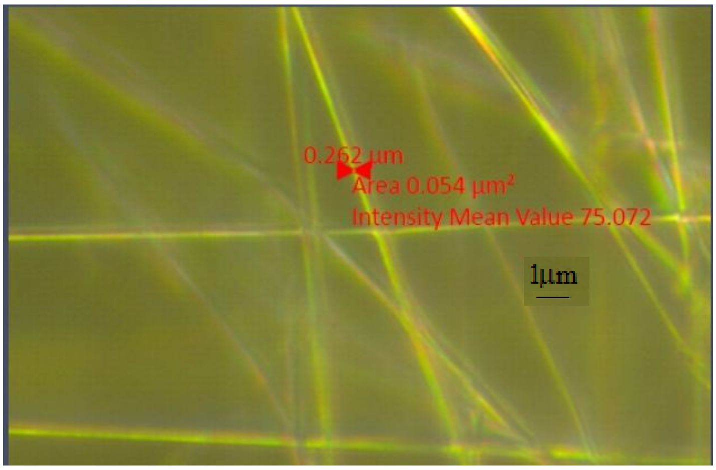

Figure 1. PMMA nanofibers net deposited at 12 kV.

Figure 2 shows the microscopic image of the nanofibers obtained using the PMMA solution of 10% and an applied voltage of 15 kV, the distance between the needle and the drum being also 100 mm. The size of the fiber obtained was between 0.282 and 0.288 µm.

Figure 3 shows the image obtained under the microscope of the nanofibers obtained by using the PMMA solution of 10% and an applied voltage of 20 kV, the distance between the needle and the drum being also 100 mm. The average size of the obtained fibers was 0.327 µm.

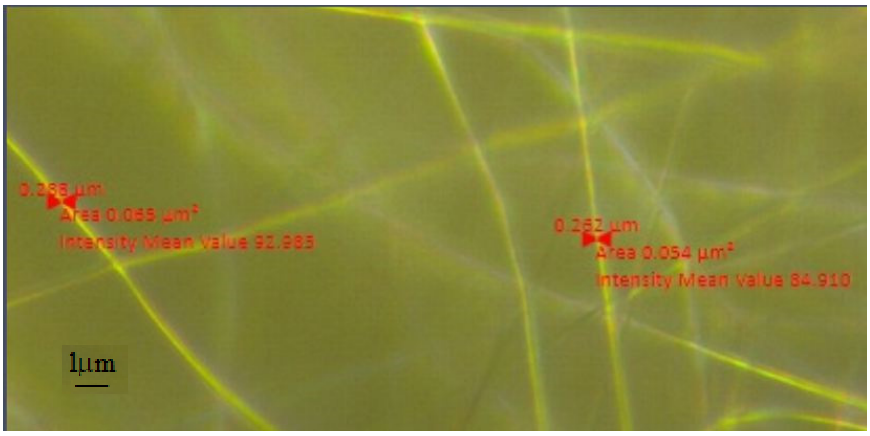

Figure 2. PMMA nanofibers net deposited at 15 kV.

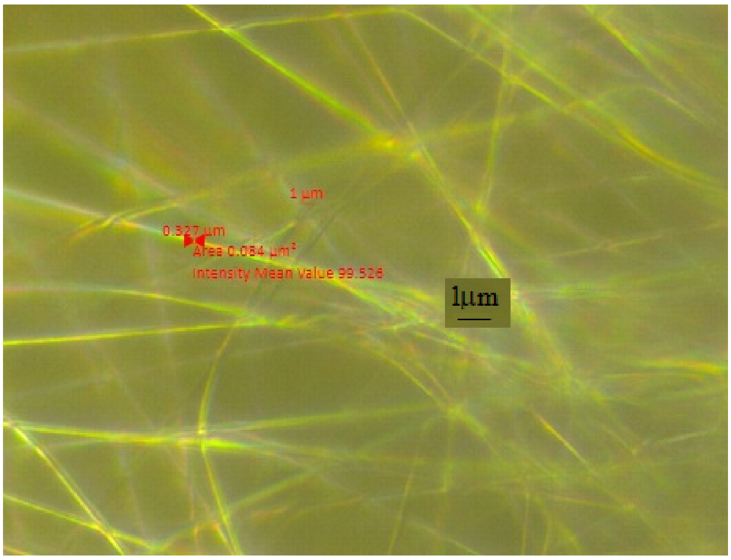

Figure 3. PMMA nanofibers net deposited at 20 kV.

In all, the best results were obtained using a 10% PMMA solution at voltages of 20 kV, with a drum rotation speed of 5 rpm, because the fiber nets were more homogenous as spatial deposition, and also more homogenous as diameter. On the other hand, due to the characteristics of ceramic thin films to be deposited on PMMA nanofibers, a minimum diameter of 0.3 µm was consider optimal for PMMA nanofibers in order to maintain the structural stability of covered fibers from the mechanical point of view.

(ii) Magnetron deposition of ceramic films

The copper frames housing the PMMA nanofibers nets underwent dual-sided coating with ceramic thin films via RF magnetron sputtering. During the deposition process, ceramic targets with dimensions of 2 inches in diameter and 0.125 inches in thickness was employed. For all involved oxides, the deposition duration for each side was 1 h, and the RF power applied to the magnetron was 200 W. Within the deposition chamber, an argon atmosphere with a purity of 99.99% as working gas, at a pressure of 5.4×10^{-3} mbar, was assured.

In Figure 4, the evolution of the dimensions of nanofibers is presented, before and after ceramic film deposition, indicating an increase from approximately 0.327 µm to approximately 0.540 µm.

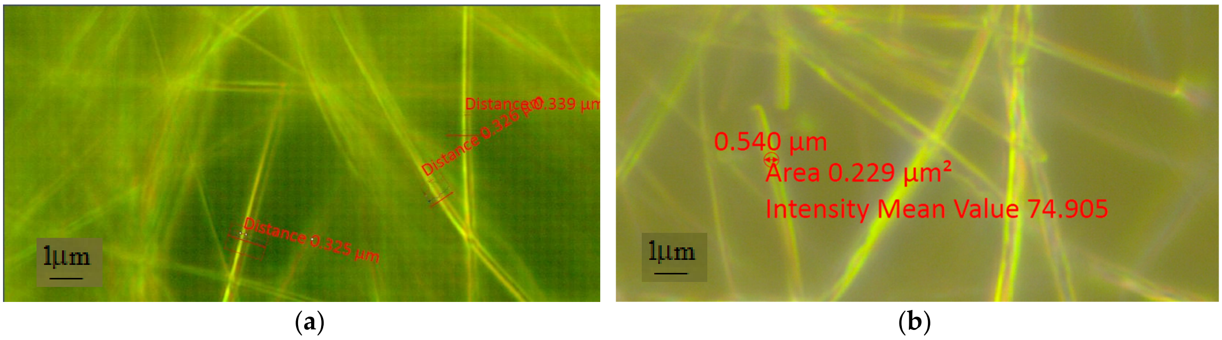

(**a**) (**b**)

Figure 4. Dimensions of nanofibers before (**a**) and after (**b**) ceramic film deposition.

(iii) Thermal treatment of nanotubes

Subsequent to this process, the PMMA nanofibers nets, coated on both sides with ceramic films, were transferred onto a Si/SiO_2 substrates (cleaned beforehand with acetone and isopropyl alcohol and dry under an argon jet) and subjected to a calcination process conducted at 600 °C for a duration of 12 h in ambient air at atmospheric pressure. Following this procedure, three-dimensional web-like networks of TiO_2, Al_2O_3 and Y_2O_3 nanotubes were achieved, after the complete combustion of PMMA support.

2.3. Characterization Equipment

- Optical scanning microscopy SEM and energy-dispersive X-ray spectroscopy (EDX) were performed with a field emission and focused ion beam scanning electron microscope (SEM) model Tescan Lyra III XMU (Libušina tř. 21 623 00, Brno-Kohoutovice, Czech Republic).
- Structural characterization was carried out by X-ray diffraction (XRD) using CuKα radiation with Ni filter Bruker AXS D8 Advance (Bruker AXS, Billerica, MA, USA) with CuKα radiation (λ = 0.154 nm). Diffraction patterns were recorded at room temperature in Bragg-Brentano geometry at an angle 2θ from 20° to 65° at a rate of 0.6°/min (2θ)/min.

2.4. Results and Discussion

The diffractograms obtained upon the analyzed samples of ceramic nanotubes, before and after thermal exposure, are presented in Figure 5 for TiO_2, Figure 6 for Al_2O_3 and Figure 7 for Y_2O_3. It can be observed that after thermal treatment is used to remove the organic material, the peaks in the diffractograms that appear before the heat treatment become more intense compared to the peaks that appear after, explained by the crystallization of the oxide materials during thermal exposure.

Thus, in Figure 5, the presence of a mixture of rutile and anatase phases specific to titanium dioxide can be observed. It can be noticed, after the heat treatment, the appearance of the characteristic maxima of the crystal planes (110) from 27° and (211) from 55°, specific to the rutile phase, as well as the crystal planes (101) from 25° and (200) from 48°, specific to the anatase phase of titanium dioxide.

In Figure 6, the existence of the amorphous phase before thermal treatment can be noticed by the presence in the diffractogram of the accentuated rise of the background only on the portion of 20–35° (not on the entire range of 2θ angles), a phenomenon that proves the existence of only some crystalline immature seeds and not an amorphous alumina in the true sense of the word.

In Figure 7, several diffraction maxima characteristic of yttrium oxide can be identified in both diffractograms, before and after thermal treatment, with the maxima at 29°, 34°, 49° and 58°.

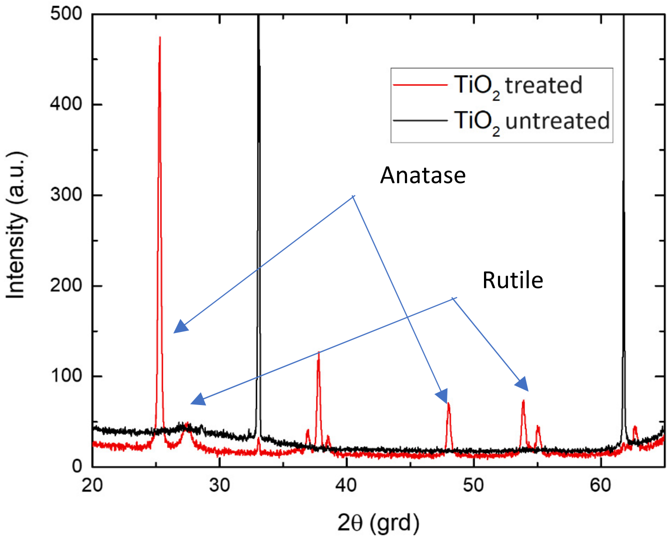

Figure 5. Diffractogram for TiO_2 ceramic nanotubes.

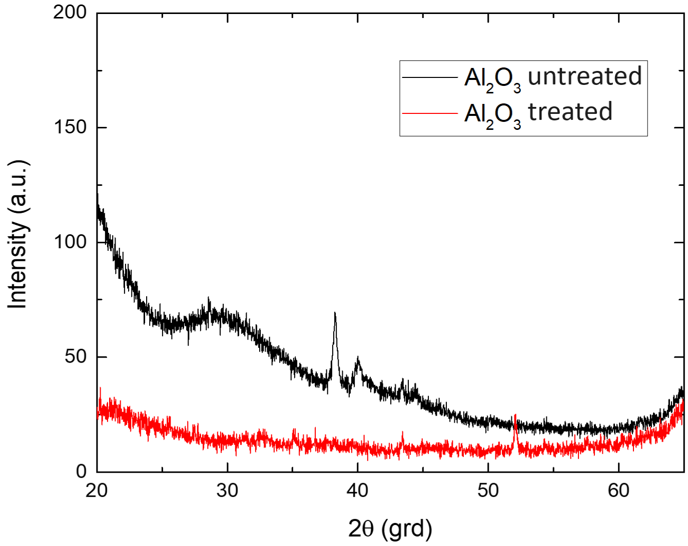

Figure 6. Diffractogram for Al_2O_3 ceramic nanotubes.

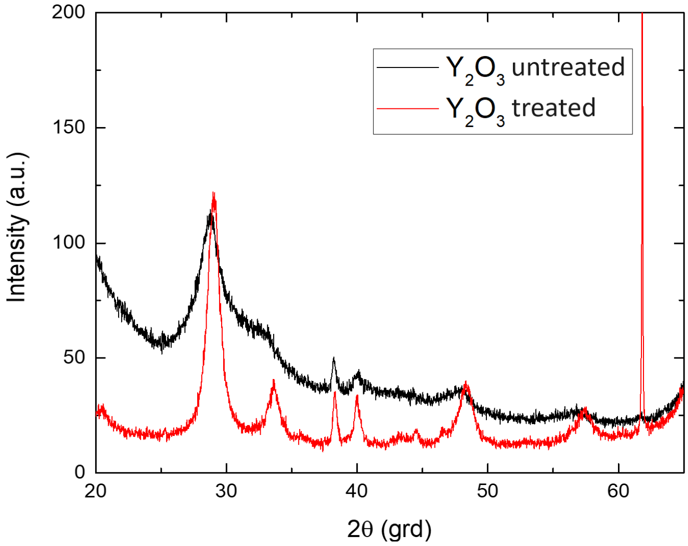

Figure 7. Diffractogram for Y_2O_3 ceramic nanotubes.

The compositions of the samples before and after heat treatment were investigated using a scanning electron microscope. Thus, the analysis of the dispersed X-ray energies (EDX) of the samples of ceramic nanotubes are presented in Figures 8–10.

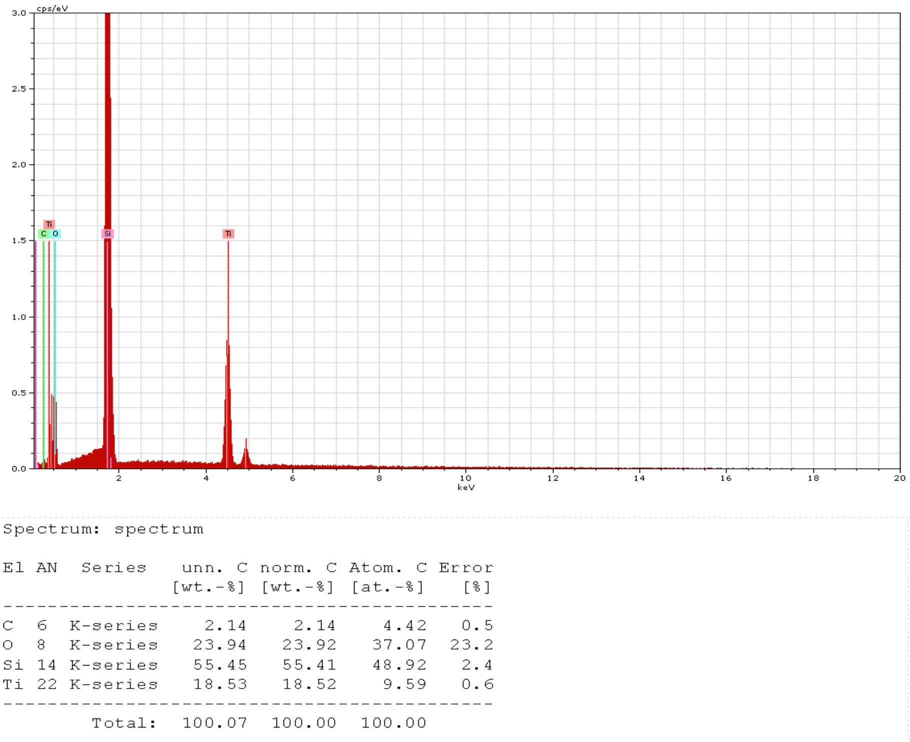

```
Spectrum: spectrum

El AN  Series   unn. C  norm. C  Atom. C  Error
               [wt.-%] [wt.-%]  [at.-%]    [%]
------------------------------------------------
C   6  K-series    2.14     2.14     4.42   0.5
O   8  K-series   23.94    23.92    37.07  23.2
Si  14 K-series   55.45    55.41    48.92   2.4
Ti  22 K-series   18.53    18.52     9.59   0.6
------------------------------------------------
        Total:  100.07   100.00   100.00
```

Figure 8. EDX results for TiO_2 ceramic nanotubes.

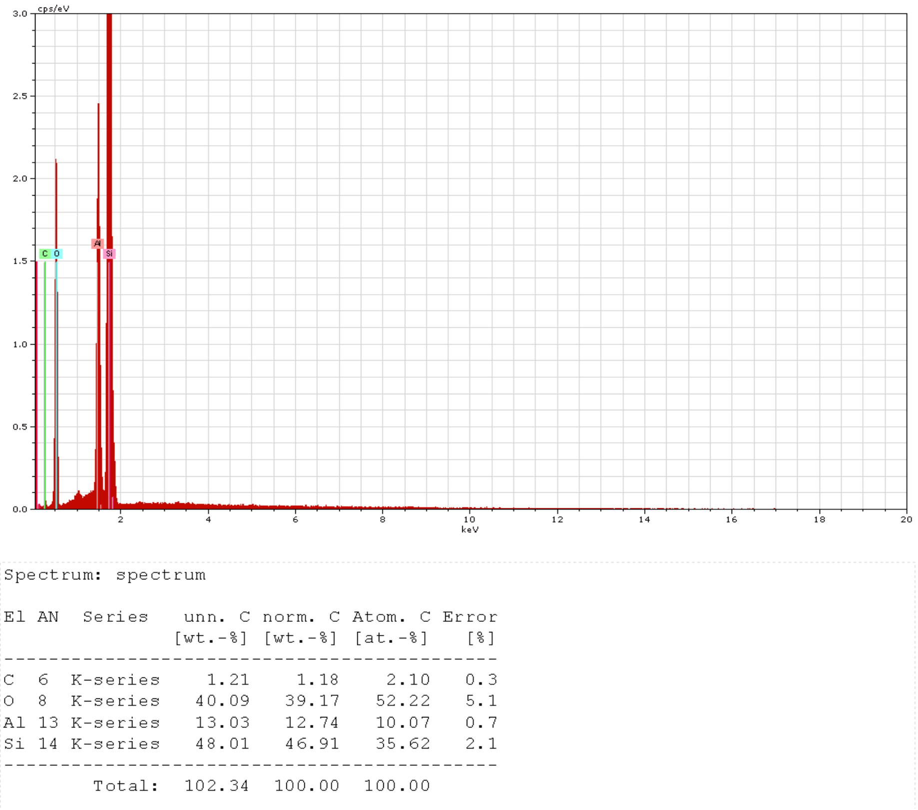

```
Spectrum: spectrum

El AN  Series   unn. C  norm. C  Atom. C  Error
               [wt.-%] [wt.-%]  [at.-%]    [%]
------------------------------------------------
C   6  K-series    1.21     1.18     2.10   0.3
O   8  K-series   40.09    39.17    52.22   5.1
Al  13 K-series   13.03    12.74    10.07   0.7
Si  14 K-series   48.01    46.91    35.62   2.1
------------------------------------------------
        Total:  102.34   100.00   100.00
```

Figure 9. EDX results for Al_2O_3 ceramic nanotubes.

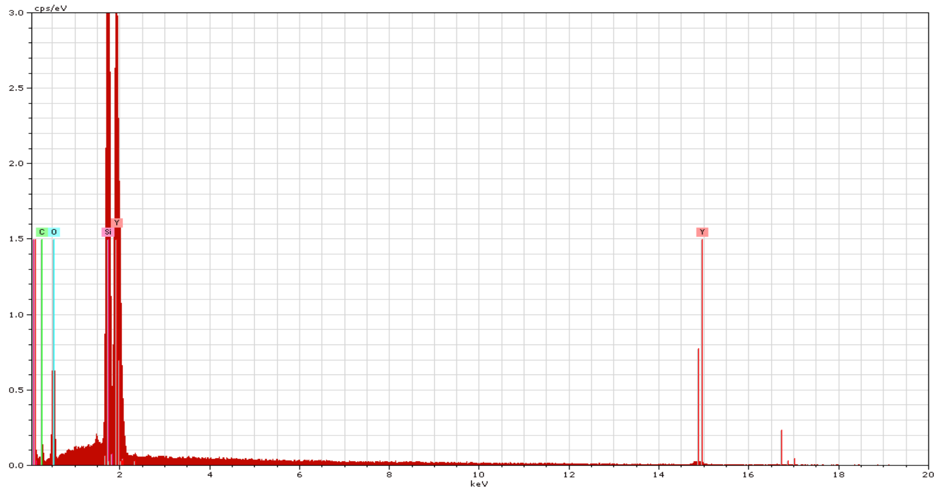

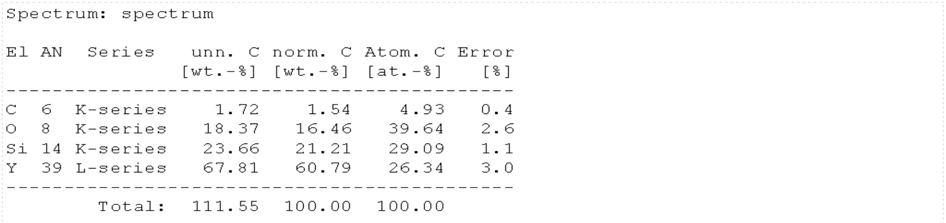

```
Spectrum: spectrum

El AN   Series    unn. C norm. C Atom. C Error
                 [wt.-%] [wt.-%] [at.-%]   [%]
-----------------------------------------------
C   6  K-series    1.72    1.54    4.93   0.4
O   8  K-series   18.37   16.46   39.64   2.6
Si 14  K-series   23.66   21.21   29.09   1.1
Y  39  L-series   67.81   60.79   26.34   3.0
-----------------------------------------------
        Total:  111.55  100.00  100.00
```

Figure 10. EDX results for Y_2O_3 ceramic nanotubes.

In the case of the ceramic nanotubes obtained after thermal treatment, EDX analysis emphasized the presence of metallic elements such as Ti (18.53%), Al (13.03%) and Y (67.8%), along with O and Si from the ceramic support on which the nanotubes were deposited. On the other hand, some residual C (under 2%) can be noticed, maybe remnants from the thermal process, captured and stabilized among the crystals of the nanotubes.

SEM Analysis

The morphological analysis of the PMMA polymer nanofibers covered with ceramic materials and of the ceramic nanotubes, obtained after thermal treatment, was performed using a high-resolution scanning electron microscope. The SEM images of the structures are presented in Figure 11 for TiO_2, Figure 12 for Al_2O_3, and Figure 13 for Y_2O_3.

In all cases, uniform dispersion of PMMA fibers within the deposited nets is noticed, with a uniform deposition of ceramic film upon PMMA fibers, as shown in Figures 11a, 12a and 13a. The nets maintained their dispersed and stable architecture after ceramic film deposition, due to the mechanical resistance assured by the optimal diameter of PMMA fibers.

Regarding the relative diameter of PMMA fibers covered with ceramic films, it is once again noticed that the dimensions are very close, between 0.5 and 0.6 µm, and the film deposition is quasi-uniform along the polymer fibers, as shown in Figures 11b, 12b and 13b, even if some vacancies can be noticed in the case of TiO_2 and Y_2O_3, where the grains themselves have a more dispersed dimension at nano-scale. Finally, the images of ceramic nanotube before and after thermal process are relevant, as shown in Figures 11c, 12c and 13c, reconfirming once again the uniformity of ceramic nanotube structures, which are really empty inside.

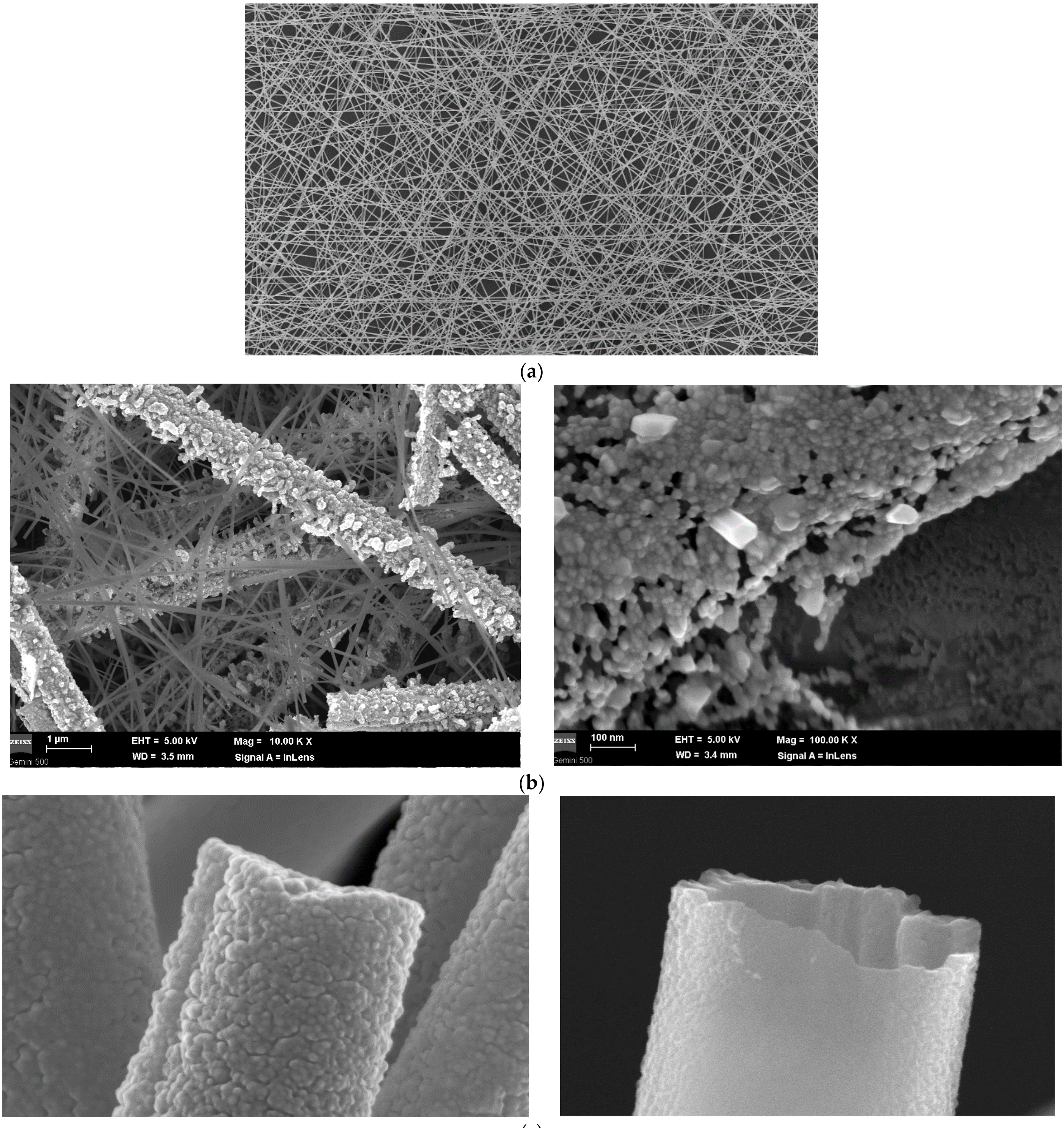

Figure 11. SEM images for TiO_2 ceramic nanotubes technology: (**a**) PMMA net with TiO_2 ceramic film (500 magnitude, selected area); (**b**) PMMA nanofiber with TiO_2 ceramic cover; (**c**) TiO_2 ceramic nanotube before and after thermal process (100 k magnitude, with image processing).

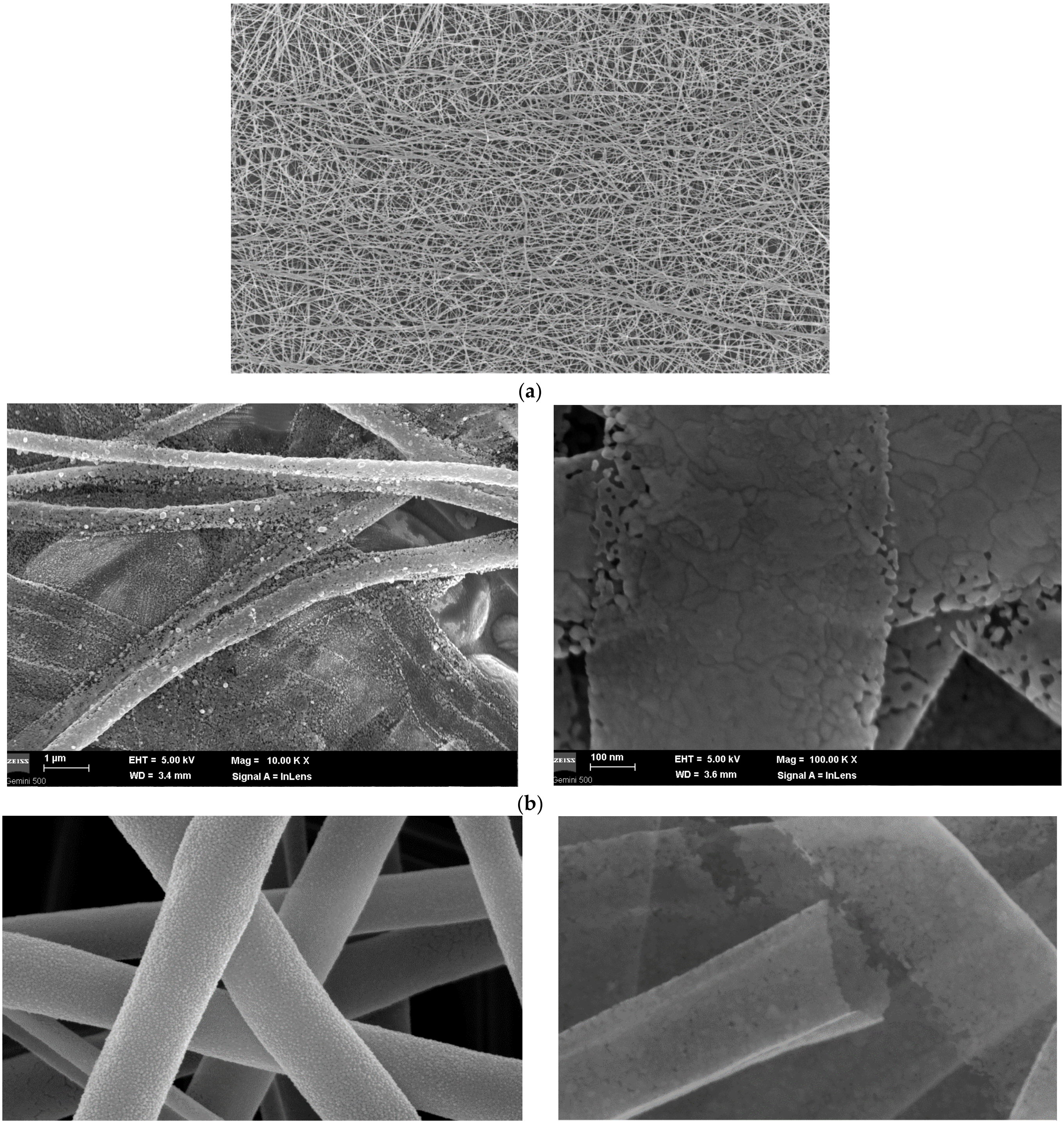
(**a**)
(**b**)
(**c**)

Figure 12. SEM images for Al_2O_3 ceramic nanotubes technology: (**a**) PMMA net with Al_2O_3 ceramic film (500 magnitude, selected area); (**b**) PMMA nanofiber with Al_2O_3 ceramic cover; (**c**) Al_2O_3 ceramic nanotube before and after thermal process (100 k magnitude, with image processing).

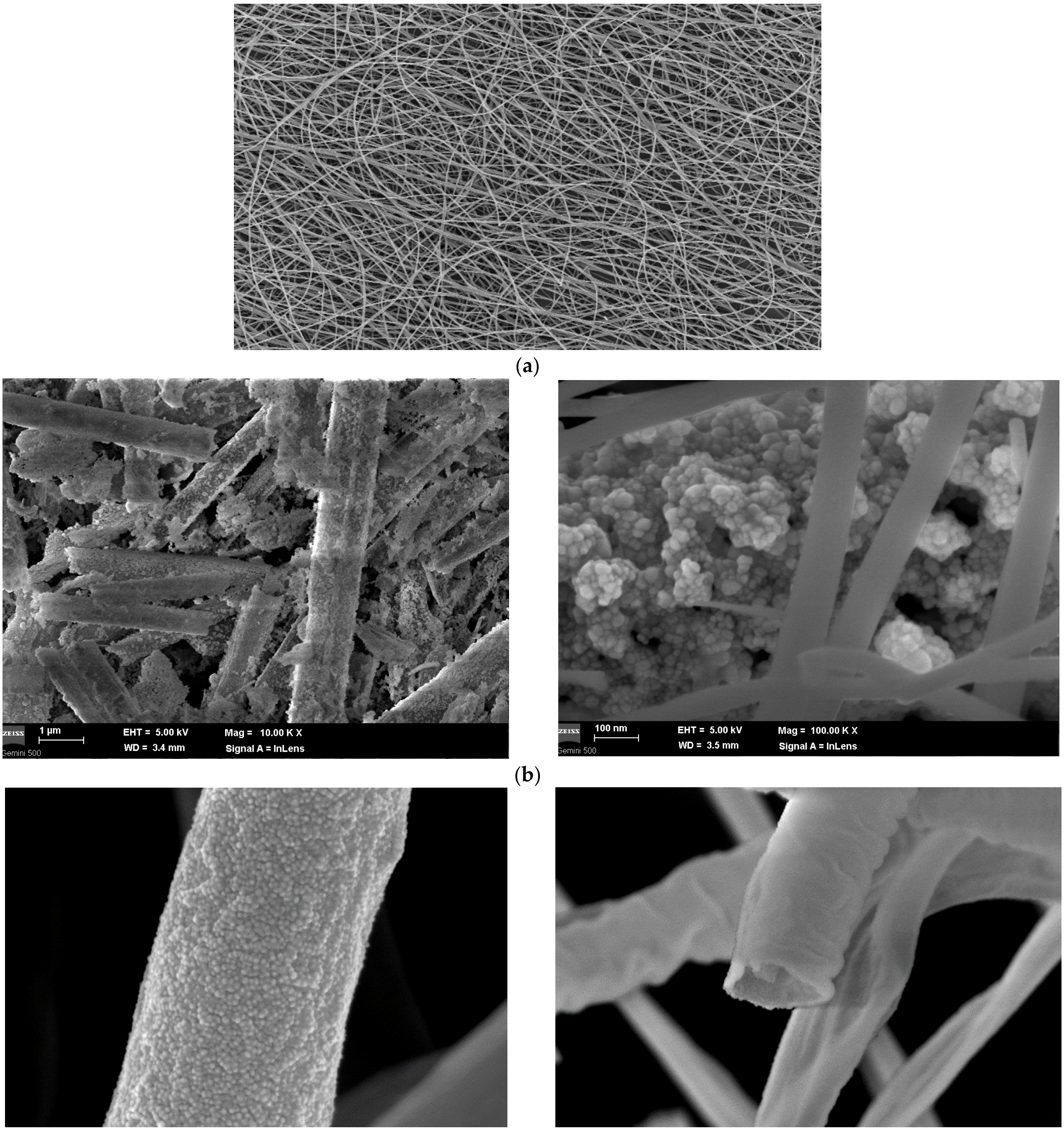

(**a**)

(**b**)

(**c**)

Figure 13. SEM images for Y_2O_3 ceramic nanotubes technology: (**a**) PMMA net with Y_2O_3 ceramic film (500 magnitude, selected area); (**b**) PMMA nanofiber with Y_2O_3 ceramic cover; (**c**) Y_2O_3 ceramic nanotube before and after thermal process (100 k magnitude, with image processing).

3. Preparation of Specialized Inks for Screen-Printed Sensors

The research was conducted towards preparation of ceramic nanotubes containing inks in order to deposit them in the form of screen-printed electrodes on both ceramic and flexible supports. Due to the proven synergy between carbon nanotubes and ceramic nanostructures described in the literature, although with other applications, e.g., in [47–50], the developed screen-printing inks started from commercial inks containing carbon nanotubes, already tested for printed electronics, to which a defined quantity of ceramic nanotubes was added. A slight increase in ink viscosity has no relevance for the screen-printing process, because the commercial inks themselves present larger values of viscosity, even if they are dedicated to printing on a wide range of materials in general [51].

3.1. Preparation of Carbon Nanotubes Containing Ink with Ceramic Nanotubes

The experimental ink was prepared by uniformly dispersing tailored quantities of ceramic nanotubes in the commercial ink mass, under continuous stirring at approximately 100 rpm. The process and the ink image (after a classical dispersion using a small brush on a SiO support) are presented in Figure 14, where the ceramic nanotubes can be identified.

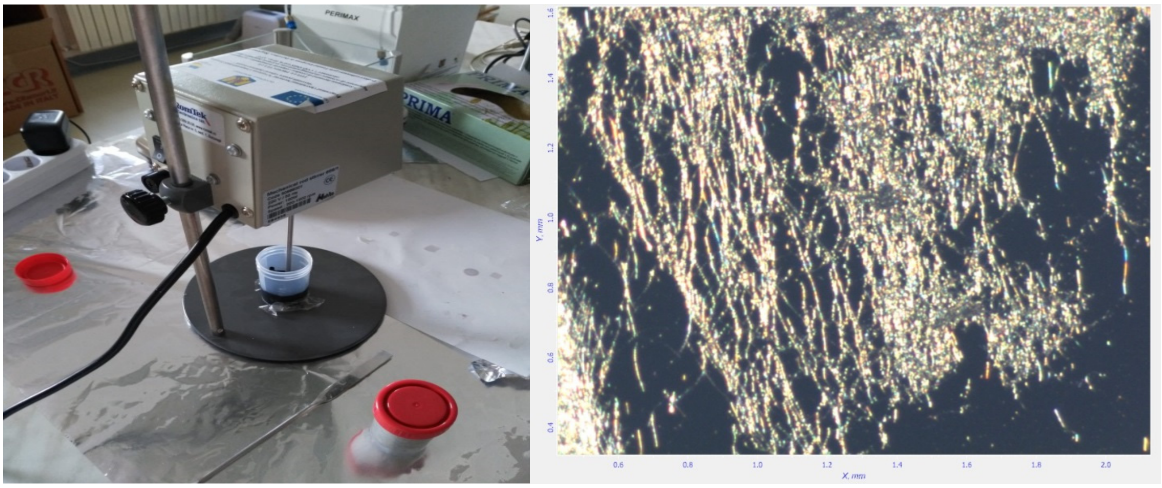

Figure 14. Preparation of experimental ink and image of the ink deposition.

The preliminary ink properties are presented in Table 2.

Table 2. Experimental ink features.

Characteristic	Value [+/− 5%]
Solids content [wt. %]	48
Density [g/mL]	2
Viscosity at 10 s^{-1}	6500
pH	6

An informal EDX microscopy analysis of ink after including the ceramic nanotubes (here TiO_2 nanotubes) is presented in Figure 15, emphasizing the active nanotube content.

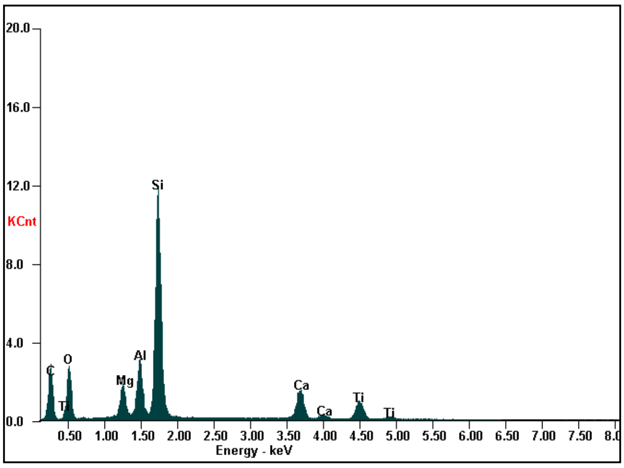

Element	*Wt%*	*At%*
CK	57.04	72.08
OK	13.96	13.24
MgK	02.41	01.50
AlK	04.22	02.37
SiK	15.61	08.44
CaK	03.53	01.34
TiK	03.25	01.03
Matrix	Correction	ZAF

Figure 15. EDX analysis of the experimental ink.

3.2. Experimental Printing and Testing Electrodes for a Classical Electrochemical Sensor

The conductive inks based on carbon and ceramic nanotubes were used for depositing the working electrode and the counter electrode of a classical electrochemical sensor (the connections are made with commercial silver-based inks).

The images of the experimental electrodes printed on the ceramic and polyethylene terephthalate (PET) supports are presented in Figure 16. The uniformity of the printing process can be noticed.

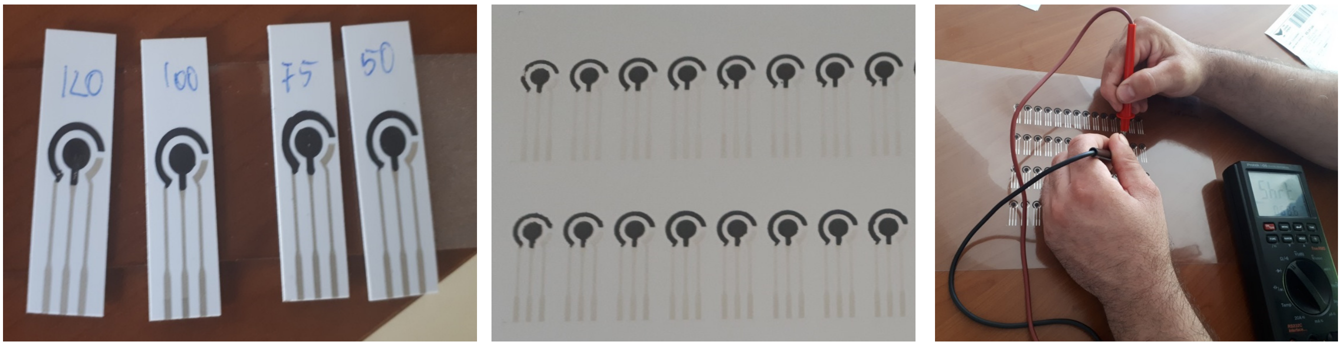

(**a**) (**b**) (**c**)

Figure 16. Experimental electrodes printed on (**a**) ceramic and (**b**) PET supports; (**c**) resistance measurements.

3.3. Results and Discussion

The SEM microscopy analysis of inks printed as experimental electrodes on PET are presented in Figures 17–19.

It can be noticed that electrodes printed with inks containing TiO_2 and Al_2O_3 nanotubes are more uniform, with lower roughness. The direction of screening can be also observed. As regards the electrodes printed with Y_2O_3 nanotubes, a higher roughness and some nonuniformity can be noticed, denoting the fact that these nanotubes are not mixing well with the carbon nanotubes within the experimental ink, and a specific additive should be tested in the future to increase the homogeneity of the ink.

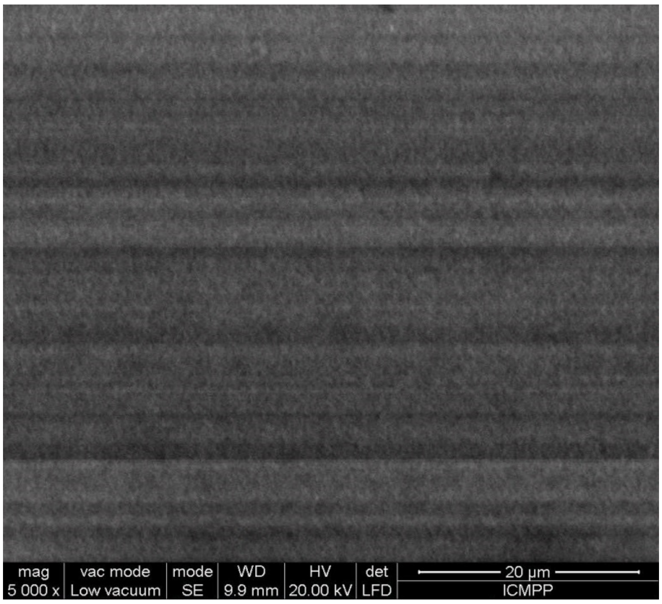

Figure 17. SEM images for the printed electrode with ink containing TiO_2 nanotubes.

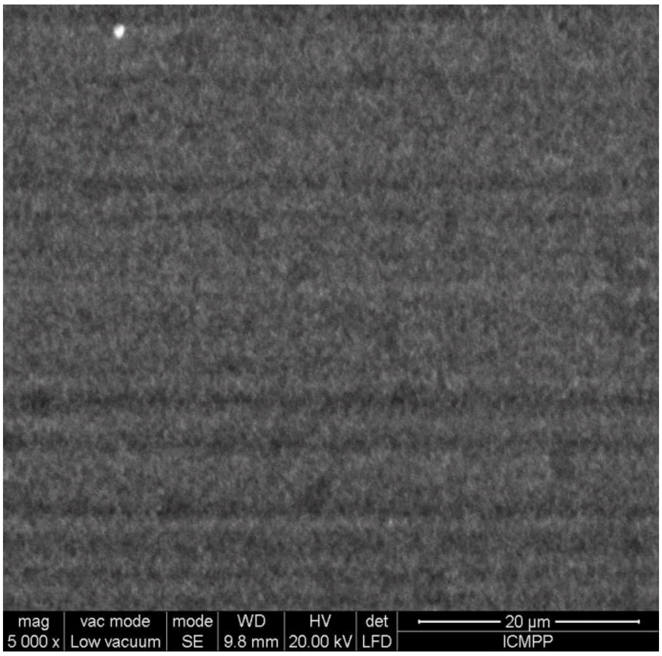

Figure 18. SEM images for the printed electrode with ink containing Al_2O_3 nanotubes.

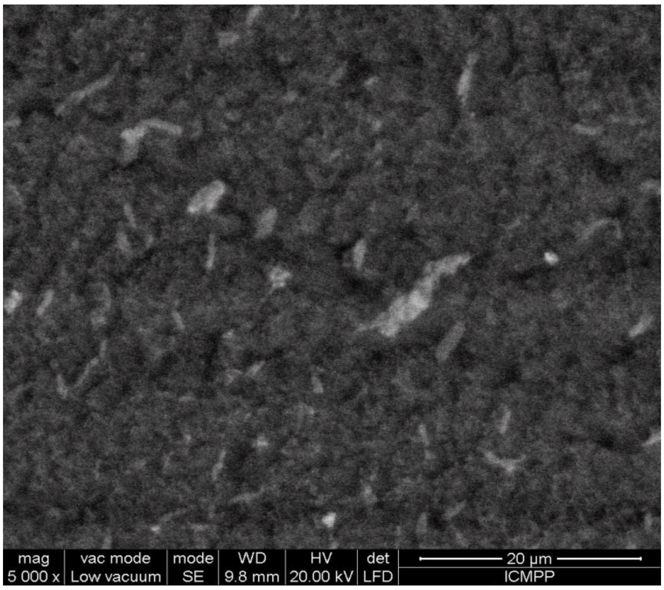

Figure 19. SEM images for the printed electrode with ink containing Y_2O_3 nanotubes.

The next step in printing technology with this experimental ink is related to the thermal maturation of printed electrodes. The commercial ink producer recommends for the ink with carbon nanotubes a maturation of up to 140 °C for maximum 10 min. We performed selective maturations from 50 °C to 120 °C (as seen in Figure 16a), but the comparative discussion was made for an exposure of 45 min at 75 °C, and of 15 min at 120 °C. In order to assess the curing of the experimental electrodes, both temperatures were taken into account, but the maturation process was assessed by the electrodes functionality, i.e., by testing their electrical resistance, measured with a precision ohmmeter, as in Figure 16. Informal images of the electrodes, after maturation at 75 °C and 120 °C, are presented in Figure 20 (here for the ink containing TiO_2 nanotubes, ceramic support).

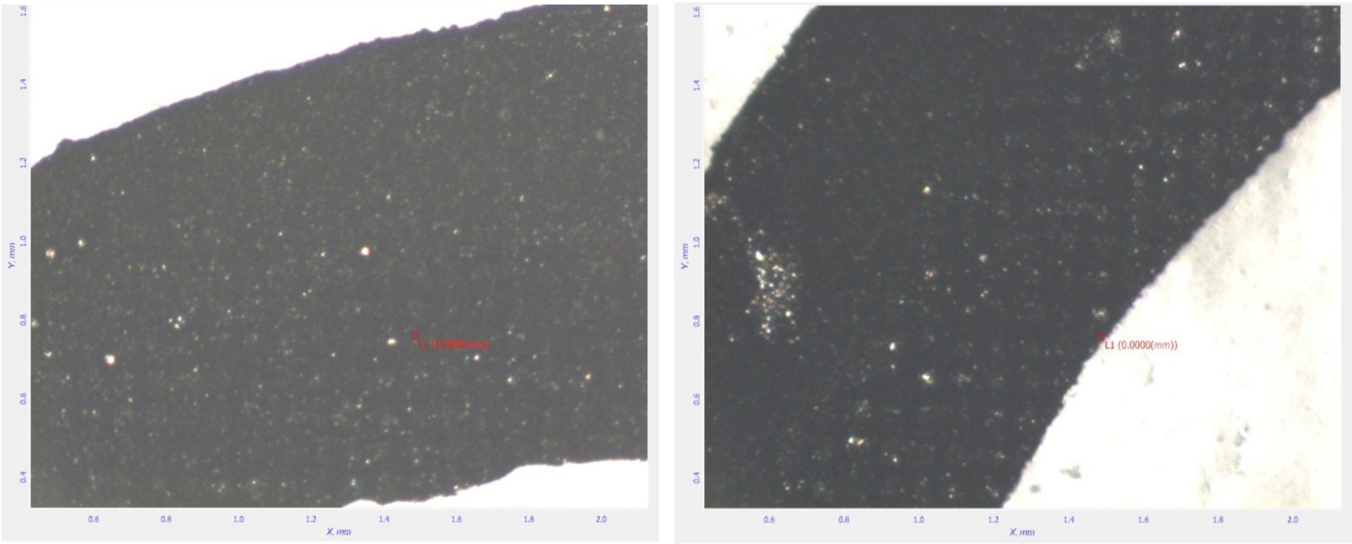

(**a**) (**b**)

Figure 20. Images of the printed electrodes containing TiO_2 nanotubes, after maturation at (**a**) 75 °C, and (**b**) 120 °C.

The darker color of the electrode maturated at 120 °C. The white dots are related to ceramic nanotube exposure.

A comparative analysis of the way the inks containing TiO_2, Al_2O_3, and Y_2O_3, dried on the PET support after maturation at 120 °C is presented in Figure 21. The most uniform printed electrode route was achieved for the ink with Al_2O_3; in the rest, some minimal ink splashes can be observed. Printing on PET is more difficult compared to on the ceramic support, due to the tendency of the ink to spread due to the different surface tension. On the other hand, the plastic support suffers a visible thermal deformation at 120 °C. That is why it is recommended that the thermal process of curing should be longer—at lower temperatures for the plastic support, i.e., at 75 °C, even if the temperature can be kept at 120 °C for the ceramic support.

The final evaluation is related to electric resistance assessment at 1 cm length for each ink containing TiO_2, Al_2O_3, and Y_2O_3, regardless of the support on which the electrode is placed. The experimental results are presented in Table 3, for electrode maturation at 75 °C and 120 °C. For comparison, the homologue resistance of the commercial carbon ink, used as a dispersion medium, was 3 Ω, in line with the values presented in Table 3, as explained by the low content of ceramic nanotubes. This is a very relevant aspect of printed electrodes, which benefit from the features of ceramic nanotubes without being detrimentally affected as regards their electrical parameters measured in direct current.

Table 3. Electric resistance of electrodes at 1 cm length.

Resistance [Ω]	Ink Containing TiO_2	Ink Containing Al_2O_3	Ink Containing Y_2O_3
75 °C	5.4	7.2	6.8
120 °C	3.2	3.4	3.6

An increase in the conductivity of electrodes can be observed in the case of printed structures thermally treated at 120 °C, compared to 75 °C. This can be explained by the stronger connections of carbon nanotubes with ceramic nanotubes, with some modifications at contact surfaces, due to some specific reactions, which are now under a separate analysis. As regards their semiconducting properties and possible relation when interfering with carbon nanotubes, we can estimate that: TiO_2 is a n-type semiconductor with a band gap of 3.2 eV, Al_2O_3 presents more insulating features, and Y_2O_3 may be assimilated with a semiconductor with a larger band gap of 5.5 eV, so the results of resistance are in line with the semiconducting features of each ceramic nanotube, i.e., the ink containing TiO_2 leads to the lowest values of resistance. Even so, for practical application for printed sensors on flexible substrate, the difference is not so significant from an electronic point of view, so caution related to imposing a lower curing temperature for inks printed on the plastic support can be maintained.

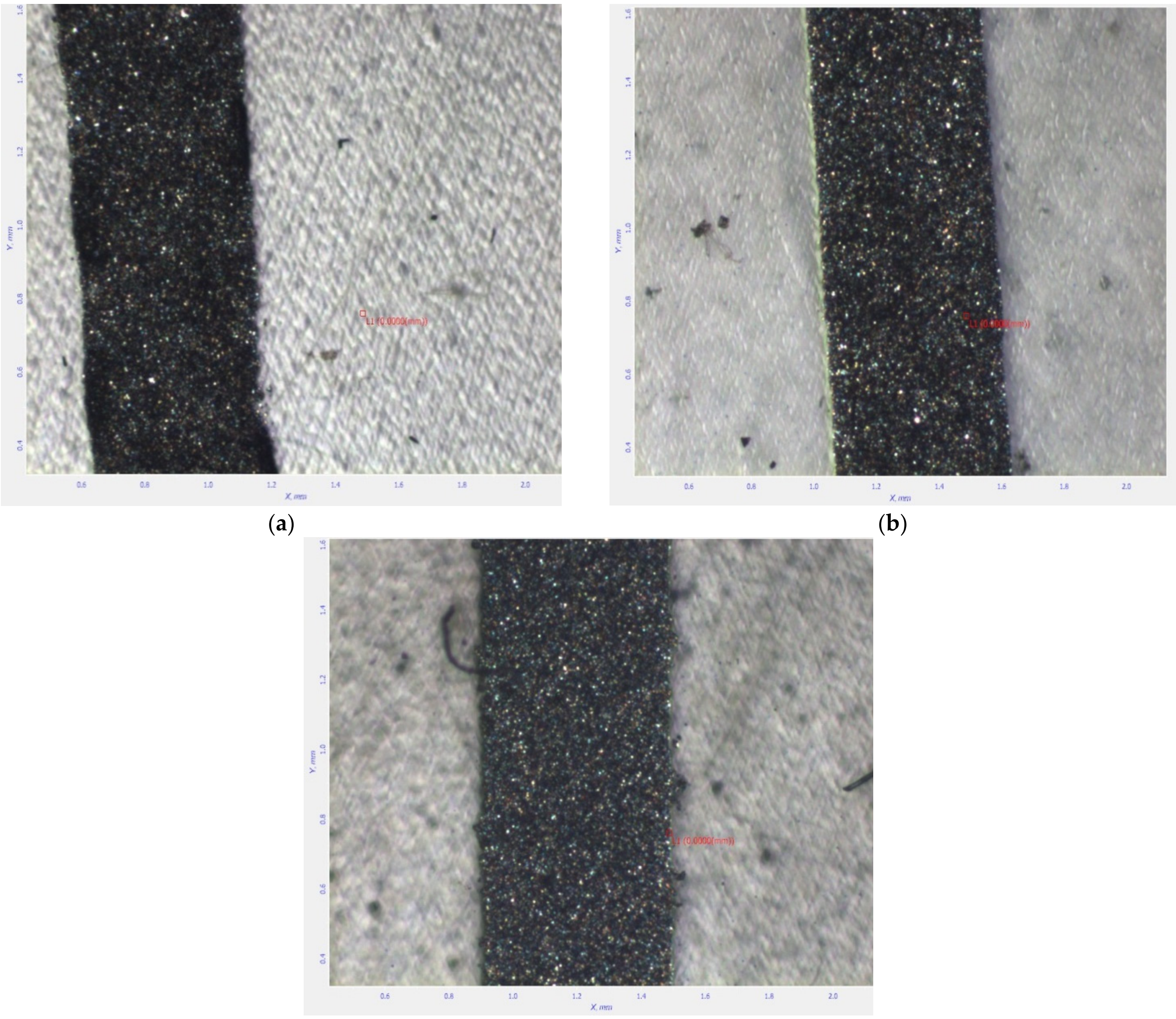

(**a**) (**b**)

(**c**)

Figure 21. Images of the printed electrodes of containing (**a**) TiO_2, (**b**) Al_2O_3, and (**c**) Y_2O_3 nanotubes, all after maturation at 120 °C.

In all, the experimental inks containing ceramic nanotubes can be considered feasible for printed electronics, because they offer fast curing at low temperatures, reasonable conductivity vs. electrode length, good printability on both ceramic or plastic (flexible) supports, good adhesion to surface after maturation (crosshatch adhesion of min. 4B) and minimal VOC exposure in electronic technology.

Further research will be dedicated to assessing the sensibility of such printed sensors in different chemical media and testing their features by using a potentiostat.

4. Conclusions

This paper describes the process to obtain ceramic nanotubes from titanium, aluminum and yttrium oxides by a feasible, replicable and reliable technology, including three stages: preliminary manufacture of polymer fibers nets of poly(methyl methacrylate) from a solution of 10 wt%, with dimethylformamide (DMF) as solvent; magnetron deposition of ceramic films upon PMMA nanofibers nets; thermal treatment of nanotubes at 600 °C for a complete combustion of PMMA support.

The best results for PMMA nanofibers nets were obtained by using a 10% PMMA solution at voltages of 20 kV, with a drum rotation speed of 5 rpm, because the fiber nets were more homogenous in spatial deposition, and also more homogenous in diameter. A minimum diameter of 0.3 µm was consider optimal for PMMA nanofibers in order to maintain the structural stability of covered fibers, from a mechanical point of view. After ceramic film deposition, the PMMA net structure leads to a fiber diameter of 0.5–0.6 µm.

After chemical–physical analyses of stages towards obtaining ceramic nanotubes, uniform dispersion of PMMA fibers within the deposited nets, with uniform deposition of ceramic film upon PMMA fibers, was noticed. Finally, images of ceramic nanotubes before and after thermal process were presented, reconfirming the uniformity of the ceramic nanotube structures, which are empty inside.

The technological purpose was to use such nanotubes as ingredients in screen-printing inks dedicated to printed electronics, with further target on innovative nano-sensor development, because no study directly targeted the subject of ceramic nanotube applications for printed electronics to date. Due to the proven synergy between carbon nanotubes and ceramic nanostructures, the developed screen-printing inks started from commercial inks containing carbon nanotubes, already tested for printed electronics, to which a defined quantity of ceramic nanotubes was added. The physical parameters of the new inks were as follows: solids content 48%; density 2 g/mL; viscosity at 10 s^{-1} 6500; pH 6. Uniform dispersion of ceramic nanotubes within the inks was demonstrated. The conductive inks based on carbon and ceramic nanotubes were used for depositing the working electrode and the counter electrode of a classical electrochemical sensor (the connections are made with commercial silver-based inks).

Electrodes printed with inks containing TiO_2 and Al_2O_3 nanotubes were more uniform, with lower roughness. After thermal curing of the electrodes, it was noticed that the most uniform printed electrodes were achieved for the ink with Al_2O_3; in the rest, some minimal ink splashes can be observed. Printing on PET is more difficult compared to on the ceramic support, due to the tendency of the ink to spread due to the different surface tension. On the other hand, the thermal process should be longer—at lower temperatures for the plastic support, because it may suffer thermal deformations.

A significant increase in the conductivity of electrodes can be observed in the case of electrodes thermally treated at 120 °C, compared to 75 °C, with at least 40%. This can be explained by the stronger connections of carbon nanotubes with ceramic nanotubes, with some modifications at contact surfaces, due to some specific reactions, to be further investigated.

The experimental inks containing ceramic nanotubes can be considered feasible for printed electronics, because they offer fast curing at low temperatures, reasonable conductivity vs. electrode length, good printability on both ceramic or plastic (flexible) supports and good adhesion to surface after maturation.

Author Contributions: Conceptualization, A.F.T. and R.C.C.; methodology, R.C.C., O.D.S., M.A. and A.F.T.; validation, R.C.C., O.D.S. and A.F.T.; formal analysis, A.F.T., S.T.A., M.A. and O.D.S.; investigation, R.C.C., O.D.S., A.F.T., M.A. and S.T.A.; data curation, R.C.C., O.D.S., M.A. and A.F.T.; writing—original draft preparation, A.F.T. and R.C.C.; writing—review and editing, R.C.C. and A.F.T.; visualization, R.C.C. and A.F.T.; supervision, A.F.T. and R.C.C. All authors have read and agreed to the published version of the manuscript.

Funding: This research received no external funding.

Data Availability Statement: The data presented in this study are available on request from the corresponding author.

Conflicts of Interest: The authors declare no conflict of interest.

References

1. Balhaddad, A.A.; Garcia, I.M.; Mokeem, L.; Alsahafi, R.; Collares, F.M.; Sampaio de Melo, M.A. Metal Oxide Nanoparticles and Nanotubes: Ultrasmall Nanostructures to Engineer Antibacterial and Improved Dental Adhesives and Composites. *Bioengineering* **2021**, *8*, 146. [CrossRef] [PubMed]
2. Lee, M.; Kim, T.; Bae, C.; Shin, H.; Kim, J. Fabrication and applications of metal-oxide nano-tubes. *JOM J. Miner. Met. Mater. Soc.* **2010**, *62*, 44–49. [CrossRef]
3. Researchers Learn to Control the Dimensions of Metal Oxide Nanotubes. Available online: https://phys.org/news/2007-08-dimensions-metal-oxide-nanotubes.html (accessed on 10 March 2024).
4. Enculescu, M.; Costas, A.; Evanghelidis, A.; Enculescu, I. Fabrication of ZnO and TiO2 Nanotubes via Flexible Electro-Spun Nanofibers for Photocatalytic Applications. *Nanomaterials* **2021**, *11*, 1305. [CrossRef]
5. Ramasamy, P.; Lim, D.H.; Kim, J.; Kim, J. A general approach for synthesis of functional metal oxide nanotubes and their application in dye-sensitized solar cells. *RSC Adv.* **2014**, *4*, 2858–2864. [CrossRef]
6. Li, D.; McCann, J.T.; Xia, Y.; Marquez, M. Electrospinning: A Simple and Versatile Technique for Producing Ceramic Nanofibers and Nanotubes. *J. Am. Ceram. Soc.* **2006**, *89*, 1861–1869. [CrossRef]
7. Li, Y.; Yang, X.Y.; Feng, Y.; Yuan, Z.Y.; Su, B.L. One-Dimensional Metal Oxide Nanotubes, Nanowires, Nanoribbons, and Nanorods: Synthesis, Characterizations, Properties and Applications. *Crit. Rev. Solid State Mater. Sci.* **2012**, *37*, 1–74. [CrossRef]
8. Azevedo, J.; Fernández-García, M.P.; Magén, C.; Mendes, A.; Araújo, J.P.; Sousa, C.T. Double-walled iron oxide nanotubes via selective chemical etching and Kirkendall process. *Sci. Rep.* **2019**, *9*, 11994. [CrossRef] [PubMed]
9. Parthangal, P. Direct synthesis of tin oxide nanotubes on microhotplates using carbon nanotubes as templates. *J. Mater. Res.* **2011**, *26*, 430–436. [CrossRef]
10. Falk, M.; Luwan, S.; Tintula, K.; Markus, A.; Sandra, S.; Ulrike, K.; Molina-Luna, L.; Duerrschnabel, M.; Kleebe, H.J.; Ayata, S.; et al. Free-Standing Networks of Core–Shell Metal and Metal Oxide Nanotubes for Glucose Sensing. *ACS Appl. Mater. Interfaces* **2017**, *9*, 771–781.
11. Kang, D.Y. Single-Walled Metal Oxide Nanotubes and Nanotube Membranes for Molecular Separations (Thesis). 2012. Available online: https://core.ac.uk/reader/10189860 (accessed on 10 March 2024).
12. Muto, H.; Sato, Y.; Tan, W.K.; Yokoi, A.; Kawamura, G.; Matsuda, A. Controlled formation of carbon nanotubes incorporated ceramic composite granules by electrostatic integrated nano-assembly. *Nanoscale* **2022**, *14*, 9669–9674. [CrossRef]
13. Mallakpour, S.; Khadem, E. Carbon nanotube–metal oxide nanocomposites: Fabrication, properties and applications. *Chem. Eng. J.* **2016**, *302*, 344–367. [CrossRef]
14. Rahat, S.S.M.; Hasan, K.M.Z.; Mondol, M.M.H.; Mallik, A.K. A comprehensive review of carbon nanotube-based metal oxide nanocomposites for supercapacitors. *J. Energy Storage* **2023**, *73*, 108847. [CrossRef]
15. Gupta, V.; Saleh, T. Syntheses of Carbon Nanotube-Metal Oxides Composites; Adsorption and Photo-Degradation, Volume: Carbon Nanotubes-From Research to Applications. 2011. Available online: https://www.intechopen.com/chapters/16834 (accessed on 10 March 2024). [CrossRef]
16. Wang, D.; Sun, W.; Su, C. Carbon Nanotube–Metal Oxide Nanocomposites. In *Metal Oxide Nanocomposites: Synthesis and Applications*; Scrivener Publishing LLC: Austin, TX, USA, 2020; Chapter 4. [CrossRef]
17. Saboor, F.H.; Ataei, A. Decoration of Metal Nanoparticles and Metal Oxide Nanoparticles on Carbon Nanotubes. *Adv. J. Chem.* **2024**, *7*, 122–145. [CrossRef]
18. Kumar, N.; Navani, N.K.; Manhas, S.K. Effect of Metal Oxide Nanoparticles on Carbon Nanotube Device Characteristics. *J. Electron. Mater.* **2021**, *50*, 528–536. [CrossRef]
19. Available online: https://eureka.patsnap.com/patent-CN103058173B (accessed on 10 March 2024).
20. Cho, H.H.; Smith, B.A.; Wnuk, J.D.; Fairbrother, D.H.; Ball, W.P. Influence of Surface Oxides on the Adsorption of Naphthalene onto Multiwalled Carbon Nanotubes. *Environ. Sci. Technol.* **2008**, *42*, 2899–2905. [CrossRef] [PubMed]
21. Elkady, M.F.; Hassan, H.S.; Amer, W.A.; Salama, E.; Algarni, H.; Shaaban, E.R. Novel Magnetic Zinc Oxide Nanotubes for Phenol Adsorption: Mechanism Modeling. *Materials* **2017**, *10*, 1355. [CrossRef]
22. Ali, M.A.; Solanki, P.R.; Srivastava, S.; Singh, S.; Agrawal, V.V.; John, R.; Malhotra, B.D. Protein Functionalized Carbon Nanotubes-based Smart Lab-on-a-Chip. *ACS Appl. Mater. Interfaces* **2015**, *7*, 5837–5846. [CrossRef] [PubMed]
23. Wang, H.; Boghossian, A. Covalent conjugation of proteins onto fluorescent single-walled carbon nanotubes for biological and medical applications. *Mater. Adv.* **2023**, *4*, 823–834. [CrossRef]
24. Hohman, M.; Shin, M.; Rutledge, G.; Brenner, M. Electrospinning and electrically forced jets. II. Applications. *Phys. Fluids* **2021**, *13*, 2221–2236. [CrossRef]
25. Zuo, W.; Zhu, M.; Yang, W.; Yu, H.; Chen, Y.; Zhang, Y. Experimental study on relationship between jet instability and formation of beaded fibers during electrospinning. *Polym. Eng. Sci.* **2005**, *45*, 704–709. [CrossRef]

26. Fridrikh, S.V.; Yu, J.H.; Brenner, M.P.; Rutledge, G.C. Controlling the Fiber Diameter during Electrospinning. *Phys. Rev. Lett.* **2003**, *90*, 144502. [CrossRef] [PubMed]
27. Tao, J.; Shivkumar, S. Molecular weight dependent structural regimes during the electrospinning of PVA. *Mater. Lett.* **2007**, *61*, 2325–2328. [CrossRef]
28. Oleiwi, A.; Jabur, A.; Alsalhy, Q. Preparation of Polystyrene/Polyacrylonitrile Blends by Electrospinning Technique. *J. Phys. Conf. Ser.* **2021**, *1879*, 022065. [CrossRef]
29. Kim, H.; Kim, W.; Jin, H.J.; Chin, I.J. Morphological Characterization of Electrospun Nano-Fibrous Membranes of Biodegradable Poly(L-lactide) and Poly(lactide-co-glycolide). *Macromol. Symp.* **2005**, *224*, 145–154. [CrossRef]
30. Nezarati, R.; Eifert, M.; Cosgriff-Hernandez, E. Effects of Humidity and Solution Viscosity on Electrospun Fiber Morphology. *Tissue Eng. Part C Methods* **2013**, *19*, 810–819. [CrossRef] [PubMed]
31. Wang, X.; Sun, M.; Murugananthan, M.; Zhang, Y.; Zhang, L. Electrochemically self-doped WO_3/TiO_2 nanotubes for photocatalytic degradation of volatile organic compounds. *Appl. Catal. B Environ.* **2020**, *260*, 118205. [CrossRef]
32. Kéri, O.; Kocsis, E.; Karajz, D.A.; Nagy, Z.K.; Parditka, B.; Erdélyi, Z.; Szabó, A.; Hernádi, K.; Szilágyi, I.M. Photocatalytic Crystalline and Amorphous TiO_2 Nanotubes Prepared by Electrospinning and Atomic Layer Deposition. *Molecules* **2021**, *26*, 5917. [CrossRef] [PubMed]
33. Stoilova, O.; Manolova, N.; Rashkov, I. Electrospun Poly(methyl methacrylate)/TiO2 Composites for Photocatalytic Water Treatment. *Polymers* **2021**, *13*, 3923. [CrossRef] [PubMed]
34. Chawraba, K.; Damiri, F.; Toufaily, J.; Lalevee, J.; Hamieh, T. TiO_2 Supported in Polymethyl methacrylate (PMMA) Properties, Preparation, and Photocatalytic Activity for the Degradation of Synthetic Dyes. *Lett. Appl. NanoBioSci.* **2024**, *13*, 13. [CrossRef]
35. Ounas, O.; El Foulani, A.; Lekhlif, B.; Jamal-Eddine, J. Immobilization of TiO_2 into a poly methyl methacrylate (PMMA) as hybrid film for photocatalytic degradation of methylene blue. *Mater. Today Proc.* **2020**, *22*, 35–40. [CrossRef]
36. Baji, A.; Mai, Y.W. Engineering Ceramic Fiber Nanostructures Through Polymer-Mediated Electrospinning, Volume: Polymer-Engineered Nanostructures for Advanced Energy Applications. 2017, pp. 3–30. Available online: https://link.springer.com/chapter/10.1007/978-3-319-57003-7_1 (accessed on 10 March 2024).
37. Mafakheri, E.; Salimi, A.; Hallaj, R.; Ramazani, A.; Kashi, M.A. Synthesis of Iridium Oxide Nanotubes by Electrodeposition into Polycarbonate Template: Fabrication of Chromium(III) and Arsenic(III) Electrochemical Sensor. *Electroanalysis* **2011**, *23*, 2429–2437. [CrossRef]
38. Lim, J.H.; Min, S.G.; Malkinskib, L.; Wiley, J. Iron oxide nanotubes synthesized via template-based electrodeposition. *Nanoscale* **2014**, *6*, 5289–5295. [CrossRef] [PubMed]
39. Alkanad, K.; Hezam, A.; Al-Zaqri, N.; Bajiri, M.A.; Alnaggar, G.; Drmosh, Q.A.; Almukhlifi, H.A.; Neratur Krishnappagowda, L. One-Step Hydrothermal Synthesis of Anatase TiO_2 Nanotubes for Efficient Photocatalytic CO_2 Reduction. *ACS Omega* **2022**, *7*, 38686–38699. [CrossRef] [PubMed]
40. Nakahira, A.; Kubo, T.; Numako, C. Formation Mechanism of TiO_2-Derived Titanate Nanotubes Prepared by the Hydrothermal Process. *Inorg. Chem.* **2010**, *49*, 5845–5852. [CrossRef]
41. Gao, H.; Tang, X.; Zhang, H.; He, Y.; Zhou, T.; Shen, J.; Zhu, L.; Si, T. Mechanical strength enhancement of $CaZr_4P_6O_{24}$ ceramics with multi-walled carbon nanotubes additions. *J. Alloys Compd.* **2024**, *976*, 173310. [CrossRef]
42. Porras, R.; Bavykin, D.V.; Zekonyte, J.; Walsh, F.C.; Wood, R.J. Titanate nanotubes for reinforcement of a poly(ethylene oxide)/chitosan polymer matrix. *Nanotechnology* **2016**, *27*, 195706. [CrossRef]
43. Hedayati, M.; Taheri-Nassaj, E.; Yourdkhani, A.; Borlaf, M.; Zhang, J.; Calame, M.; Sebastian, T.; Payandeh, S.; Clemens, F.J. $BaTiO_3$ nanotubes by co-axial electrospinning: Rheological and microstructural investigations. *J. Eur. Ceram. Soc.* **2020**, *40*, 1269–1279. [CrossRef]
44. Lin, Z.; Yang, Y.; Zhang, A. (Eds.) Engineering Ceramic Fiber Nanostructures Through Polymer-Mediated Electrospinning. In *Polymer-Engineered Nanostructures for Advanced Energy Applications*; Springer: Berlin/Heidelberg, Germany, 2017; Volume 3. [CrossRef]
45. Moreno, M.; Arredondo, M.; Ramasse, Q.M.; McLaren, M.; Stötzner, P.; Förster, S.; Benavente, E.; Salgado, C.; Devis, S.; Solar, P.; et al. ZnO nucleation into trititanate nanotubes by ALD equipment techniques, a new way to functionalize layered metal oxides. *Sci. Rep.* **2021**, *11*, 7698. [CrossRef]
46. Karacaoglu, E.; Öztürk, E.; Uyaner, M.; Losego, M.D. Atomic layer deposition (ALD) of nanoscale coatings on SrAl2O4-based phosphor powders to prevent aqueous degradation. *J. Am. Ceram. Soc.* **2020**, *103*, 3706–3715. [CrossRef]
47. Liu, H.; Takagi, D.; Ohno, H.; Chiashi, S.; Chokan, T.; Homma, Y. Growth of Single-Walled Carbon Nanotubes from Ceramic Particles by Alcohol Chemical Vapor Deposition. *Appl. Phys. Express* **2008**, *1*, 014001. [CrossRef]
48. Lamnini, S.; Pugliese, D.; Baino, F. Zirconia-Based Ceramics Reinforced by Carbon Nanotubes: A Review with Emphasis on Mechanical Properties. *Ceramics* **2023**, *6*, 1705–1734. [CrossRef]
49. Marinho, T.; Costa, P.; Lizundia, E.; Costa, C.M.; Corona-Galván, S.; Lanceros-Méndez, S. Ceramic Nanoparticles and Carbon Nanotubes Reinforced Thermoplastic Materials for Piezocapacitive Sensing Applications'. Available online: https://repositorium.uminho.pt/bitstream/1822/64639/1/37.pdf (accessed on 10 March 2024).

50. Single-Walled Carbon Nanotube-Ceramic Composites and Methods of Use (Patent). Available online: https://patents.google.com/patent/AU2004234395A1/en (accessed on 10 March 2024).
51. Chu, Z.; Peng, J.; Jin, W. Advanced nanomaterial inks for screen-printed chemical sensors. *Sens. Actuators B Chem.* **2017**, *243*, 919–926. [CrossRef]

International Journal of
Molecular Sciences

IMPACT FACTOR 4.9

Indexed in: PubMed

CITESCORE 9.0

Article

Chemiresistors Based on Hybrid Nanostructures Obtained from Graphene and Conducting Polymers with Potential Use in Breath Methane Detection Associated with Irritable Bowel Syndrome

Alexandru F. Trandabat, Romeo C. Ciobanu, Oliver Daniel Schreiner, Thomas Gabriel Schreiner and Sebastian Aradoaei

Special Issue
Two- and Three-Dimensional Nanostructured Materials for Biosensing Applications

Edited by
Dr. Ádám Juhász

MDPI

https://doi.org/10.3390/ijms25105552

International Journal of
Molecular Sciences

Article

Chemiresistors Based on Hybrid Nanostructures Obtained from Graphene and Conducting Polymers with Potential Use in Breath Methane Detection Associated with Irritable Bowel Syndrome

Alexandru F. Trandabat [1], Romeo C. Ciobanu [1,*], Oliver Daniel Schreiner [1], Thomas Gabriel Schreiner [1,2] and Sebastian Aradoaei [1]

[1] Department of Electrical Measurements and Materials, Gheorghe Asachi Technical University, 700050 Iasi, Romania; ftranda@tuiasi.ro (A.F.T.); oliver090598@yahoo.com (O.D.S.); schreiner.thomasgabriel@yahoo.com (T.G.S.); arsete@tuiasi.ro (S.A.)

[2] Department of Medical Specialties III, Faculty of Medicine, University of Medicine and Pharmacy "Grigore T. Popa", 700115 Iasi, Romania

* Correspondence: r.c.ciobanu@tuiasi.ro

Abstract: This paper describes the process of producing chemiresistors based on hybrid nanostructures obtained from graphene and conducting polymers. The technology of graphene presumed the following: dispersion and support stabilization based on the chemical vapor deposition technique; transfer of the graphene to the substrate by spin-coating of polymethyl methacrylate; and thermal treatment and electrochemical delamination. For the process at T = 950 °C, a better settlement of the grains was noticed, with the formation of layers predominantly characterized by peaks and not by depressions. The technology for obtaining hybrid nanostructures from graphene and conducting polymers was drop-casting, with solutions of Poly(3-hexylthiophene (P3HT) and Poly[(9,9-dioctylfluorenyl-2,7-diyl)-co-bithiophene] (F8T2). In the case of F8T2, compared to P3HT, a 10 times larger dimension of grain size and about 7 times larger distances between the peak clusters were noticed. To generate chemiresistors from graphene–polymer structures, an ink-jet printer was used, and the metallization was made with commercial copper ink for printed electronics, leading to a structure of a resistor with an active surface of about 1 cm^2. Experimental calibration curves were plotted for both sensing structures, for a domain of CH_4 of up to 1000 ppm concentration in air. A linearity of the curve for the low concentration of CH_4 was noticed for the graphene structure with F8T2, presenting a sensitivity of about 6 times higher compared with the graphene structure with P3HT, which makes the sensing structure of graphene with F8T2 more feasible and reliable for the medical application of irritable bowel syndrome evaluation.

Keywords: graphene; conducting polymers; chemiresistor; breath methane detection; irritable bowel syndrome

check for updates

Citation: Trandabat, A.F.; Ciobanu, R.C.; Schreiner, O.D.; Schreiner, T.G.; Aradoaei, S. Chemiresistors Based on Hybrid Nanostructures Obtained from Graphene and Conducting Polymers with Potential Use in Breath Methane Detection Associated with Irritable Bowel Syndrome. *Int. J. Mol. Sci.* **2024**, *25*, 5552. https://doi.org/10.3390/ijms25105552

Academic Editor: Ádám Juhász

Received: 19 April 2024
Revised: 15 May 2024
Accepted: 16 May 2024
Published: 20 May 2024

1. Introduction

Graphene, the thinnest and most resistant material, has extraordinary thermal conductivity and electronic mobility and has been the center of attention in recent years worldwide due to its exceptional characteristics with applicability in many fields. Graphene has been studied since the 1960s as monolayer graphite-on-metal substrates and even earlier as individual layers in graphite intercalation compounds. The first electrical measurements on monolayer graphene were published in 2004 [1], sparking interest in the fabrication of isolated samples by mechanical exfoliation of graphite. In order to make large volumes of devices, it is necessary to obtain graphene on large surfaces that are easy to handle and with as few defects as possible; an essential condition for the performance of the devices. There are different techniques for producing monolayer graphene but the most popular method at the moment is the so-called chemical vapor deposition (CVD) [2] on a

Ni or Cu film as a catalyst [3–8]. Using this method, large graphene surfaces—mono-bi- or multi-layered—of relatively high quality can be produced. The benefits of using CVD for the deposition of materials on the substrate include the very good quality of the resulting material, represented by impermeability, high purity, fine grain, and increased hardness compared to other coating methods. A major problem that the scientific world is still trying to solve is that although it is possible to obtain high-quality graphene on a substrate using CVD, successfully separating or exfoliating the graphene from the substrate proves to be more complicated because the bond between the graphene and the substrate is not yet fully understood. It is not easy to achieve the separation without damaging the graphene structure or the properties of the material. Separation techniques differ depending on the type of substrate used. Traditional delamination methods for graphene transfer use corrosive substances to remove the substrate which, in addition to high costs, produces polluting residues for the environment and dissolution of the substrate. Such techniques limit applicability at the industrial level. A feasible method is to obtain graphene by CVD on a Cu substrate. During the reaction that takes place between the Cu substrate and graphene, a high hydrostatic compression is created, coupling the graphene to the substrate [9]. It has been found possible, however, to intercalate a layer of copper oxide (which is mechanically and chemically weak) between the graphene and the substrate to reduce this pressure and allow the graphene to be removed relatively easily at low cost and without harmful chemicals, and the substrate can be even reused [10]. Electrochemical delamination can also use a non-polluting electrolyte resulting in the separation of, e.g., polymethyl methacrylate (PMMA)/graphene film from the substrate, which can be reused to obtain graphene. In this way, a non-destructive transfer of graphene from the metal substrate can be achieved [11,12]. In [13], a "bubble-free" transfer method was developed to avoid mechanical damage, i.e., the removal of the oxide layer formed by the infiltrated air at the graphene/Cu interface, resulting in a lower percentage of defects.

By its specific properties, graphene is targeting the global challenges in transparent electrodes, field-effect transistors, flexible touch screens, sensors for single-molecule gas detection, superconductivity, DNA sequencing, etc., as described in [14–16] for example. In the last few years, hybrid structures made by graphene with different polymers have largely been studied. In [17], a technology for obtaining graphene/polyaniline, graphene/poly(3,4 ethyldioxythiophene), and graphene/polypyrrole(PPy) nanocomposites is emphasized. In [18], a vast description of different hybrid structures including metallic oxides, graphene, and conducting polymers such as polyindole, polypyrrole, and polyaniline, is presented. In [19], an introduction to similar structures of graphene oxide/conducting polymer composites, this time as hydrogels, is offered. Other descriptions of similar technologies may be found in [20–25]. The development of such hybrid nanostructures is related to their special semiconducting features, exploitable for micro-electronic and/or electrochemical applications.

The first main application of the hybrid structures obtained from graphene and conducting polymers is related to sensors. In the last 15 years, various types of sensors have been developed, starting from the simplest ones, e.g., for humidity [26,27], temperature [28], gas detection [29–33], including waste gas evaluation [34] or other types of chemical sensors [35,36]; continuing with biosensors with different applications for the detection of dopamine, serotonin, cholesterol, bilirubin, uric acid, etc. [37–42]; dedicated sensors for environmental monitoring by the detection of pollutants in water, including heavy ions [43,44]; finalizing with food and drug analyses [45,46]. The second main application of the hybrid structures obtained from graphene and conducting polymers, occurring mainly in the last 10 years, is related to photovoltaic energy generation and energy storage applications/supercapacitors [47–49] as well as other photocatalytic applications [50].

In line with the above-described applications of bio-sensors, our paper intends to investigate the base of a new type of chemiresistors, with potential use in breath methane detection associated with irritable bowel syndrome. Hydrogen/Methane breath testing [51,52] is a widely used diagnostic tool based on the concept that some specific gases represent by-products of faulty fermentation, beyond the ones assured by gut microorganisms. On the other hand, the prevalence of irritable bowel syndrome, characterized by inflammation of the gastrointestinal tract—which has become a common disorder nowadays due to exposure to pollutants, food additives, and stress—represents a day-by-day preoccupation of many subjects, affecting their quality of life. Glucose, lactose, and fructose are normally absorbed mainly in the small intestine, and further in the colon; increased gas production following their ingestion is associated with malabsorption or premature fermentation due to excessive bacteria activity, micro-gas formation, and chemical attack at the level of intestinal cells. Consequently, methane gas is absorbed from the gastrointestinal tract, exhaled via the lungs, and is potentially measurable in breath. Increased gas production may predict small intestinal bacterial overgrowth, a precursor to irritable bowel syndrome. Secondly, such a phenomenon may be also related to intolerances to some food or food allergies, aspects which largely extend the importance of the use of such sensors. Unfortunately, detection of methane in the breath is challenging due to relatively small concentrations and inherent interferents, which is why only a few studies have been conducted in this direction but no commercial sensor has been developed to date.

Resistive gas sensors are versatile and cost-effective solutions for detecting a wide range of gases in diverse applications. Such sensors have a much simpler design, which allows for mass production and facile integration within signal processing systems. Using an adequate choice of sensing material, resistive gas sensors can be tailored to detect a specifically targeted gas, in our case methane [53–55]. On the other hand, they have reduced selectivity and longer response and recovery times [55–57]. Factors such as temperature and humidity may impact the performance of resistive gas sensors [58].

The importance of this research consists in the development of a simple and feasible concept of a resistive gas sensor based on graphene—conducting polymer assemblies, for the detection and evaluation of methane in breath—which can be related to the real occurrence and severity of irritable bowel syndrome. The sensor principle presented in the paper is much simpler, cost-effective, and more efficient compared to the homolog methods used nowadays [59]. It is considered that for the purpose of preliminary investigations related to irritable bowel syndrome, or for periodic checks at home, under room temperature conditions, the proposed chemiresistor can respond in a feasible way as long as the measurements are not taken in quick succession, and the syndrome detection is based on exceeding a pre-defined threshold value and not requiring a very exact assessment of the exhaled gas concentration.

2. Technology for Obtaining Graphene on Copper Substrate

2.1. Materials and Preparation Methods

The technology of graphene dispersion and support stabilization on chemical vapor deposition (CVD) equipment was based on the use of the AS-One 100 HT Rapid Thermal Processor installation (ANNEALSYS, Montpellier, France) placed in a clean room laboratory ISO 7 [60]. To obtain graphene, Cu foils (purity 99.9%) with dimensions of 2 × 2 cm and a thickness of 25 μm were used as substrates. Initially, the Cu foils were subjected to successive steps of ultrasonic cleaning in acetone and isopropyl alcohol (immersion time in each solvent being 10 min). The ultrasound was performed in an Elmasonic S 10 H ultrasound bath. After the cleaning step, the Cu foils were introduced into the CVD installation in order to deposit the graphene layers. The use of graphite as a susceptor has several advantages including good mechanical properties, thermal conductivity at high temperatures, and a low level of metal impurities. To further increase the purity, the susceptor was coated with a layer of silicon carbide (SiC) through a CVD process. The maximum temperature at which the SiC-coated graphite susceptor can be used is up to 1250 °C. Because SiC-coated graphite susceptors are sensitive to temperature gradients, low heating rates were used, especially for temperatures lower than 700 °C. After the cleaning process, the Cu foils were introduced into the working area of the CVD installation on the surface of the SiC-coated graphite susceptor. The process started with successive steps for cleaning the work area (pumping and purging) using Argon. Next, the preliminary pump was started up to 10 mBar in an atmosphere of Hydrogen. The process temperatures were 900 °C and 950 °C, respectively. To reach these temperatures, several heating and stabilization steps were used (250, 300, 500, and finally 900 °C) at a heating rate of 5 °C/s to extend the life of the susceptor. Finally, to reach the temperature of 900 °C, for good stabilization of the process, a 900 s duration was needed. Next, after the temperature was stabilized at 900 °C, the Cu substrate underwent treatment for 1800 s in an atmosphere of hydrogen during which the graphene layers formed on the crystallites of the Cu. After the process was finished, a 10-min pause was included before opening the work area for the susceptor to cool down. After cooling, the sample of Cu substrate covered with a graphene layer was taken with the help of tweezers, positioned on a special support in the clean room in the chemical niche, and submitted to a cleaning process with acetone and isopropyl alcohol.

To transfer the graphene to the substrate of interest, the following steps were carried out: First, a PMMA layer of approximately 600 nm was deposited by spin-coating at a speed of 3000 rpm for 60 s; second, a thermal treatment of the PMMA/graphene/Cu assembly at 100 °C for 20 min was applied, on a hot plate, resulting in the strengthening of the PMMA.

The next technological step was represented by the electrochemical delamination by use of a PARSTAT 4000 potentiostat (AMETEK Scientific Instruments Inc., Oak Ridge, TN, USA) with the related software. A cell with three electrodes and 0.5 M NaCl solution was used, i.e., a working electrode—the PMMA/graphene/Cu assembly—a calomel reference electrode (SCE), and a counter electrode—a Pt plate. A potential of −1.4 V was applied at the SCE, and after about 5 min, the detachment of graphene from the edges of the Cu substrate was observed. After about 7 min, the graphene was completely detached and the PMMA/graphene assembly floated. The assembly was further extracted by immersing it in a solution at 45 °C and transporting it in a vessel with demineralized water. After collecting the assembly, and drying (with a very weak nitrogen jet and then in dry air), acetone was used to dissolve the PMMA layer—a process that normally takes about 1 h—and finally, it was immersed in isopropyl alcohol to clean the sample of any debris and dried with a nitrogen jet. The samples were finally transferred onto a SiO_2/Si substrate.

2.2. Characterization Equipment

Scanning electron microscopy (SEM) was performed with Lyra III XMU equipment (TESCAN GROUP a.s., Brno-Kohoutovice, Czech Republic). A progressive morphological analysis was performed to evaluate the obtained graphene layer.

Atomic force microscopy (AFM) optical analysis was performed with a Dimension Edge unit (Bruker, Billerica, MA, USA). The roughness evaluation was conducted with the following derived parameters: Ra = Roughness Average; R_{Sk} = Skewness; RMS = Root Mean Square Roughness; R_{Ku} = Kurtosis. The results for the roughness parameters are presented as average for 4 scanned zones on each sample type.

2.3. Results and Discussion

2.3.1. SEM Analysis

Figures 1 and 2 show samples of graphene on Cu foil obtained by CVD at two temperatures, 900 °C and 950 °C, respectively. The difference in contrast is due to the number of monolayers in the obtained material.

In general, for both cases, the same morphology of grains—even when of different sizes—is present, with uniform distribution over the surface.

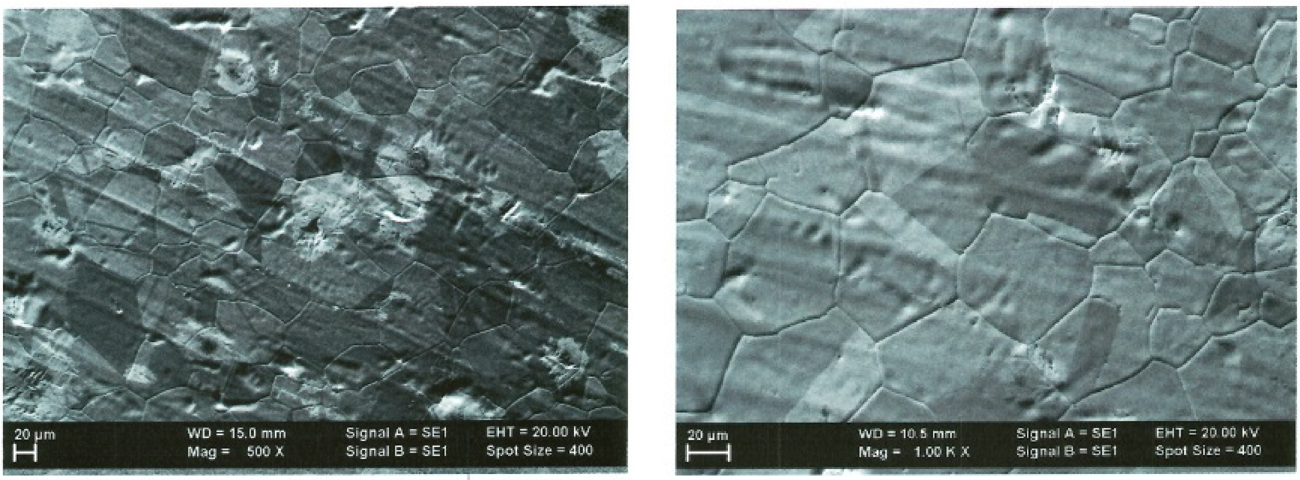

Figure 1. SEM images at 500× and 1000× magnification process at T = 900 °C.

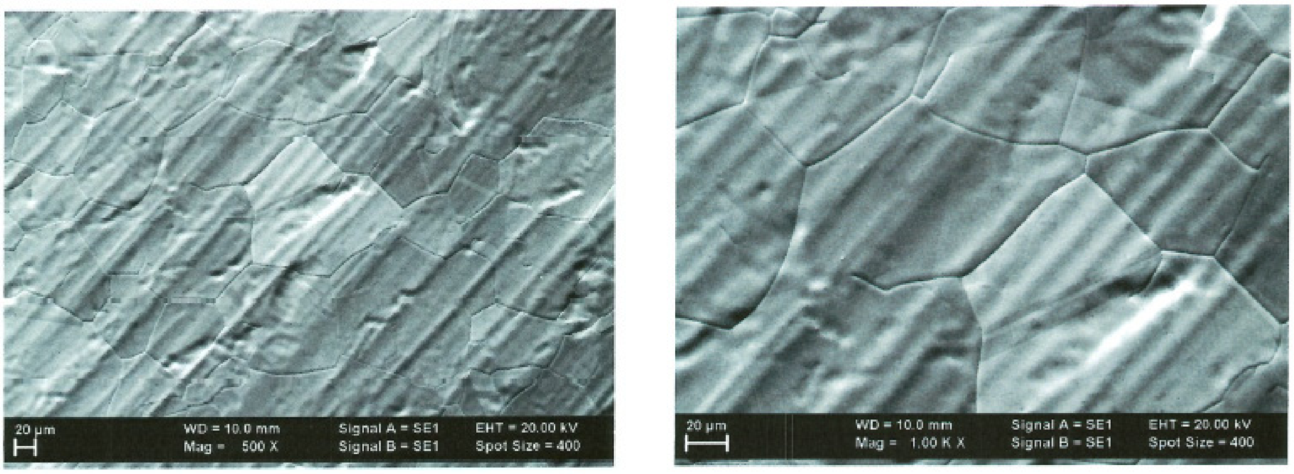

Figure 2. SEM images 500× and 1000× magnification process at T = 950 °C.

2.3.2. AFM Analysis

The AFM optical analysis shows the grain dimension, their distribution vs. surface, and the general roughness of the surfaces. The comparative optical analysis is presented in Figure 3.

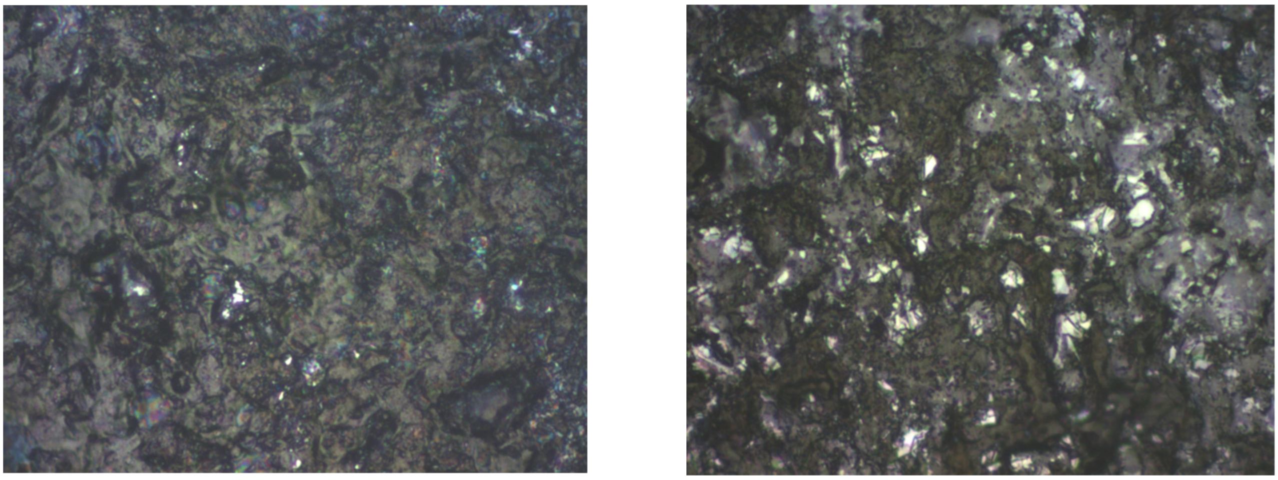

Figure 3. Optical analysis at 100× magnification process at T = 900 °C and T = 950 °C, respectively.

For the process at T = 900 °C, the grain size exceeds 2 µm, as seen in Figure 4. The grains are generally arranged either in smaller clusters or in slightly larger clusters, leading to the formation of zones characterized by slightly different R_{ku} or R_{sk} parameters but the coherence of statistical parameters led to the conclusion of a symmetric distribution of grains.

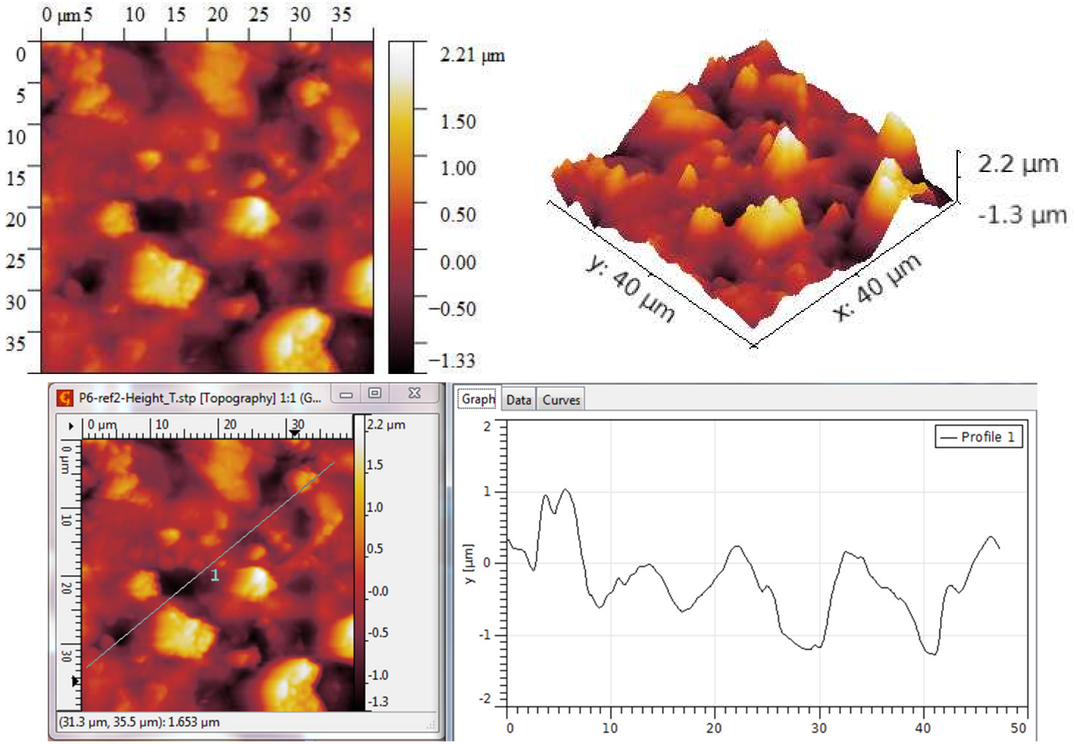

Figure 4. AFM Topographic 2D and 3D images and profile lines—process at T = 900 °C.

The R_{ku} value is above three, which means that the grains are placed such that they do not form depressions between them, and the R_{sk} value is also relatively high, which also suggests that no large depressions are formed, and hence more dense peaks are occurring, Table 1.

Table 1. Average roughness parameters determined by AFM lines—process at T = 900 °C.

Scanned Area	RMS (nm)	Ra (nm)	R_{Sk}	R_{Ku}
40 × 40 µm	489	376	0.447	3.63

For the process at T = 950 °C, the grain size is lower even if they exceed 1.5 µm, as seen in Figure 5. The grains are generally arranged mainly in larger clusters, leading to the formation of zones characterized by slightly different R_{ku} or R_{sk} parameters. Also, in this case, the coherence of statistical parameters led to the conclusion of a symmetric distribution of grains.

The R_{ku} value is above three, which means that the grains are placed such that they do not form large depressions between them, Table 2. The R_{sk} value is lower compared to the process at T = 900 °C, which suggests that more depressions are formed but they are not so deep. The density of peaks is lower, leading to a better balance between peaks and depressions.

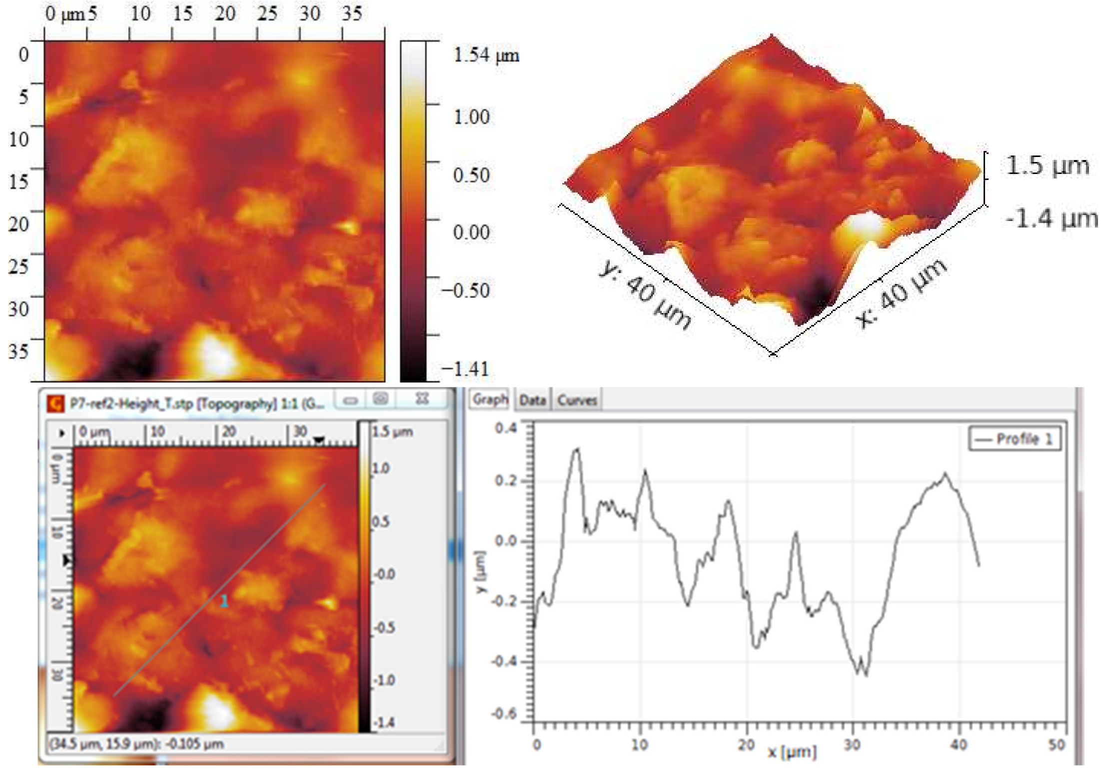

Figure 5. AFM Topographic 2D and 3D images and profile lines—process at T = 950 °C.

Table 2. Average roughness parameters determined by AFM lines—process at T = 950 °C.

Scanned Area	RMS (nm)	Ra (nm)	R_{Sk}	R_{Ku}
40 × 40 µm	339	243	0.261	4.26

In all, the process at T = 950 °C led to graphene structures characterized by RMS and R_a roughness parameters with lower values compared to the graphene structures obtained at T = 900 °C. This decrease may be due to a better settlement of the grains. Beyond this, the values of the parameters R_{ku} and R_{sk} indicate, in both cases, the formation of layers predominantly characterized by peaks and not by depressions, which means that the grains settle in such a way that they do not form holes between them. Accordingly, the graphene structures are uniform and without structural defects.

3. Technology for Obtaining Hybrid Nanostructures from Graphene and Conducting Polymers

3.1. Materials and Preparation Methods

Graphene structures obtained at T = 950 °C were chosen due to their lower values of roughness and better settlement of the grains compared to the graphene structures obtained at T = 900 °C. The technology for obtaining hybrid nanostructures from graphene and conducting polymers was drop-casting, and five samples of each type were manufactured for comparison of technological feasibility.

In the case of Poly 3-hexylthiophene (P3HT), 15 mg/mL of polymer was dissolved in $CHCl_3$ at room temperature in an ultrasonic bath and kept for 30 min for uniform dispersion.

In the case of Poly[(9,9-dioctylfluorenyl-2,7-diyl)-co-bithiophene] (F8T2), 20 mg/mL of polymer was dissolved in toluene at 60 °C in an ultrasonic bath, and kept for 30 min for uniform dispersion.

In both cases, 120 µL of each polymer solution was deposited on graphene (SiO_2/Si substrate) by the drop-casting method using Pasteur pipettes. The evaporation of each solvent took place for 30 min in vacuum, using a Pfeiffer vacuum pump connected to a desiccator.

3.2. Results and Discussion

3.2.1. Hybrid Nanostructures from Graphene and P3HT

For graphene covered with P3HT, a different topography is observed by AFM analysis compared to the graphene structures. Although, at first glance, at 100× it seems to have a fairly uniform grain distribution, at 500× it can be noticed that the roughness is quite high and the grains are arranged in different modes, Figure 6. Grains of different sizes but also smoother stretches can be observed.

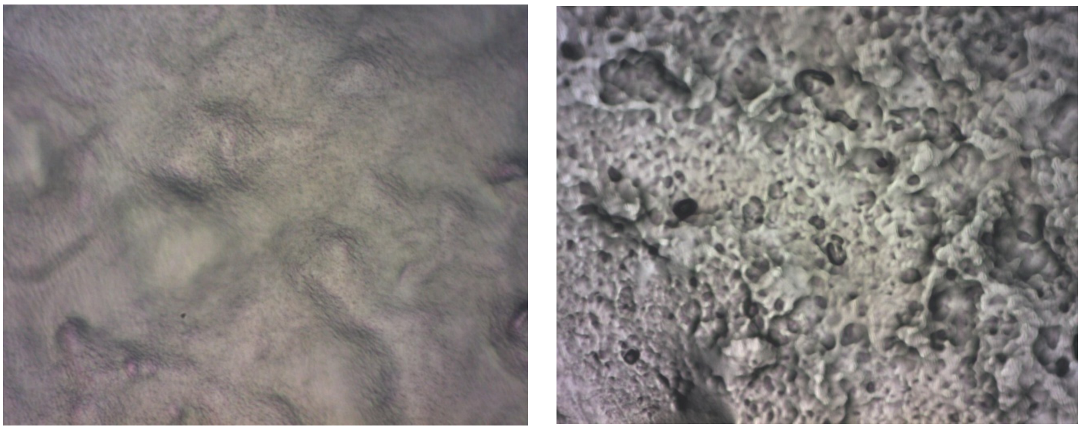

Figure 6. Optical analysis of graphene–P3HT at 100× and 500×.

The grain size is low, generally under 0.3 µm, as seen in Figure 7. The grains are generally arranged in larger clusters. The R_{ku} values are not very high, still around three, which means that the grain distribution is quite symmetrical. The R_{sk} values are low, even lower compared to graphene, indicating that more depressions are formed by polymer deposition, even if not so deep (no pits have been formed). In this case, we can estimate an about equal percent of peaks and depressions spread upon the surface, Table 3.

Table 3. Average roughness parameters determined by AFM lines—graphene, P3HT.

Scanned Area	RMS (nm)	Ra (nm)	R_{Sk}	R_{Ku}
40 × 40 µm	64	53	0.143	3.31

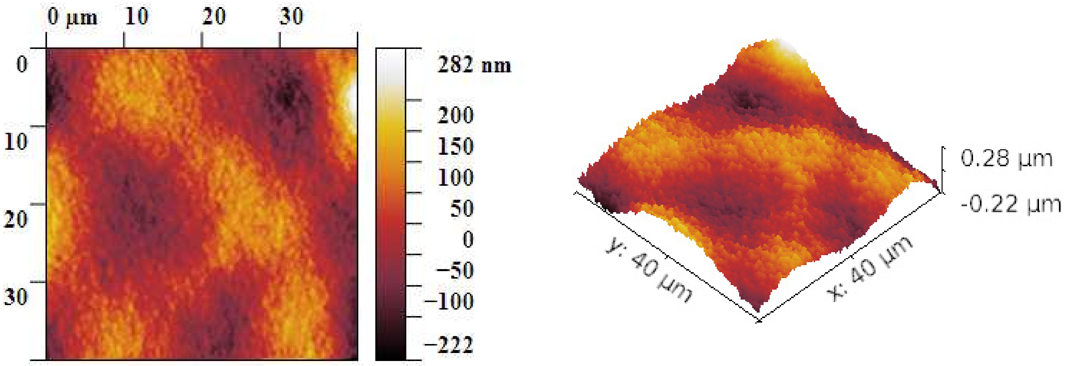

Figure 7. *Cont.*

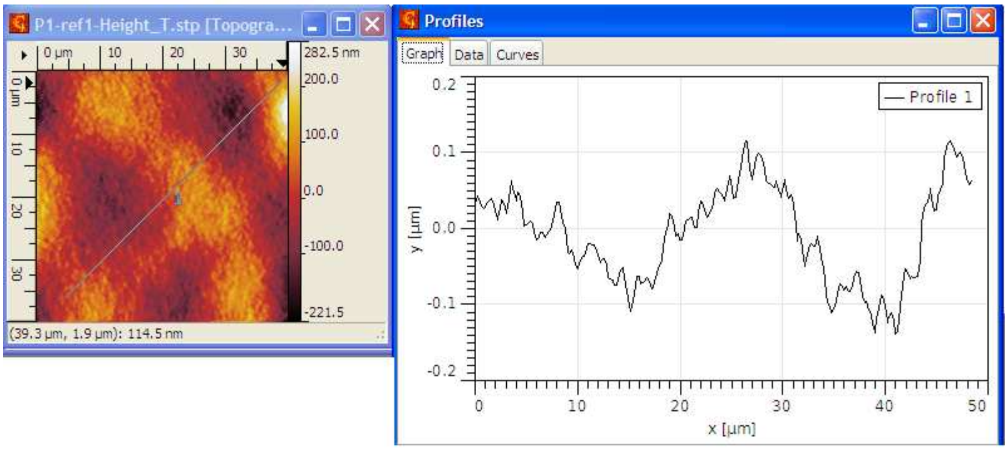

Figure 7. AFM Topographic 2D and 3D images and profile lines for graphene–P3HT.

3.2.2. Hybrid Nanostructures from Graphene and F8T2

For graphene covered with F8T2, a different topography is observed compared to graphene structures too. Analyzing Figure 8, at 500×, it seems to have a fairly uniform grain distribution but the roughness is high, much higher compared to the graphene deposited with P3HT. The grains are arranged less uniformly, and there are grains of different sizes separated by smoother stretches.

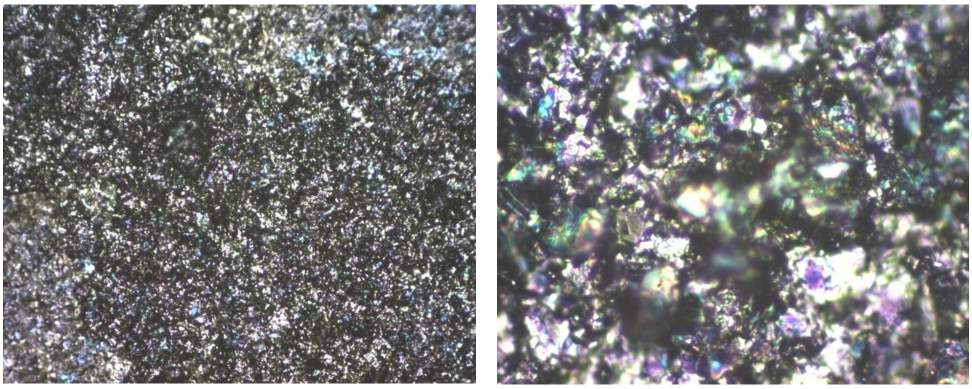

Figure 8. Optical analysis of graphene–F8T2 at 100× and 500×.

The grain size is generally 3 µm, about 10 times larger compared to the graphene deposited with P3HT, as seen in Figure 9. The grains are generally arranged in smaller clusters. The R_{Sk} values are low, indicating that some depressions are formed by polymer deposition but the depressions architecture is dispersed, and in general the grains settle without leaving too much free space between them. The R_{ku} values are not very high, still around three, which means that the grain distribution is quite symmetrical, Table 4.

Table 4. Average roughness parameters determined by AFM lines—graphene–F8T2.

Scanned Area	**RMS (nm)**	**Ra (nm)**	**R_{Sk}**	**R_{Ku}**
40 × 40 µm	705	546	0.191	3.36

In all, AFM emphasized a higher roughness in the case of F8T2 compared to P3HT and a much larger dimension of grain size. In both cases, a quite symmetrical distribution of grains was noticed, with reduced free space between them. Such structures with symmetrical distribution and roughness dimension at a micrometer-scale are considered optimal for the application as gas sensors.

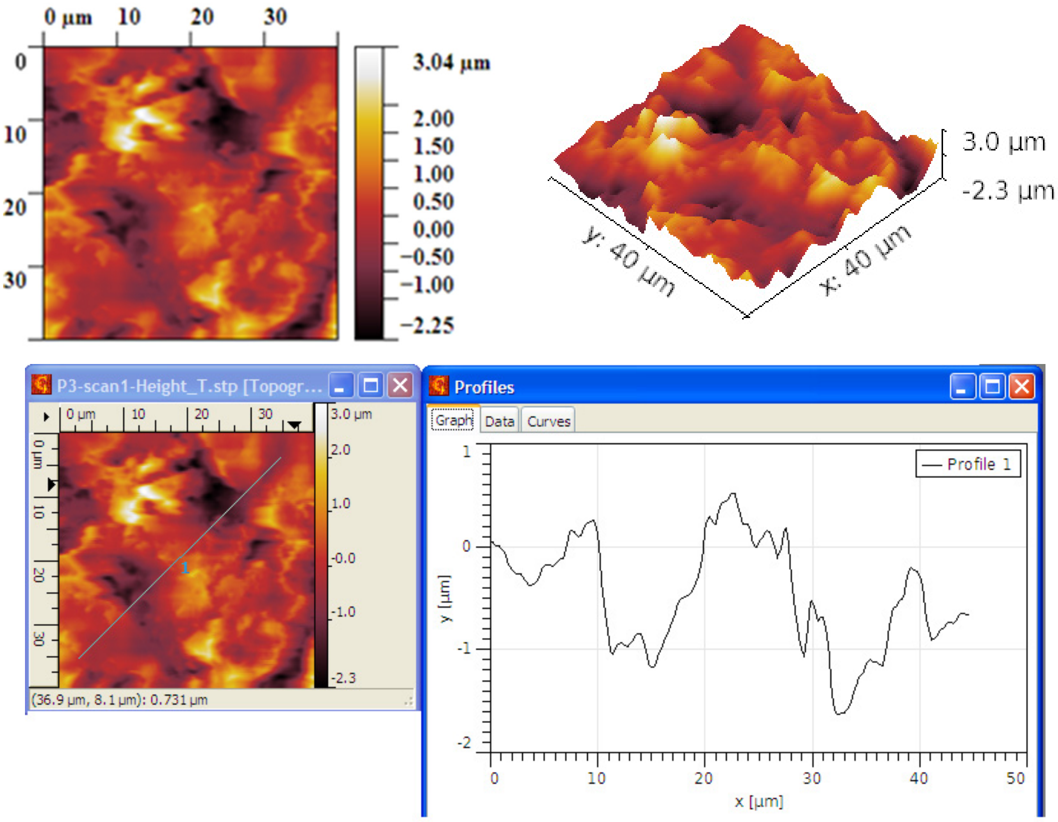

Figure 9. AFM Topographic 2D and 3D images and profile lines for graphene–F8T2.

4. Analysis of Functionality as Gas Sensors for Methane

In the literature, different processes of metallization of graphene-supported composite materials are described, e.g., in [61], most of them are inadequate for simple sensor purposes. In our case, an ink-jet printer was used, and the metallization was made with commercial copper ink for printed electronics. A structure of a resistor was generated, with an active surface of about 1 cm^2, limited by two metalized areas forming the conductive connections. Its functionality as a gas sensor was tested using an experimental system, similar to the one described in [62]. The sensor was introduced in a closed enclosure, which only allowed the exchange of gases by two valves and access to the electrical connections. The resistance of the sensor was measured externally, by a precision ohmmeter. Variable mixtures of CH_4 in synthetic air (80% nitrogen and 20% oxygen) were passed through the closed enclosure through one of the valves and let free on the other, to maintain a pressure of 1 atm. The exact content of CH_4 in synthetic air was separately analyzed, sample by sample, by use of a 7890 portable combustible gas detector (Seitron SpA, Mussolente, Italy) in order to correlate the resistance and CH_4 concentrations on the calibration curves.

Due to the large difference in roughness (grain size), the behavior of both graphene structures with F8T2 and with P3HT deposition were comparatively analyzed for their potential features on methane detection. As observed in Figures 10 and 11, the distribution of the cavities between peaks is different but still uniformly dispersed. In these figures, some distances between the peak clusters are marked with yellow arrows. In the case of the graphene–F8T2 structure, the distances between the peak clusters are about 7 times larger compared to the graphene–P3HT structure (e.g., about 20 µm compared to about 3 µm), under the circumstances that also the peaks were found about 10 times higher (Figures 7 and 9). Consequently, any potential difference in sensitivity of the developed sensing structures can be explained further by this spatial architecture.

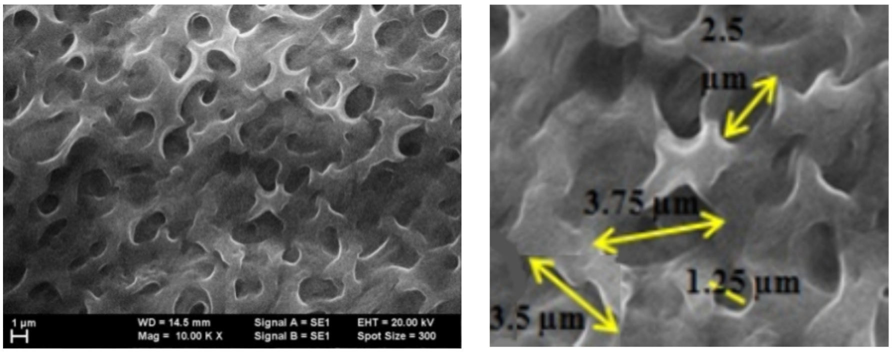

Figure 10. SEM image for graphene–P3HT structure.

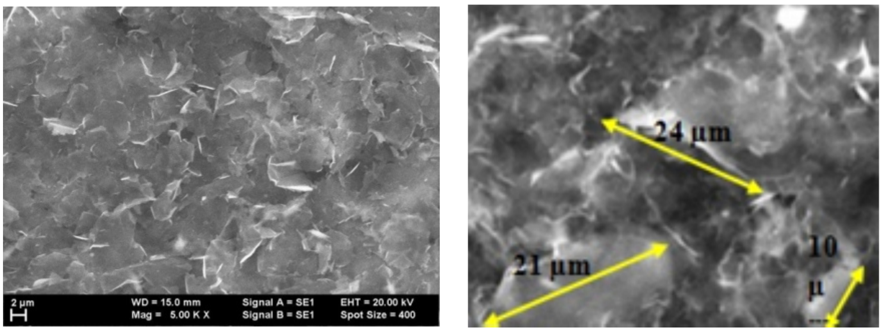

Figure 11. SEM image for graphene–F8T2 structure.

Experimental calibration curves were plotted for both sensing structures (Graphene-P3HT/G-P3HT and Graphene-F8T2/G-F8T2) for a larger domain of CH_4, concentration in air, of up to 1000 ppm CH_4. The limit of detection (LoD) was found as 50 ppm, a very reasonable value for many potential applications, as presented in Figure 12.

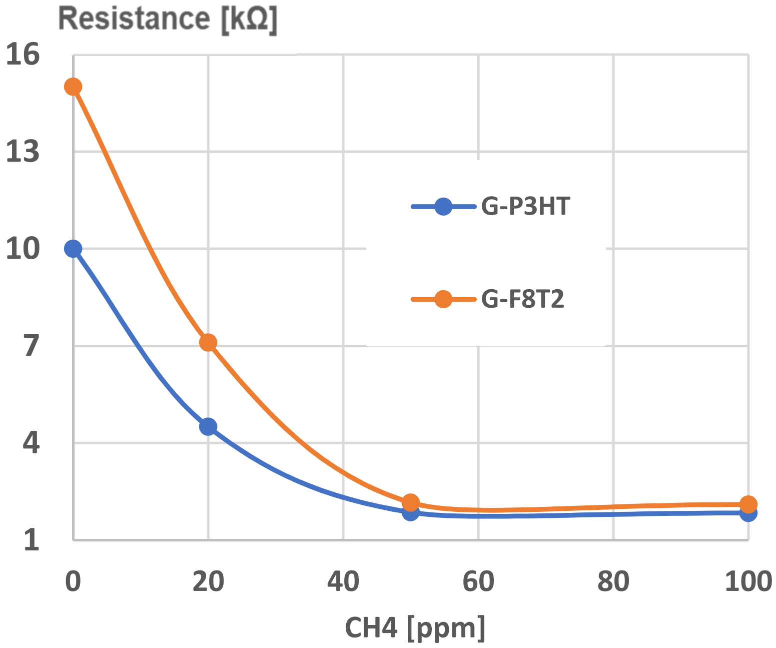

Figure 12. Limit of detection for sensing CH_4.

Under this value of CH_4 concentration in air, the resistance of both sensors presents extremely high values, with low credibility to be put in correlation with lower values of gas concentration.

A preliminary experimental calibration curve for sensing CH_4 for general use is presented in Figure 13. A high degree of correlation can be noticed in both cases. The curve for the graphene structure with P3HT presents a high linearity and lower values of resistance, which makes it useful for large-scale determination of CH_4 concentrations in air when using a simple signal processing system. By comparison, the curve for the graphene structure with F8T2 may be approximated with a polynomial curve of at least second degree, which makes the signal processing approach more difficult, and, consequently, may increase the sensor cost. On the other hand, the slope of the characteristic for the graphene structure with P3HT is low, an aspect that indicates a lower sensitivity of the sensor. The sensor sensitivity can be clearly put in relation to the active surface of the sensor exposed to the targeted gas, and in our case, the surface architecture of the graphene structure with F8T2 presents a larger active surface due mainly to higher and more dense peaks, as noticed in Figures 9 and 11.

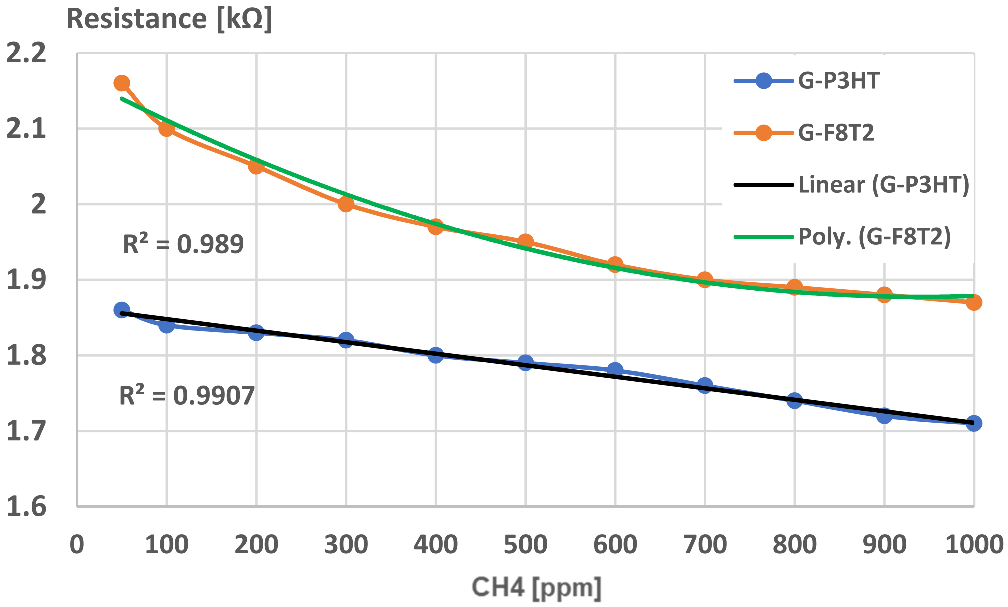

Figure 13. Experimental calibration curve for sensing CH_4 for general use.

But, if the application for testing the breath methane detection associated with irritable bowel syndrome is targeted, lower CH_4 concentrations in air must be detected, with a threshold value of, e.g., 100 ppm, which may indicate the syndrome occurrence [62,63]. In this case, a new experimental calibration curve was analyzed, Figure 14. Here, one can notice that both curves have a high degree of linearity for this CH_4 concentration domain but the slope for graphene structure with F8T2 is 6 times higher compared with the graphene structure with P3HT, which makes this structure more sensitive, feasible, and reliable for medical application. The inferior limit of CH_4 concentration detection, here 50 ppm, is considered enough when taking into account the correlation of CH_4 production with the severity of irritable bowel syndrome because lower concentrations do not particularly indicate a real occurrence of irritable bowel syndrome, [62,63]. In some studies, e.g., as described in [64,65], lower concentrations of CH_4 (20–40 ppm) were also analyzed but only for the purpose of detecting specific intestinal bacterial overgrowth, which may eventually influence the occurrence of irritable bowel syndrome; however, this approach was not the purpose of this paper as it targets the already established irritable bowel syndrome.

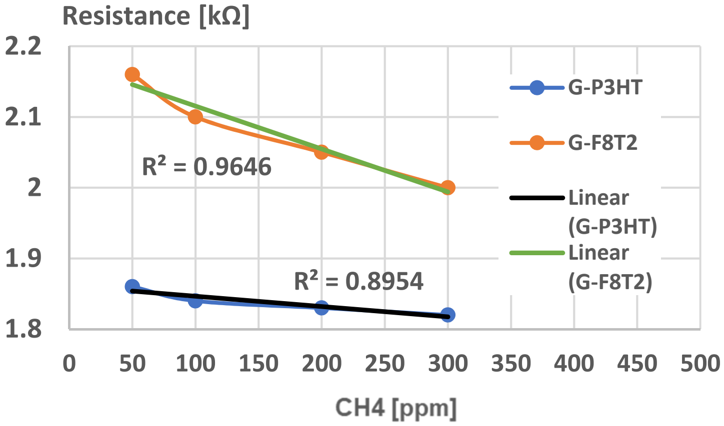

Figure 14. Experimental calibration curve for sensing CH_4 for medical use.

A final comparative analysis of the sensing structures of graphene with P3HT, and, respectively, with F8T2, is presented in Figure 15, indicating the resistance–time evolution when measuring four different concentrations of CH_4 (50, 100, 200, and 300 ppm). "On" marks the moment when starting the measurements with CH_4 and synthetic air-tailored mixtures, till the stationary value of resistance is obtained, as indicated in Figure 14. "Off" indicates the moment when only synthetic air is sent to the sensor, till it reaches the initial value of resistance in air. Both resistance decrease and restoration display a quasi-exponential characteristic. At first view, the increased sensitivity of the structure of graphene with F8T2 is noticed, leading to a quicker response.

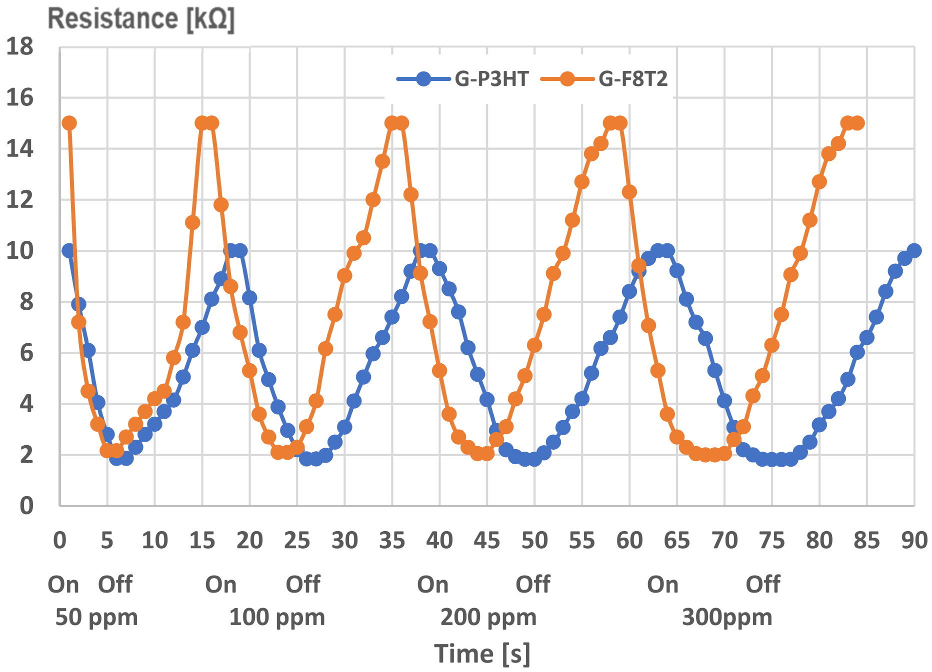

Figure 15. Experimental resistance–time curves for the sensing structures.

The evaluation of the experimental response (on) and recovery time (off) for the sensing structures is presented in Figure 16. It was noticed that, in general, both response and recovery time values are lower for the structure of graphene with F8T2. The difference is even much higher at lower concentrations of CH_4 (50, 100 ppm). An interesting phenomenon occurs at higher concentrations of CH_4 (200, 300 ppm) regarding the recovery time when both structures seem to reach the same values, exceeding 12 s.

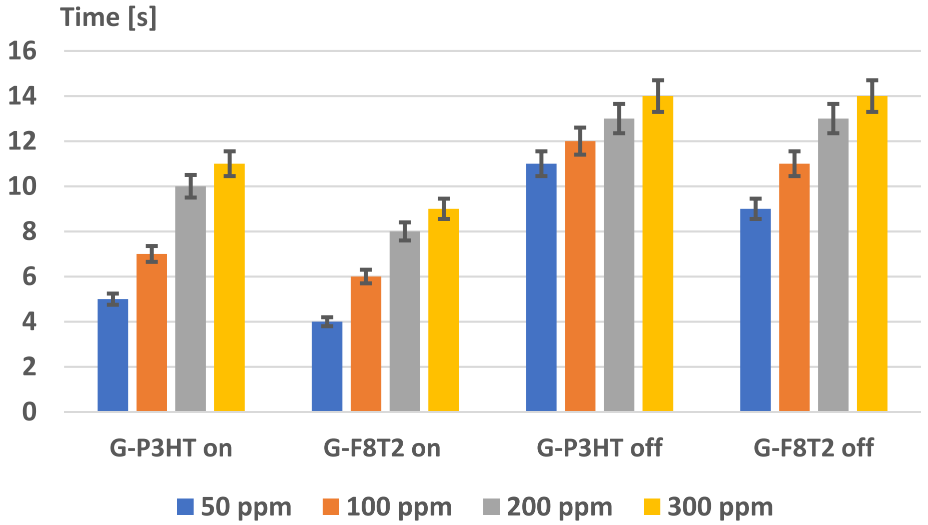

Figure 16. Experimental response (on) and recovery time (off) for the sensing structures.

The obtained values of response time of about 4 s for the structure of graphene with F8T2, at a concentration of CH_4 of 50 ppm, is very reliable in the quick detection of irritable bowel syndrome, being associated with a relatively quick exhalation of air through the mouth. Once the syndrome is detected, its severity can be further reevaluated by a slow exhalation of air, of about 9 s, which is reasonable as a procedure. As regards the recovery time value, it is considered also feasible because even at a higher concentration of CH_4 of, e.g., 300 ppm, it takes only about 14 s for the sensor to recover its initial resistance, and, for medical use, to wait about 1 min between two measurements is quite reasonable, even if needing to use the same device to evaluate more patients.

The response and recovery time values for the developed sensing structures are in line with other homolog gas sensors, e.g., based on semiconductive assemblies, as in [32,34,66,67] but in our case, the response time values are lower due to the direct use and higher conductivity of graphene-conducting polymers assemblies. The sensor characteristic is superior to, e.g., [54], regarding the minimum detection limit, and can be tailored for different threshold values of CH_4 concentrations in air, depending on the type of investigation and syndrome extent. In all, the use of a simple, low-value, and robust device for individual use is beneficial at the patient level because the syndrome evolution or treatment efficiency can be more effectively surveyed. Due to these successful results, even if preliminary, the sensor features will be further analyzed in the presence of perturbing factors, determined also by the breathing process, i.e., the potential influences of exhaled CO_2 and exhaled humidity.

5. Conclusions

This paper describes the process of producing chemiresistors based on hybrid nanostructures obtained from graphene and conducting polymers.

The technology of graphene dispersion and support stabilization was based on the chemical vapor deposition technique. The transfer of the graphene to the substrate of interest was made by spin-coating of PMMA and further thermal treatment of the PMMA/graphene/Cu, followed by an electrochemical delamination. The samples were finally transferred onto a SiO_2/Si substrate for microscopy analysis. The process at T = 950 °C led to graphene structures characterized by RMS and Ra roughness parameters with lower values compared to the graphene structures obtained at T = 900 °C. A better settlement of the grains was noticed, with the formation of layers predominantly characterized by peaks and not by depressions.

The technology for obtaining hybrid nanostructures from graphene and conducting polymers was drop-casting, with solutions of P3HT and F8T2. AFM analysis emphasized a higher roughness in the case of F8T2 compared to P3HT, with about a 10 times larger dimension of grain size. In both cases, a quite symmetrical distribution of grains was noticed, with reduced free space between them. SEM analysis emphasized that the distribution of the cavities between peaks are different but still uniformly dispersed for both polymers; however, in the case of the graphene–F8T2 structure the distances between the peaks clusters are about 7 times larger compared to graphene—P3HT structure.

To generate chemiresistors from graphene–polymer structures, an ink-jet printer was used, and the metallization was made with commercial copper ink for printed electronics. A structure of a resistor was generated, with an active surface of about 1 cm^2. Experimental calibration curves were plotted for both sensing structures, for a larger domain of CH_4 concentration in air, of up to 1000 ppm CH_4. The limit of detection was found to be 50 ppm. The curve for the graphene structure with P3HT presents a high linearity and lower values of resistance, which makes it useful for large-scale determination of CH_4 concentrations in air, by use of a simple signal processing system.

For testing the breath methane associated with irritable bowel syndrome, only lower CH_4 concentrations in air must be detected, with a threshold value of, e.g., 100 ppm, which may indicate the syndrome occurrence. The linearity for this CH_4 low concentration domain was noticed also for the graphene structure with F8T2, and, more than this, the respective slope was found to be 6 times higher compared with graphene structure with P3HT, which makes the sensing structure of graphene with F8T2 more feasible and reliable for the medical application for irritable bowel syndrome assessment.

Author Contributions: Conceptualization, A.F.T., R.C.C. and O.D.S.; methodology, R.C.C., O.D.S., S.A. and T.G.S.; validation, R.C.C., S.A., T.G.S. and A.F.T.; formal analysis, A.F.T., S.A. and R.C.C.; investigation, R.C.C., O.D.S., T.G.S., A.F.T. and S.A.; data curation, R.C.C., O.D.S., T.G.S. and A.F.T.; writing—original draft preparation, A.F.T. and R.C.C.; writing—review and editing, R.C.C., A.F.T. and S.A.; visualization, R.C.C., O.D.S. and A.F.T.; supervision, A.F.T. and R.C.C. All authors have read and agreed to the published version of the manuscript.

Funding: This research received no external funding.

Institutional Review Board Statement: Not applicable.

Informed Consent Statement: Not applicable.

Data Availability Statement: Data are contained within the article.

Conflicts of Interest: The authors declare no conflicts of interest.

References

1. Novoselov, K.S.; Geim, A.K.; Morozov, S.V.; Jiang, D.; Zhang, Y.; Dubonos, S.V.; Grigorieva, I.V.; Firsov, A.A. Electric field effect in atomically thin carbon films. *Science* **2004**, *306*, 666–669. [CrossRef] [PubMed]
2. Li, X.; Magnuson, C.W.; Venugopal, A.; Tromp, R.M.; Hannon, J.B.; Vogel, E.M.; Colombo, L.; Ruoff, R.S. Large-Area Graphene Single Crystals Grown by Low-Pressure Chemical Vapor Deposition of Methane on Copper. *J. Am. Chem. Soc.* **2011**, *133*, 2816–2819. [CrossRef] [PubMed]
3. Reina, A.; Jia, X.; Ho, J.; Nezich, D.; Son, H.; Bulovic, V.; Dresselhaus, M.S.; Kong, J. Layer Area, Few-Layer Graphene Films on Arbitrary Substrates by Chemical Vapor Deposition. *Nano Lett.* **2009**, *9*, 3087. [CrossRef]
4. Lee, J.S.; Jang, C.W.; Kim, J.M.; Shin, D.H.; Kim, S.; Choi, S.-H.; Belay, K.; Elliman, R. Graphene synthesis by C implantation into Cu foils. *Carbon* **2014**, *66*, 267–271. [CrossRef]
5. Cheng, Q.; Duan, J.; Zhang, Q.; Jiang, L. Learning from Nature: Constructing Integrated Graphene-Based Artificial Nacre. *ACS Nano* **2015**, *9*, 2231–2234. [CrossRef]
6. Lim, W.S.; Kim, Y.Y.; Kim, H.; Jang, S.; Kwon, N.; Park, B.J.; Ahn, J.-H.; Chung, I.; Hong, B.H.; Yeom, G.Y. Atomic layer etching of graphene for full graphene device fabrication. *Carbon* **2012**, *50*, 429–435. [CrossRef]
7. Liu, W.; Li, H.; Xu, C.; Khatami, Y.; Banerjee, K. Synthesis of high-quality monolayer and bilayer graphene on copper using chemical vapor deposition. *Carbon* **2011**, *49*, 4122–4130. [CrossRef]
8. Chen, X.; Zhang, L.; Chen, S. Large area CVD growth of graphene. *Synth. Met.* **2015**, *210 Pt A*, 95–108. [CrossRef]
9. Hazbun, R.; Hart, J.; Hickey, R.; Ghosh, A.; Fernando, N.; Zollner, S.; Adam, T.N.; Kolodzey, J. Silicon epitaxy using tetrasilane at low temperatures in ultra-high vacuum chemical vapor deposition. *J. Cryst. Growth* **2016**, *444*, 21–27. [CrossRef]
10. Wang, Y.; Zheng, Y.; Xu, X.; Dubuisson, E.; Bao, Q.; Lu, J.; Loh, K.P. Electrochemical Delamination of CVD-Grown Graphene Film: Toward the Recyclable Use of Copper Catalyst. *ACS Nano* **2011**, *5*, 9927–9933. [CrossRef]

11. Matsumura, H. Catalytic Chemical Vapor Deposition (CTC–CVD) Method Producing High Quality Hydrogenated Amorphous Silicon. *Jpn. J. Appl. Phys.* **1986**, *25*, L949. [CrossRef]
12. Kathalingam, A.; Ajmal HM, S.; Ramesh, S.; Kim, H.S.; Kim, S.D.; Choi, S.H.; Yang, W.; Kim, K.K.; Kim, H.-S. Poly(methyl methacrylate)-derived graphene films on different substrates using rapid thermal process: A way to control the film properties through the substrate and polymer layer thickness. *J. Mater. Res. Technol.* **2019**, *8*, 3752–3763.
13. Iwasaki, T.; Endo, K.; Watanabe, E.; Tsuya, D.; Morita, Y.; Nakaharai, S.; Noguchi, Y.; Wakayama, Y.; Watanabe, K.; Taniguchi, T.; et al. Bubble-Free Transfer Technique for High-Quality Graphene/Hexagonal Boron Nitride van der Waals Heterostructures. *ACS Appl. Mater. Interfaces* **2020**, *12*, 8533–8538. [CrossRef] [PubMed]
14. Graphene. Available online: https://www.graphene.manchester.ac.uk/learn/applications/ (accessed on 12 March 2024).
15. What Is the Graphene Flagship? Available online: https://graphene-flagship.eu/ (accessed on 12 March 2024).
16. Ghuge, A.D.; Shirode, A.R.; Kadam, V.J. Graphene: A Comprehensive Review. *Curr. Drug Targets* **2017**, *18*, 724–733. [CrossRef] [PubMed]
17. Zamiri, G.; Haseeb, A.S.M.A. Recent Trends and Developments in Graphene/Conducting Polymer Nanocomposites Chemiresistive Sensors. *Materials* **2020**, *13*, 3311. [CrossRef] [PubMed]
18. Cai, X.; Sun, K.; Qiu, Y.; Jiao, X. Recent Advances in Graphene and Conductive Polymer Composites for Supercapacitor Electrodes: A Review. *Crystals* **2021**, *11*, 947. [CrossRef]
19. Bai, H.; Sheng, K.; Zhang, P.; Li, C.; Shi, G. Graphene oxide/conducting polymer composite hydrogels. *J. Mater. Chem.* **2011**, *21*, 18653–18658. [CrossRef]
20. Conducting Polymer/Graphene-Based Material Composites, and Methods for Preparing the Composites. Available online: https://patents.google.com/patent/US20140087192A1/en (accessed on 12 March 2024).
21. Chauhan, A.K.; Gupta, S.K.; Taguchi, D.; Manaka, T.; Jha, P.; Veerender, P.; Sridevi, C.; Koiry, S.P.; Gadkari, S.C.; Iwamoto, M. Enhancement of the carrier mobility of conducting polymers by formation of their graphene composites. *RSC Adv.* **2017**, *7*, 11913–11920. [CrossRef]
22. Kausar, A. Conjugated Polymer/Graphene Oxide Nanocomposites—State-of-the-Art. *J. Compos. Sci.* **2021**, *5*, 292. [CrossRef]
23. Sharma, S.; Sudhakara, P.; Omran, A.A.B.; Singh, J.; Ilyas, R.A. Recent Trends and Developments in Conducting Polymer Nanocomposites for Multifunctional Applications. *Polymers* **2021**, *13*, 2898. [CrossRef]
24. Dunlop, M.J.; Bissessur, R. Nanocomposites based on graphene analogous materials and conducting polymers: A review. *J. Mater. Sci.* **2020**, *55*, 6721–6753. [CrossRef]
25. Adedoja, O.S.; Sadiku, E.R.; Hamam, Y. Prospects of Hybrid Conjugated Polymers Loaded Graphene in Electrochemical Energy Storage Applications. *J. Inorg. Organomet. Polym. Mater.* **2023**, *33*, 3915–3934. [CrossRef]
26. Shalini, A.; Kothai, S.; Jaisankar, V. Graphene Deposited Conducting Polymers: Synthesis and Sensing Applications. *Int. J. Curr. Res. Aca. Rev.* **2021**, *9*, 94–103.
27. Zhu, Z.; Lin, W.-D.; Lin, Z.-Y.; Chuang, M.-H.; Wu, R.-J.; Chavali, M. Conductive Polymer (Graphene/PPy)–$BiPO_4$ Composite Applications in Humidity Sensors. *Polymers* **2021**, *13*, 2013. [CrossRef] [PubMed]
28. Das, P.; Chakraborty, K.; Pan, A.; Ghosh, S.; Pal, T. Conductivity relaxation and photocurrent generation in reduced graphene ox-ide-poly(9,9′-dioctyl-fluorene-co-bithiophene) composite with application in temperature sensing. *J. Appl. Phys.* **2019**, *125*, 085104. [CrossRef]
29. Pinelli, F.; Nespoli, T.; Fiorati, A.; Farè, S.; Magagnin, L.; Rossi, F. Graphene nanoplatelets can improve the performances of graphene oxide—Polyaniline composite gas sensing aerogels. *Carbon Trends* **2021**, *5*, 100123. [CrossRef]
30. Lee, S.J.; Yoon, S.J.; Jeon, I.-Y. Graphene/Polymer Nanocomposites: Preparation, Mechanical Properties, and Application. *Polymers* **2022**, *14*, 4733. [CrossRef] [PubMed]
31. Cheng, S.; Wang, Y.; Zhang, R.; Wang, H.; Sun, C.; Wang, T. Recent Progress in Gas Sensors Based on P3HT Polymer Field-Effect Transistors. *Sensors* **2023**, *23*, 8309. [CrossRef]
32. Cheon, H.J.; Shin, S.Y.; Van Tran, V.; Park, B.; Yoon, H.; Chang, M. Preparation of conjugated polymer/reduced graphene oxide nano-composites for high-performance volatile organic compound sensors. *Chem. Eng. J.* **2021**, *425*, 131424. [CrossRef]
33. Khanh, T.S.T.; Trung, T.Q.; Giang, L.T.T.; Nguyen, T.Q.; Lam, N.D.; Dinh, N.N. Ammonia Gas Sensing Characteristic of P3HT-rGO-MWCNT Composite Films. *Appl. Sci.* **2021**, *11*, 6675. [CrossRef]
34. Verma, A.; Gupta, R.; Verma, A.S.; Kumar, T. A review of composite conducting polymer-based sensors for detection of industrial waste gases. *Sens. Actuators Rep.* **2023**, *5*, 100143. [CrossRef]
35. Lei, W.; Si, W.; Xu, Y.; Gu, Z.; Hao, Q. Conducting polymer composites with graphene for use in chemical sensors and biosensors. *Microchim. Acta* **2014**, *181*, 707–722. [CrossRef]
36. Kim, Y.; An, T.K.; Kim, J.; Hwang, J.; Park, S.; Nam, S.; Cha, H.; Park, W.J.; Baik, J.M.; Park, C.E. A composite of a graphene oxide derivative as a novel sensing layer in an organic field-effect transistor. *J. Mater. Chem. C* **2014**, *2*, 4539–4544. [CrossRef]
37. Rahman, A.; Pal, R.K.; Islam, N.; Freeman, R.; Berthiaume, F.; Mazzeo, A.; Ashraf, A. A Facile Graphene Conductive Polymer Paper Based Biosensor for Dopamine, TNF-α, and IL-6 Detection. *Sensors* **2023**, *23*, 8115. [CrossRef] [PubMed]
38. Kumar, A.; Gupta, G.H.; Singh, G.; More, N.; Keerthana, M.; Sharma, A.; Jawade, D.; Balu, A.; Kapusetti, G. Ultrahigh sensitive graphene oxide/conducting polymer composite based biosensor for cholesterol and bilirubin detection. *Biosens. Bioelectron. X* **2023**, *13*, 100290. [CrossRef]

39. Al-Graiti, W.; Foroughi, J.; Liu, Y.; Chen, J. Hybrid Graphene/Conducting Polymer Strip Sensors for Sensitive and Selective Electrochemical Detection of Serotonin. *ACS Omega* **2019**, *4*, 22169–22177. [CrossRef]
40. Văduva, M.; Baibarac, M.; Cramariuc, O. Functionalization of Graphene Derivatives with Conducting Polymers and Their Applications in Uric Acid Detection. *Molecules* **2023**, *28*, 135. [CrossRef]
41. Song, J.; Kim, Y.; Kang, K.; Lee, S.; Shin, M.; Son, D. Stretchable and Self-Healable Graphene–Polymer Conductive Composite for Wearable EMG Sensor. *Polymers* **2022**, *14*, 3766. [CrossRef] [PubMed]
42. DiFrancesco, M.L.; Colombo, E.; Papaleo, E.D.; Maya-Vetencourt, J.F.; Manfredi, G.; Lanzani, G.; Benfenati, F. A hybrid P3HT-Graphene interface for efficient photostimulation of neurons. *Carbon* **2020**, *162*, 308–317. [CrossRef]
43. Yazid, S.N.A.M.; Adnan, A.A.C.; Isa, I.M.; Saidin, M.I.; Ahmad, M.S.; Fun, C.S. Conducting polymer functionalized graphene-based electrochemical sensors for sensing pollutants in water. *J. Electrochem. Sci. Eng.* **2023**, *13*, 251–274. [CrossRef]
44. Diédhiou, I.; Fall, B.; Gaye, C.; Sall, M.L.; Diaw, A.K.D.; Gningue-Sall, D.; Fall, M.; Raouafi, N. Preparations and applications of organic conducting polymers/graphene composites in heavy metal ion sensing: A review. *Int. J. Mater. Res.* **2023**, *114*, 79–99. [CrossRef]
45. Lin, C.-H.; Lin, J.-H.; Chen, C.-F.; Ito, Y.; Luo, S.-C. Conducting polymer-based sensors for food and drug analysis. *J. Food Drug Anal.* **2021**, *29*, 544–558. [CrossRef] [PubMed]
46. Mulyono, T.; Siswoyo, A.; Lestari, P.B.; Zulfikar; Mufliha, Y.M. Development of A Resistive Sensor Array Based on Graphene and Conducting Polymer Composites for Coffee Aroma Classification. *E3S Web Conf.* **2024**, *481*, 06012. [CrossRef]
47. Moyseowicz, A.; Minta, D.; Gryglewicz, G. Conductive Polymer/Graphene-based Composites for Next Generation Energy Storage and Sensing Applications. *ChemElectroChem* **2023**, *10*, e202201145. [CrossRef]
48. Shen, F.; Pankratov, D.; Chi, Q. Graphene-conducting polymer nanocomposites for enhancing electrochemical capacitive energy storage. *Curr. Opin. Electrochem.* **2017**, *4*, 133–144. [CrossRef]
49. Magu, T.O.; Agobi, A.U.; Hitler, L.; Dass, P.M. A Review on Conducting Polymers-Based Composites for Energy Storage Application. *J. Chem. Rev.* **2019**, *1*, 19–34. [CrossRef]
50. Achary, S.; Barik, B.; Dash, P. *Graphene Oxide-Polymer Nanocomposites Towards Sensing and Photocatalytic Applications, Handbook of Polymer and Ceramic Nanotechnology*; Springer: Cham, Switzerland, 2021; pp. 965–986. [CrossRef]
51. Hydrogen/Methane Breath Test. Available online: https://www.nationaljewish.org/conditions/tests-procedures/gastroenterology/hydrogen-methane-breath-test (accessed on 12 March 2024).
52. Costello, B.P.J.d.L.; Ledochowski, M.; Ratcliffe, N.M. The importance of methane breath testing: A review. *J. Breath Res.* **2013**, *7*, 024001. [CrossRef] [PubMed]
53. John, R.A.B.; Kumar, A.R. A review on resistive-based gas sensors for the detection of volatile organic compounds using metal-oxide nanostructures. *Inorg. Chem. Commun.* **2021**, *133*, 108893. [CrossRef]
54. Resistive Gas Sensor. Available online: https://www.electricity-magnetism.org/resistive-gas-sensor/ (accessed on 12 March 2024).
55. Ansari, H.R.; Mirzaei, A.; Shokrollahi, H.; Kumar, R.; Kim, J.-Y.; Kim, H.W.; Kumar, M.; Kim, S.S. Flexible/wearable resistive gas sensors based on 2D materials. *J. Mater. Chem. C* **2023**, *11*, 6528–6549. [CrossRef]
56. Chesler, P.; Hornoiu, C. MOX-Based Resistive Gas Sensors with Different Types of Sensitive Materials (Powders, Pellets, Films), Used in Environmental Chemistry. *Chemosensors* **2023**, *11*, 95. [CrossRef]
57. Baier, D.; Priamushko, T.; Weinberger, C.; Kleitz, F.; Tiemann, M. Selective Discrimination between CO and H_2 with Copper–Ceria-Resistive Gas Sensors. *ACS Sens.* **2023**, *8*, 1616–1623. [CrossRef] [PubMed]
58. Jian, Y.; Hu, W.; Zhao, Z.; Cheng, P.; Haick, H.; Yao, M.; Wu, W. Gas Sensors Based on Chemi-Resistive Hybrid Functional Nanomaterials. *Nano-Micro Lett.* **2020**, *12*, 71. [CrossRef] [PubMed]
59. Tansel, A.; Levinthal, D.J. Understanding Our Tests: Hydrogen-Methane Breath Testing to Diagnose Small Intestinal Bacterial Overgrowth. *Clin. Transl. Gastroenterol.* **2023**, *14*, e00567. [CrossRef] [PubMed]
60. ISO 14644-1:2015 Cleanrooms and Associated Controlled Environments. Available online: https://www.iso.org/standard/53394.html (accessed on 10 March 2024).
61. Rafailović, L.D.; Jovanović, A.Z.; Gutić, S.J.; Wehr, J.; Rentenberger, C.; Trišović, T.L.; Pašti, I.A. New Insights into the Metallization of Graphene-Supported Composite Materials–from 3D Cu-Grown Structures to Free-Standing Electrodeposited Porous Ni Foils. *ACS Omega* **2022**, *7*, 4352–4362. [CrossRef] [PubMed]
62. Lin, Y.; Manalili, D.; Khodabakhsh, A.; Cristescu, S.M. Real-Time Measurement of CH_4 in Human Breath Using a Compact CH_4/CO_2 Sensor. *Sensors* **2024**, *24*, 1077. [CrossRef] [PubMed]
63. The Methane Breath CH4ECK™. Available online: https://thefunctionalgutclinic.com/blog/news/the-methane-breath-ch4eck/ (accessed on 12 March 2024).
64. Ndong, P.O.; Boutallaka, H.; Marine-Barjoan, E.; Ouizeman, D.; Mroue, R.; Anty, R.; Vanbiervliet, G.; Piche, T. Prevalence of small intestinal bacterial overgrowth in irritable bowel syndrome (IBS): Correlating H-2 or CH4 production with severity of IBS. *JGH Open* **2023**, *7*, 311–320. [CrossRef] [PubMed]
65. Gandhi, A.; Shah, A.; Jones, M.P.; Koloski, N.; Talley, N.J.; Morrison, M.; Holtmann, G. Methane positive small intestinal bacterial overgrowth in inflammatory bowel disease and irritable bowel syndrome: A systematic review and meta-analysis. *Gut Microbes* **2021**, *13*, 1933313. [CrossRef] [PubMed]

66. Chen, W.; Zhou, Q.; Wan, F.; Gao, T. Gas Sensing Properties and Mechanism of Nano-SnO_2-Based Sensor for Hydrogen and Carbon Monoxide. *J. Nanomater.* **2012**, *2012*, 612420. [CrossRef]
67. Niyat, F.Y.; Abadi, M.H.S. COMSOL-Based Modeling and Simulation of SnO_2/rGO Gas Sensor for Detection of NO_2. *Sci. Rep.* **2018**, *8*, 2149. [CrossRef]

Multi-node potentiostat device and multiplatform mobile application for on-field measurements

João Monge
ISCTE-Instituto Universitário de Lisboa
IT – Instituto de Telecomunicações
Lisbon, Portugal
jpdme@iscte-iul.pt

Octavian Postolache
ISCTE-Instituto Universitário de Lisboa
IT – Instituto de Telecomunicações
Lisbon, Portugal
opostolache@lx.it.pt

Alexandru Trandabat
Gh. Asachi" Technical University of Iasi,
S.C Intelectro Iasi SRL,
Iasi, Romania
ftranda@yahoo.com

Stefan Macovei
S.C Intelectro Iasi SRL,
Iasi, Romania
macovei_stefan1988@yahoo.com

***Abstract*— The use of electrochemical sensors proved to be efficient in terms of accuracy and capability to measure the analyte concentration even in the field in a short time. Thus, in this paper, we propose a mobile system, including hardware and software, to facilitate the use of a potentiostat commonly used with an electrochemical sensor. The software expressed by a mobile application allows the control of the developed wireless potentiostat. It assures the remote selection of specific parameters associated with implemented voltammetry methods. The APP enables the control of multiple potentiostats simultaneously that materialize the electrochemical sensor network. The developed software can also store the electrochemical data on the cloud. The implemented mobile system allows to perform real-time measurements for different applications, including healthcare, agriculture, or water quality.**

Keywords— electrochemical sensors, mobile potentiostat, WSN, potentiostat, cross-platform APP

I. INTRODUCTION

Early diagnosis in medicine can be vital in saving a patient life. The latest advances in technology have been proved essential in this field, and the scientific community has developed increasingly sophisticated solutions that enable accurate and early diagnosis. Electrochemistry proves to be very useful in quantifying the concentration of analyte solutions in a matter of seconds [1] [2] that reduces the time required for diagnosis. This paper introduces a system characterized by hardware and software components, specific data storage being associated with cloud storage services. This mobile system is controlled through developed APPs that works on major mobile devices and laptops. The cloud data storage made this data available for advanced analysis anywhere in the world where Internet access is provided. The electrochemical measurements are carried out using a miniaturized potentiostat. This hardware offers quick response for a substance under analysis. Sodium and lactate present in sweat can be used as physiological indicators of intensive physical activity [3]. The potentiostat miniaturization provides the ability to be part of wearable real-time analytes' monitors. Important component of the mobile monitor is the Analog Front End (AFE) that is characterized by the latest CMOS circuits' advances.

The AFE is part of mobile systems that can perform amperometry sensing of glucose, lactate, and sodium into sweat-analyzing wearable devices [4]. Despite being extremely versatile devices, potentiostats require additional embedded computational platforms and appropriate firmware associated with control and measured data analysis. The development of software solutions characterized by higher usability illustrated by friendly user interface designs for low-level trained users is also considered in this work. It is proposed a set of mobile Android, iOS, and web app IoT compatible that include easy to use User Interface (UI) and cloud data storage capabilities. Mobile health (mHealth) is the term to define mobile applications use to monitor the health condition; for example, smartwatches are often equipped with a heart rate sensor allowing constant monitoring of heart rate.

Another example is presented in [6], a glucose monitoring system using a smartphone application Bluetooth paired with an electrochemical device. The latest design provides miniaturization, portability, and easy to use interfaces. Therefore, the presented potentiostat embedded system offers wireless connectivity, cloud data, configuration storage, and concentration measurement for some substances. The implemented system combines a cloud-hosted server and a complete set of tools to be used for electrochemical tests in the field taking into account the mobility and robustness characteristics of the system.

II. SYSTEM DESCRIPTION

The system was designed to perform different electrochemical techniques such as cyclic voltammetry (CV)

978-1-7281-8126-4/20/$31.00 ©2020 European Union

and Chronoamperometry. The system is characterized by high efficiency and scalability and allows easy configuration of various electrochemical techniques and intuitive user interface for common users without extended training in electrochemistry. The developed hardware includes an embedded computation platform characterized by easy firmware updates. The system is characterized by wireless communication capabilities that assure data exchange with common mobile devices as smart phone or tablets. The system includes a battery charger circuit and a small lithium battery assuring higher autonomy of mobile electrochemical measurement unit. A Mobile APP was developed for control, processing and visualization of the characteristics of the measured analyte.

A. System Hardware

This system was designed to be wearable, taking into account the necessity to provide on-line monitoring of the health status in real-time. Different Integrated Circuits (ICs) potentiostats that provide the miniaturization required for this system [7] – [10] were analyzed. The selected IC for the wearable potentiostat was the LMP91000 from Texas Instruments since it provides a controlled potential selection at 14 levels of the voltage reference. It also has Ohmic drop compensation and a trans-impedance amplifier to convert the current to a readable voltage value by Analog-to-Digital Converter (ADC) in a small package, 4mmx4mm [9].

The LMP91000 potentiostat is controlled via I2C protocol by almost any microcontroller or microcomputer available. It can perform several electrochemical techniques with proper software development. It includes cyclic voltammetry (CV) and Chronoamperometry (CA), for which we present in the results section of this paper. According to designs reported in it, this IC also performs other electrochemical techniques to perform Square Wave Voltammetry (SWV) and Normal Pulse Voltammetry (NPV).

A microcontroller with an embedded Bluetooth Low Energy (BLE) designated RFDuino was considered to improve those designs and maintain the required hardware miniaturization. The RFDuino provides the data processing and communication capabilities and full control of the LMP91000 to applying different electrochemical techniques. It was also included a precision 3.3V voltage reference IC to improve the sampling quality and provide a more comprehensive voltage range.

Figure 1 describes the schematic of the LMP91000. As shown in Figure 1, it is possible to connect a capacitor to act as a filter between C1 and C2 pins. It has a built-in temperature sensor that can be alternated if the user desires. It is configurable through I2C, and the pin MENB enables and disables the IC to reduce power usage. When connecting several capacitors in an array, it does not provide a way to change the I2C address. The internal variable bias allows for alternating the applied potential between the working and counter electrode. The RFDuino microcontroller includes wireless capabilities in a fingerprint sized package. The Cortex-M0 is a processing unit with an ArmV6-M architecture. Other features of the RFDuino are Analog-to-Digital Converter (ADC) that allows our system to read the voltage from the trans-impedance amplifier of the LMP91000 and convert it back to current by applying the correct equation. SPI and I2C are also present in this microcontroller, making it versatile to work with different sensors.

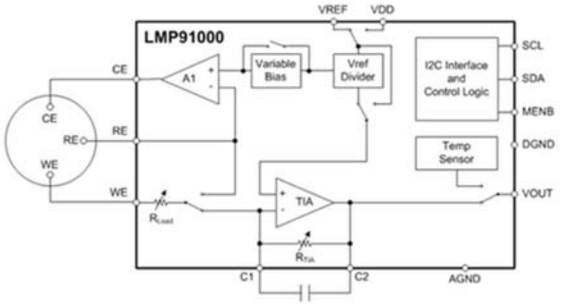

Figure 1: LMP91000 Schematic

The LMP91000 is controlled via I2C with the parameters coming from the mobile or web applications Bluetooth packets. The RFDuino firmware was developed so that it can handle different electrochemical techniques and configurable wirelessly. Thus, it does not require any cable, just a small battery to make it work, becoming very easy to wear due to its small size. The RFduino was programmed using the Arduino Development Environment, and an FTDI programmer included in the design of our printed circuit board (PCB) to make it easier to program.

B. Mobile and web application

The software was developed with compatibility in mind. The application works with powerful smartphones, tablets, and laptops. The mobile apps were developed using React Native to produce multiplatform native apps for IOS and Android operative systems using JavaScript as the programming language. Furthermore, the Web Application was made with HTLM5, CSS, and JQuery and relied on Chrome Web Bluetooth for connectivity with our potentiostat Bluetooth boards. Figure 2 presents the flowchart associated with the developed application.

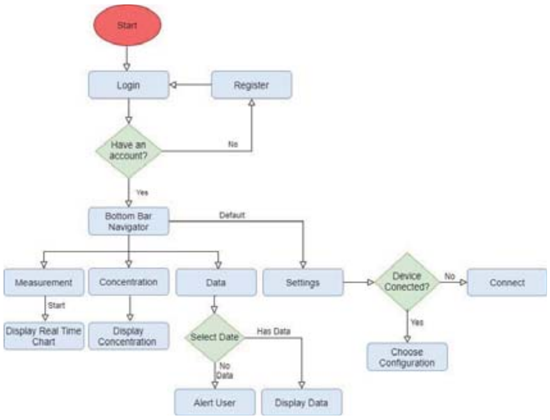

Figure 2: Cross-platform application flowchart

The start button represents the initialized application. When this app opens, the login menu is displayed. If the user has not registered yet, he can load the register menu to create an account. After such, the login menu will be displayed so that the user can login. As soon as the login is done, the menu is opened. This menu displays three different buttons, the "Measurement" button, the "Concentration" button, and the "Data" button. If none of these buttons are tapped, then by default, the user goes to the Settings menu. This Settings menu allows the user to connect with a device if none is associated. After the user is connected, the main menu reappears. If the user presses the "Measurement" button, then the reading begins, and there is a displayed real-time chart. Suppose the "Concentration" button is pressed. In that case, there is a representation of the substances concentration automatically. The user has to put the substance and the type of sensor, and the system will return the concentration value. If the "Data" button is tapped, the user is asked to select a date. If the date has no data, then an alert is showed to the user. If the date has information, then this information is displayed for the user. A configuration menu screen was included to interact with the hardware. It is possible to configure up to seven potentiostats that we developed and perform different electrochemical techniques individually. For example, this system can act as a universal glucose meter since it is compatible with several test strips available on the market. This requires that we insert the configuration for each sensor in our database. This system will select the proper configuration and calibration equation from the database and measure the concentration.

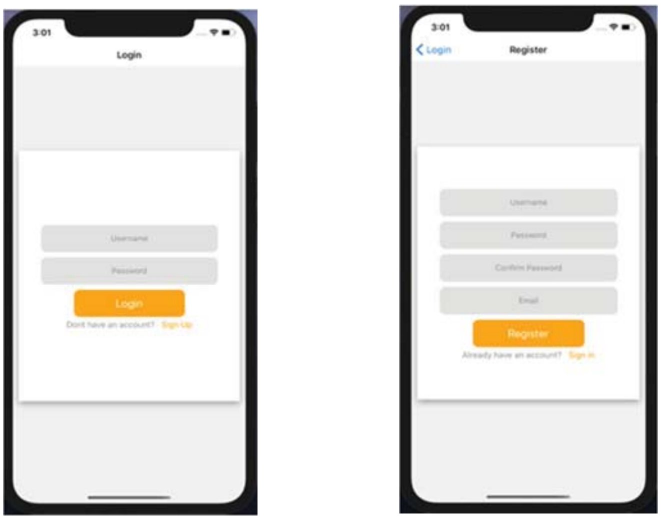

a) b)

Figure 3: a) Login page for the cross-platform application b) Register page for the cross-platform application

In Figure 3 a) is presented the detailed login page, including username and password fields. Figure 3 b) illustrates the register page, which allows the user to create and submit new account information. The register page has four input text fields that are necessary to register a user in our database. Users cannot have the same username or email.

Figure 4 a) presents the most complex part of the mobile application, having the most input fields, both text and numeric. To facilitate user interaction, we added the possibility to save and load configuration and included both personal and general configuration for all users using this system

Figure 4: a) Hardware connection and configuration page b) Real-time data visualization page

. Figure 4 b) presents the user real-time graphical characteristic of the current measurement, and it is also possible to visualize multiple hardware instances.

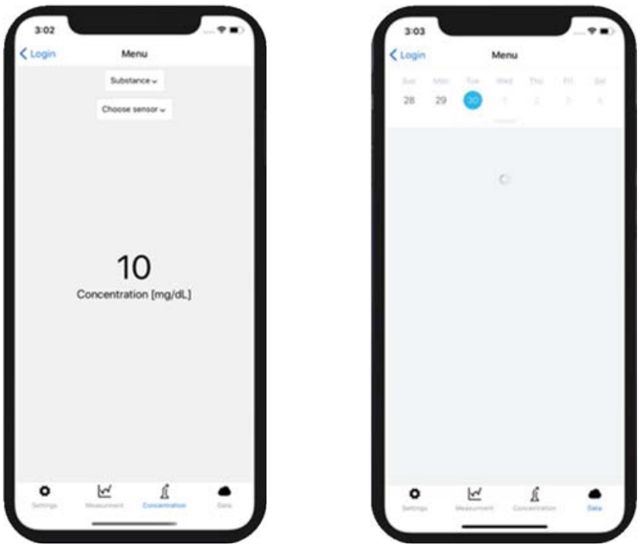

a) b)

Figure 5: a) Login page for the cross-platform application b) Register page for the cross-platform application

One of the main features that differentiate this application from others in the market is revealing specific analytes concentration. This is possible by having a preloaded equation and using our hardware with a compatible electrochemical sensor. This is described in Figure 5 a).

Another feature of this system is storing the measurements in the cloud. Figure 5 b) enables the selection of a date to observe the measurements done by this user. Storing electrochemical data in the cloud is also an innovative feature not seen in the commercial potentiostats.

III. EXPERIMENTAL RESULTS AND DISCUSSION

We made tests to obtain the concentration and compare the response with a commercial potentiostat Dropsens µStat 8000. A solution of TBABF4 (tetrabutylammonium tetrafluoroborate) was prepared in acetonitrile. The acetonitrile contains 0.05 mM Ferrocene, and a CV was used to observe the oxidation-redox process. After, this solution was applied to a Dropsens SPE DRP110 and performed cyclic voltammetry using our system and the Dropsens µStat 8000 potentiostat for result comparison. The results of this experiment are presented in the results section. One of these systems main features is the measurement of concentration by just connecting and dropping the solution. The application will tell the user the concentration using stored configuration and embedded algorithms.

To validate the developed hardware and the implemented APP, a solution of TBABF4 (tetrabutylammonium tetrafluoroborate) in acetonitrile containing 0.05 mM Ferrocene was considered. The CV method was applied. The system response is then compared with the response obtained from a reference potentiostat that is commercially available (Dropsens µStat 8000). The imposed CV test parameters were the same for both systems. We had a potential range from [-0.6V, +0.6V], and we performed the test starting from 0V to 0.6V and then back to 0V, completing a cycle. Both devices had small differences in configuration. The electrodes used were Dropsens DRP-110 with a WE of carbon, a CE of Carbon, and the RE silver.

The potential was applied in several steps until it reaches the maximum possible without using an external reference with the LMP91000. Despite being equipped with a 3.3V reference voltage that allows a range from [-08, 0.8]V, a range of 0.6V was enough for this solution.

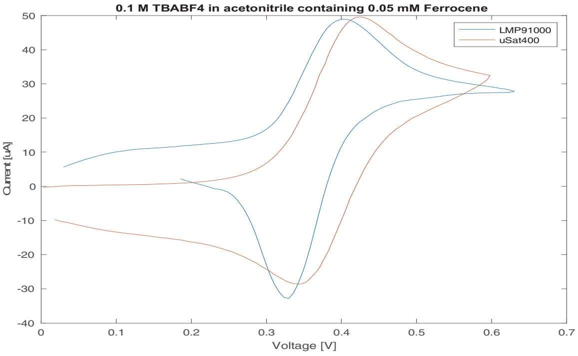

Figure 6: Cyclic voltammetry comparison between LMP91000 and µStat 8000

The graphical characteristics are presented in Figure 6. The obtained results were similar comparing our device with the commercial one. Some variations are due to the circuit differences of both potentiostats. The current evolution graphs are very similar.

The presented system demonstrated to perform electrochemistry techniques efficiently, and it is easy to configure using the developed app and has the advantages of data visualization and recording.

IV. CONCLUSION

The implemented mobile potentiostat allows operation in the field. It is characterized by high accuracy and mobility and brings new possibilities in terms of real-time analyte analysis. The mobile APP can be installed in any smart device running Android OS or iOS assuring the control of multiple electrochemical measurement units. Future work will focus on the complex solutions analysis embedding machine learning capabilities on the system level.

ACKNOWLEDGMENT

This work was supported by a grant of the Romanian National Authority for Scientific Research and Innovation, NANO-IMUNELCHIM-PLAT Project/Competitiveness Operational Programme 2014-2020, under grant P_37_766, cod my 103847, nr. 68/08.09.2016. Finally, special acknowledgments to Fundação para a Ciência e Tecnologia Project UIDB/50008/2020, and Instituto de Telecomunicações.

REFERENCES

[1] J. Wang, "Electrochemical glucose biosensors,"*Chem. Rev.*, vol. 108, no. 2, pp. 814–825, 2008.

[2] J. Monge, O. Postolache, O. Plopa, A. Trandabat, O. Schreiner, and T. Schreiner, “Glucose detection in sweat using biosensors,” in *2019 7th E-Health and Bioengineering Conference, EHB 2019*, 2019.

[3] W. Gao *et al.*, "Fully integrated wearable sensor arrays for multiplexed in situ perspiration analysis,"*Nature*, vol. 529, no. 7587, pp. 509–514, Jan. 2016.

[4] A. Ganguly, P. Rice, K.-C. Lin, S. Muthukumar, and S. Prasad, "A Combinatorial Electrochemical Biosensor for Sweat Biomarker Benchmarking,"*SLAS Technol. Transl. Life Sci. Innov.*, vol. 25, no. 1, pp. 25–32, Feb. 2020.

[5] S. Kumar *et al.*, "Mobile health technology evaluation: The mHealth evidence workshop,"*Am. J. Prev. Med.*, vol. 45, no. 2, pp. 228–236, Aug. 2013.

[6] D. Ji *et al.*, "Smartphone-based cyclic voltammetry system with graphene modified screen printed electrodes for glucose detection,"*Biosens. Bioelectron.*, vol. 98, pp. 449–456, Dec. 2017.

[7] A. F. D. Cruz, N. Norena, A. Kaushik, and S. Bhansali, "A low-cost miniaturized potentiostat for point-of-care diagnosis,"*Biosens. Bioelectron.*, vol. 62, pp. 249–254, 2014.

[8] M. Carminati, G. Ferrari, F. Guagliardo, M. Farina, and M. Sampietro, "Low-noise single-chip potentiostat for nano-bio-electrochemistry over a 1MHz bandwidth," in *2009 16th IEEE International Conference on Electronics, Circuits and Systems, ICECS 2009*, 2009, pp. 952–955.

[9] “LMP91000 data sheet, product information and support | TI.com.” [Online]. Available: https://www.ti.com/product/LMP91000. [Accessed: 11-Jun-2020].

[10] “AD5940 Datasheet and Product Info | Analog Devices.” [Online]. Available: https://www.analog.com/en/products/ad5940.html#. [Accessed: 11-Jun-2020].

PLOS | ONE

RESEARCH ARTICLE

New experimental model for single liver lobe hyperthermia in small animals using non-directional microwaves

Ionuț Tudorancea[1☯], Vlad Porumb[2,3☯]*, Alexandru Trandabăț[4☯], Decebal Neaga[5☯], Bogdan Tamba[6☯], Radu Iliescu[6‡], Gabriel M. Dimofte[2,3‡]

1 Department of Physiology, Grigore T. Popa University of Medicine and Pharmacy, Iasi, Romania, **2** Department of Surgery, Grigore T. Popa University of Medicine and Pharmacy, Iasi, Romania, **3** Department of Surgery, Regional Institute of Oncology, Iasi, Romania, **4** Faculty of Electrical Engineering, Gheorghe Asachi Technical University, Iaşi, Romania, **5** Department of Engineering, Regional Institute of Oncology, Iasi, Romania, **6** Department of Pharmacology, Grigore T. Popa University of Medicine and Pharmacy, Iasi, Romania

☯ These authors contributed equally to this work.
‡ These authors are joint senior authors on this work.
* porumbvlad@ymail.com

Abstract

Purpose

Our aim was to develop a new experimental model for *in vivo* hyperthermia using non-directional microwaves, applicable to small experimental animals. We present an affordable approach for targeted microwave heat delivery to an isolated liver lobe in rat, which allows rapid, precise and stable tissue temperature control.

Materials and methods

A new experimental model is proposed. We used a commercial available magnetron generating 2450 MHz, with 4.4V and 14A in the filament and 4500V anodic voltage. Modifications were required in order to adjust tissue heating such as to prevent overheating and to allow for fine adjustments according to real-time target temperature. The heating is controlled using a virtual instrument application implemented in LabView® and responds to 0.1˚ C variations in the target. Ten healthy adult male Wistar rats, weighing 250–270 g were used in this study. The middle liver lobe was the target for controlled heating, while the rest of the living animal was protected.

Results

In vivo microwave delivery using our experimental setting is safe for the animals. Target tissue temperature rises from 30˚C to 40˚C with 3.375˚C / second ($R^2 = 0.9551$), while the increment is lower it the next two intervals (40–42˚C and 42–44˚C) with 0.291˚C/ s ($R^2 = 0.9337$) and 0.136˚C/ s ($R^2 = 0.7894$) respectively, when testing in sequences. After reaching the desired temperature, controlled microwave delivery insures a very stable temperature during the experiments.

OPEN ACCESS

Citation: Tudorancea I, Porumb V, Trandabăț A, Neaga D, Tamba B, Iliescu R, et al. (2017) New experimental model for single liver lobe hyperthermia in small animals using non-directional microwaves. PLoS ONE 12(9): e0184810. https://doi.org/10.1371/journal.pone.0184810

Editor: Alfred S Lewin, University of Florida, UNITED STATES

Received: April 22, 2016

Accepted: August 31, 2017

Published: September 21, 2017

Data Availability Statement: All relevant data are within the paper and its Supporting Information files.

Funding: This work was developed within the research grant CheTherDel (Chemo-hyperthermal Delivery—Combined chemo-hyperthermal control of hepatic tumors, based on microwave-activated subendothelial-targeted nano-assemblies), funded by ERA-Net EuroNanoMed JTC 2011 program.

Competing interests: The authors have declared that no competing interests exist.

Conclusions

We have developed an inexpensive and easy to manufacture system for targeted hyperthermia using non-directional microwave radiation. This system allows for fine and stable temperature adjustments within the target tissue and is ideal for experimental models testing below or above threshold hyperthermia

Introduction

Numerous experiments have been undertaken using heat in cancer therapies, with a wide range of delivery methods, generating a local, regional or whole-body hyperthermia [1–10]. As compared with normal tissues, cancer bearing tissues have been shown to be more susceptible to death in hyperthermia [11,12] and experimental treatment strategies have used thermal manipulation of tumors either by nonspecific tissue disruption, or as an adjuvant to chemotherapy in local or systemic delivery [11,13–17]. Heat induced alterations in target tissue depend on the temperature achieved and the duration of the exposure. Applying heat over 45˚C quickly induces necrosis, due to protein coagulation [18–20]. However, tissue exposed to temperatures below 43–45˚C displays minimal and even reversible changes, usually without structural alterations visible in light microscopy, but the threshold for subliminal changes is variable and depends on the model used and the tissue exposed to hyperthermia [20–25]. Nevertheless, the failure of the early approaches using direct heat-induced cell killing has prompted interest in the biological effects of mild hyperthermia (39–42˚C), especially in conjunction with other cancer therapies. Indeed, mild hyperthermia improves tumor oxygenation, inhibits damage repair while also potentially improving nanotechnology-based targeted delivery [26].

Exposure of three-dimensional tissue volumes to temperatures within the narrow interval of 42–45˚C may induce variable effects, ranging from minimal functional alterations to necrosis, due to non-uniform spatial distribution of the temperature load, which is highly dependent on the modalities used for heat delivery [27–29]. All current methods for thermal manipulation fall short of the goal of achieving a uniform temperature load within target tissues volume. Consequently, a range of thermal responses will be generated within the tissue and temperature-specific effects will be difficult to discern. Therefore, in order to study the selective effect of hyperthermia, especially in subliminal conditions (42–45˚C), tissue temperatures must be precisely controlled and tissue volume heating achieved in a uniform manner.

Our aim was to develop a new experimental model for *in vivo* mild hyperthermia using non-directional microwaves, applicable to small live animals. We present an affordable approach for targeted microwave heat delivery to an isolated liver lobe in rat, which allows rapid, precise and stable tissue temperature control, while completely avoiding extraneous heating of non-targeted tissues. This experimental model may be useful for the study of temperature–specific alterations in tissues exposed to a uniform temperature load, with potential applications in therapeutic strategies involving hyperthermia.

Material and methods

Microwave heating model

A modified commercial microwave oven was used in order to deliver non-directional microwaves to live tissue, which in our experiments was the middle liver lobe of the experimental

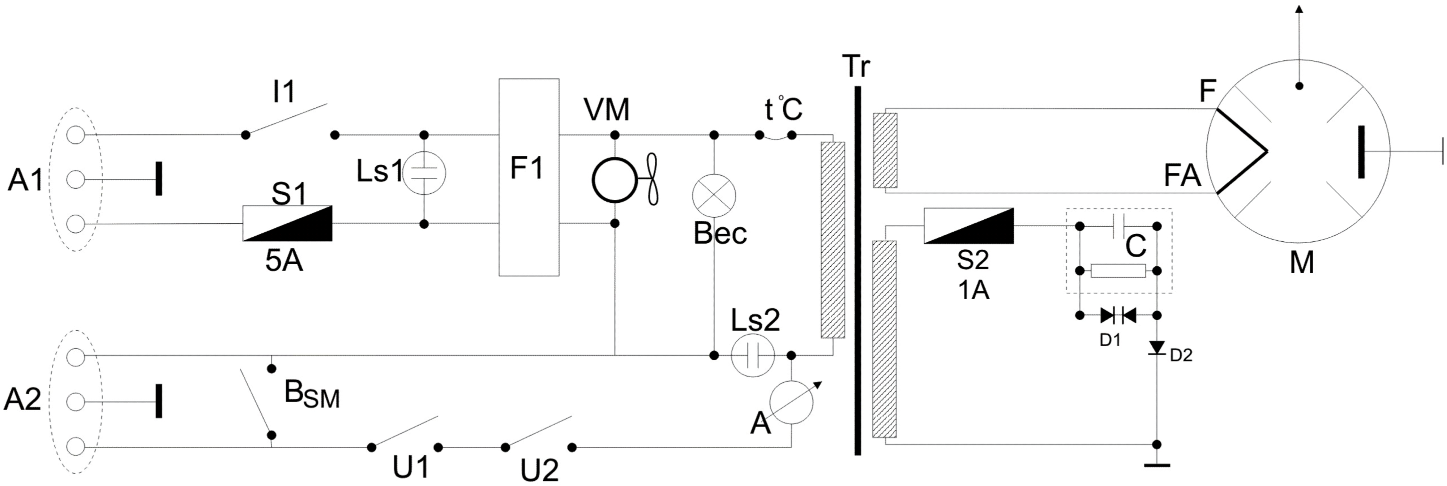

Fig 1. Wiring diagram of the magnetron. U1, U2 –dor close switch; A1, A2 –connectors; I1 –main breaker; Ls1, Ls2 –signaling lamps; Tr–transformer; S1, S2 –fuses; BSM–manual command button; A–ampermeter; F1 –power filter; C–capacitor; D1 –diode HVR-U62; D2 –diode HVR; VM–magnetron chiller; M–magnetron.

https://doi.org/10.1371/journal.pone.0184810.g001

animal. We used a commercial available 2M214-LG® (LG, Seoul, South Korea) magnetron generating 2450 MHz, with 4.4V and 14A in the filament and 4500V anodic voltage. Modifications were required in order to adjust tissue heating such as to prevent overheating and to allow for fine adjustments according to real-time target temperature.

Electrical circuits were removed from the original microwave, leaving only the magnetron power supply, magnetron cooling system, chamber light circuit and safety circuits that protects against the accidental door opening. A new electronic controller was designed for the magnetron, designed to operate on a feed-back loop, connected to temperature sensors in target tissue (Fig 1).

A1 connector is used for power supply (230V/10A), while A2 connector is used for temperature-dependent control. The original configuration of the microwave oven magnetron generates excessive energy in form of microwaves (1000 W), unsuitable for fine thermal manipulation in small tissue volumes. Selective targeting of the middle lobe of the rat liver creates the problem of a relatively small absorptive volume (less than a cubic centimeter), thus we introduced an additional target in the form of a 100-ml water-filled microwave resistant plastic container. This additional target, much larger than the targeted tissue volume, will absorb (using proportional distribution) most of the energy generated by the magnetron and prevent uncontrolled, rapid heating of the rat liver lobe [30]. Experiments run without the additional microwave energy trap (water target) resulted in excessive, uncontrolled heating of the target organ. A small plastic tube was used to evacuate water vapors outside the microwave oven chamber. The desired temperature inside the tissue target was achieved using a feedback-controlled, rapid pulse technology to power the magnetron, thus allowing for fine adjustments of the total energy transferred to tissue. Computer controlled adjustment of the ratio between the on and off intervals, based on tissue temperature measurements, led to the adequate decrease of the time-integrated power output and maintain tissue temperature with high accuracy.

The sequence of magnetron activation is correlated with temperature readings in an experiment in order to increase the tissue temperature to 42° C (Fig 2).

When tissue temperature is below the established limit, the magnetron is powered continuously thus achieving a progressive, linear increase in target temperature. After reaching the set

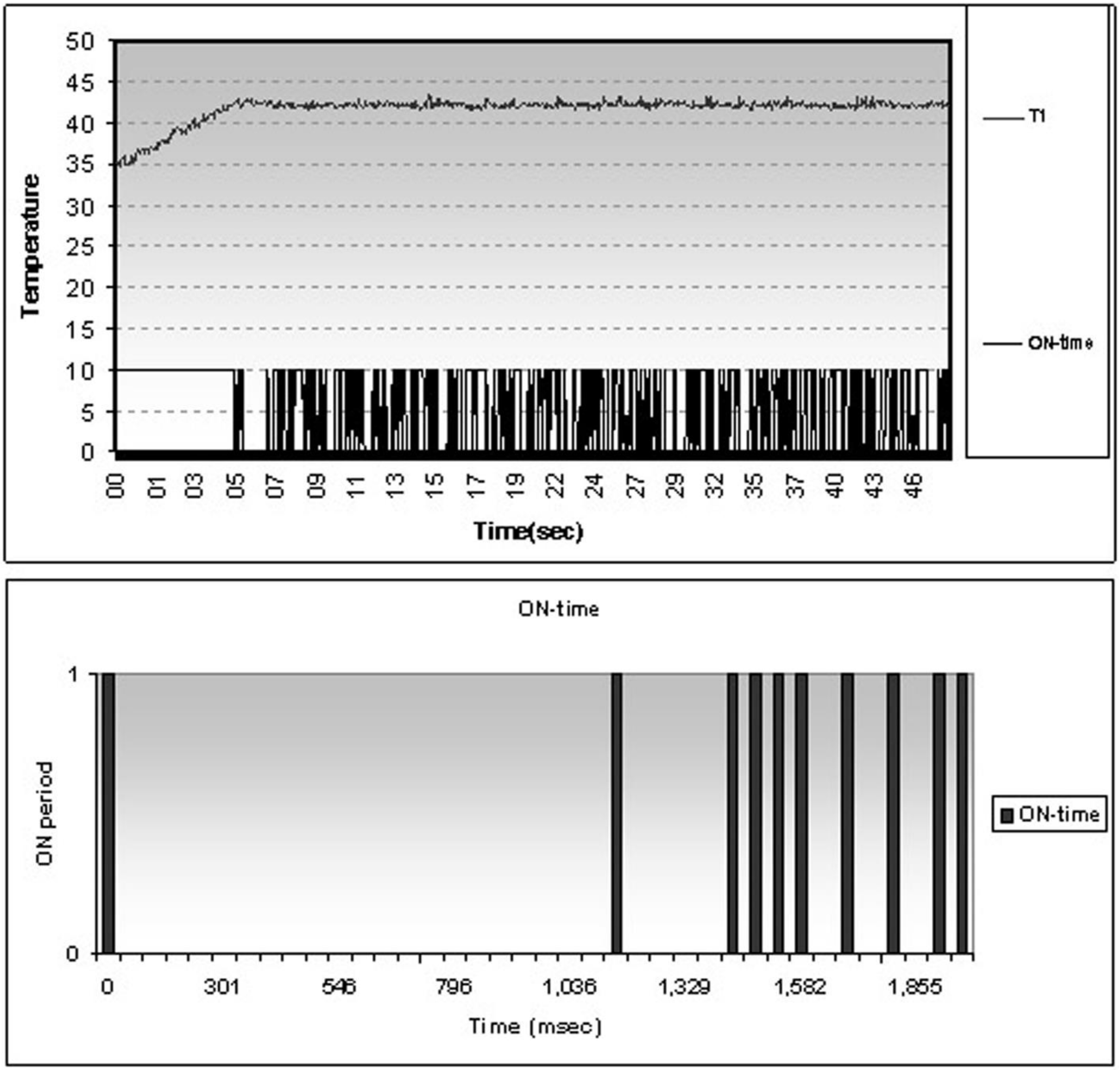

Fig 2. Magnetron duty cycle. Magnetron duty cycle in an experiment aiming to liver heating at 42˚C (graph in the upper panel); On-off cycle during the first 2 seconds after reaching set temperature (graph in lower panel).

https://doi.org/10.1371/journal.pone.0184810.g002

limit (42˚ C) the controller maintains the temperature using a rapid on-off switching, for a resulting magnetron duty cycle of 20.5% of time-period spent at the desired temperature.

Combining the additional water target and rapid pulsed activation of the magnetron we were achieved fine tuning of the amount of microwave energy delivered to target tissue, without the need of complex engineering required to change the power of the magnetron.

The revolving table was removed to allow for direct observation of live experimental animals, as well as for accurate positioning of the thermocouples. While we cannot exclude the possibility that the absence of a stirrer or rotating table generates a microwave pattern of interference inside the cavity, the presence of the energy absorbing water container and the reflecting surfaces in the random arrangement of the aluminum foil used to cover the body of the animal, minimized the likelihood of a hot spot affecting the small tissue sample exposed.

Simulation of the thermal effect were performed using CST Studio Suite® (CST Darmstadt, Germany) using a predefined microwave chamber and source with parameters similar with those in the prototype. Thermal effect was simulated in a rectangular (2x2x0.5cm) tissue sample centrally placed in the oven using available parameters for relaxation and thermal characteristics of tissue samples (Foundation for Research on Information Technologies in Society, Zurich, Switzerland, http://www.itis.ethz.ch/itis-for-health/tissue-properties/downloads/; Institute for Applied Physics, Florence, Italy, http://niremf.ifac.cnr.it/, accessed on April 2016). Simulation performed with FDTD electromagnetic simulator at 2.45 GHz, central tissue temperature maintained at 40˚C, wall temperature kept constant at 20˚C and CST option "Bio-heat"—not active. Computer simulation of the thermal effect predicts a homogenous heat distribution within the simulated tissue (Fig 3).

Temperature probes are placed centrally in the experimental middle liver lobe, approximately 1.5–2.0 mm from either border. Control temperature probes are placed in lateral liver

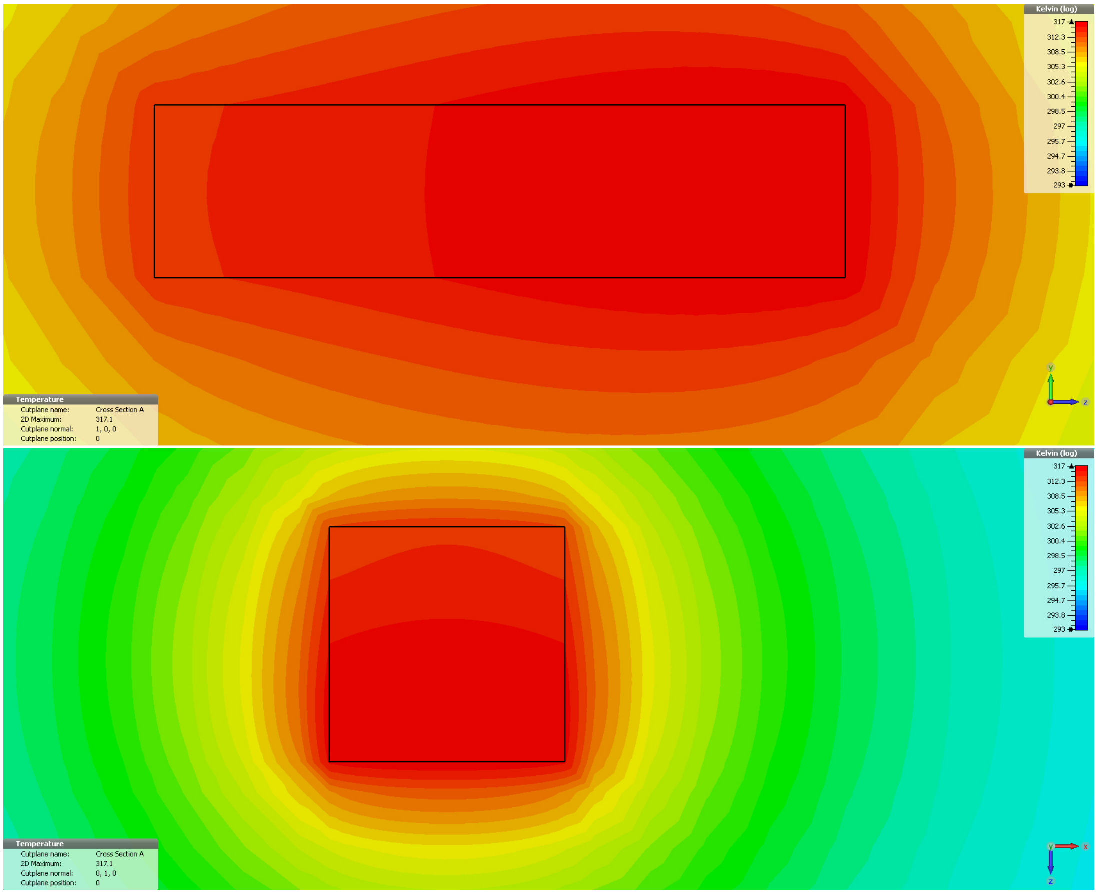

Temperature
Cutplane name: Cross Section A
2D Maximum: 317.1
Cutplane normal: 1, 0, 0
Cutplane position: 0

Temperature
Cutplane name: Cross Section A
2D Maximum: 317.1
Cutplane normal: 0, 1, 0
Cutplane position: 0

Fig 3. Electromagnetic/Thermal co-simulation. Electromagnetic/Thermal co-simulation using CST Studio Suit; vertical plane—upper panel; horizontal plane -lower panel.

https://doi.org/10.1371/journal.pone.0184810.g003

lobes and peritoneal cavity. All metallic components were grounded, thus preventing microwave-induced electrical discharges in the capacitive field of the oven. Although we did not interfere with the oven's operator safety structures, we evaluated microwave radiation, 5 cm in front of the oven door and around the oven body. Measured microwave energy was inferior to 1mW/cm, similar to a commercial microwave oven working in standard operation mode. As the heat dissipated from the water container was the only source of heating inside the cavity, a slight decrease in central body temperature of the experimental animal was observed (2–3 degrees).

Tissue temperature was monitored using highly sensitive J thermocouples, designed and produced especially for this experiment from 23G syringe needles. The sensitive junction was introduced into the hypodermic needle that acts as a shield. Signal wires were protected using a twisted shield cable [31]. The sensors shields (needle and shield cable) were connected to the system ground in order to avoid discharges in microwave field, as previously described [32–34].

Temperature data acquired from target tissue was used in order to maintain target temperature constant during the time-frame of the experiments. Thermal probes feed information into a virtual instrument (VI) application implemented in LabView® (National Instruments Corporation, Texas, USA). The temperature readings from the target tissue are analyzed in real time and the system responds to variations of 0.1° C, controlling the power of the magnetron by switching it automatically on/ off. For this purpose, we developed a virtual instrument (VI) that allows us to control the temperature in the liver lobe (S1 Fig).

The VI software component aims to keep the target temperature within a set narrow interval for a given period of time. The VI contains two parts: the user interface and the programming module. The user interface (S2 Fig) is used during the experiment and allows the user to adjust main parameters: upper temperature limit, lower temperature limit, length of time, and filter accuracy. Heating time starts once the desired temperature is reached in T1 or T2 sensors. Once the instrument is running, the user can start the test by pressing the recording button, with real time temperature readings displayed in analogical and graphic modes. The programming module is the program behind the VI and the block diagram is presented in Fig 4.

The implemented algorithm is a controller that keeps at least one parameter value between set limits in imposed conditions (time). For that reason, we acquire analogical signals from J type thermocouples, through a data acquisition board. Data are compared with preset limits, and the relay controls the magnetron by switching it on or off, in order to maintain the desired temperature in target tissue.

The Virtual Instrument hierarchy highlights the dependency between program sub-VI, the dataflow between program sub-VI and one of its main advantages: modularity. Due to this modular implementation of the algorithm, the researchers can easy modify the functions or can add supplementary functions to main VI core. Therefore, the microwave heating virtual instrument is one versatile tool that can be easily adapted in order to conduct experiments with different test procedure requests.

Due to the high sensibility of the thermocouples (0.01°C), high amplification factor on DAQ settings, and high sampling rate (10 kHz), any discharge or any voltage artifact can induce false peaks on reading values. Therefore, we introduced in the main program a data filtering routine. The original temperature values sampled at 100 kHz are smoothed by a moving average window of 10 samples, and compared with set limits. The relay is switched on/off through a 5V DAQ digital port if measured average is outside or inside preset limitations. The system will activate the magnetron using a classical feed-back algorithm. Using a common grounding for magnetron, oven protective cage and all shields (animal shield and thermocouples shielding components) we manage to eliminate all spikes in our experiments, but we continue to use the filtering routine as an additional safety measure (S3 Fig).

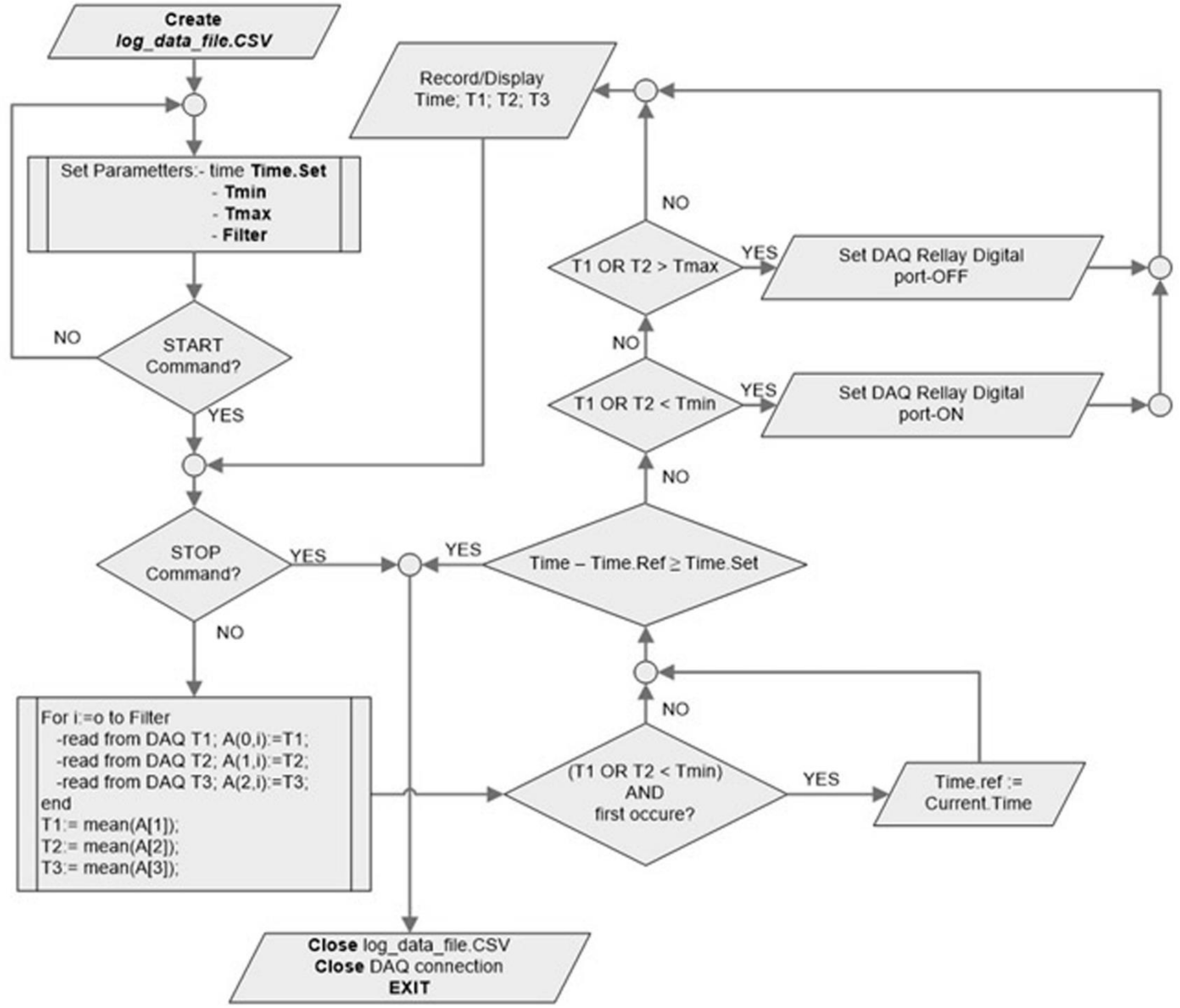

Fig 4. Virtual instrument programming module. Block diagram.

https://doi.org/10.1371/journal.pone.0184810.g004

Animals

Ten healthy adult male Wistar rats, weighing 250–270 g were used in this study. The experimental animals were maintained in individually ventilated polyethylene cages with food and water *ad libitum*, under controlled ambient temperature (21 ± 0.5˚C) and a 12h/12h light–dark cycle. All procedures were approved by the Ethical Committee of the Grigore T. Popa University of Medicine and Pharmacy, Iasi. Animals were clinically monitored daily throughout the study to ensure well-being and normal behavior.

Surgery

Each rat was anaesthetized with a mixture of Ketamine (65 mg/kg) and Xylazine (15 mg/kg) administrated intraperitoneally. Before starting experiments, deep anesthesia was verified by pinching the hind paw or gently swabbing the cornea of the rat. Lack of any response was considered the confirmation of deep anesthesia. None of the animals required supplementation of

Fig 5. Aluminum foil wrapping. Mobilized middle liver lobe remains uncovered for microwave exposure.

https://doi.org/10.1371/journal.pone.0184810.g005

anaesthesia during the experiment, and recovered within 60 minutes. During anesthesia and surgical procedure rats were placed on a heating surface in order to maintain the central temperature of the body around 37˚C, as monitored by a rectal temperature probe.

Liver exposure was made after incision of the anterior wall on the *linea alba*, starting from the xiphoid process and extended 3 cm to the pubis. An optimal exposure of the middle liver lobe is necessary, and that is possible due to particular anatomy of rat liver. In this species, the middle liver lobe is rather isolated and mobile, especially after cutting the falciform ligament. We used in all experiments the middle lobe of the liver as a target tissue for microwave delivery, while the lateral lobes served as control.

The anaesthetized rat was protected from microwaves using aluminum foil that allows for a rapid and versatile wrapping (Fig 5). The whole body and non-target liver tissue were protected by this Faraday-type cage that was electrically connected to the oven protective cage and magnetron grounding electrode.

The efficiency of the protecting foil was assessed by two isolated temperature microprobes, one inserted into the abdominal cavity and the other one in the lateral liver lobe. A thermal image obtained immediately after targeted heating demonstrates that aluminum wrapping remains cold, while the liver lobe and water container are heated to a significantly higher temperature than the surrounding structures (Fig 6).

After the procedure (total time in microwave oven <3 minutes), the foil was removed, the micro sensors were detached and the abdomen was closed using non-absorbable suture silk. All animals survived the experimental procedure and were monitored during recovery and were brought back in special cages for postoperative follow-up. Meloxicam 1mg/kg was administered subcutaneously in the first 2 postoperative days, in order to ensure analgesia. No animals died or became ill before the experimental endpoint. Normal feeding was restored within 24 hours and animals were sacrificed by Xilazine/ Ketamine overdose followed by decapitation, 7 days after the procedure, for tissue evaluation in different experimental settings. For temperatures below 42˚C there were no structural changes in light microscopy and no signs of burns associated with abnormal hot spots inside the experimental lobe.

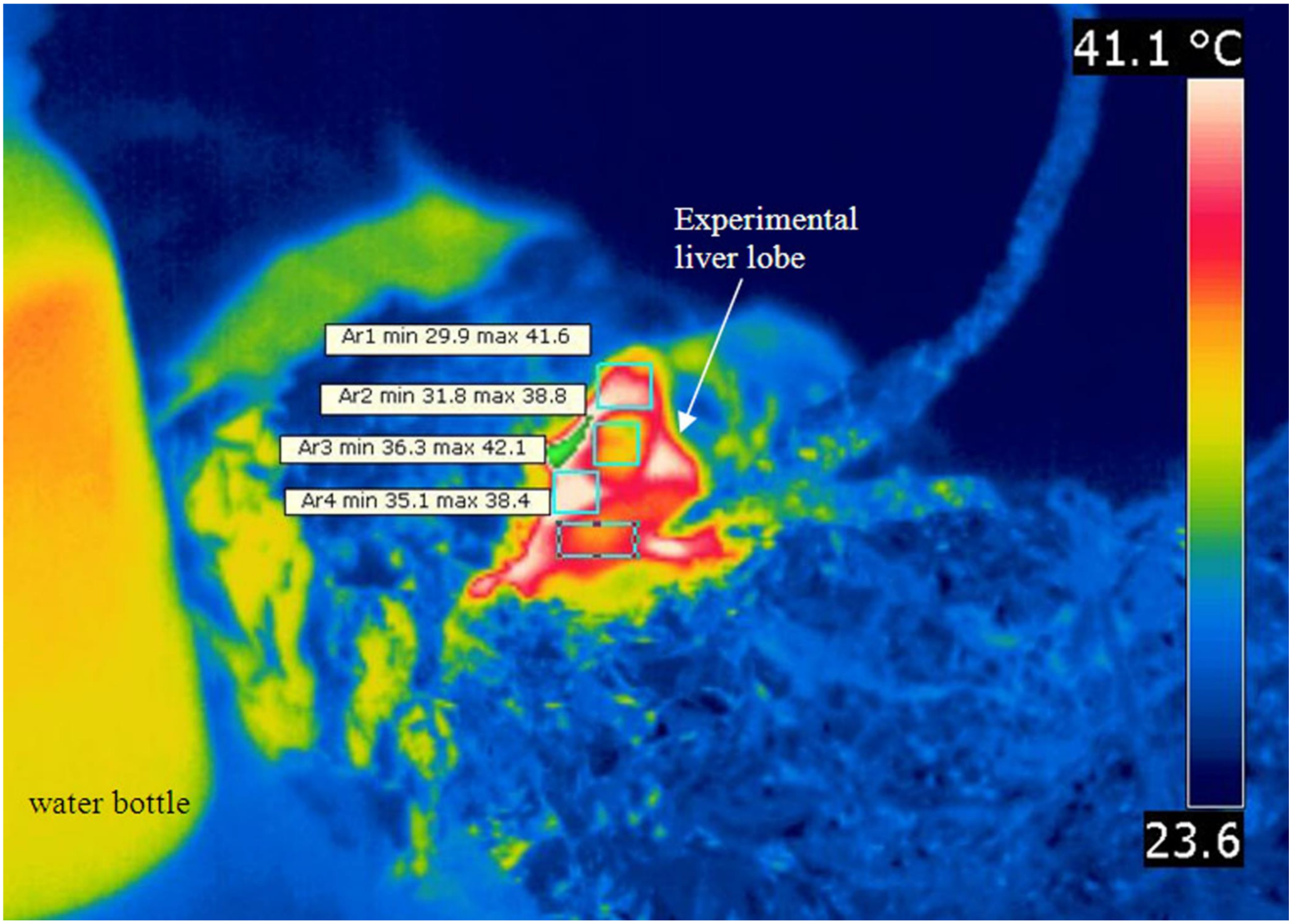

Fig 6. Thermal imaging after microwave exposure. Demonstration of the lack of hot spots outside experimental tissue. Infrared image obtained seconds after microwave heating—thermal gradient on the surface of the liver are inherent to rapid cooling in the periphery of the experimental lobe.

https://doi.org/10.1371/journal.pone.0184810.g006

Results

Experimental data clearly demonstrates that the exposed middle lobe is being heated, while the rest of the animal is protected by the aluminum foil. After euthanasia, we harvested liver (heated and aluminum protected lobes), spleen, kidney and lungs. There were no changes associated with heat exposure that could be identified in light microscopy, as compared to normal rat histology. Just before heating, the temperature in exposed liver is somewhat lower than normal (Fig 7).

The 4˚C difference at the beginning of the experiment is determined by the exposure to room temperature during surgical dissection and wrapping. The temperature in the experimental microwave chamber is also at room temperature before magnetron activation. Heat generated in the microwave chamber will not raise the central temperature of the rat as the aluminum protection acts as a very efficient screen. Two microprobes measured temperatures in the target tissue (T1) while two microprobes are positioned in the lateral liver lobe and the peritoneal cavity (T2). While desired temperature was maintained in the experimental lobe at set levels the rest of the body appears not to be affected, with very small variations around

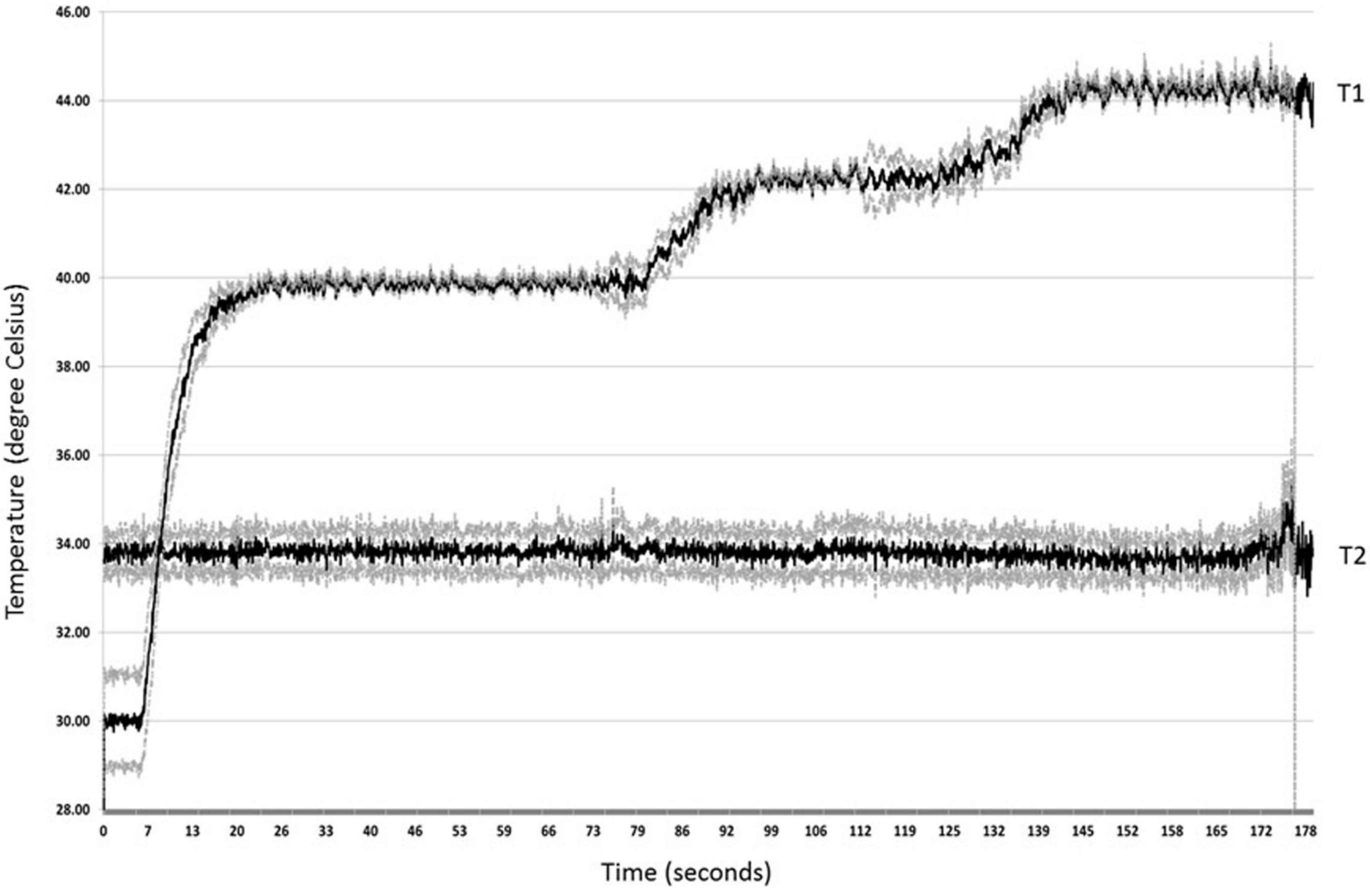

Fig 7. Continuous recording of tissue temperature. Temperature recorded for three successive targets (40, 42 and 44˚C) (n = 10). T1—average of the temperatures values acquired from heated liver lobe. T2—average of the temperatures values acquired from control liver lobe. Dotted lines represent standard deviation.

https://doi.org/10.1371/journal.pone.0184810.g007

baseline. Fig 7 represents the plot for 10 experiments conducted in a similar manner, with target tissue heating set to 40˚C, 42˚C and 44˚C in successive testing, with data presented as mean (black line) and standard deviation of the mean (dotted lines). We assume that successive increments in target temperature may be slightly biased due to tissue drying, but we minimized the effect by a rapid succession of intervals. All animals recovered after the experiment without any side effects, demonstrating the efficacy of the aluminum foil cage to protect the whole animal from the harmful effect of microwaves. In addition to the requirement for anesthesia, heating- induced dehydration of the target tissue limits the duration of the hyperthermic exposure in this experimental setup.

Increasing the target temperature from baseline to the desired level depends apparently on the temperature interval, which in turn is dependent on the feed-back algorithm. Larger thermal intervals imply a coarser microwave delivery, without frequent on-off switches that are needed to prevent overshooting. Temperature rises from 30˚C to 40˚C with 3.375˚C / second (R^2 = 0.9551), while the increment is lower it the next two intervals (40–42˚C and 42–44˚C) with 0.291˚C/ s (R^2 = 0.9337) and 0.136˚C/ s (R^2 = 0.7894) respectively, with very accurate linear regressions (Fig 8).

The differences in the slopes are generated by the temperature gradient required to achieve the set limit. A large temperature interval will allow for continuous activation of the magnetron

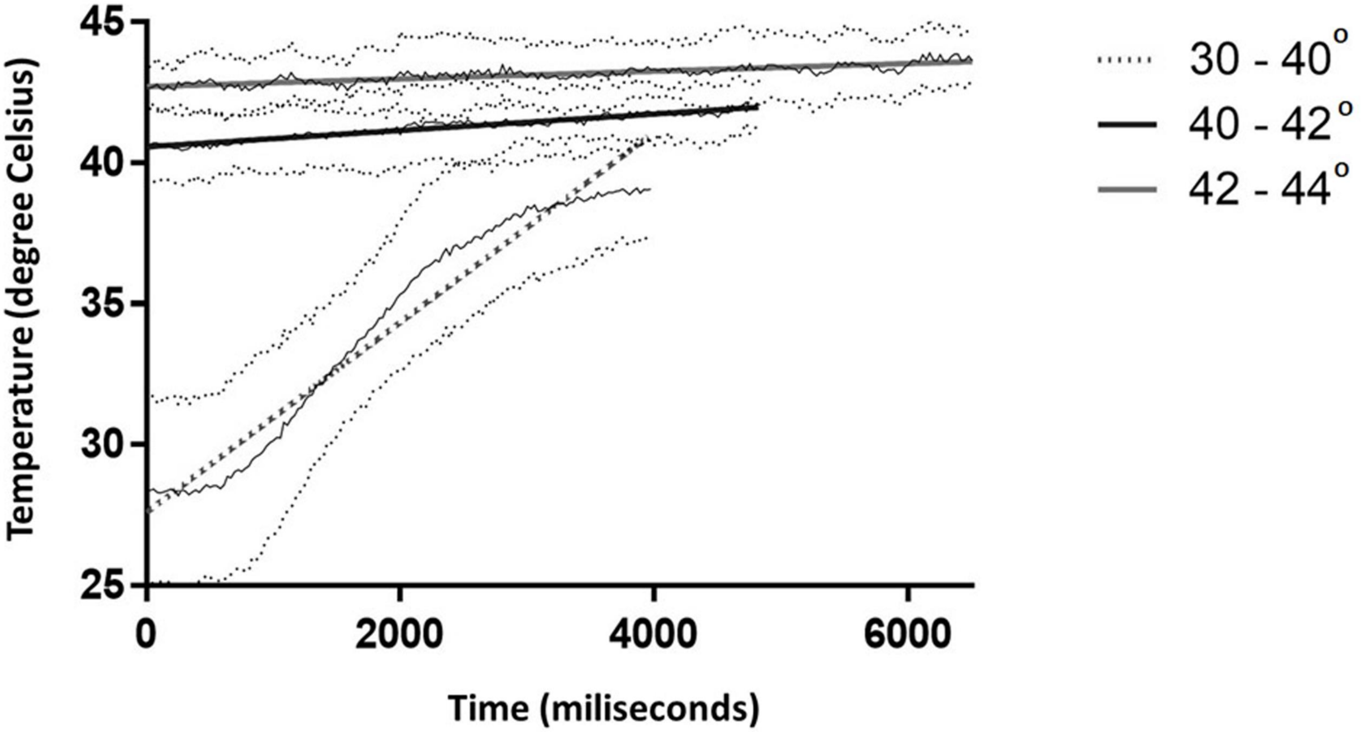

Fig 8. Linear regression indicating the rate of temperature increase in the heated lobe (n = 10). Thick dotted line: 30˚C to 40˚C at 3.375˚C / second (R2 = 0.9551; p<0.0001); Thick black line: 40 to 42˚C at 0.291˚C/ second (R2 = 0.9337; p<0.0001); Thick gray line: 42 to 44˚C at 0.136˚C/ s (R2 = 0.7894; p<0.0001). Thin solid and dotted lines are average and respectively, standard deviation of recorded temperatures.

https://doi.org/10.1371/journal.pone.0184810.g008

and a steep slope, while a 2˚C increment will generate short lived point temperatures within the set margins, as such turning the magnetron off and prolonging the time required to achieve a steady temperature. That is, in our view, an advantage of the system, that will prevent the rapid increase of temperature around the set limit and more precise heating of tissue volume.

Discussions

Microwave induced heating has first been proposed for the treatment of recurrent breast cancer, and that opened the door to a wide series of applications using a range of thermal effects [35]. Microwaves generate heat at a rate which is proportional to the square of the applied electric field magnitude and the effective conductivity, a measurement of microwave absorption [36]. The precise mechanisms of interaction with tissue are very complex and difficult to predict, as energy delivery varies with radiating power, specific absorption rate, permittivity, depth of penetration and tissue conductivity.

Animal tissues contain ~ 70% water and thus will easily absorb microwave energy, producing a direct heating [37]. Widespread use of microwave energy for hyperthermic cancer therapy is limited due to rapid absorption in any water containing structures, unpredictable and rapid thermal changes, and deleterious effects to normal tissues. Targeted microwaves exposure would provide a conceptual advantage, although physical methods to focus microwave radiation are rather impractical in clinical or experimental settings. However, collimated microwave radiation would induce a significant thermal gradient within the targeted tissue along the direction of propagation, as effective microwave energy would decrease exponentially with the distance from the source. In contrast, a uniform distribution of the microwave radiation across the entire surface of the tissue, will allow a certain temperature to be achieved in the center, while the temperature gradient will be blunted as compared to that generated by directional microwaves.

We developed an experimental model for tissue hyperthermia designed to generate accurate mild heating of target tissue in vivo. Pathophysiological alterations in subthreshold conditions, although not lethal, may induce temporary abnormalities that may be used for targeted therapy as certain antigens or specific proteins may be over-expressed or become more available to portal or systemic drug delivery [38–39]. We aimed to develop an affordable and simple model that allows a versatile setting for experimentation with the live animal while controlling accurately the temperature and timing according to principles of thermal dosimetry [40]. Our experimental heating device offers the possibility of early in vivo modeling of therapeutic approaches combining hyperthermia with pharmacological approaches, thus it is not designed to immediately translate as such in clinical usage. However, we intend to offer this platform as a screening tool, with the possibility to select efficient therapies for translational research in clinical trials.

Delivering microwaves in selected tissue for subthreshold heating in small mammals, comes with problems related to miniaturization and animal protection. Miniaturized antennas using a self-resonant cavity can deliver microwaves with precise frequency [40]. However, a significant local thermal gradient due to unidirectional delivery and possible side irradiation of lateral liver lobes (which we used as controls in normal and metastatic liver), together with the high cost and technical challenges may limit their wide-spread usage. Choosing a microwave oven may appear counterintuitive when aiming to heat a small tissue sample (middle liver lobe) and this approach is generally considered suitable for whole body hyperthermia. While alternative strategies for targeted microwave treatment have been put forth [41], we have shown that efficient screening of the living animal can be achieved and microwave treatment can be restricted to a selected organ without effects on the experimental animal and without safety concerns for the personnel. The effects of thermal gradients within the volume of tissue, such as those generated by the use of antennas [42–44], may be unimportant when thermal destruction is desired, but even small thermal gradients in the range between 40–42˚C generated during subthreshold tissue manipulation may alter the outcome of the therapy [26]. Our aim for thermal manipulation is in the same range with HIPEC conditions, in which situation differences in temperature between specific points in the peritoneal cavity can differ by 2˚ C [45]. For thermal pretreatment, we assume that such a gradient may produce uneven effects that can alter drug delivery if dependent on antigenic or protein expression. In our experiment, we aim to create an overheating of the target tissue of 5˚C (above the normal core temperature) and monitoring the temperature in the central part of the experimental lobe ensures a minimal temperature gradient between the core and the surface of the heated liver lobe. Thermal camera readings have major procedure related limitations and were used only to show that the liver surface is adequately heated and no off-target hotspots are created. Accurate 3D temperature dosimetry [46] for such an experimental model is technically difficult, and use of multiple implanted thermocouples is bound to create tissue injury. However, we used electromagnetic/thermal co-simulation that shows a uniform thermal distribution throughout a small target volume ($\leq 2.0 cm^3$) as long as the core temperature is maintained at a constant temperature (as recorded by implanted thermocouple). Furthermore, using pulse activation of the magnetron during steady temperature function allows heat to dissipate across the volume producing a more homogenous effect.

Our work is a proof of concept study demonstrating the feasibility of an experimental setup system for *in vivo* hyperthermia using non-directional microwaves. Targeted heat delivery to specific parts of an organ or specific tissues can be done with our model with the added advantage of very easy adjustment of experimental setup, without additional costs. While not an ideal model for clinical usage for microwave delivery, the proposed system is well adapted for experimental thermal manipulation of living organs in the context of targeted delivery of drugs in heat modified structures. Microwave radiation-induced hyperthermia is emerging as new tool in cancer treatment in adjuvant setting, but is especially susceptible to extraneous energy delivery, affecting off-target tissues [47]. To overcome this limitation, we have used a novel conceptual approach of insulating the entire living organism, with the exception of the targeted tissue. This approach is easy to implement, as the Faraday-type insulator can be conveniently manufactured out of aluminum foil and using a common grounding with the magnetron prevents extraneous electrical discharges and associated hotspots. Furthermore, this insulation technique could be used to target other organs or tissues such as kidneys, intestines, urinary bladder, spleen, and testis.

One desirable feature of our system is the achievement of a rapid increment of tissue temperature with minimal lag between the start of the magnetron and achievement of the desired temperature in the target tissue. In all experiments, the desired temperature was achieved within 7.5 seconds, with minimal variations reflected in the standard deviations of individual measured points. Almost similar intervals are required for each 1˚C thermal increment with more variation in individual readings, probably associated with changes in the specific absorption rate, when dielectric tissue properties are changed due to water evaporation. The steep curve suggests that in experimental settings when exposure is in the range of minutes, this activation part can be ignored as far as exposure to a certain temperature needs to be quantified.

Another feature of the system presented here is the stability of the temperature inside target tissue, with minimal variations during the plateau. Setting a desired temperature in the feedback loop is versatile and does not need a set procedure, the system being permanently adapted to local temperature and thus being able to accurately maintain it during the experiment. Taking into account that the system was set to respond to variations of 0.1˚C, we consider that the temperatures achieved inside target tissue are very well controlled and the system is functional.

In conclusion, we have developed an inexpensive and easy to manufacture system for targeted hyperthermia using non-directional microwave radiation. This system allows for fine and stable temperature adjustments within the target tissue for various time intervals. Furthermore, the use of non-directional microwave energy is likely to minimize the generation of thermal gradients within the targeted tissue, thus allowing uniform temperature loads.

Perspectives

Liver tumors may be addressed by heating them at different temperature, but most therapeutic approaches consist in complete destruction using radio, cryo or microwave ablation. Confined tumoral growth can be often destroyed with physical agents, with very good short-term results. This approach is increasingly used, especially in combination with surgery and/ or radio/chemotherapy.

Modern oncology showed that for some non-resectable primary or metastatic tumors, long term management as a chronic disease may produce better results, with better control in its place of occurrence. According to this concept, using bellow-threshold energy delivered in liver tissue, we wish to produce structural changes that will allow further therapeutic manipulations. Using our system, we are capable to induce different degrees of alterations in liver tissue, opening the door for future oncologic therapeutic approaches.

Supporting information

S1 Fig. Virtual instrument hardware setup. J thermocouples (1 and 2) send electric signals that are acquired through analogical ports from NI USB DAQ 6211 acquisition board (6), connected to a computer that runs the software developed under LabView®. The magnetron (4) is automatically controlled through the digital port of the DAQ board (6) that commands the relay (5) to open or close. The microwave trap (3) was installed between the magnetron waveguide (4) and the target in order to provide an additional target.
(TIF)

S2 Fig. The virtual instrument (VI) front panel. 1-start button; 2-time interval and temperature limit adjustment; 3-filter accuracy button; 4-recording button; 5-time stamp tag; 6,7-real time temperature readings in analogical and graphic display.
(TIF)

S3 Fig. The Filter sub-routine and algorithm. The Filter sub-routine: left side and feed-back algorithm: right side.
(TIF)

Author Contributions

Conceptualization: Ionuț Tudorancea, Decebal Neaga, Bogdan Tamba, Radu Iliescu, Gabriel M. Dimofte.

Data curation: Vlad Porumb, Bogdan Tamba.

Funding acquisition: Gabriel M. Dimofte.

Investigation: Ionuț Tudorancea, Vlad Porumb, Alexandru Trandabăţ, Radu Iliescu.

Methodology: Vlad Porumb, Alexandru Trandabăţ, Decebal Neaga, Radu Iliescu.

Project administration: Gabriel M. Dimofte.

Resources: Decebal Neaga.

Software: Alexandru Trandabăţ.

Supervision: Radu Iliescu, Gabriel M. Dimofte.

Validation: Radu Iliescu.

Writing – original draft: Ionuț Tudorancea, Vlad Porumb, Alexandru Trandabăţ, Bogdan Tamba.

Writing – review & editing: Radu Iliescu, Gabriel M. Dimofte.

References

1. Vernon CC, Hand JW, Field SB, Machin D, Whaley JB, van der Zee J, et al. Radiotherapy with or without hyperthermia in the treatment of superficial localized breast cancer: results from five randomized controlled trials. International Collaborative Hyperthermia Group. Int J Radiat Oncol Biol Phys. 1996; 35 (4): 731–44. PMID: 8690639
2. Maeta M, Koga S, Wada J, Yokoyama M, Kato N, Kawahara H, et al. Clinical evaluation of total-body hyperthermia combined with anticancer chemotherapy for far-advanced miscellaneous cancer in Japan. Cancer 1987; 59 (6): 1101–6. PMID: 3815283
3. Shari Lieberman, A review of Whole Body Hyperthermia and the experience of Klinik St. Georg, Townsend Letter, Aug/Sept 2009. Available from: https://www.thefreelibrary.com/A+review+of+whole+body+hyperthermia+and+the+experience+of+Klinik+St. . ..-a0206620309.

4. Vertree RA1, Leeth A, Girouard M, Roach JD, Zwischenberger JB. Whole-body hyperthermia: a review of theory, design and application. Perfusion. 2002 Jul; 17(4):279–90. https://doi.org/10.1191/0267659102pf588oa PMID: 12139385
5. Herman TS, Sweets CC, White DM, Gerner EW. Effect of heating on lethality due to hyperthermia and selected chemotherapeutic drugs. J Natl Cancer Inst. 1982 Mar; 68(3):487–91. PMID: 6950177
6. Suvernev AV. An experience of whole body hyperthermia in treatment of oncological pathology. Visceral Tumors. Tomsk. 1995; 97–99.
7. Horsman MR, Overgaard J. Hyperthermia: a potent enhancer of radiotherapy. Clin Oncol (R Coll Radiol). 2007; 19(6):418–26.
8. Carrafiello G, Lagana D, Mangini M, Fontana F, Dionigi G, Boni L, et al. Microwave tumors ablation: principles, clinical applications and review of preliminary experiences. Int J Surg. 2008; 6 Suppl 1: S65–9.
9. Wehner H, Von Ardenne A, Kaltofen S. Whole-body hyperthermia with water-filtered infrared radiation: technical-physical aspects and clinical experiences. Int J Hyperthermia. 2001; 17(1):19–30. PMID: 11212877
10. Issels R. Hyperthermia combined with chemotherapy—biological rationale, clinical application, and results. Onkologie. 1999; vol. 22:374–381.
11. Witkamp AJ, De Bree E, Van Goethem R, Zoetmulder FA. Rationale and techniques of intra-operative hyperthermic intraperitoneal chemotherapy. Cancer Treat Rev. 2001; 27(6):365–74. https://doi.org/10.1053/ctrv.2001.0232 PMID: 11908929
12. Mathe G. From mechanisms of action to relation indications of hyperthermia at 40˚C of 43˚C in cancer treatment. XXIV International Congress on Clinical Hyperthermia. Rome. 2001.
13. Baronzio GF, Hager ED. Hyperthermia In Cancer Treatment: A Primer. Springer Science & Business Media; 2006.
14. Rijnen Z, Togni P, Roskam R, van de Geer SG, Goossens RH, Paulides MM. Quality and comfort in head and neck hyperthermia: A redesign according to clinical experience and simulation studies. Int J Hyperthermia. 2015; 1–8.
15. Kok HP, Wust P, Stauffer PR, Bardati F, van Rhoon GC, Crezee J. Current state of the art of regional hyperthermia treatment planning: a review. Radiat Oncol. 2015; 10(1):196.
16. Chatterjee DK, Diagaradjane P, Krishnan S. Nanoparticle-mediated hyperthermia in cancer therapy. Ther Deliv. 2011; 2(8):1001–14. PMID: 22506095
17. Mallory M, Gogineni E, Jones GC, Greer L, Simone CB. Therapeutic hyperthermia: The old, the new, and the upcoming. Crit Rev Oncol Hematol. 2016; 97:56–64. https://doi.org/10.1016/j.critrevonc.2015.08.003 PMID: 26315383
18. Kano E. Fundamentals of thermochemotherapy of cancer. Gan No Rinsho. 1987; 33(13):1657–63. PMID: 2447303
19. Katrina F. Chu, Damian E. Dupuy. Thermal ablation of tumours: biological mechanisms and advances in therapy. Nat Rev Cancer. 2014; 14(3):199–208. https://doi.org/10.1038/nrc3672 PMID: 24561446
20. Yarmolenko PS, Moon EJ, Landon C, Manzoor A, Hochman DW, Viglianti BL, et al. Thresholds for thermal damage to normal tissues: an update. Int J Hyperthermia. 2011; 27(4):320–43. https://doi.org/10.3109/02656736.2010.534527 PMID: 21591897
21. Suzuki T, Kurokawa K, Suzuki K, Matsumoto K, Yamanaha H. Histological and immunohistochemical changes after transurethral ballon laser hyperthermia in the canine prostate. Tohoku J Exp Med. 1995; 177(1): 39–48. PMID: 8693485
22. Singh LP, Chauchan NR, Mishra BN, Khandal RK, Nanda S, Singh SB. Histological changes in mammalian liver and heart in response to graded hyperthermia. Int j Curr Pharm Clinical Res. 2015; 5(3): 184–188.
23. Bollemeijer JG, Lagendijk JJW, van Best JA, de Leeuw AAC, van Delft JL, de Wolff-Rouendaal D, et al. Effects of microwave-induced hypethermia on the anterior segment of healthy rabbit eyes. Laboratory Investigations, 1998; 227(3): 271–276.
24. Ichinoseki-Sekine N, Naito H, Saga N, Ogura Y, Shiraishi M, Giombini A, et al. Changes in muscle temperature induced by 434 MHz microwave hyperthermia. British Journal of Sports Medicine, 2007; 41 (7): 425–429. https://doi.org/10.1136/bjsm.2006.032540 PMID: 17261552
25. Diakite M, Payne A, Todd N, Parker DL. Irreversible change in T1 temperature dependence with thermal dose using proton resonance frequency-T1 technique. Magn Res Med. 2013; 69(4):1122–1130.
26. Dewhirst MW, Vujaskovic Z, Jones E, Thrall D. Re-setting the biologic rationale for thermal therapy. Int J Hyperthermia, 2005; 21(8): 779–790 https://doi.org/10.1080/02656730500271668 PMID: 16338861

27. Vargas Hernan I., Dooley William C., Gardner Robert A., Gonzalez KD, Venegas R, Heywang-Kobrunner SH, et al. Focused Microwave Phased Array Thermotherapy for Ablation of Early-Stage Breast Cancer: Results of Thermal Dose Escalation. Ann Surg Oncol. 2014; 11(2): 139–146.
28. Goldberg SN, Gazelle GS, Halpern EF, Rittman WJ, Mueller PR, Rosenthal DI. Radiofrequency tissue ablation: importance of local temperature along the electrode tip exposure in determining lesion shape and size. Acad Radiol. 1996; 3(3):212–8. PMID: 8796667
29. Hume SP, Marigold JCL. Time-temperature relationships for hyperthermal radiosensitisation in mouse intestine: Influence of thermotolerance. Radiotherapy & Oncology. 1985; 3(2): 165–171.
30. Planinsic G, Vollmer M. The surface-to-volume ratio in thermal physics: from cheese cube physics to animal metabolism. Eur J Phys, 2008; 29: 369–384
31. Winkler R. A Twisted/Shielded Tale Putting a Lid on Electromagnetic Interference. Available from: https://www.omega.com/Temperature/pdf/Twisted_Shielded_Case.pdf
32. Okmen Z, Bayindirli A. Modification of a household microwave oven for continuous temperature and weight measurements during drying of foods. Journal of Microwave Power and Electromagnetic Energy, 2000; 35(4): 225–231 PMID: 11257824
33. Wäppling-Raaholt B, Scheerlinck N, Galt S, Banga J R, Alonso A, Balsa-Canto E, et al. A combined electromagnetic and heat transfer model for heating of foods in microwave combination ovens. Journal of Microwave Power and Electromagnetic Energy, 2002; 37(2): 97–110
34. Ramashwamy H, Van De Voort F, Raghavan G, Lightfoot D, Timbers G. Feed-back temperature control system for microwave ovens using a shielded thermocouple. J. Food Sci, 1991; 56: 550–552
35. Brace CL. Microwave ablation technology: what every user should know. Curr Probl Diagn Radiol. 2009; 38(2):61–7. https://doi.org/10.1067/j.cpradiol.2007.08.011 PMID: 19179193
36. Cheung AY, Neyzari A. Deep local hyperthermia for cancer therapy: external electromagnetic and ultrasound techniques. Cancer Res. 1984; 44(10 Suppl):4736s–44s.
37. Duck FA. Physical properties of tissue: A comprehensive reference book. Academic Press; London; 1990.
38. Jauchem JR, Ryan KL, Walters TJ. Pathophysiological alterations induced by sustained 35-GHz radiofrequency energu heating. J Basic Physiol Pharmacol 2016; 27(1): 79–89.
39. Morimura Y, Okada AA, Hayashi A, Fujioka S, Hashida N, Kawahara S, et al. Histological effect and protein expression in subthreshold transpupillary thermotherapy in rabbit eyes. Arch Ophthalmol, 2004; 122(10): 1510–1515. https://doi.org/10.1001/archopht.122.10.1510 PMID: 15477463
40. Dewhirst MW, Viglianti BL, Lora Michiels M, Hanson M, Hoopes PJ. Basic principles of thermal dosimetry and thermal thresholds for tissue damage from hyperthermia. Int J Hyperthermia. 2003 May-Jun; 19 (3):267–94.41. https://doi.org/10.1080/0265673031000119006 PMID: 12745972
41. Chakaravarthi G, Arunachalam K. Design and characterization of miniaturized cavity-backed patch antenna for microwave hyperthermia. Int J Hyperthermia. 2015; 31(7): 737–748. https://doi.org/10.3109/02656736.2015.1068957 PMID: 26365603
42. Zhang H, Nan Q, Liu Y. Thermal distribution of microwave antenna for atrial fibrillation catheter ablation. Int J Hyperthermia. 2013; 29(6):582–9. https://doi.org/10.3109/02656736.2013.803606 PMID: 23829511
43. Zhai F, Nan Q, Guo X. The effects of fat layer on temperature distribution during microwave atrial fibrillation catheter ablation. Electromagn Biol Med. 2016; 35(1):8–14. https://doi.org/10.3109/15368378.2014.954289 PMID: 26296248
44. Ibitoye ZA, Nwoye EO, Aweda MA, Oremosu AA, Annunobi CC, Akanmu ON. Optimization of dual slot antenna using floating metallic sleeve for microwave ablation. Med Eng Phys. 2015; 37(4):384–91. https://doi.org/10.1016/j.medengphy.2015.01.015 PMID: 25686672
45. Rettenmaier MA, Mendivil AA, Gray CM, Chapman AP, Stone MK, Tinnerman EJ et al. Intra-abdominal temperature distribution during consolidation hyperthermic intraperitoneal chemotherapy with carboplatin in the treatment of advanced stage ovarian carcinoma. Int j Hyperthermia, 2015; 31(4): 396–402. https://doi.org/10.3109/02656736.2015.1007399 PMID: 25707816
46. Verhaart RF, Verduijn GM, Fortunati V, Rijnen Z, van Walsum T, Veenland JF et al. Accurate 3D temperature deosimetry during hyperthermia therapy by combining invasive measurements and patient specific simulations. Int J Hyperthermia, 2015; 31(6): 686–692 https://doi.org/10.3109/02656736.2015.1052855 PMID: 26134740
47. Gao S, Zheng M, Ren X, Tang Y, Liang X. Local hyperthermia in head and neck cancer: mechanism, application and advance. Oncotarget. 2016 Aug 30; 7(35): 57367–57378. https://doi.org/10.18632/oncotarget.10350 PMID: 27384678

The 7th IEEE International Conference on E-Health and Bioengineering - EHB 2019
Grigore T. Popa University of Medicine and Pharmacy, Iasi, Romania, November 21-23, 2019

Wearable Devices for Studying Microvascular Reactivity – It Is Feasible?

Gabriela Postolache[1,2], Alexandru Trandabat[2,3], Olga Plopa[2,3], Pedro Silva Girão[1,4], Octavian Postolache[1,5]
[1] Instituto de Telecomunicações, Lisbon, Portugal
[2] Intelectro, Iasi, Romania,
[3] Facultatea de Electrotehnica, Universitatea Gheorghe Asachi, Iasi, Romania
[4] Instituto Superior Técnico, Universidade de Lisboa, Lisbon, Portugal
[5] ISCTE- Instituto Universitário de Lisboa, Lisbon, Portugal, opostolache@lx.it.pt

***Abstract*— We investigate what information can be obtained on daily changes in microcirculation using wearable technologies in out-of hospital or laboratory setting. The pulse wave, electrocardiogram, body temperature and blood pressure data obtained from seven days with normal physical activity was compared with data from seven days with 50% increase in physical activity. The number of steps and heart rate during daily activities were acquired using an electronic wrist watch. Radial artery and big toe digital artery pulse wave signals, wrist and big toe skin temperature, heart rate variability, were analyzed. The sympathetic nervous system influence on microcirculation was evaluated using frequency domain analysis of heart rate variability. The plantar signal was more influenced by movements artifact than pulse wave signal from radial artery. Low frequency component and ratio of low and high frequency component of heart rate variability, associated with sympathetic branch of autonomic nervous system was higher at night than in the morning and after positional changes. LF/HF ratio decreased in the week with more physical activity. Relevant information on determinants of microcirculation changes can be obtained using multimodal sensing supported by small devices that measure individual and environmental parameters.**

Keywords—microvascular reactivity, heart rate variability, wearable

I. INTRODUCTION

There is a large spectrum of microvascular dysfunction: i) peripheral arterial disease (e.g., intermittent claudication); ii) venous insufficiency (e.g., varicose veins or deep vein thrombosis); iii) lymphedema affecting lymphatic vessels; iv) vasculitis produced by inflammation of the wall of a blood vessel of any size; v) ischemic disease (e.g., microvascular ischemic disease that affect blood vessels in the brain). In different pathological conditions, organ dysfunction and mortality were correlated with microvascular dysfunction [1-5]. Several determinants of microvascular changes were identified - physical inactivity [6], food that induced hypertension [7-8], psychological stress [9], environmental stressor [10-11], immunity [12-14], genetics, low birth weight, obesity, aging [15]. Different technologies are currently used for microcirculation assessment. However, these technologies present different disadvantages and limitation [16] and many required complex procedure for calibration and measurements, which limits their use in clinical practice. Many of these technologies are mainly used in laboratory research. Unobtrusive, non-invasive technologies that would collect data on microcirculation from individuals in their natural environments, are required.

The goal of the present study was the investigation of putative information that can be obtained on microcirculation using a monitoring procedure based on wearable devices. Also was investigated the procedure acceptability and demand for the monitored subject.

II. TECHNIQUES FOR MICROCIRCULATION ASSESSMENT

In addition to anamnesis and pulse palpation, different non-invasive techniques are currently used to assess the location and hemodynamic changes in microvasculature (i.e., arterioles, metarterioles, capillaries, and venules), to diagnose microcirculatory diseases and to document the disorder concerning microcirculation disease severity. Assessment of microcirculation is a difficult task, due to small dimension of vessels (i.e. the microvasculature can be anatomically defined as blood vessels with a diameter <200–150 µm [15]) as well as because of complexity of the involved structures and relationships between structures in different physiological and physiopathological processes.

In Table I different techniques used for microvasculature assessment are presented. The currently used non-invasive techniques for the assessment of microcirculation give information on vessels anatomy (e.g., imaging techniques), tissue perfusion (e.g., Laser Doppler Flowmetry), different hemodynamic parameters (e.g., vascular pressure).

The data obtained using different techniques could have diagnostic value and can be used for planning detailed intervention if is needed, or for diseases preventive measures implementation. However, many of these techniques are used mainly for scientific research and less in clinical diagnosis and treatment planning. The time constraints, issues related with financial reimbursement of using different technologies for

978-1-7281-2603-6/19/$31.00 ©2019 IEEE

microcirculation assessments, and lack of equipment [17] were reported as main barriers for using different technologies for non-invasive assessment of microcirculation. Moreover, the high price and complexity of the procedures of different used technologies contribute also for higher reliance of health professionals on more subjective testing methods for microcirculation assessment.

Methods that facilitate objective assessment of timely progressive changes in microcirculation, preferable those at lower costs and that consider the daily living might give important support for understanding of microvascular ageing mechanisms or microvascular dysfunction, and for clarifying what changes in microvasculature precede or are secondary to different body function impairments. Several studies have reported that microvascular variables might help for better estimation and prediction of organ or system dysfunction and even mortality [1-2].

TABLE I. TECHNIQUES FOR MICROCIRCULATION ASSESSMENT

Imaging Techniques	Other Techniques
1.Using Light Emiting Source	9. Doppler Ultrasonography
1.1. Laser Doppler Imaging	10. Continuous-Wave Doppler Ultrasound
1.2. Diffuse Reflectance Spectroscopy	11. Ankle-Brachial Index
1.3. Laser Speckle Contrast Imaging	12. Toe-Brachial Index
1.4. Polarized Light	13. Segmental Limb Pressure
1.5. Orthogonal Polarization Spectral Imaging	14. Plethysmography
1.6. Sidestream Dark Field	15. Photoplethysmography
1.7. Incident Dark Field	16. Transcutaneous Oxygen Pressure
1.8. NADH fluorescence	17. Laser Dopple Flowmetry
2. Duplex Ultrasound	18. Hyperspectral Tissue Oxygenation
3. Computed Tomography Angiography	19. Temperature
4. Magnetic Resonance Angiography	20. Near Infrared Spectroscopy
5. Positron Emission Tomography	21. Vascular Reactivity to Occlusion
6. Radioisotopic Imaging Technique	22. Vascular Reactivity to Temperature Change
7. Digital Substraction Angiography	23. Vascular Reactivity to Posture Change
8. Infrared Termography	24. Haemodynamic Induced Changes by Exercises

Technologic advances particularly those related to small, mobile devices, have now made possible non-invasive, low-cost assessment and monitoring of microvasculature functions. Recent study from Stanford University [18] has shown that using wearable technologies that records data on weight, heart rate, oxygen in the blood, skin temperature, activities (i.e., including steps, acceleration, walking, biking and running, calories expended, sleeps and even exposure to gamma rays and X ray) a baseline range of values for each person can be obtained with higher precision, and that allow to identify health problem by monitoring deviations from normal and associating those deviations with environmental conditions. Taking into account the data presented in this study from one participant, 58 years old, male, that was routinely monitored using different wearable devices over a period of 24 months, the data from the study collected over a period of 11 months from 43 participants, ages 35 to 70 years old, monitored using Basis Peak (Intel, U.S.A.), health tracker for fitness, sleep and stress, as well as other data from recent literature on microcirculation assessment our hypothesis was that multimodal sensing based on small, low-cost devices might be used for estimation of microcirculation changes in out-of hospital or laboratory setting.

III. METHODS

Photoplethysmography (PPG) using green light was obtained using Shimmer GSR (Shimmer Sensing, Ireland) module and PPG sensors. The PPG sensors were positioned at wrist over radial artery and at level of plantar proximal phalanx of big toe. Shimmer ECG (Shimmer Sensing, Ireland) module was used to acquire electrocardiogram with a sampling frequency of 512 Hz. Skin temperature was measured at wrist and big toe level using a thermometer (Oregon Scientific, U.S.A.). Number of steps and heart rate were acquired using Forerunner 235 (Garmin, U.S.A.). Room and outside temperature, and humidity were acquired using meteorological station OH!Haus&Co 1000HomePro. The amplitude of PPG signals, heart rate, heart rate variability and body temperature were analyzed. The frequency domain analysis of heart rate variability (i.e., power spectral density and wavelet transform decomposition of the R-R signals) was carried out. Discrete Wavelet Transform (DWT) and Continuous Wavelet Transform (CWT) was applied using Daubechies4 mother wavelets. The data of low frequency (LF) and high frequency (HF) components of heart rate variability (HRV) was considered according the established standard [19]. Considering the controversies regarding interpretation of HRV as reflecting sympathetic activity (i.e., the putative influence of respiration and parasympathetic branch of autonomic nervous system on low frequency components of heart rate variability), the sympathetic outflow was estimated by analysis of three parameters – the frequency energy in the bandwidth 0.04-0.15 Hz; the normalized LF expressed as percentage of LF in LF and HF bandwidth (0.04-0.4 Hz); and as the ratio of low frequency and high frequency (LF/HF).The values were extracted after fast Fourier transform (FFT) and Wavelet Transform (WT) were applied for segments of 5 minutes of R-R signals, which were obtained from acquired ECG during 15 minutes in the morning and at night. The lower value of R-R signals recorded during the first seconds of position changes were not considered in the analysis as these values might interfere with FFT algorithm and highly increase the low frequency component in the spectral analysis. Therefore, spectral analysis was carried out in 84 R-R signals.

A healthy human subject, age 51 years, body max index – 28, no smoker, no coffee, no alcohol or other stimulatory beverages consumer was monitored for 14 days. The subject received a half of hour training on the devices use and protocol for recording data. The study was realized following World Medical Association (WMA) Declaration of Helsinki. The data from seven days with normal physical activity was compared with data from seven days with 50% increase in physical activity. The electrocardiogram and pulse wave were recorded in the morning after the person got out of bed and at night before going to sleep. Data was obtained for 10 minutes sitting on chair and 5 minutes standing.

IV. RESULTS AND DISCUSSIONS

During standing, the averaged amplitude of pulse waves at plantar level was decreased. Positional change produces a small increase in the amplitude of pulse wave that was recorded at radial artery (Fig. 1). Both PPG signals were highly influenced even by small movements. The plantar signal was more influenced by movements artifact than pulse wave signal from radial artery. In 42% of cases the photopletismography signals during standing were lost, possibly by inadequate positioning of the PPG sensor. More variation on skin temperature was recorded at level of big toe, and in the week with more physical activities. Skin temperature at level of big toe was at night 35.03°C (32.90-36.10) in the week with more physical activities, lower than at night skin temperature in the first week, which was 36.00°C (35.60–36.10). In the first 7 days the average and range of normalized low frequency component of HRV during 10 minutes of sitting was 63.20% (43.45-80.20) in the morning and increased during standing - 71.66% (58.56-86.39).

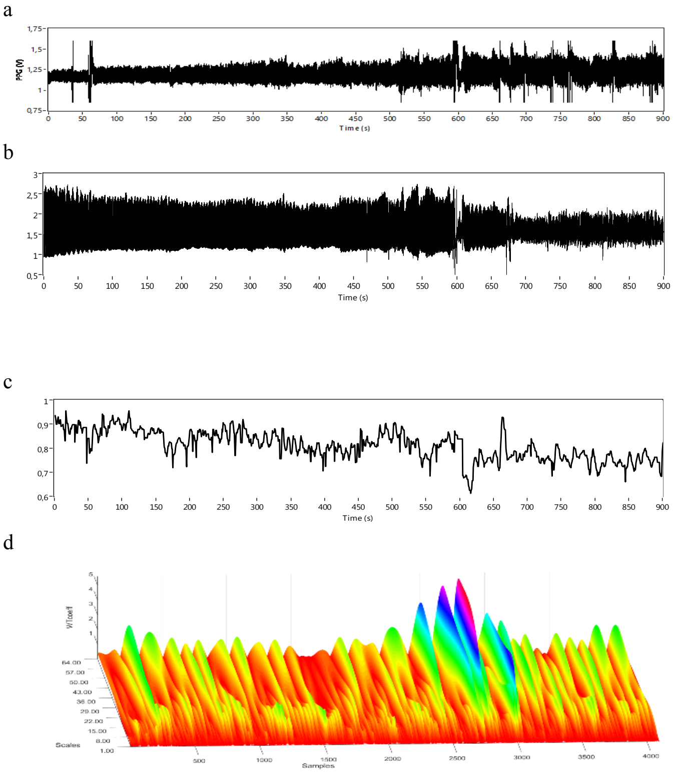

Fig. 1. Photopletismography signals obtained at level of radial artery (a) and big toe (b), the R-R signal (c) and continuous wavelet decomposition of R-R signal (d) obtained from 10 minutes sitting and 5 minutes standing. A position change produces a decreased in amplitude of PPG from big toe, a slightly increased in radial artery PPG, a decreased in R-R intervals and increased in sympathetic outflow (scale 32-64 in CWT decomposition of cardiac signal).

Increase in normalized LF was registered at night with changing posture - 83.41% (78.86-88.91) during standing in comparison with 74.31% (58.78-87.97). LF/HF ratio also increased during standing. The values of normalized LF and LF/HF ratio were lower in the morning than at night. Increased physical exercises have produced a reduction in resting sympathetic outflow estimated by normalized LF and LF/HF ratio both in sitting and standing, in the morning and at night. Average normalized low frequency component of heart rate variability increased less during standing both in the morning 68.36 % (60.05-84.47) *versus* 65.95 % (55.77-82.87) and at night 73.76 % (62.11-90.19) *versus* 73.81 % (54.93-85.25) (Fig. 2). The lower increased in sympathetic outflow during standing in the week with more physical activity was reflected also in LF/HF ratio and in smaller changes in average HRV (Fig. 3). No relevant variations were observed on averaged daily heart rate and resting heart rate recorded with Garmin wrist watch, although an increase in maximal value of heart rate was recorded in the week with increased physical activity. Average and range of resting heart rate in the first week obtained from Garmin wrist watch was 59.29 bpm (53-67) and 57.86 bpm (46-70) in the second week. Maximal heart rate in the first 7 days was 127.14 bpm (113-145), and higher in the week with more physical exercises – 143.57 bpm (130-163). In the first week the average and range step/day were 10113.56 (8108-14397) and in the second week 14673.71 (9538-20159). Average and range room temperature was 24.23°C (21-25). Room humidity in the morning was 55.3 (51-63) and at night 61.8 (53-74), being the values of room humidity highly correlated with outside humidity. The subject reported no difficulty on using the technology. Although the monitored subject has more knowledge on the wearable technology than general population, the study reveals the need of introducing in the procedure of technique for sensors position and person movements monitoring, during acquisition of the PPG and ECG, in order to improve the analysis of data and information processing. Different artifacts in the registered signals might be related to different person movements or position of the PPG.

V. DISCUSSIONS AND CONCLUSSIONS

In the paper is described a method in which wearable technologies were used for monitoring cardiorespiratory influence on microcirculation. The feasibility of using small devices to document the determinants (mainly those related to neurogenic influence) of microvascular dysfunction in out-of hospital, clinics or laboratory setting was tested. The study has shown that relevant information can be obtained using multimodal sensing based on wearable technologies that can be used for better understanding of microcirculation mechanisms in a more realistic, natural environment. The results suggest that techniques for usability testing and for accurate detection of influence of body movements on signal acquisition should be included to improve the procedure of microcirculatory investigation in out of laboratory setting.

From the eight general areas (identified in the study of Bowen et al, [20], which the studies on feasibility should focus, we evaluated the acceptability (reaction to intervention), the implementation setting, and practicality of the proposed method for microcirculation investigation.

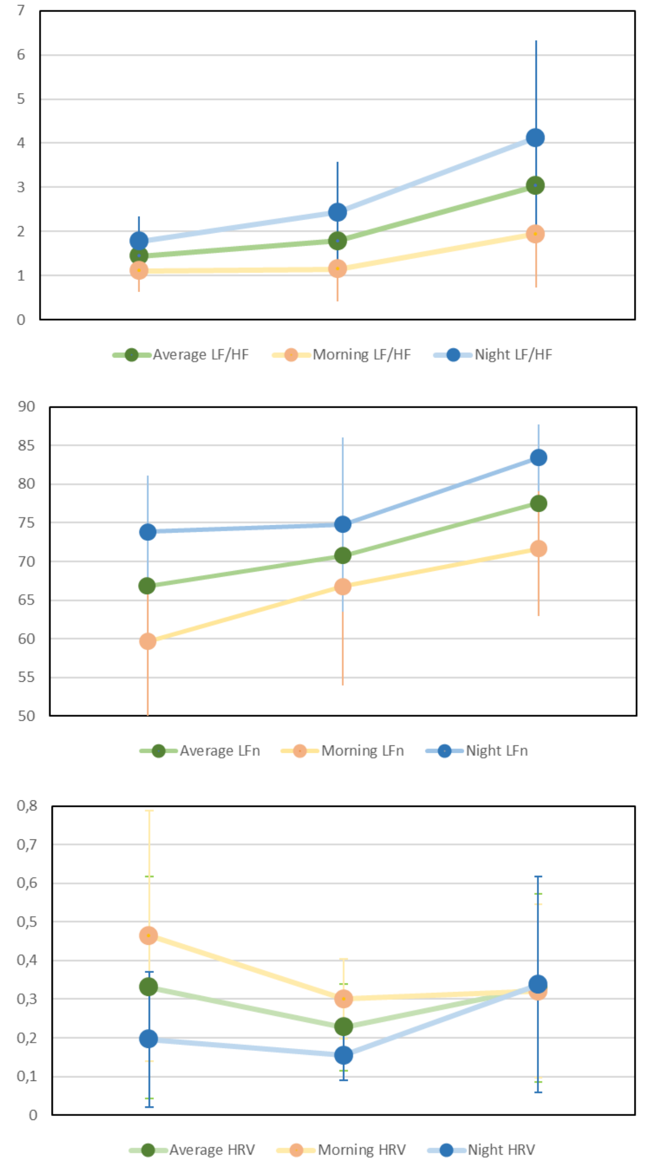

Fig. 2. Changes in average LF/HF ratio (top graph), LFn and average HRV (bottom graph) of cardiac signals: data collected in the first week during interval of 10 minutes sitting and 5 minutes standing in the morning and at night.

Recent advances in mobile technologies open possibilities for different diagnosis and treatments approaches. In many healthcare areas, have already shown higher cost-effectiveness of for health assessment and therapies than traditional methods [21-22].Our results are according to the findings from recent study of team from Stanford University [18] that shown that data collected with wearable technologies in out of hospital condition give relevant information on deviations from normal and their relationship with environmental conditions.

In the present study, technologies used to monitor physical activity are applied in microcirculatory research with special focus in the autonomic nervous system activity. An increase sympathetic outflow was documented in standing and with increase psychological stressor.

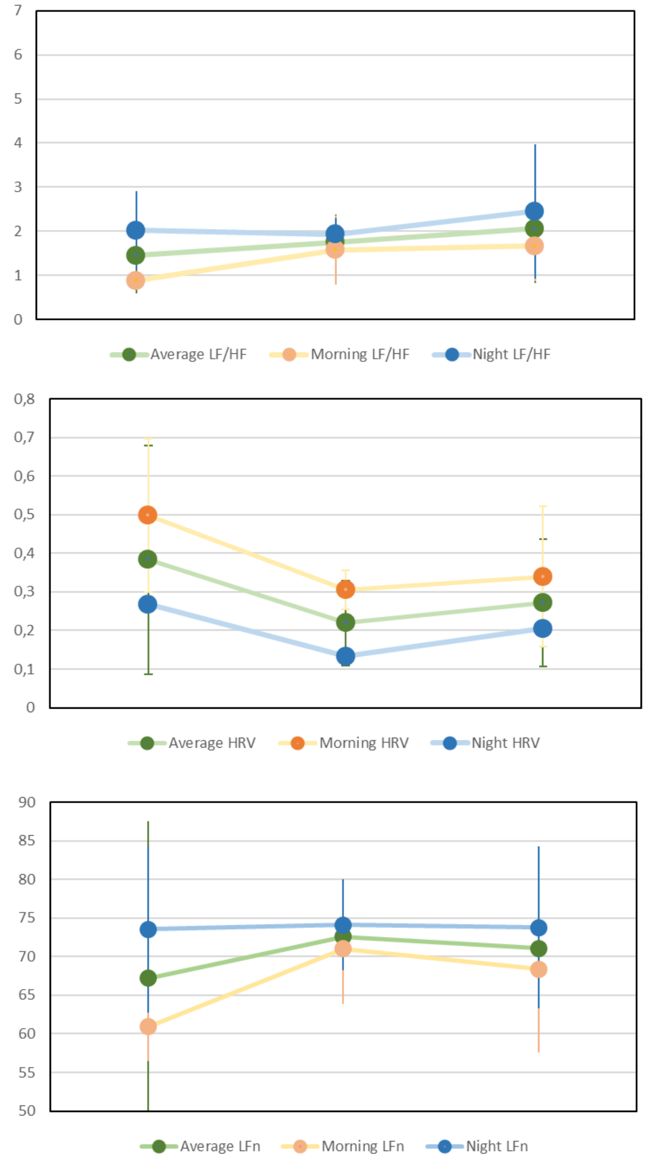

Fig. 3. Changes in average LF/HF ratio (top graph), LFn and average HRV (bottom graph) of cardiac signals: data collected in the second week during interval of 10 minutes sitting and 5 minutes standing in the morning and at night.

The diminished averaged values of microvasculature pulse wave correlated with data from previous study [23] in which decreased perfusion in plantar region was observed by changing position from supine to sitting. More physical exercises possibly increased the velocity of blood flow control mechanism, as the ratio between sympathetic and parasympathetic outflow measured by using 5 minutes cardiac signal was less affected during position change than in the week with lower physical activity. Research on the relation between the modality, duration and intensity of movements is important as several studies have shown that the sedentarism [24] is associated with microvascular dysfunction and that aerobic physical exercises can be used in treatment of various microvascular diseases [25-26]. More research on movements induced changes on microcirculation may contribute to find optimal setting for more effective prevention and treatment of microvascular dysfunctions.

For better analysis and information processing, the method based on self-monitoring of parameters related with microcirculation should include usability of the wearable devices.

ACKNOWLEDGEMENTS

The work was supported by: grant P_37_766, cod my 103847, nr. 68/08.09.2016 of the Romanian National Authority for Scientific Research and Innovation, NANO-IMUNELCHIM-PLAT Project/Competitiveness Operational Programme 2014-2020; Fundação para a Ciência e Tecnologia Project UID/EEA/50008/2019; and Instituto de Telecomunicações.

REFERENCES

[1] E.N. Schorr, D. Treat-Jacobson, "Methods of symptom evaluation and their impact on peripheral artery disease (PAD) symptom prevalence. A review", Vasc. Med., **18(2)**, 2013, pp. 95-111.

[2] S. Trzeciak, R.P. Dellinger, J.E. Parrillo, M. Guglielmi, J. Bajaj, N.L. Abate, R.C. Arnold, S. Colilla, S. Zanotti, S.M. Hollenberg, Microcirculatory Alterations in Resuscitation and Shock Investigators, "Early microcirculatory perfusion derangements in patients with severe sepsis and septic shock: relationship to hemodynamics, oxygen transport, and survival", Ann. Emerg. Med., **49(1)**, 2007, pp. 88-98, 98.e1-2.

[3] G.C. Leng, A.J. Lee, F.G. Fowkes, M. Whiteman, J. Dunbar, E. Housley, C.V. Ruckley, "Incidence, natural history and cardiovascular events in symptomatic and asymptomatic peripheral arterial disease in the general population", Int. J. Epidemiol., **25**, 1996, pp. 1172–1181.

[4] R.M. Schainfeld, "Management of peripheral arterial disease and intermittent claudication. JABFP (J. Am. Board Fam. Pract.), 14(6), 2001, 14(6):443-450

[5] A. Banerjee, F.G. Fowkes, P.M. Rothwell, "Associations between peripheral artery disease and ischemic stroke", Stroke, **41**, 2010, pp. 2102-2107.

[6] V.R. Vranish, B.E. Young, J. Kaur, J.C. Patik, J Padilla, P.J. Fadel, "Influence of sex on microvascular and macrovascular responses to prolonged sitting", Am. J. Physiol. Heart Circ. Physiol., **312**, 2017, pp. H800-H805.

[7] C.D.A. Stehouwer, "Microvascular dysfunction and hyperglycemia: a vicious cycle with widespread consequences", Diabetes, **67(9),** 2018, pp. 1729-1741.

[8] B. Rodrigues-Iturbe, R.J. Johnson, "The role of renal microvasculature disease and interstitial inflammation in salt-sensitive hypertension", Hypertension Res., **33(10),** 2010, pp. 975-980.

[9] H. Bomhof-Roordink, A. Soldenrijk, H.P.J. van Hout, H.W.J. van Marwijk, M. Diamant, B.W.J.H. Phenninx, "Associations between the stress and subclinical cardiovascular disease are partly mediated by depressive and anxiety symptoms", J. Psychosomatic Res., **78**, 2015, pp. 332-339.

[10] X. Zhang, N. Staimer, T. Tjoa, D.L. Gillen, J.J., Schauer, M.M. Shafer, S. Hasheminassab, P. Pakbin, J. Longhurst, C. Sioutas, R.J. Delfino, "Associations between microvascular function and short-term exposure to traffic-related air pollution and particulate matter oxidative potential", Environmental Health, **15**, 2016, 81.

[11] P.L. Ljungman, E.H. Wilker, M.B. Rice, E. Austin, J. Schwartz, D.R. Gold, P. Koutrakis, E.J. Benjamin, J.A. Vita, G.F. Mitchell, R.S. Vasan, N.M. Hamburg, M.A. Mittleman, "The impact of multi-pollutant clusters on the association between fine particulate air pollution and microvascular function", Epidemiology, **27(2),** 2016, pp. 194-201.

[12] A.V. Sima, C.S. Sancu, M. Simionescu, "Vascular endothelium in atherosclerosis", Cell and Tissue Res., 2009, pp. 335-191.

[13] M. Guo, Y. Cai, C. He, Z. Li, "Coupled modeling of lipid deposition, inflammatory response an intraplaque angiogenesis in atherosclerotic plaque", Annals of Biomedical Engineering, **47(2)**, 2019, pp. 439-452.

[14] S. Uttarkar, N.C. Brembilla, W.H. Boehncke, "Regulatory cells in the skin: pathophysiologic role and potential targets for anti-inflammatory therapies", J. Allergy Clin. Immunol., 2019, pp. 1-9.

[15] A.H.M. Houben, R.J.H. Martens, C.D.A. Stehouwer, "Assessing microvascular function in humans from a chronic disease perspective" J. Am. Soc. Nephrol., **28(12),** 2017, pp. 3461-3472.

[16] P. Cao, H.H. Eckstein, P. De Rango, C. Setacci, J.B. Ricco, G. de Donato, F. Becker, H. Robert-Ebadi, N. Diehm, J. Schmidli, M. Terra, F.L. Moll, F. Dick, A.H. Davies, M. Lepantalo, J. Apelqvist, "Diagnostic methods", European J. Vascular and Endovascular Surgery, **42(S2),** 2011, pp. S13-S32.

[17] P.E. Tehan, V.H. Chuter, "Vascular assessment techniques of podiatrists in Australia and New Zeeland: a web based survey", J. Foot and Ankle Res., 8(71), 2015, pp.1-8.

[18] X. Li, J. Dunn, D. Salins, G. Zhou, W. Zhou, S.M.S.F. Rose, D. Perelmn, E. Colbert, R. Runge, S. Rego, R. Sonecha, S. Dalta, T. McLaughlin, M.P. Snydar, "Digital Health: tracking physiomes and activity using wearable biosensors reveals useful health-related information", PLoS Biol, **15(1)**, e2001402, 2017, pp. 1-30.

[19] Task Force of the European Society of Cardiology and the North American Society of Pacing and Electrophysiology, "Heart rate variability: standards of measurement, physiological interpretation and clinical use", Circulation, **93(5),** 1996, pp. 1043-1065.

[20] D.J. Bowen, M. Krenter, B. Spring, L. Cofta-Woerpel, L. Linnan, D. Weiner, S. Bakken, C.P. Kaplan, L. Squiers, C. Fabrizio, M. Fernandez, "How we design feasibility studies" Am. J. Prev. Med., **36(5)**, 2009, pp. 452-457.

[21] G. Pariyo, A.C. Wosu, D.G. Gibson, A.B. Labrique, J. Ali, A.A. Hyder, "Moving the agenda on noncommunicable diseases: policy implications of mobile phone surveys in low and middle-income countries", J. Med. Internet Res., **19(5):e115**, 2017, pp. 1-18.

[22] M.J. Palmer, S. Barnard, P. Perel, C. Free, "Mobile phone-based interventions for improving adherence to medication prescribed for the primary prevention of cardiovascular disease in adults", Cochrane Database Syst. Rev., **6(CD012675)**, 2018, pp. 1-60.

[23] I.Tulevski, D.T. Ublink, M.J.H.M. Jacobs, "Red and green laser Doppler compared with capillary microscopy to assess skin microcirculation in the feet of healthy subjects", Microvas Res, **58(2),** 1999, pp. 83-88.

[24] J. Padilla, P.J. Fadel, "Prolonged sitting leg vasculopathy: contributing factors and clinical implications", Am. J. Physiol. Heart Circ. Physiol., **313(4),** 2017, pp. H722-H728.

[25] O. Mutlak, M. Aslam, N.J. Standfield, "Chronic venous insufficiency: a new concept to understand pathophysiology at the microvascular level – a pilot study", Perfusion, **34(1)**, 2019, pp. 84-89.

[26] R. Lane, A. Harwood, L. Watson, G.C. Leng GC, "Exercise for intermittent claudication (review)", Cochrane Database of Systematic Reviews, **12(CD0009990)**, 2017, pp. 1-138.